



**HAL**  
open science

## Diffuse radio sources in galaxy clusters

Gerardo Martinez Aviles

► **To cite this version:**

Gerardo Martinez Aviles. Diffuse radio sources in galaxy clusters. Astrophysics [astro-ph]. COMUE Université Côte d'Azur (2015 - 2019), 2017. English. NNT : 2017AZUR4076 . tel-01720462

**HAL Id: tel-01720462**

**<https://theses.hal.science/tel-01720462>**

Submitted on 1 Mar 2018

**HAL** is a multi-disciplinary open access archive for the deposit and dissemination of scientific research documents, whether they are published or not. The documents may come from teaching and research institutions in France or abroad, or from public or private research centers.

L'archive ouverte pluridisciplinaire **HAL**, est destinée au dépôt et à la diffusion de documents scientifiques de niveau recherche, publiés ou non, émanant des établissements d'enseignement et de recherche français ou étrangers, des laboratoires publics ou privés.



École doctorale Sciences Fondamentales et Appliquées  
Unité de recherche: Lagrange

# Thèse de doctorat

Présentée en vue de l'obtention du  
grade de docteur en Astrophysique Relativiste  
de  
Université Côte D'Azur

par

**Gerardo Martinez Aviles**

Titre de la thèse:

**SOURCES RADIO DIFFUSES DANS LES AMAS DE  
GALAXIES**

Dirigée par Chiara Ferrari

Soutenue le 12 Octobre 2017  
Devant le jury composé de:

Annalisa Bonafede	Chargé de Recherche, INAF - IRA	Examinatrice
Luigina Feretti	Directrice de Recherche, INAF - IRA	Rapporteur
Chiara Ferrari	Astronome, OCA, Laboratoire Lagrange	Directrice de la thèse
Federica Govoni	Chargé de Recherche, INAF	Examinatrice
Oliver Hahn	Professeur, UNS, OCA, Laboratoire Lagrange	President
Melanie Johnston-Hollitt	Professeur Associé, Victoria University of Wellington	Examinatrice
Sophie Maurogordato	Directrice de Recherche, OCA, Laboratoire Lagrange	Examinatrice
Philippe Salomé	Astronome Adjoint, Laboratoire LERMA, UMR, CNRS	Rapporteur

---

## Résumé

Les connaissances sur l'origine de Radio Halos (RHs), les émissions radio diffuses de brillance superficielle bas à échelle de Mpc observées dans les amas de galaxies massives, ont progressé vers un consensus général sur les dernières années. Le scénario généralement accepté pour le mécanisme responsable de ce type d'émission diffuse c'est la ré-accélération des électrons relativistes par la turbulence générée par les fusions des amas. Sur ce cadre, on attend des modèles qu'une fraction plus grande de l'apparition des RHs apparaissent à  $z = 0.3-0.4$ . Cependant, les observations radio des amas de galaxies dans ce régime de redshift sont encore limitées. Le projet MACS-Planck Radio Halo Cluster Project vise à explorer l'origine et l'apparition des RH, ainsi que leur lien avec l'état dynamique des systèmes hôtes, en explorant une gamme de redshift plus élevée que les études précédentes. Dans cette thèse, je présente les données publiées du sous-échantillon ATCA du projet et les perspectives pour les travaux futurs.

## Abstract

The knowledge on the origin of Radio Halos (RHs), Mpc-scale low surface brightness diffuse radio emission observed in massive galaxy clusters, has moved towards a general consensus on the recent years. The generally accepted scenario for the mechanism responsible of this kind of diffuse emission is the re-acceleration of relativistic electrons by the turbulence generated in cluster mergers. On this framework, it is expected from models that a larger fraction of RH occurrence may appear at  $z=0.3-0.4$ . However, radio observations of galaxy clusters in this redshift regime are still limited. The MACS-Planck Radio Halo Cluster Project has the aim of exploring the origin and occurrence of RHs, as well as their connection with the dynamical state of the host systems by exploring a higher redshift range than previous studies. In this thesis, I present the published data of the ATCA subsample of the project and prospects for the future work.

---

*“Lo que nos toca es ser lectores de la historia de la astronomía, para tal vez algún día escribir nosotros mismos algunas líneas”*

—Camilo Delgado Correal

*“However variable its aspects may be, the whole universe obeys a permanent law and its elements, however variegated they may be, are governed by harmony.”*

—Ibn al-Haitham, d. ca. 1040 c.e.

# Contents

<b>1</b>	<b>Introduction to Radio Astronomy</b>	<b>1</b>
1.1	A brief history of radio astronomy . . . . .	1
1.2	The radio sky . . . . .	4
<b>2</b>	<b>Galaxy Clusters</b>	<b>15</b>
2.1	Introduction . . . . .	15
2.2	Detecting Galaxy Clusters . . . . .	18
2.2.1	Optical and near infrared . . . . .	20
2.2.2	X-Ray . . . . .	21
2.2.3	The Sunyaev-Zel'dovich effect . . . . .	21
<b>3</b>	<b>Diffuse radio sources in Galaxy clusters</b>	<b>23</b>
3.1	Introduction . . . . .	23
3.2	Radio Relics . . . . .	25
3.3	Radio Mini-halos . . . . .	27
3.4	Radio Halos . . . . .	28
3.4.1	Physical models of creation of Radio Halos . . . . .	30
3.4.2	Observational constraints . . . . .	32
3.4.2.1	Scaling Relations . . . . .	32
3.4.2.2	Radio Halo - Merger connection . . . . .	32
<b>4</b>	<b>The Macs-Planck Radio Halo Project</b>	<b>39</b>
4.1	Introduction . . . . .	39
4.2	Sample selection . . . . .	42
4.3	The ATCA sub-sample . . . . .	43
4.3.1	Observations and data reduction . . . . .	43
4.3.2	Radio Images Processing . . . . .	45
4.3.2.1	Full resolution maps . . . . .	45
4.3.2.2	Tapering and diffuse source search . . . . .	45
4.3.2.3	Upper limit determination . . . . .	47
4.4	The GMRT sub-sample . . . . .	48
4.4.1	Observations and data reduction . . . . .	48
4.4.2	Tapering, diffuse source search and upper limit determination . . . . .	50
<b>5</b>	<b>Analysis of the ATCA sub-sample</b>	<b>53</b>
5.1	Radio image analysis . . . . .	53
5.1.1	Full resolution maps . . . . .	53
5.1.2	Compact source subtracted tapered images . . . . .	54

5.2	X-ray dynamical state of the ATCA clusters . . . . .	56
5.3	Results . . . . .	59
5.3.1	A Radio Halo in PSZ2 G284.97-23.69 . . . . .	59
5.3.1.1	Detection of the source using PyBDSM . . . . .	62
5.3.1.2	Radio luminosity vs. cluster mass correlation . . . . .	64
5.3.2	Diffuse radio source in the cluster PSZ2 G262.73-40.92. . . . .	67
5.4	Clusters without diffuse radio emission . . . . .	68
5.4.1	The Cool-core cluster PSZ2 G271.18-30.95 . . . . .	68
5.4.1.1	Highly disturbed clusters without radio emission . . . . .	69
5.4.2	The triple system of low mass clusters PLCK G334.8-38.0 . . . . .	70
5.4.2.1	Detection limits . . . . .	71
5.5	Conclusions . . . . .	72
<b>6</b>	<b>A first analysis of the GMRT sub-sample</b>	<b>77</b>
6.1	Full resolution and tapered residual radio maps . . . . .	77
6.2	X-ray-optical dynamical analysis of GMRT sub-sample . . . . .	77
6.3	Radio properties of GMRT sub-sample . . . . .	82
6.3.1	Classification 1 clusters . . . . .	82
6.3.2	Classification 2 . . . . .	83
6.3.3	Classification 3 and 4 . . . . .	84
6.3.4	Clusters with missing dynamical state analysis . . . . .	84
6.4	Detection limits . . . . .	85
<b>7</b>	<b>Conclusion and Perspectives</b>	<b>89</b>
<b>A</b>	<b>High resolution images of the ATCA sub-sample</b>	<b>93</b>
<b>B</b>	<b>High resolution radio images of the GMRT sub-sample</b>	<b>97</b>
<b>C</b>	<b>Papers Published</b>	<b>107</b>
C.1	ATCA observations of the MACS-Planck Radio Halo Cluster Project. I. New detection of a radio halo in PLCK G285.0-23.7 . . . . .	107
C.2	ATCA observations of the MACS-Planck Radio Halo Cluster Project II. Radio observations of intermediate redshift ATCA cluster sample . . . . .	119
	<b>Bibliography</b>	<b>141</b>

# Introduction to Radio Astronomy

---

## Contents

---

<b>1.1 A brief history of radio astronomy</b> . . . . .	<b>1</b>
<b>1.2 The radio sky</b> . . . . .	<b>4</b>

---

In this introductory chapter, I would like to present a short overview of astronomical observations in the radio band. As we will see, what we consider contemporary astrophysics was born a bit more than one century ago, and the very nucleus of this thesis, radio astronomy, more or less half of the way back. On the way to our times, radio astronomers have found a good number of totally unexpected objects which opened the window to a new world of research and understanding of our Universe. I consider that in the dawn of the golden era of radio astronomy, its worth while recalling this story...

## 1.1 A brief history of radio astronomy

The astrophysicist Michael Longair considers that the birth of modern astrophysics at the end of the 19th Century was possible because of four great technological achievements (Longair, 2013). The first one is the invention of photography. By exposing a photographic plate to an astronomical source for a long amount of time, we are able to integrate the number of photons coming from the source, allowing us to reach very faint features of celestial objects. The second achievement is the discovery of spectroscopy. By analysing the spectrum of the light coming from an astronomical source, astronomers are able to know a great number of its characteristics, such as its chemical composition, temperature, density, etc. Another very important astronomical use of spectroscopy is that it also allows to measure the line of sight speed of the source relative to the observer by measuring the Doppler shift of known spectral lines. The third achievement is the measurement of stellar parallax. By knowing the parallax of stars, astronomers are able to estimate their distances, and use this information to know their absolute magnitudes, for example. This is of great importance as it is one of the first steps on climbing the "cosmic distance ladder", or the succession of methods by which astronomers determine the distances to celestial objects. The fourth achievement is the access to wavelengths and frequencies outside the visible window. The visible band goes from  $\sim 0.4 - 0.7$  micrometers. If it is true that it is a very narrow window, we are also

lucky enough so that the Earth's atmosphere is transparent to these range of wavelengths. This is not the case for most of the wavelengths coming from space. Our atmosphere blocks the light that corresponds to the ultraviolet (UV), Infra-red, microwave, X-Ray and Gamma-Ray bands. The access of humankind to most of the electromagnetic spectrum coming from space had to wait to the age of satellites, in the middle of the 20th Century. Apart from the optical band, radio, millimetre and submillimetre bands are also observable from the Earth's surface. The radio band reaches a limit for long wavelengths because of reflection from the ionosphere (see Figure 1.1).

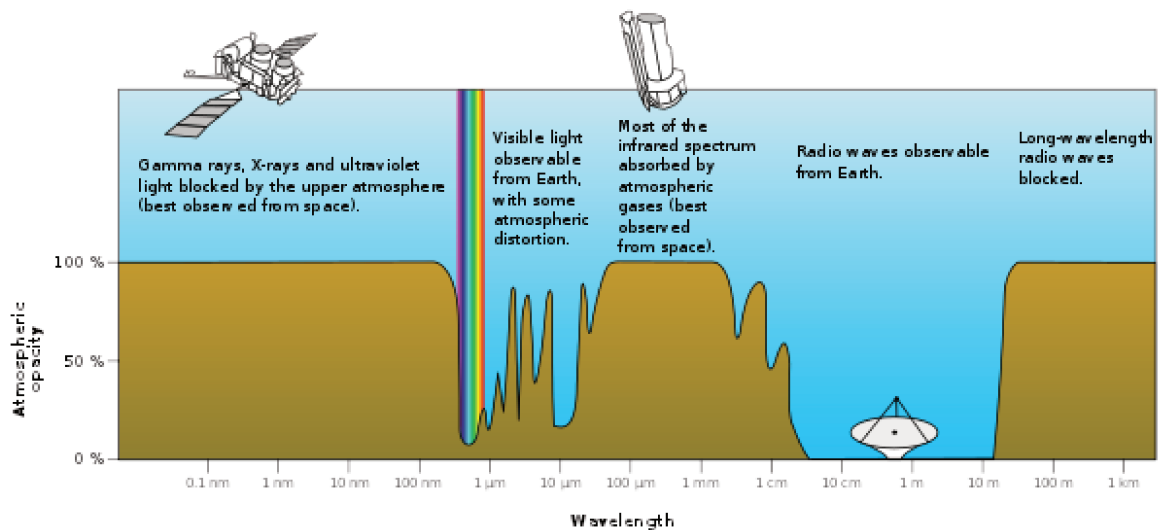


Figure 1.1: Most of the electromagnetic spectrum coming from space is blocked by the Earth's atmosphere except for visible, radio, millimetre and sub-millimetre bands. Credit: Wikipedia.

The first detection of electromagnetic radiation coming from space outside the visible band was in 1933, when Karl Jansky announced the discovery of radio emission from the Milky Way (Longair, 2013). Jansky was not interested on astronomical research when he made his historical discovery. He was indeed working for the Bell Telephone Laboratories, trying to identify naturally occurring sources of noise that could interfere with radio communications. His observations, made at 20.5 MHz, turned out to be originated in the center of our Galaxy. Some years after, this result was confirmed by Grote Reber, who proposed that this radiation had no thermal origin, but it had to be of bremsstrahlung or free-free emission. Even if this results were matter of a small controversy, the astronomical community paid little attention to them.

The Second World War gave new impetus to the evolution of radio astronomy (Mitton, 2011). The development of radar technology, and the possibility of having radio sources that could interfere with the use of radars, lead James Hey and his colleagues from the Army Operational Research Group of the United Kingdom to the discovery of intense radio emission

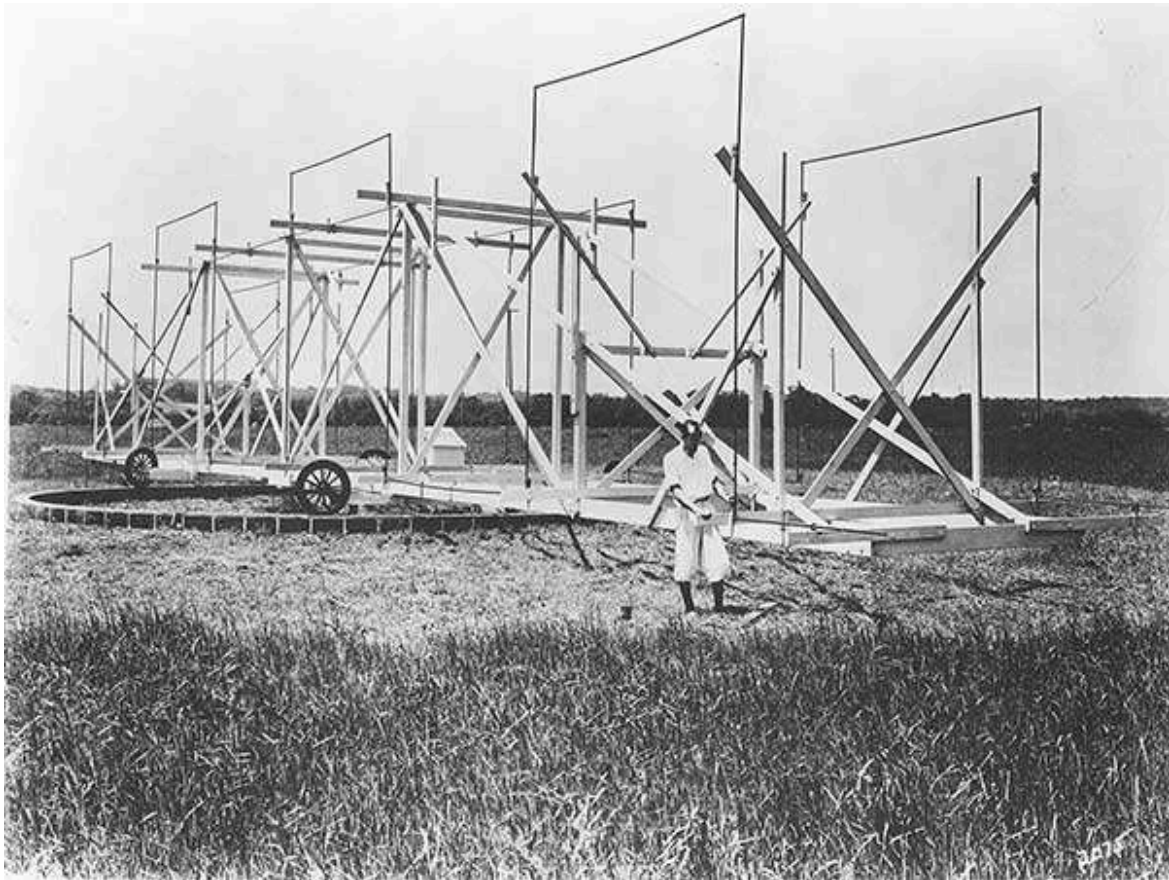


Figure 1.2: Karl Jansky and the antenna used to make his historical radio observations. Photo: Bell Telephone Laboratories.

coming from the Sun in 1942 (Longair, 2013), the emission coincided with an unusually high sunspot activity. The same team discovered in 1946 the first discrete radio source in the sky. The source became famous with the name Cygnus A; which is a radio galaxy and one of the brightest radio sources in the sky (Figure 1.3).

Radio astronomy became a field of study on its own right until the mid 1950's. Since then, a number of large dish antenna radio telescopes were constructed around the world. Even if single dish telescopes had excellent sensitivities, the angular resolution  $\theta$  is limited by the diameter,  $D$ , of the antenna. One way of solving the problem is by the use of *interferometry* (Munns, 2013). The resolution of a telescope is given by the Rayleigh criterion  $\theta \approx \lambda/D$  (Longair, 2013), with  $\lambda$  the wavelength of the incoming wave. By measuring the amplitudes and phases of the incoming radio signals, the distribution of radio brightness across the sky can be reconstructed. One of the key characters on the development of techniques in radio interferometry was Martin Ryle (Longair, 2013; Mitton, 2011), who in the mid-1960s developed a technique known as aperture synthesis. By using the data obtained with two radio antennas, and changing the distance among them, the resolving power increases

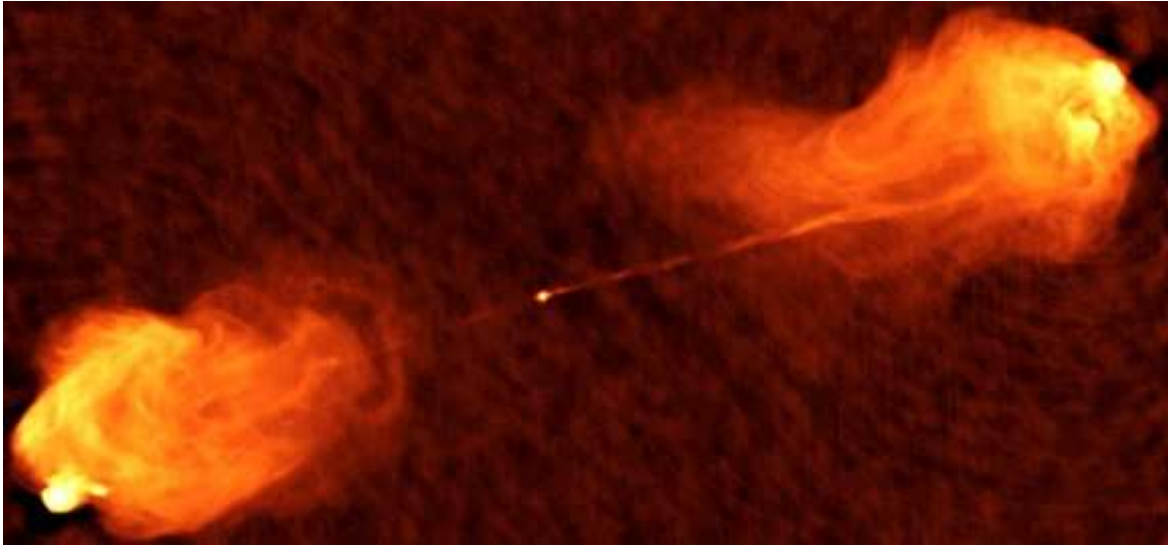


Figure 1.3: Image of the radio galaxy Cygnus A (3C 405), one of the brightest radio sources in the sky. Image courtesy of NRAO/AUI

tremendously. A number of radio interferometers were constructed around the world, such as the Westerbork Synthesis Telescope in Netherlands, The Very Large Array in New Mexico, USA, or the Giant Metrewave Radio Telescope in India. The discoveries in the field of Radio Astronomy on the last 60 years are among the most fundamental ones in the history of modern astrophysics. The most remarkable examples are the discovery of quasars, the Cosmic Microwave Background (CMB), neutron stars, pulsars, interstellar molecules and other cosmic objects that we will briefly explore in the following sections.

## 1.2 The radio sky

Why is the night sky dark? This apparently innocent question have profound cosmological consequences. The question was formulated by Johannes Kepler and later on by Wilhelm Olbers, and it is known as Olbers' paradox (Harrison, 1990). There have been proposed several solutions to the paradox, and here I would like to propose a radio astronomer's one: The night sky is not dark at all!! It is just a matter of observing in the correct frequency. The radio sky looks totally different to the optical sky, because the origin of the radiation is of different nature. Being most of the strongest astronomical radio sources of non-thermal origin, the radio sky looks brighter at lower frequencies. The whole sky will start to glow at frequencies below  $\sim 100$  MHz. If we continue to perform observations at lower frequencies, the radio emission from our own galaxy (see Fig. 1.4) will be indistinguishable from the background. However, we will notice that at frequencies of tens of MHz, the sky will become darker because nearby thermal interstellar gas will absorb radio waves. Finally, the lowest frequency part of the spectrum (below  $\sim 10$  MHz) is blocked by Earth's ionosphere,

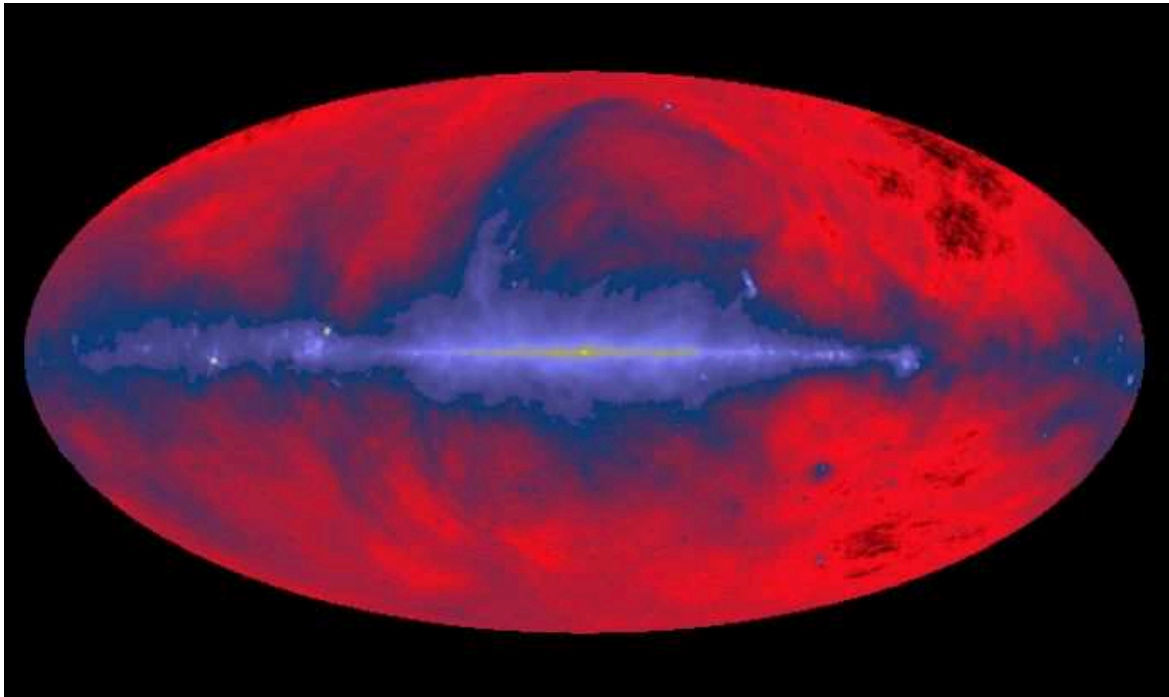


Figure 1.4: The radio sky at 408 MHz. Credit: C. Haslam et al., MPIfR, SkyView

preventing ground-based radio observations to be performed. In short, the radio sky will change depending on the chosen frequency (Verschuur, 2007).

### Radiation mechanisms

In all the processes where we observe radio emission we must find a fundamental ingredient: the movement of charged particles. In particular, changes on the velocities of these particles make them lose energy, which is radiated away in the form of an electromagnetic wave in the radio band. Radio waves may be produced, for example, by electrons moving relatively slowly, with speeds of  $\sim 10^2$  km/s found in hot clouds of gas surrounding a star. Another possibility is the movement of electrons at much higher relativistic speeds on larger length scales. These two different kind of emission are coined, respectively, thermal and non-thermal (Verschuur, 2007).

Everything that has temperature shines. This is another way of saying that matter which has temperature higher than the absolute zero emits thermal radiation. Inter-atomic collisions of the particles causes their kinetic energy to change, which results effectively in a charge acceleration, and therefore electromagnetic radiation emission. The emitted radiation from a thermal origin comes in a wide spectrum of frequencies of emission, as a result of the wide spectrum of kinetic energy changes (or particle accelerations) involved in the process. This characterizes the spectrum of thermal radiation as a continuous dispersion of photon energies. A thermal radiating body can reach thermodynamic equilibrium with its surface,

and if the surface has perfect absorptivity at all wavelengths, then the body is characterized as a black body, which follows the Planck's law of thermal radiation power:

$$u(\nu, T) = \frac{2h\nu^3}{c^2} \cdot \frac{1}{e^{h\nu/k_B T} - 1} \quad (1.1)$$

where  $\nu$  is the frequency,  $h$  is Planck's constant,  $c$  is the speed of light,  $T$  is the temperature and  $k_B$  is Boltzmann's constant.

The other kind of emission, the non-thermal radiation, is also called synchrotron radiation. This process of emission involves cosmic rays spiralling magnetic field lines because of the Lorentz force:

$$q\vec{v} \times \vec{B}. \quad (1.2)$$

where  $q$  is the charge of the particle,  $\vec{v}$  its velocity, and  $\vec{B}$  the magnetic field. Charged particles emit photons when accelerated, and if the velocity is relativistic, the radiation can be particularly intense. Synchrotron radiation is beamed in the direction of the velocity of the moving particle and can also exhibit polarization if there is large scale coherence of magnetic field directions in the source region. The spectrum of synchrotron radiation reflects the distribution of energies of the radiating particles, usually being a *power law*:

$$I = K\nu^{-\alpha} \quad (1.3)$$

where  $I$  is the specific intensity,  $\alpha$  a dimensionless exponent called spectral index, and  $K$  a proportionality constant. The wavelengths of emission can fall in any of the values across the electromagnetic spectrum depending on the energy of the particle and on the strength of the magnetic field. In the following sections, we will briefly explore the most usual astrophysical radio sources.

### The Sun

The Sun is a source of radio signals generated by both the synchrotron process of high speed electrons spiralling around solar magnetic fields and thermal emission from the movement of electrons in the hot plasma. There is a third mechanism where oscillations of the solar plasma generate radio emission (Dulk, 1985). The Sun has some radio activity during the sunspot minimum coming from regions in the low corona. By definition, the radio quiet sun is observed when there is little violent activity in its surface. There has been observed a slowly varying component of radio activity which coincides with the rotation of the Sun each 28 days (Hood and Hughes, 2011). In some cases, regions of the solar surface grow hotter and brighter until a flare explosion occurs. For example, the so-called Solar Radio Bursts have been observed to occur near this active regions of the Sun (see e.g. Kupriyanova et al., 2016).

### The Moon and the Planets

The case of the Moon is very interesting for radio astronomers. For example, by timing occultations by the Moon of radio sources in the sky, their positions can be calculated with great accuracy. By this method a quasi-stellar radio source was accurately positioned for the first time (Clarke, 1966). Besides the thermal emission due to its temperature, the Moon radio emission has also some non-thermal components due to: a) Reflection of Man-made or Earth-shine radio waves, b) Reflection of galactic emission and c) Reflection of solar emission (Vedantham et al., 2015).

The Moon, Mercury and Mars are relatively normal sources of thermal radio emission, being the radio brightness a function of their temperatures. Venus, however, has a relatively high temperature at its surface because of the greenhouse effect of the carbon dioxide present in its atmosphere. Among the first measurements of Venus' temperature were done by performing radio observations of the planet (Young and Young, 1975). Jupiter has a strong radio activity. The giant planet produces intense bursts with a peak energy concentrated around 20 MHz, even if the parent mechanism is not completely understood (Verschuur, 2007) and some radiation belts which are the source of non-thermal radio waves have been detected in the giant planet. Furthermore, new generation radio telescopes, such as LOFAR, are carrying observational programmes to detect radio emission from exoplanets (Zarka, 2011).

### Supernova Remnants

The radio source Taurus A (Tau A) is one of the brightest radio sources in the sky. Also known as the Crab Nebula, it is the remnant of a supernova observed by Chinese and native American astronomers in the year 1054. The radio spectrum of Taurus A is non-thermal in nature and its light is polarized. Another very famous radio source, actually the brightest in the sky, is another supernova remnant called Cassiopeia A (Cas A). Both Tau A and Cas A are remnants of the explosions of single massive stars. These explosions, called Type II supernovae, are the violent end of the life of massive stars (Dubner and Giacani, 2015). When the pressure on the core of the star cannot longer support its weight they suffer a dramatic collapse. When the collapse is complete, the central part of the core is converted into nuclear matter. The nuclear matter is compressed beyond its equilibrium density and then rebounds, launching a powerful shock wave (Brown and Bethe, 1985). Radio emission from core-collapse supernovae generally occurs when the forward shock sweeps up the dense, slow-moving wind generated by a red supergiant progenitor. Radio observations of supernovae remnants can give crucial information to know, for example, the electron density of the stellar winds or the mass loss rate of the progenitor star (Callingham et al., 2016).

### Nebulae and Star Forming Regions

Stars are formed by the gravitational collapse in dense regions within molecular clouds in the interstellar space. The created young stars heat the remaining gas of the molecular clouds which then radiates light, heat and radio waves by thermal emission processes. When

a UV photon from a hot star hits a hydrogen atom, the energy exchange can free an electron, ionizing the gas and leaving a free proton and a free electron. A large cloud with a mix of free protons and electrons emits thermal radiation, and it is known as an HII region. Thermal radio emission from HII regions can be used to estimate the electron temperature, the electron density or the ionized volume (NRAO, 2016).

### **Planetary nebulae**

Planetary nebulae account for the majority of compact continuum radio sources in our Galaxy. We have seen that massive stars end their lives in core-collapse supernova explosions. However, less massive stars suffer less violent deaths. In this case, when the nuclear reactions of the center of the star can no longer support the weight of the outer layers, their gravity toll on the structure of the star and forces the inner parts to contract and heat up. This temperature increase drives the outer layers of the star away in energetic stellar winds that last just few thousands of years. At the end of this process, the remaining core is uncovered and it heats the distant and expanded gases, and they start to glow (Jacoby, 2016). As planetary nebulae are essentially clouds of strongly ionized gas, it is expected that they show continuous radio emission from thermal origin. However, planetary nebulae are very weak radio sources (Gurzadyan, 1997), but they are not subject to the dust extinction suffered by the optical frequencies. This, plus the fact that they are the most numerous discrete radio continuum sources, makes planetary nebula useful tools to know, for example, the last stages of the life of a star or can be used as records of low-mass star formation through the history of the galaxy (NRAO, 2016).

### **Interstellar Hydrogen**

The interstellar space is filled with diffuse hydrogen and in any lack of energetic sources, like nearby hot stars, the hydrogen remains cold and neutral. This form of neutral hydrogen is known as HI. The neutral hydrogen atom is formed by a proton which has an electron in an orbit around it. It is known from quantum mechanics that both, the proton and the electron, possess a property called spin, and both spins can point in the same direction (parallel) or in opposite directions (antiparallel). The proton and the electron are charged particles, and the fact of having a spin produces magnetic fields. If the electron is in its ground state, this means, in the closest possible orbit around the proton, the magnetic interaction between the two particles becomes measurable. If the magnetic axis of the proton and the electron are parallel, the system is in a higher energy state than if their magnetic axis are antiparallel. The electron spin can flip from parallel to antiparallel, or from a higher to a lower energy state, and in this process it emits photons with an energy correspondent to the difference between these two hyperfine energy levels, with a frequency of 1420 MHz or a wavelength of 21 cm (Ewen, 1953). The study of the 21 cm hydrogen line has been useful to study the movement of neutral hydrogen in the Milky Way and the Magellanic clouds (Ewen, 1953). Knowing the structure

of the distribution of hydrogen in detail provides considerable information to the study of turbulence in interstellar matter and to make direct measurements of the temperature of the gas clouds. The splitting of radio-absorption lines also offers the possibility of measuring the very weak magnetic fields in interstellar space (Lilley, 1957). The study of HI is fundamental to get knowledge on galactic dynamics, since it can give us information about the evolution of the gas content in galaxies. However, the observation of HI requires high angular resolution and sensitivities to very low column densities. One of the most promising new generation radio telescopes, the Square Kilometre Array (SKA), has the study of HI as one of its main scientific drivers (de Blok et al., 2015).

### Interstellar molecules

The existence of molecules in the interstellar space was discovered because they emit radio waves in the form of spectral lines. Interstellar molecules are found usually in dense clouds of dust or in shells around stars (Verschuur, 2007). ~ 190 molecules have been discovered in the interstellar medium or around stars and another ~ 60 are extragalactic (Koeln Physikalisches Institut, 2016). Some of these molecules are composed by more than 12 atoms. Moreover, ~ 500 molecular spectral lines have been detected but not identified (Verschuur, 2007). Between the identified molecules we find carbon monoxide, water, ammonia, hydrogen sulfide, formaldehyde and methyl alcohol. The knowledge of the chemistry of space molecules is extremely important specially in the new fields of research on exoplanets and astrobiology. The discovery of complex molecules in space changed the picture of the physical conditions needed for molecules either to form or to emit (or absorb) spectral lines. The change of the state of motion of molecules and their electrons result in the emission or absorption of spectral lines. Molecules tend to rotate around their axis of symmetry. Changes in this rotation causes the molecule to absorb or emit radiation. The vibration of the atoms that compose molecules have energy levels associated, and changes on the modes of vibration also involve the emission or absorption of spectral lines. Finally, the electrons of the molecules can occupy different orbits, and changes of orbit are also responsible of the observed spectral lines (Turner, 1973). Instruments such as the Atacama Large Millimeter Array (ALMA), for instance, has the sensitivity and resolution to perform complete spectral surveys between 2.7 and 3.6 mm, allowing amazingly challenging detections, such as the discovery of complex organic molecules in gas clouds close to the galactic center (Max-Planck-Gesellschaft, 2014).

### Masers

Astrophysical masers (Microwaves Amplified by Stimulated Emission of Radiation) are sources of stimulated spectral line emission, typically in the microwave band. Their origins may vary from planetary or stellar atmospheres, comets or molecular clouds. There are several cases of astrophysical environments that allow the conditions for maser emission.

Masers (and their optical equivalent, lasers) arise from a condition coined "population inversion". In this kind of populations, the number of atoms or molecules in a higher-energy state exceeds the number of those with lower energies. As a result, the response of the population to an incoming photon is to emit another photon. Each photon emitted triggers the release of additional photons, resulting in the amplification of the incoming light (Elitzur, 1995). Just to give an example, masers on stars can provide radio astronomers very high precision astrometric measurements, giving new insight on the kinematics and evolution of the Milky Way galaxy and its Local Group neighbours (Green et al., 2015).

### Pulsars

We have mentioned that massive stars end their lives as core-collapse supernova explosions. A so-called neutron star is the remnant of a very massive star after a core collapse supernova explosion. After the star expands to become a red giant, its nucleus becomes extremely dense, compressing several solar masses in a radius of several thousand kilometres. Unable to maintain its own gravitational attraction, in some cases the fundamental particles that compose the star nucleus -protons and electrons- are squeezed together to create neutrons during the collapse. The result is a super dense star of 1.4 solar masses within a radius of  $\sim 10$  km (Piran, 1995). Neutron stars possess strong magnetic fields which should emit high energy charged particles from its magnetic poles (Ostriker, 1971). Moreover, the magnetic poles should not necessarily coincide with the rotation poles, which creates a "lighthouse effect", the beam of radiation is just detected if an observer is aligned with the beam responsible of the emission. The extremely rapid periods of pulsation are due to the fact that rotating neutron stars retain most of the original angular momentum of the star, and its very dense composition allows them to rotate at such high rates without being disrupted. The discovery of pulsars is one of the most remarkable ones in the history of radio astronomy. The fact of being extremely precise astronomical clocks makes them extremely useful as, for example, lighthouses to define coordinates in the galaxy, or as laboratories for testing general relativity predictions (McNamara, 2008). For instance, by performing observations of a large sample of pulsars spread across the celestial sphere forming a Pulsar Timing Array (PTA), makes possible a positive detection of the Gravitational Wave background in the Galaxy (Manchester, 2010).

### Radio Galaxies, Quasars and AGNs

We have seen that a "normal" galaxy, as the Milky Way, will present some radio emission due to synchrotron radiation from electrons moving through the galaxy and being accelerated by magnetic fields. It has been observed that the power of radio emission shows a close relation with two observable parameters that are at the same time related to the last episode of star formation of the galaxy. These observables are: a) The rate of supernovae occurrence and b) the emissivity in the far infrared. The most energetic of these kind of galaxies are

known as starburst galaxies, and their radio emission is composed by synchrotron, free-free and thermal components. Radio emission is observed in a number of spiral galaxies, but there are relatively faint compared with Radio Galaxies or Quasars.

Radio Galaxies (RGs) can shine up to 3 kpc across (much farther than the borders of the visible galaxies to which they are usually associated). The most common hosts of the most luminous radio galaxies are sometimes giant ellipticals. The typical structure of radio galaxies is mainly determined by the presence of energetic jets that interact with ionized gas surrounding the host galaxy, which is seen in other frequencies, such as in the X-ray emission of galaxy clusters. The interaction of the electron population present in jets and lobes with magnetic fields causes radio galaxy emission to be of synchrotron origin (Burke and Graham-Smith, 2014). RGs are separated in two different luminosity classes according to their particular radio morphology (Fanaroff and Riley, 1974). The so-called Fanaroff-Riley (FR) IIs possess radio lobes with very prominent hot spots and bright outer edges, while FR Is the radio emission is more diffuse. There are fundamental differences between the two types of RGs, which might arise from a dichotomy in their central engine (see Padovani, 2016, and references therein), being the FR I type caused by low accretion rate sources and higher accretion rates responsible of FR II types. There are some newly discovered radio sources without extended emission and therefore no FR I/II distinction possible. The study of these FR 0 RGs is still in its infancy but, so far, it looks that this class can be quite heterogeneous and to explain the physical mechanism responsible for their origin is a challenge for radio-astronomers.

Radio quasars are much more compact objects (with core dimensions ranging from 1 to 0.01 pc (Burke and Graham-Smith, 2014)). The amount of energy required to feed this compact object was so huge, that it was proposed that supermassive black holes accreting matter should be responsible for the mechanism (Lynden-Bell, 1969). Therefore, radio quasars are intrinsically the same sources as RGs. Radio quasars and Radio galaxies belong to a rich zoology of objects based on their observational characteristics, which classification is complicated, but that now-a-days are studied in a "unified scheme" of Active Galactic Nuclei (AGN). In this paradigm, the main source of energy is a disk of baryonic matter infalling onto a supermassive black hole (Tasse, 2008). An obscuring dusty torus and the inclination angle of the disk-torus with respect to the observer may account for the different observed characteristics of the AGN (Urry and Padovani, 1995).

After the discovery of the first quasars it was realized that a number of similar sources were undetected by radio telescopes and were called Radio-quiet AGNs, although they are not really radio-quiet, but more accurately "radio faint". They constitute more than 90 % of the AGN class. The studies on this kind of sources have shown that they are intrinsically different to Radio loud AGNs, whose emission is dominated by thermal emission instead of synchrotron (Padovani, 2016)

Relatively strong radio emitters, hosted by spiral and irregular galaxies are the so-called Star-forming galaxies (SFGs). The radio emission of SFGs is synchrotron emission that results from the relativistic plasma accelerated by supernova remnants associated with massive

star formation, and not from a central AGN as we have seen above. It has been observed that the fraction of SFGs increases rapidly with redshift. This means that at high redshifts most galaxies are undergoing star formation, while SFGs are rare in the local Universe. Local RGs are associated with the concept of starburst (SB) galaxies, which are probably triggered by major mergers or dense SF regions. A correlation between the galaxy's SF rate (SFR) and its stellar mass discovered in the last decade and referred as the "main sequence" (MS). This correlation is used in the modern definition of SFGs, which is redshift dependent, denotes SFG the ones that belong to the MS, being SB galaxies above the correlation and passive galaxies below (Padovani, 2016).

### Radio Cosmology

Finally, I would like to outline the contributions that radio astronomy have done, and is still doing, for the study of the Universe in its largest scales, and thus for cosmology. If it is true that the questions about the origin and composition of the Universe have been in the minds of human beings since very antique times, it was until the 20th century, with the advent of General Relativity, that cosmology became finally a field of study on the modern scientific sense. Combining the theoretical framework with astronomical observations and particle physics experiments, it is current to find that we are actually living the era of high-precision cosmology. The standard model of cosmology can be named after its major components: The Big Bang inflationary lambda cold dark matter ( $\Lambda$ CDM) model.

How can radio astronomy contribute to research in cosmology? At this point, it is worth mentioning the role that radio-astronomy has played in modern cosmology. For instance, in previous sections, we have presented quasars and radio galaxies. These astronomical objects actually have very large radio luminosities, and that is the reason why they can be easily observed up to very large distances. This property of radio sources makes them extremely useful as probes of the geometry of the Universe on large scales. It was actually by counting the distribution of compact radio sources that astronomers tried to measure the geometry of the Universe before the Big Bang theory was well established (Narlikar and Burbidge, 2008; Mitton, 2011; Kragh, 1999). These results, however, remained as a matter of controversy until a major discovery was done:

In 1965 Arno Penzias and Robert Wilson, from the Bell Telephone laboratories (again!) discovered serendipitously the presence of a low temperature cosmic background microwave radiation. The cosmic background radiation consist of electromagnetic waves of thermal origin that travel from all directions in space with a black body temperature of  $\sim 2.73$  K (Harrison, 2000). It is proposed that the Cosmic Microwave Background CMB is the most ancient light available for astronomers, originating in the distant past, when in a much smaller, hotter and denser Universe photons were constantly interacting with free electrons in the hot plasma. Roughly 380,000 years after the Big Bang, the Universe expanded and cooled enough to allow the free electrons to combine with protons, and permitting light to travel freely in the expanding space (Peebles et al., 2009). The CMB contains the imprint of the presence of

small fluctuations (anisotropies) on its temperature at the level of 1 part in  $10^5$ , measured by the Cosmic Background Explorer (COBE) (Smoot et al., 1992), and improved by the Wilkinson Microwave Anisotropy Probe (WMAP). These anisotropies are the "seeds" from which stars, galaxies and galaxy clusters are formed. The study of the CMB improved dramatically in precision after the mission Planck, launched in 2009 by the European Space Agency (ESA). Planck measurements are throwing light into still open questions in cosmology, such as the nature of Dark matter and Dark energy, besides providing more robust estimates of the age, geometry and temperature of the Universe (Malik, 2012).

Understanding of the evolution of the Universe is another of the open questions in modern cosmology. It is thought that the growth of structure in the Universe follows a "bottom-up" fashion, being the formation of galaxies on the earliest stage on this chain. The energetic radiation from the first galaxies transformed the intergalactic medium from neutral to ionized (Zaroubi, 2013). Through power-spectral radio measurements of the highly redshifted 21-cm "spin-flip" transition line of neutral hydrogen in the primordial intergalactic medium, it will be possible to directly constrain the topology and evolution of reionization, opening a unique window into the complex astrophysical interplay between the first luminous objects and their environments (DeBoer et al., 2017). The study of the epoch of reionization is one of the main science drivers for a range of current projects for future radio telescopes, such as the Square Kilometre Array (SKA) (and its precursors and pathfinders such as LOFAR, MWA, PAPER and GMRT, and the planned HERA, see Koopmans et al., 2015) which in combination with future optical and infrared surveys, such as Euclid or LSST are aimed to address fundamental open questions in cosmology, such as the nature of Dark Matter, Dark Energy or the distribution of galaxies in the Large Scale Structure of the Universe, among others (Jarvis et al., 2015; SKA, 2017).



CHAPTER 2

# Galaxy Clusters

---

## Contents

---

<b>2.1 Introduction</b> . . . . .	<b>15</b>
<b>2.2 Detecting Galaxy Clusters</b> . . . . .	<b>18</b>
2.2.1 Optical and near infrared . . . . .	20
2.2.2 X-Ray . . . . .	21
2.2.3 The Sunyaev-Zel'dovich effect . . . . .	21

---

The modern research in astrophysics and cosmology meet in the fascinating structures known as galaxy clusters, and that is why they are sometimes called the "crossroads" between this two fields. The study of clusters as cosmological probes is extremely important because they are very sensitive tracers of structure growth, and a census of cluster population as a function of redshift can test different cosmological models (e.g [Borgani and Guzzo, 2001](#); [Vikhlinin et al., 2003](#)), or values of cosmological parameters ([Bohringer and Werner, 2009](#)). Here, we will briefly discuss the properties of these so-called "largest gravitationally bounded structures in the Universe".

## 2.1 Introduction

It is usual to read in a scientific paper on galaxy clusters the following mantra: "Galaxy clusters are the largest gravitationally bound structures in the Universe". Why is it so? Why does gravity reaches a halt in binding structures?

It is not so easy to get an intuitive idea of how massive galaxy clusters are. To make a comparison, a galaxy cluster is more massive relative to a human being than a human being relative to a subatomic particle ([Henry et al., 1998](#)). Since the birth of what is now called "extragalactic astronomy" it was noticed that galaxies are not evenly distributed in the observable universe. As early as the 18th Century, the great astronomers Charles Messier and William Herschel produced the catalogues of what they used to call "nebulae", and noticed that they tend to accumulate in certain regions of the sky, while other regions are relatively empty ([Biviano, 2000](#)). The controversy of whether this objects belong or not to the Milky Way lasted until the first quarter of the 20th Century, when Edwin Hubble identified Cepheid

variable stars in some nebulae, and by calculating their distances concluded that they lie much farther away than the limits of the Milky Way (Nussbaumer and Bieri, 2010).

Gravity plays a fundamental role on the creation of structures in the Universe. It is the force behind the shaping of planets, stars, planetary systems, stellar clusters and galaxies. The so-called "bottom up" scenario (see e.g. Bahcall et al., 1999, and references therein) is the one favoured by observations to explain the formation of cosmic structures. The  $\Lambda$ CDM (being  $\Lambda$  the non-zero cosmological constant) cosmology provides us with the framework for the creation of galaxies, galaxy clusters and large scale structure of the Universe. We have seen that the CMB contains the footprints of small fluctuations in temperature. This means that the initial plasma was not perfectly homogeneous, and there were regions of slightly higher (or lower) density than the average. As the Universe expands, the regions of higher density acquired still more mass from their surroundings as they had a slightly larger gravitational force than the average regions. If the gravity is high enough in a denser region, then the material inside can decouple from the cosmic expansion. From this moment on, the structure formation start from the bottom-up. In other words, smaller structures form first, and then merged to form larger ones. In this scenario the first structures emerging from the collapsed material were of the sizes of dwarf galaxies or globular clusters, this new structures merge to create galaxies, galaxy groups and ultimately, clusters of galaxies (Gott, 2016).

There is a second reason why in principle we can not find larger gravitationally bound structures than galaxy clusters *right now*. It turns that the time of relaxation of a galaxy cluster, or in other words, the time for the cluster to reach virial equilibrium, is of the order of  $\sim 10^{10}$  yrs (Gott, 2016). This point in the history of the Universe is just occurring now in the case of clusters of galaxies (Henry et al., 1998). This means that there is no time enough in the cosmic history for larger structures to be bounded by gravity.

This doesn't mean, however, that there are not larger structures present in the Universe. There have been observed enormous structures coined superclusters -clusters of clusters!-. Superclusters alternate in space with equally enormous voids; regions of space that contain very little or no luminous matter. The discovery of superclusters has been a great observational achievement and it has put together astronomy, cosmology and particle physics (Courtois, 2016). It is believed that Superclusters formed very early in the history of the Universe. Briefly after the Big Bang, some 13.7 billion years ago, the four forces that rule the Universe -gravity, electromagnetic, weak and strong forces- were unified in a single force, which at some point separated in the four that we know today. This separation of forces, together with the quantum nature of the early Universe, shaped minuscule fluctuations in the density and temperature of the primordial Universe (Burns, 1986). Superclusters are the fossil records of this primordial fluctuations that grew with the expansion of the Universe. However, this structures are not *gravitationally bounded* structures and will dissolve with the cosmic expansion.

It has been proposed that there could be gravitationally bounded structures larger than clusters of galaxies. These are the so-called Superstes clusters (meaning "survivors" in Latin) (Chon et al., 2015). We have mentioned that even if galaxies in Superclusters are following

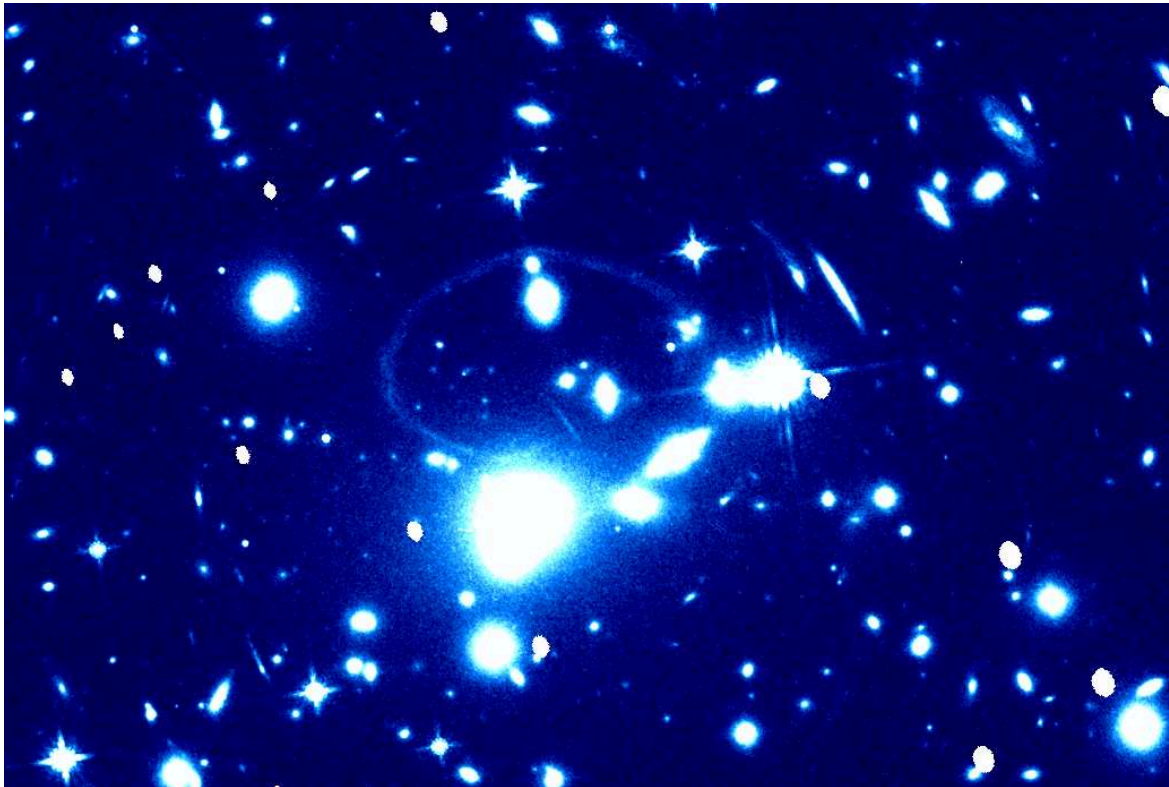


Figure 2.1: Optical image of the galaxy cluster MACSJ0520.7-1328, one of our clusters from the MACS-Planck Radio Halo Cluster Project. Credit: Hubble Space Telescope archive.

flows guided by gravity, the gravitational force will lose against the accelerated expansion of the Universe, "dispersing" the Superclusters. But this will not be the case with some overdensities, where the collapse *will occur in the future*. Superclusters are those structures that, in principle, will survive the accelerating cosmic expansion and collapse in the future (Chon et al., 2015), just as galaxy clusters have done up to now.

In 1933, the astronomer Fritz Zwicky first estimated the mass of a cluster of galaxies (Zwicky, 1933) by measuring the speed of individual galaxies in the Virgo Cluster (Henry et al., 1998). It was found that in order to explain the measured velocities, a great amount of missing mass was needed. This is what we call today Dark Matter; a form of matter which only manifest itself by its gravitational interaction. The second component in terms of mass of a galaxy cluster is gas. As we will see in more details in further sections, galaxy clusters show X-ray emission caused by the presence of hot gas in the so called Intra Cluster Medium (ICM). This hot gas also leaves a mark on observations of the Cosmic Microwave Background (CMB) via the Sunyaev-Zel'dovich effect (see section 2.2.3). The masses of galaxy clusters range from  $\sim 10^{13} M_{\odot}$  to  $\sim 10^{15} M_{\odot}$ .  $\sim 70\text{-}80\%$  of this mass is in the form of Dark Matter,  $\sim 15\text{-}20\%$  is in the form of hot and tenuous gas in the ICM and just  $\sim 5\%$  is in the form of galaxies. It could be useful to imagine galaxy clusters as huge spheroids of Dark Matter and hot tenuous gas, where a few hundreds or even thousands of galaxies are

Table 2.1: Typical quantities of Galaxy Clusters

Mass range	$\sim 10^{13}M_{\odot} - \sim 10^{15}M_{\odot}$
Size	$\sim \text{Mpc}$
Gas Temperature	$10^8 \text{ K}$
Gas Number density	$10^{-1}-10^{-4}cm^{-3}$
Magnetic Field	$\sim 1\mu G$

Table 2.2: Mass composition of Galaxy Clusters

Dark Matter	$\sim 70-80\%$
Hot tenuous gas	$\sim 15-20\%$
Mass in forms of galaxies	$\sim 5\%$

embedded like raisins in a cake.

The merging of galaxy clusters are the most energetic events in the Universe since the Big Bang (Sarazin, 2002). As we have seen, it is thought that galaxy clusters are assembled by mergers of sub-cluster structures. These collisions occur at velocities of  $\sim 2000 \text{ km/s}$ . The gravitational energies released are of orders of  $\gtrsim 10^{64}$  ergs on timescales of  $\sim \text{Gyr}$  (Brunetti and Jones, 2014). The picture is the following: sub-cluster structures, such as smaller galaxy groups, occasionally join together to form a cluster. Each of these substructures gives hot gas and dark matter to the cluster, and also enriches it with more galaxies (Henry et al., 1998). An important consequence of cluster mergers are the shocks driven in the ICM, which are the main source of heat for the X-ray emission (see Sect. 2.2.2). The shocks can dissipate energies of  $\sim 3 \times 10^{63}$  ergs. Shocks due to mergers have two important effects on the ICM: on one side they heat and compress the intercluster gas responsible of X-ray emission; this process increases the entropy of the gas. The other major effect of merger shocks is expected to be particle acceleration and magnetic field amplification (Keshet and Loeb, 2010). The presence of relativistic electrons and ions can produce synchrotron radiation in radio frequencies, inverse Compton (IC) extreme ultra violet (EUV), hard X-ray and gamma-ray emission. As we will see in Sect. 3, cluster mergers may play a fundamental role on the formation of diffuse radio sources, the main subject of this thesis.

## 2.2 Detecting Galaxy Clusters

Galaxy clusters can be observed at different frequencies, and each of these frequencies unveils different components of the cluster. For instance, the X-ray emission give us information about the thermal processes in the ICM, while radio gives us information about the non-thermal component. Up to now, there are mainly three ways in which we can detect clusters of galaxies:

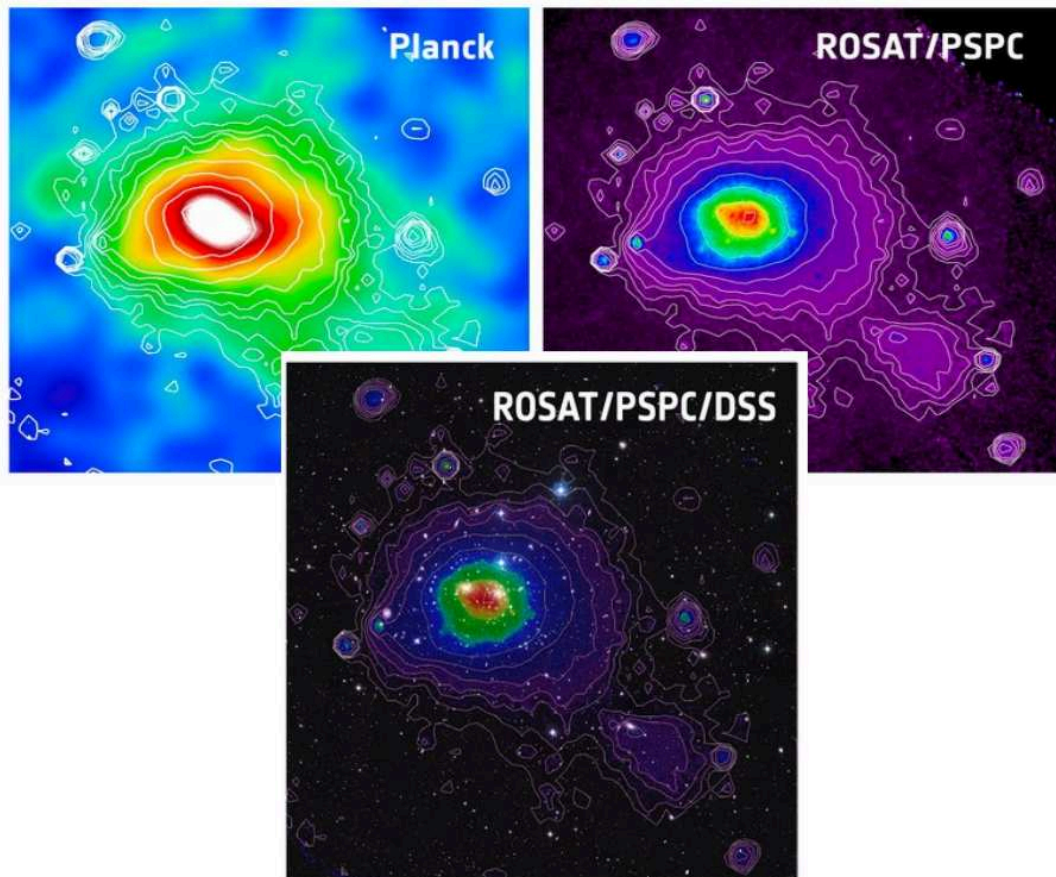


Figure 2.2: Example of the multi-wavelength images of the Coma cluster. In the top left panel the Planck Sunyaev-Zeldovic image is shown, it looks like a spot of different temperature in the CMB. The top right panel shows the thermal X-ray emission of the cluster, from the ROSAT PSPC survey. In the bottom panel we show the ROSAT PSPC X-ray image overlaid with the optical DSS image of the cluster. Credit: European Space Agency.

### 2.2.1 Optical and near infrared

We have seen in Sect. 2.1 that galaxies represent just around  $\sim 5\%$  of the total mass of galaxy clusters. It was however by the observation of galaxies that the existence of clusters was discovered (see [Biviano, 2000](#), and references therein). The first approaches to detect a galaxy cluster was to find over-densities of galaxies in particular regions of the sky.

Later on, more accurate definitions for cluster membership were needed. George O. Abell created a "Northern Survey" of galaxy clusters based on visual inspection of photographic plates. Abell established some criteria to define the membership to his catalogue ([Abell, 1958](#)):

- *Richness criterion:* Clusters must contain at least 50 members not fainter than 2 mag. the third brightest member.
- *Compactness criterion:* Clusters must be sufficiently compact, so that its fifty or more members lie within a given radial distance<sup>1</sup> from its center.
- *Distance criterion:* Clusters must be sufficiently distant so that its members do not extend over more than one plate or, at most, part of an adjacent plate.
- *Galactic-latitude criterion:* Clusters must avoid confusion with stars or objects from the Milky Way.

In the Northern survey, Abell discovered 2712 galaxy clusters, and later on the number increased to 4073 clusters from observations of the southern hemisphere ([Abell et al., 1989](#)).

Even if visual inspection of photographic plates was a successful approach for relatively nearby clusters, this method suffers the major danger of projection effects, having the possibility to include false positives in the cluster. Knowledge of spectroscopic redshifts from galaxies may be useful, but are extremely time consuming up to now. The need for a different approach became evident for farther clusters and larger regions of the sky. In 1996, [Postman et al. \(1996\)](#) developed a match-filter algorithm to identify cluster candidates by using simultaneously positional and photometric data. The central regions of galaxy clusters are populated mainly by red galaxies. In a color-magnitude diagram, such galaxies follow a prominent linear feature with low scatter called the "red sequence" (e.g., [Stott et al., 2009](#)). Studies based on the red sequence have improved the characterization of cluster members. There are catalogues as large as containing 13823 nearby clusters ([Koester et al., 2007](#)) extracted from the Sloan Digital Sky Survey (SDSS).

---

<sup>1</sup>The radial distance  $r$  is arbitrary, as long as it is the same for all clusters, see [Abell \(1958\)](#)

### 2.2.2 X-Ray

We have mentioned that the greatest amount of baryonic matter present in a galaxy cluster is in the form of hot and tenuous gas. Most of this gas is in the form of Hydrogen and Helium from the primordial nucleosynthesis. The gas is slurped down by the huge gravitational well of the cluster. As the captured gas falls down in the gravity well, it is accelerated and crashes into itself, converting its potential energy into thermal motion of individual atoms (Scharf, 2012). This process is called *thermal bremsstrahlung*, and can heat the gas as much as  $\sim 10^8 \text{K}$ , which shines in the X-ray band.

It was discovered by the Uhuru satellite that galaxy clusters were the most common bright extragalactic sources of X-rays (Sarazin, 1988), with luminosities as large as  $\sim 10^{43-45}$  ergs/sec. Launched in 1999, the ROSAT satellite performed an all-sky survey and was later devoted to pointed observations of selected astrophysical sources (Voges et al., 1999). Satellite X-ray observatories such as *Chandra* have detected among the most distant galaxy clusters (Chandra, 2016), and more recently the *XMM-Newton* has made great advancement in X-ray cluster surveys. It is important to mention that up to now, X-ray observations are still the most attractive method to detect and characterize galaxy clusters (Böhringer et al., 2007).

### 2.2.3 The Sunyaev-Zel'dovich effect

An extremely interesting effect of the gas in the ICM is the interaction with photons coming from the CMB and passing through a cluster of galaxies. Let's briefly remember that the Universe possesses a background radiation of thermal origin that is isotropic to roughly one part in 100,000. The photons of this radiation, which appears in the microwave band at  $z \sim 1100$ , are scattered to highest frequencies via inverse Compton scattering when they collide with the hot electrons present in the ICM (Sunyaev and Zeldovich, 1970, 1972). The result of this scattering is that the spectrum of the CMB seen in the direction of the cluster of galaxies shifts to higher energies, which decreases the intensity of the radiation in the Rayleigh-Jeans regime of the Black-body radiation curve and increases it in the Wien regime (see Fig. 2.3). This effect is known as the Sunyaev-Zeldovich (SZ) effect.

Just as the X-Ray emission on galaxy clusters, the SZ effect is related to the physics of the hot gas in the ICM. It is worth to notice that the observed radiation is the CMB itself, and not the cluster of galaxies. This means that the SZ do not suffer the cosmic attenuation of flux that affects other emissions when the distance to the object grows (Adam, 2015). This makes the SZ effect to be limited just by the angular resolution and the sensibility of the observations, which makes it a powerful tool for doing high redshift cosmology (Carlstrom et al., 2002). Currently, a number of cluster surveys via the SZ effect are ongoing. A paradigmatic example of galaxy cluster detection via the SZ effect was the Planck mission, which first results were released in Planck Collaboration et al. (2011b).

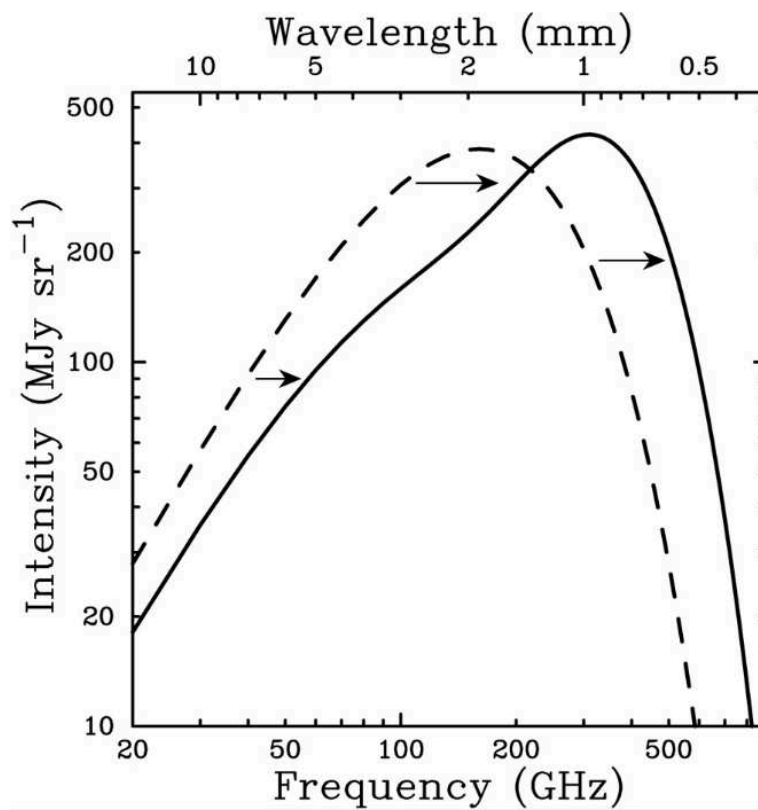


Figure 2.3: The undistorted spectrum of the CMB (dashed line) and the distorted spectrum by the SZ effect (solid line). The CMB intensity increases at frequencies higher than  $\sim 218$  GHz (Wien Regime) and decreases for lower frequencies (Rayleigh-Jeans regime). Credit: ned.ipac.caltech.edu.

# Diffuse radio sources in Galaxy clusters

---

## Contents

---

<b>3.1 Introduction</b> . . . . .	<b>23</b>
<b>3.2 Radio Relics</b> . . . . .	<b>25</b>
<b>3.3 Radio Mini-halos</b> . . . . .	<b>27</b>
<b>3.4 Radio Halos</b> . . . . .	<b>28</b>
3.4.1 Physical models of creation of Radio Halos . . . . .	30
3.4.2 Observational constraints . . . . .	32
3.4.2.1 Scaling Relations . . . . .	32
3.4.2.2 Radio Halo - Merger connection . . . . .	32

---

In this chapter my aim is to unify the topics presented on the two previous chapters; radio astronomy and galaxy clusters. In particular, I will present an overview of the current knowledge of the non-thermal properties of the ICM. This chapter will present the framework of the core of our research: diffuse radio sources in clusters of galaxies.

## 3.1 Introduction

As we have seen in Sect. 2.2.2, great part of the knowledge of the physics of the ICM is obtained by studying the X-ray properties on galaxy clusters. However, radio observations have shown that apart from the thermal radiation from the hot tenuous gas, there is also a non-thermal component. It has been of particular interest the presence of diffuse synchrotron emission in the center and peripheries of clusters. This emission has shown no obvious connection with optical counterparts such as galaxies present in the cluster, and it has been associated to the ICM.

The presence of synchrotron emission on the ICM is considered as evidence of the existence of two important components of the cluster volume: magnetic fields and a population of relativistic particles (Feretti et al., 2012). The magnetic fields, which intensities are of 0.1-1 $\mu$ G (see Table 2.1) have been further explored by studies of Faraday rotation on polarized radio galaxies in the cluster or in its background. The population of relativistic particles has been estimated to have number densities of  $10^{-10}\text{cm}^{-3}$ , to possess Lorentz' factors of

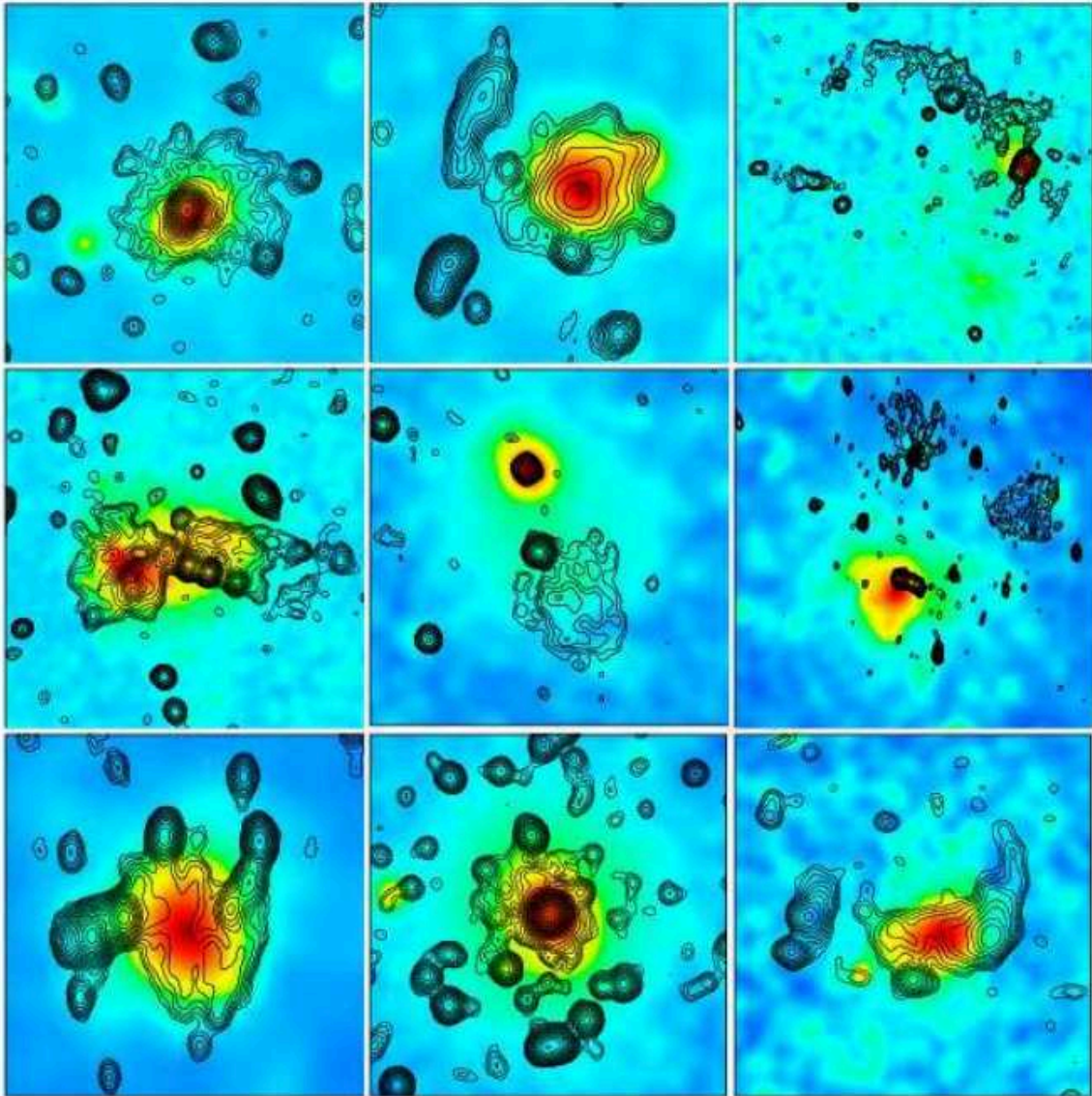


Figure 3.1: Examples of different kinds of diffuse radio sources in galaxy clusters, shown as black contours overlaid on the X-ray images of the clusters. From left to right and from top to bottom: A radio halo in A2219; a halo plus a radio relic in A2744; a radio relic in A115; a complex halo + relic in A754; relics in A1664 and A548. Finally, a halo in A520; a radio mini-halo in A2029 and a radio halo + a double relic in RXCJ1314.4-2515. Image taken from [Feretti et al. \(2012\)](#).

$\gamma \gg 1000$  (Feretti et al., 2012). Diffuse synchrotron sources are considered useful tools to explore the physics of the ICM. For instance, it is expected from some physical models that diffuse radio sources can be tracers of turbulence and shocks in the ICM (Brunetti and Jones, 2014). Based on the estimated values of the magnetic fields and the energies of the relativistic electrons emitting synchrotron radiation, a lifetime of  $\sim 0.1$  Gyr in the ICM has been calculated. This lifetime is quite short compared with the excessively long time needed for the Cosmic Ray electrons (CRE) to diffuse to the observed Mpc-scale sizes of some diffuse sources known as radio halos and relics, which we will discuss below. This fact, known as the *diffusion problem*, requires a continuous acceleration or generation *in situ* of the particles (Brunetti and Jones, 2014).

The first discovery of a diffuse synchrotron source is present in the center of a galaxy cluster was the one in the Coma cluster (Large et al., 1959; Willson, 1970), now classified as a giant radio halo (see Sect. 3.4). Some years after this discovery, it was also noted that on the periphery of the same galaxy cluster, some diffuse synchrotron emission was also present (Ballarati et al., 1981; Giovannini et al., 1991).

The different characteristics of diffuse radio sources has led to a main classification. Depending on their features, such as their sizes, location in the clusters, dynamical status of the cluster, etc. diffuse radio sources have been classified in three big groups: radio halos, radio relics and radio mini-halos (Feretti and Giovannini, 1996, see Figure 3.1). The main characteristics of each of this groups are going to be discussed in the following sections. A very interesting fact of diffuse radio sources in galaxy clusters is that they are not ubiquitous, as has been shown by Giovannini et al. (1999). This poses fundamental questions on the nature and distribution of the mechanisms responsible of the formation of these objects.

## 3.2 Radio Relics

Extended low surface brightness diffuse emission present in the periphery of galaxy clusters are coined Radio Relics. Relics are characterized by a large size (from  $\sim 10^2 - 10^3$  kpc, Ferrari et al. (2008)) and a steep synchrotron spectrum ( $\alpha \gtrsim 1$ )<sup>1</sup>. Being most of them elongated in shape, with their axis usually found to be perpendicular to the line connecting the relic with the cluster center, they also show to have relatively strong polarization ( $\sim 15 - 20$  %). The polarization observed in relics has been interpreted as evidence of the presence of a significant anisotropy in the magnetic field on large scales (Brunetti and Jones, 2014). Based on their polarization degrees, morphologies and location in clusters, it has been suggested that large scale shocks crossing the ICM during cluster mergers may accelerate a population of locally injected electrons or re-accelerate some pre-existing energetic electrons to the required energies for the emission of synchrotron radiation through the so-called Diffuse Shock Acceleration (DSA) mechanism (Brüggen et al., 2012; Brunetti, 2011; Kang et al., 2012).

In a number of cases, relics appear in pairs on opposite sides of the center of the host

<sup>1</sup>Throughout this thesis I will use the convention  $S(\nu) \propto \nu^{-\alpha}$ , being  $S(\nu)$  the radio flux density.

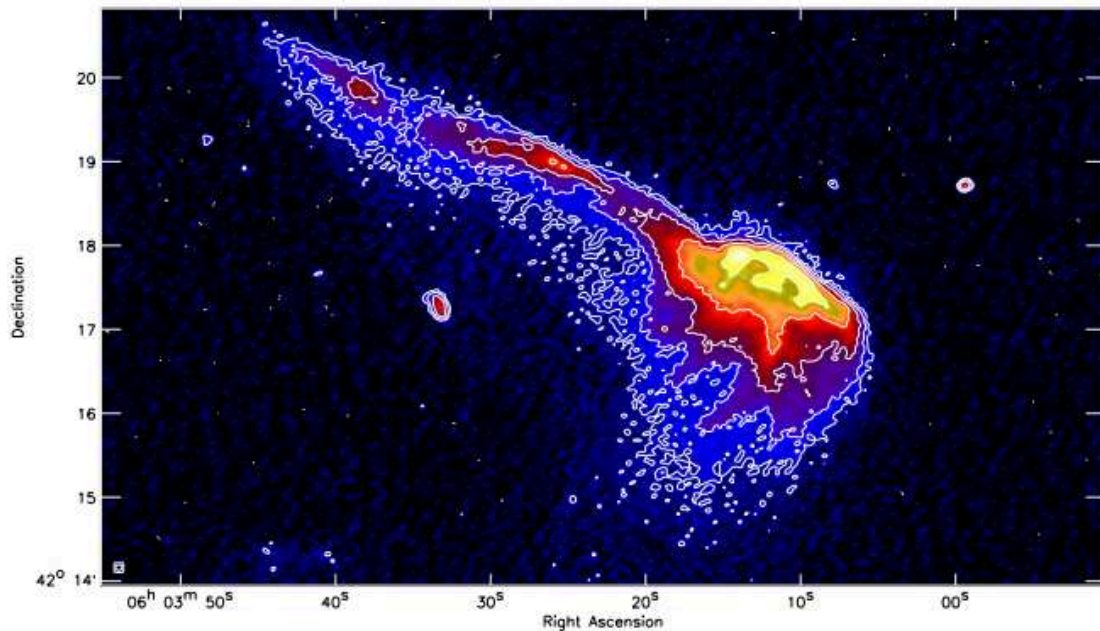


Figure 3.2: LOFAR HBA 120-181 MHz images of a radio relic in the Toothbrush cluster, one of the brightest radio relic sources known. Credit: [van Weeren et al. \(2016\)](#).

clusters (e.g. [Bonafede et al., 2014a](#); [van Weeren et al., 2010](#); [Rottgering et al., 1997](#)). Since merger shocks should occur in such configurations, a shock-relic connection has been proposed ([Brunetti and Jones, 2014](#)). To reinforce the shock scenario, there is also evidence of magnetic field alignment with the long axis of the relic, suggesting that relics probably occur in regions of compression of the magnetic fields in the shock plane ([Clarke and Ensslin, 2006](#)). Moreover, a connection between the X-ray evidence of merger shocks and the presence of radio relics has been observed in a few cases ([Markevitch, 2010](#); [Giacintucci et al., 2008](#)). There are, however, some problems with the shock re-acceleration models. There is observational evidence that shocks determined by X-ray measurements are apparently weak ([Markevitch and Vikhlinin, 2007](#)), which is supported by cosmological simulations ([Pfrommer et al., 2006](#)). There is also evidence of the presence of shock fronts without detected relics ([Russell et al., 2011](#)). Indeed, it has been showed that the acceleration efficiency at shocks should be low, preventing the electrons from the thermal pool in the ICM to be accelerated to the required energies via the DSA mechanism. In addition, some relics have shown regions with flat spectra, in disagreement with the Mach numbers measured via X-ray observations ([van Weeren et al., 2017a](#)). The fact that some problems arise from taking DSA as the only explanation for the generation of radio relics, an "AGN-relic connection" has been proposed ([Bonafede et al., 2014a](#); [Shimwell et al., 2016](#)). The scenario proposes that fossil relativistic electrons from active galactic nuclei are re-accelerated at cluster shocks, meaning that radio galaxies play an important role on the creation of relics ([van Weeren et al., 2017a](#)).

### 3.3 Radio Mini-halos

There is observational evidence that some relaxed cool-core clusters host small scale ( $\sim 50$  -  $300$  kpc), centrally located diffuse radio emission called mini-halos (Giacintucci et al., 2014b). This low surface brightness emission surrounds a radio loud dominant galaxy of the cluster (Bravi et al., 2016), nearly always found in the center of a cool-core cluster. Mini-halos also possess steep spectra ( $\alpha > 1$ ), and their origin is still debated (Giacintucci et al., 2017a). It is thought that the active galaxies embedded in mini-halos play a role by injecting electrons, but the timescales required for their diffusion across the cooling region is much longer than the radiative cooling timescales. Therefore, injection or re-acceleration *in situ* of relativistic particles is needed.

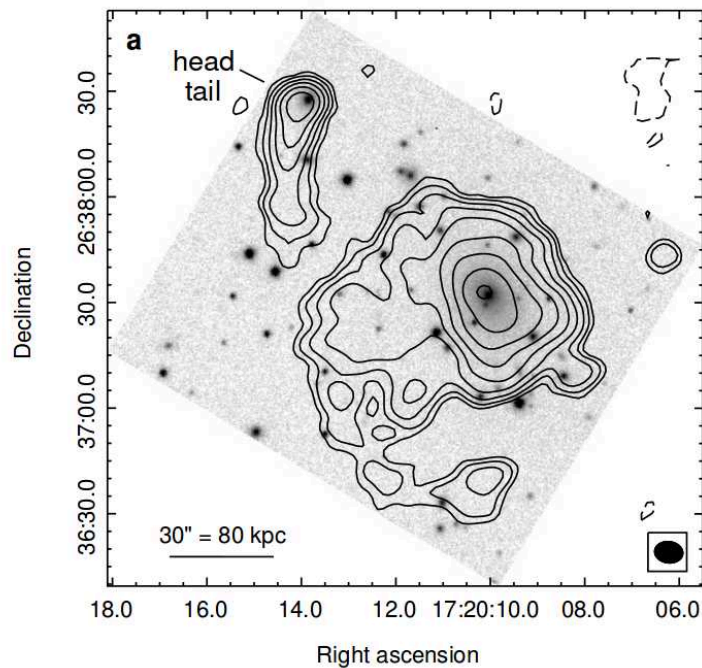


Figure 3.3:  $3\sigma \times 2n$  contours of the 617 MHz GMRT radio map of the cluster RX J1720.1+2638, overlaid on the optical r-band SDSS image of the same sky region. The contours show a typical radio mini-halo around the dominant galaxy of the cluster. Credit: Giacintucci et al. (2014a).

Two physical mechanisms have been proposed to explain the origin of mini-halos. According to the first models, also called re-acceleration of CRE or leptonic models, the origin of mini-halos is due to the re-acceleration by turbulence of a previously present population of relativistic electrons in the core of the cluster (Gitti et al., 2002) or by gas sloshing in the cluster cool core (Mazzotta and Giacintucci, 2008). The second model to explain mini-halos is the generation of secondary particles via inelastic collisions of Cosmic Ray protons (CRp) and thermal protons present in the ICM (Pfrommer and Enßlin, 2004). In a recent study,

[Giacintucci et al. \(2017a\)](#) found on a selected sample of clusters that a large fraction of cool-core clusters (80%) posses a mini-halo, and the occurrence of mini-halos may be lower in lower mass cool-core clusters. Moreover, no mini-halos were find in non-cool-core clusters. With these new evidence provides crucial information on the physical processes required for the generation of mini-halos.

### 3.4 Radio Halos

Radio Halos (RHs) are Mpc-scale diffuse emission appearing centred on massive galaxy clusters. RHs have typical extensions of  $\sim 1$  Mpc and surface brightness of  $\sim 1 - 0.1 \mu\text{Jy arcsec}^{-2}$  at 1.4 GHz. The level of polarization of the emitted radiation of RHs is limited to just a few percentage. The possible interpretation for the difficulty of detecting polarized emission in halos is the result of two effects. The first one is due to mixture of the ICM gas with the relativistic plasma generates significant depolarization. The second effect is a consequence of the extremely low surface brightness of halos that are usually observed with low spatial resolution, which could result in a decrease of the observed fractional polarization ([Govoni, 2006](#)). This absence of significant observed levels of polarization, together with their morphological connection with the thermal X-ray emission suggest that the relativistic plasma that generates the synchrotron radiation occupies a large fraction of the volume filled by the hot X-ray emitting ICM ([Brunetti and Jones, 2014](#)).

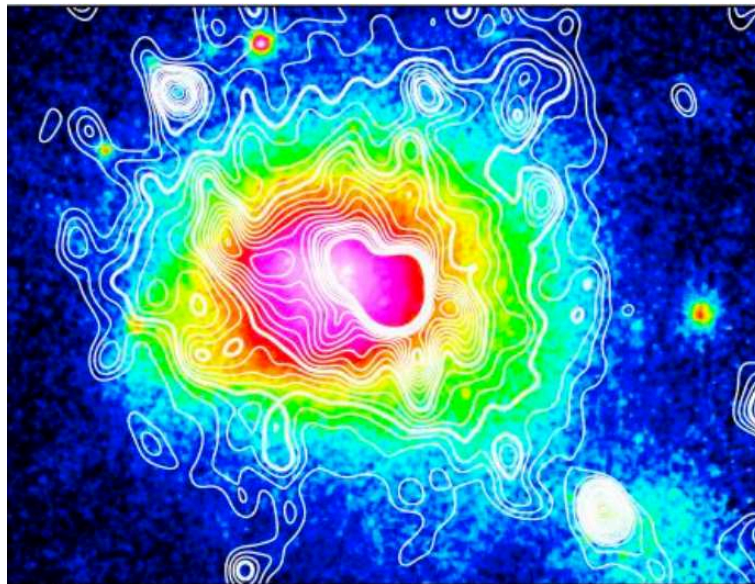


Figure 3.4: Contours of diffuse Westerbork Synthesis Radio Telescope (WSRT) 352 MHz radio emission over ROSAT PSPC diffuse X-ray emission of Coma cluster (see Fig. 2.2), a typical radio halo. Credit: [Brown and Rudnick \(2011\)](#).

As we have mentioned in Sect. 3.1, diffuse radio sources are not present in every observed

galaxy cluster. This is a very interesting case for RHs. In seminal works by [Giovannini et al. \(1999\)](#) and [Giovannini and Feretti \(2002a\)](#) it was found that the detection rate of RHs is actually quite low: 5 % in a complete cluster sample, and the ratio increasing by considering only the most X-ray luminous clusters. This evidence has been improved in more recent studies, [Venturi et al. \(2007, 2008\)](#) showed that RHs appear in  $\sim 30\%$  of radio observed clusters with X-ray luminosities of  $L_x[0.1-2.4 \text{ keV}] > 5 \times 10^{44} \text{ erg/seg}$ . Moreover, [Cuciti et al. \(2015\)](#) show that the fraction of galaxy clusters hosting a RH increases with the selection of the cluster mass.

Table 3.1: Characteristics of Radio Halos

Size	$\sim 1 \text{ Mpc}$
Surface brightness	$\sim 1 - 0.1 \mu\text{Jy arcsec}^{-2}$ at 1.4 GHz
Location on cluster	center
Level of polarization	< few percentage

There is evidence from observational results showing connections between the radio and X-ray properties of clusters. This is suggested by the close similarity of RH morphology and the cluster X-ray emission. The first results pointing in this direction were more qualitative (e.g. [Deiss et al., 1997](#); [Feretti, 1999](#)) and later on in a more quantitative way, by finding a relation between the point to point surface brightness of the radio and X-ray emission in the cluster ([Govoni et al., 2001a](#); [Feretti et al., 2001](#)). Moreover, there is strong evidence showing a connection between the presence of RHs and the dynamical state of the host systems (see Sect. 3.4.2.2). [Cassano et al. \(2010a\)](#) found that clusters with and without RH can be quantitatively differentiated in terms of their dynamical properties, being the RH host clusters dynamically disturbed and clusters without a RH more "relaxed" systems. However, it is worth mentioning some curious exceptions appearing in the literature. [Bonafede et al. \(2014b\)](#) discovered a Giant RH in the cool-core cluster CL1821+643. The presence of a cool-core in galaxy clusters may be a likely indication that a major merger hasn't occurred in the recent history of the cluster. Therefore, if a merger event is causing the radio emission, then it should be either a minor one, one off-axis or one in an early phase. However, a recent study of this system by [Kale and Parekh \(2016\)](#) show that CL1821+643 is not a relaxed system, and the authors propose that the cluster experienced a non-core-disruptive merger. [Russell et al. \(2011\)](#) on the other hand, have found that the galaxy cluster Abell 2146, despite showing a complex structure associated with a major merger event (see also [White et al., 2015a](#)), shows no evidence of a RH or any other diffuse radio emission through the deep GMRT observation at 325MHz. The authors propose that a possible explanation to this lack of diffuse emission may be the relatively low mass of the cluster.

Spectral measurements of RHs are challenging and still poor in statistics. However, it is generally known that RHs have usually steep spectra ( $\alpha > 1$ ) [Feretti et al. \(2012\)](#) reports the following spectral behaviour in the 0.3-1.4 GHz frequency range:

- Average spectral index  $\alpha=1.7\pm 0.2$  for RHs hosted by clusters with average temperature less than 8 keV.
- Average spectral index  $\alpha=1.4\pm 0.4$  for RHs hosted by clusters with temperature range of 8 to 10 keV.
- Average spectral index  $\alpha=1.2\pm 0.2$  for RHs hosted by clusters with temperature greater than 10 keV.

As we will see in Sect. 3.4.1, spectral behaviour of RHs can give us crucial information about the mechanism responsible of their origin. Moreover, the distribution of the spectral index across a RH is a useful tool to understand the variation of the electron energy distribution and the magnetic field in which they move (Feretti et al., 2012).

### 3.4.1 Physical models of creation of Radio Halos

There are two different physical mechanisms proposed to explain the origin and observed properties of RHs. Here, I will present a brief description of the main features and challenges of each of the two models.

- *The "re-acceleration" model*

The first model considers the re-acceleration of relativistic particles by Magnetohydrodynamic (MHD) turbulence in the ICM (Brunetti and Jones, 2014) created in the cluster volume during merger events (Cassano and Brunetti, 2005).

In this scenario it is assumed that cluster mergers generates strong turbulence in the intracluster gas. Among the different possible sources of turbulence in the ICM, the most important one to accelerate particles and amplify the magnetic fields on large scales is the merger of clusters (Roettiger et al., 1999). A fraction of the total energy dissipated in the merger event goes into the re-acceleration of CRs via the so-called Fermi II-type mechanisms, where cosmic rays are accelerated primarily by collisions against moving magnetic fields (Fermi, 1949). However, it has been calculated (Petrosian and East, 2008) that MHD turbulence is quite inefficient in accelerating CRs directly from the thermal pool in the ICM. Therefore, an initial "seed" of CRs need to be re-accelerated by turbulence in order to reach the needed relativistic speeds. This re-acceleration *in situ* potentially solves the slow diffusion problem (see Sect. 3.1), by keeping the acceleration to the needed timescales of  $\sim 1$  Gyr. One of the most important predictions of this model is a tight connection between the dynamical state of the cluster and the presence or absence of a RH. It is also expected from this model that RHs could have spatially varying, complex and potentially very steep spectra (see Sect. 3.4) due to the complex morphology of the spatially varying acceleration and cooling of the emitting CRs (Brunetti and Jones, 2014). These USSRHs are particularly difficult to detect at higher frequencies. Indeed, a number of Ultra Steep Spectrum (USS) radio halos have been reported in the literature (Brunetti et al., 2008; Macario et al., 2010)

in concordance with the prediction, but lacking proper statistical studies. Another observational milestone in favour of the re-acceleration model is the fact that most of known RHs appear in dynamically disturbed clusters, as we discussed in Sect. 3.4.

- *The "hadronic" model*

The other mechanism proposed to explain the origin of RHs is known as the hadronic model. This model is based on the fact that an important number of CRe are generated as secondary particles because of inelastic collisions between the thermal protons present in the ICM and CRp. One of the virtues of this model is that it also solves the slow diffusion problem, because the collisions result in a population of relativistic secondary electrons and positrons formed *in situ* on the cluster (Mpc) scale (Dennison, 1980). The decay chain from the inelastic proton-proton collision is (Brunetti and Jones, 2014, and references therein):

$$\begin{aligned} p + p &\longrightarrow \pi^0 + \pi^+ + \pi^- + \text{anything} \\ \pi^0 &\longrightarrow \gamma\gamma \\ \pi^\pm &\longrightarrow \mu^\pm + \nu_\mu(\bar{\nu}_\mu), \mu^\pm \longrightarrow e^\pm + \bar{\nu}_\mu(\nu_\mu) + \nu_e(\bar{\nu}_e). \end{aligned}$$

Where  $e$  accounts for electrons (or positrons),  $p$  for protons,  $\mu$  for muons,  $\pi$  for pions,  $\nu$  for neutrinos and  $\gamma$  for gamma ray photons.

Another of the strengths of this model is that it explains naturally the correspondence between the X-ray and RH coincidence in morphologies. In fact, this model proposes that the thermal protons which are responsible for the X-ray emission are actually the pool from which the relativistic electrons are subtracted as the result of the hadronic collisions (Brunetti and Jones, 2014).

This model has, however, some drawbacks that are worthwhile mentioning. As we have seen, one of the products of the hadronic collisions are gamma ray photons due to the decay of the  $\pi^0$ . In this scenario, the  $\gamma$ -ray luminosity is dependent on the strength of the magnetic field on the ICM (Brunetti and Jones, 2014), and current upper limits on  $\gamma$ -ray detections performed with the *Fermi*-LAT Gamma-ray Space Telescope are in tension with the derived values of magnetic fields measured by Faraday rotation (Brunetti, 2009; Jellima and Profumo, 2011; Brunetti et al., 2012).

- *"Hybrid" models?*

It is fair to say at this point that current radio and  $\gamma$ -ray detectors suffer from serious sensitivity constrains and the data that they have provided is not enough to firmly discriminate between the two previous scenarios. For instance, it is expected that hadronic models should act at some level, because it is certain that CRp exist and interact with the thermal protons in the ICM. Therefore, all clusters should have low-level radio emission from secondary electrons. There are indeed some attempts to detect the "off-state" radio emission from clusters (Brown et al., 2011b). Therefore, some *hybrid* models have been proposed, where RHs are assumed to be created by the re-acceleration via merger turbulence of secondary particles (Brunetti and Lazarian, 2011; Brunetti and Blasi, 2005), while relaxed clusters should have some radio emission marginally smaller than current upper limits of radio detection.

## 3.4.2 Observational constraints

### 3.4.2.1 Scaling Relations

A number of correlations between observed thermal and non-thermal properties of galaxy clusters have been found in the last years, suggesting physical connections between them. Concerning the observed properties of RHs, the increase of their monochromatic radio power at 1.4 GHz ( $P_{1.4}$ ) with the cluster's X-ray luminosity, temperature and total mass, are of particular interest (see e.g. Feretti, 2002; Govoni et al., 2001a; Cassano et al., 2006, 2013, and references therein). These scaling relations are not a surprise, but they are expected from the theoretical models of RH formation (Cassano et al., 2013).

A fundamental work that shows the thermal/non-thermal correlations by using homogeneous radio, X-ray and SZ measurements is the one performed by Cassano et al. (2013). In Figs. 3.5 and 3.6 we show, respectively, the scaling relations of  $P_{1.4}$  with X-ray luminosity  $L_{500}$  and cluster mass  $M_{500}$  derived from the SZ signal of the cluster within  $R_{500}^2$ .

An interesting feature from Figs. 3.5 and 3.6 apart from the scaling relations is the bi-modality in the distribution of clusters into two different populations: on one side we have the "radio loud" X-ray luminous (Massive) clusters following the correlation, and the second population of "radio quiet" clusters, appearing as upper limits, well below the correlation. USSRHs lie in an intermediate region, a bit under-luminous with respect to the correlation.

Even if both, re-acceleration and hadronic models predict scaling relations, the scaling predicted by hadronic models are flatter than the ones observed (Cassano et al., 2013). Re-acceleration models, on the other side, predict slopes that are in good agreement with observations. Another problem for hadronic models is that it can't explain the bi-modality, which arises naturally in the re-acceleration models, as we will see in the following section.

### 3.4.2.2 Radio Halo - Merger connection

As we have mentioned in Sect. 3.4, a significant number of works in the literature have found evidence that RHs appear mainly in clusters with complex gas temperature distributions or signs of complex substructure in their X-ray morphologies (Schuecker et al., 2001; Govoni et al., 2004; Cassano et al., 2010a). The first quantitative comparison of the dynamical states of clusters possessing radio halo was provided by Buote (2001), where the author finds a correlation between  $P_{1.4}$  and the magnitude of the dipole power ratio ( $P_1/P_0$ ), where  $P_m$  is the square of the  $m$ th multipole of the two-dimensional pseudo-potential generated by the X-ray surface brightness evaluated over a circular aperture centred in the peak of the X-ray image (see Buote, 2001). More specifically, the correlation implies that the strongest radio halos appear only in those clusters currently experiencing the largest departures from a virialized state ( $P_{1.4} \propto P_1/P_0$ ), and are more common in X-ray luminous clusters.

---

<sup>2</sup> $R_{500}$  is the radius at which the mean mass density is 500 times the critical density at the cluster redshift. Similarly  $L_{500}$  corresponds to the X-ray luminosity within the same radius

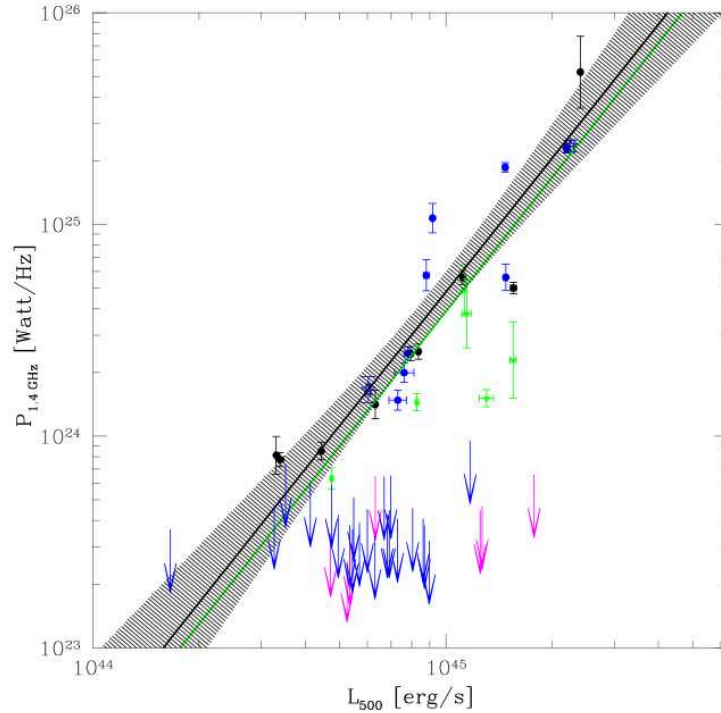


Figure 3.5: Distribution of galaxy clusters in the  $P_{1.4}-L_{500}$  diagram. The blue filled dots corresponds to halos belonging to the EGRHS (see sect. 4.1), while radio powers taken from the literature are shown as open black dots. Halos with USS are shown in green. Blue arrows are radio upper limits and magenta arrows are upper limits for cool-core clusters. The black line is the best fit relation for RHs. The green line also fits USSRHs. The shadowed region is the 95% confidence region for the black line fit. Credit: [Cassano et al. \(2013\)](#).

Based on an X-ray selected sample ( $L_x \geq 5 \times 10^{44}$  erg/s and  $0.2 \leq z \leq 0.32$ ), [Cassano et al. \(2010a\)](#) show that *RH loud* and *RH quiet* clusters can be segregated in a quantitative way by characterizing their dynamical states. The authors confirm the association of RHs to disturbed clusters, while *RH quiet* clusters are generally more relaxed.

For their analysis the authors make use of several methods to characterize the X-ray substructures:

- *The power ratios*  $P_3/P_0$  as defined above.
- *The centroid shifts* (e.g. [Mohr et al., 1993](#); [Poole et al., 2006](#); [Maughan et al., 2008](#); [Böhringer et al., 2010](#)), computed in a series of circular apertures, all centred in the X-ray peak. In [Cassano et al. \(2010a\)](#), the apertures are decreased in steps of 5% from  $R_{ap} = 500$  kpc to  $0.05R_{ap}$ . The centroid shift is denoted by  $w$ , and it's defined as the standard deviation of the projected separation between the peak and the centroid in unit of  $R_{ap}$ , or:

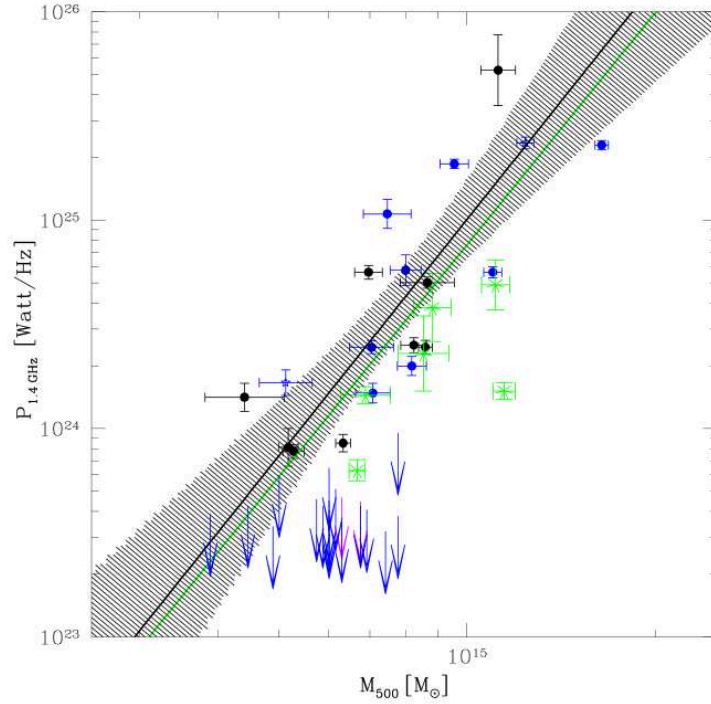


Figure 3.6: Distribution of galaxy clusters in the  $P_{1.4}-M_{500}$  plane. The symbols are the same as in Fig. 3.5. Credit: [Cassano et al. \(2013\)](#).

$$w = \left[ \frac{1}{N+1} \sum (\Delta_i - \langle \Delta \rangle)^2 \right]^{1/2} \times \frac{1}{R_{ap}} \quad (3.1)$$

where  $\Delta_i$  stands for the distance between the X-ray peak and the centroid of the  $i$ th aperture. The centroid shift was found to be sensitive to the dynamical state of clusters in numerical simulations of cluster mergers ([Poole et al., 2006](#)).

- The X-ray brightness concentration parameter ([Santos et al., 2008](#)), defined as the ratio of the peak over the ambient surface brightness,  $S$ , or:

$$c = \frac{S(r < 100kpc)}{S(< 500kpc)} \quad (3.2)$$

The concentration parameter is used to discriminate between cool-core and non cool-core clusters, and in terms of the dynamical state it discerns between cores not disrupted from a recent merger event from the ones that are disturbed from a recent merger event.

In Fig. 3.7 the main results of [Cassano et al. \(2010a\)](#) are presented. A clear correlation between the centroid shift  $w$  and the power ratio  $P_3/P_0$  (Fig. 3.7 b), and two anti-correlations, one between the concentration parameter  $c$  and  $w$  and another between  $c$  and  $P_3/P_0$  (Figs.

3.7 a and c, respectively). Moreover, by choosing the median values of each parameter ( $w \simeq 0.012$ ,  $c \simeq 0.2$  and  $P_3/P_0 \simeq 1.2 \times 10^{-7}$ ) the sample of clusters hosting a RH and clusters without RH is splitted into regions, being most of RHs in the quadrants corresponding to the disturbed clusters.

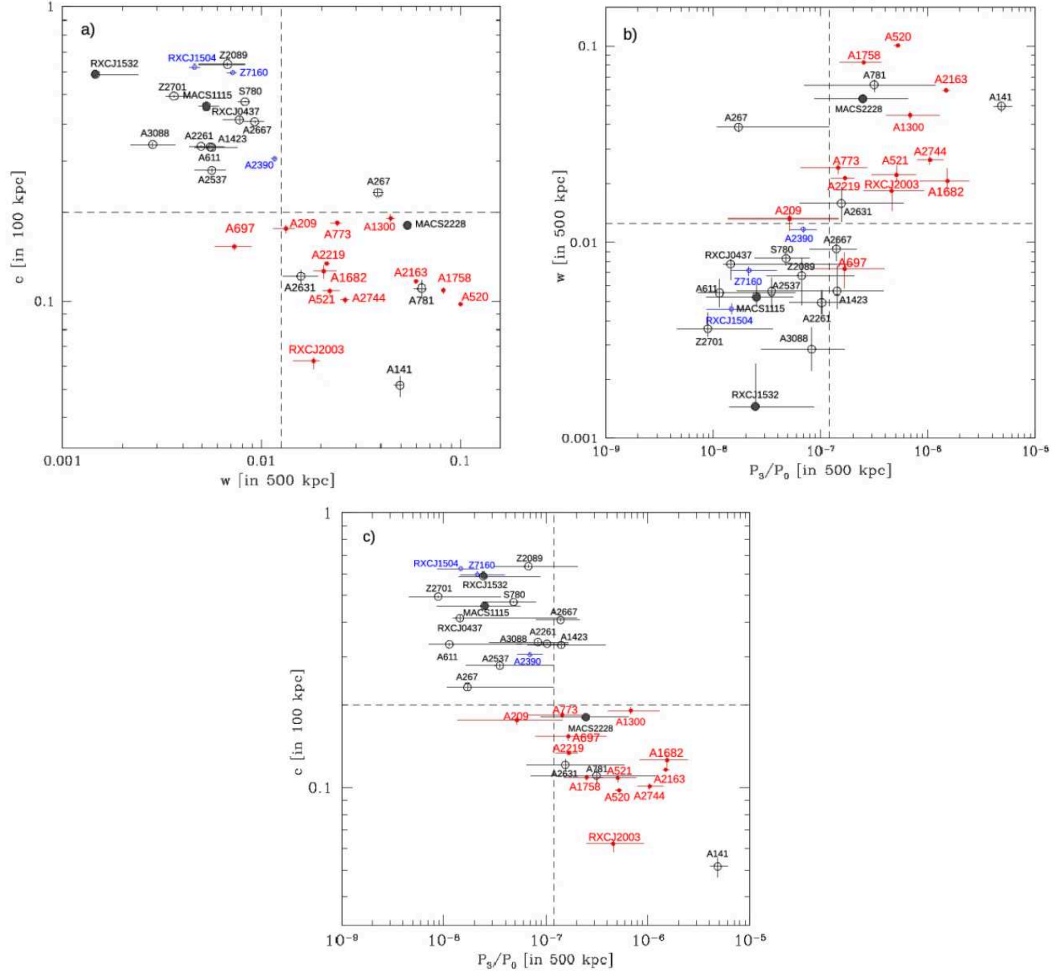


Figure 3.7: a) Concentration parameter  $c$  versus centroid shift  $w$  plane; b)  $w$  vs. power ratio  $P_3/P_0$ ; c)  $c$  vs  $P_3/P_0$ . Clusters hosting a RH are represented as red dots. Black, open dots are RH quiet clusters. gray filled dots are clusters of  $z > 0.32$  and blue open dots are mini halos. The dashed line values are the median values of each parameter (see text), splitting the diagrams into regions of "relaxed" and "disturbed" clusters. Most clusters hosting RHs fall into the disturbed quadrants. Credit: [Cassano et al. \(2010a\)](#).

Name	$M_{500}$ ( $\times 10^{14} M_{\odot}$ )	$z$	Radio Power at 1.4 GHz ( $\times 10^{24} W/Hz$ )	References
A209	$8.4642^{+0.2837}_{-0.3160}$	0.206	$2.19 \pm 0.17$	1
A399	$5.2393^{+0.2917}_{-0.2321}$	0.0722	$0.21 \pm 0.03$	2
A401	$6.7458^{+0.2207}_{-0.1721}$	0.0739	$0.23 \pm 0.01$	1
A520	$7.8003^{+0.4033}_{-0.4131}$	0.203	$4.32 \pm 0.29$	1
A521	$7.2556^{+0.4743}_{-0.4887}$	0.2475	$1.31 \pm 0.14$	1
A523	-	0.1036	$1.21 \pm 0.07$	3
A545	$5.3940^{+0.4059}_{-0.4098}$	0.154	$1.57 \pm 0.09$	1
A665	$8.8590^{+0.3230}_{-0.3202}$	0.1818	$4.01 \pm 0.28$	1
A697	$10.9984^{+0.3716}_{-0.3671}$	0.282	$2.29 \pm 0.29$	1, 4, 5
A746	$5.3352^{+0.3917}_{-0.4028}$	0.2323	$3.03 \pm 0.69$	4
A754	$6.8539^{+0.1249}_{-0.1277}$	0.0542	$0.62 \pm 0.03$	1
A773	$6.8474^{+0.3362}_{-0.3110}$	0.2172	$1.86 \pm 0.22$	1
A781	$6.1307^{+0.4596}_{-0.4955}$	0.2952	$6.16 \pm 1.57$	6
A800	-	0.2223	$1.56 \pm 0.16$	7
A851	-	0.4069	$2.41 \pm 0.30$	1
A1213	-	0.0469	$0.38 \pm 0.02$	1
A1300	$8.9713^{+0.4587}_{-0.4537}$	0.3075	$7.57 \pm 0.95$	1
A1351	$6.8676^{+0.3799}_{-0.3812}$	0.322	$14.63 \pm 1.73$	1
A1550	$5.8776^{+0.3809}_{-0.4243}$	0.254	$1.62 \pm 0.35$	7
A1656	$7.1652^{+0.0674}_{-0.1073}$	0.0231	$0.65 \pm 0.06$	1
A1689	$8.7689^{+0.3368}_{-0.3368}$	0.1832	$7.46 \pm 0.52$	9
A1758	$8.2173^{+0.2727}_{-0.2824}$	0.2799	$1.03 \pm 0.13$	1
A1914	$7.2358^{+0.2582}_{-0.2612}$	0.1712	$5.99 \pm 0.39$	1
A1995	$4.9242^{+0.3773}_{-0.3691}$	0.3179	$1.47 \pm 0.28$	1
A2034	$5.8503^{+0.2294}_{-0.2337}$	0.113	$0.46 \pm 0.04$	1
A2061	$3.5898^{+0.2076}_{-0.2122}$	0.0777	$0.27 \pm 0.07$	10
A2065	$4.0811^{+0.1863}_{-0.1900}$	0.0723	$0.43 \pm 0.14$	10
A2069	$5.3074^{+0.2212}_{-0.2396}$	0.1145	$1.01 \pm 0.25$	10
A2142	$8.7713^{+0.1858}_{-0.2093}$	0.0894	$1.31 \pm 0.13$	10
A2163	$16.1164^{+0.2968}_{-0.2922}$	0.203	$18.76 \pm 1.00$	1
A2218	$6.5851^{+0.1598}_{-0.1642}$	0.1709	$0.42 \pm 0.02$	1
A2219	$11.6918^{+0.2500}_{-0.2743}$	0.228	$12.24 \pm 0.93$	1
A2254	$5.5870^{+0.3597}_{-0.3548}$	0.178	$3.14 \pm 0.22$	1
A2255	$5.3828^{+0.0586}_{-0.0612}$	0.0809	$0.96 \pm 0.06$	1
A2256	$6.2107^{+0.1012}_{-0.0915}$	0.0581	$0.86 \pm 0.02$	1
A2294	$5.9829^{+0.3671}_{-0.3741}$	0.178	$0.54 \pm 0.05$	1
A2319	$8.7351^{+0.1132}_{-0.1240}$	0.0557	$1.13 \pm 0.06$	1,10
A2744	$9.8356^{+0.3947}_{-0.3754}$	0.3066	$17.32 \pm 1.57$	1
A3411	$6.5925^{+0.3094}_{-0.3106}$	0.1687	$0.38 \pm 0.04$	11
A3444	$7.3676^{+0.3637}_{-0.3686}$	0.2542	$3.08 \pm 0.29$	1
A3562	$2.4429^{+0.2133}_{-0.2442}$	0.049	$0.12 \pm 0.01$	1

Table 3.2: Collection of clusters known to host a radio halo. See continuation in Table 3.3

Name	$M_{500}$ ( $\times 10^{14} M_{\odot}$ )	$z$	Radio Power at 1.4 GHz ( $\times 10^{24} W/Hz$ )	References
PLCKG147.3-16.6	-	0.65	$5.22 \pm 1.59$	12
PLCKG285.0-23.7	$8.3925^{+0.3332}_{-0.3404}$	0.39	$1.72 \pm 0.22$	This work
PLCKG171.9-40.7	$10.7102^{+0.4931}_{-0.4963}$	0.27	$4.98 \pm 0.58$	13
PSZ1G108.18-11.53	$7.7387^{+0.5694}_{-0.5996}$	0.336	$2.23 \pm 0.41$	14
RXCJ0949.8+1708	$8.2387^{+0.4644}_{-0.4561}$	0.38	$1.75 \pm 0.76$	15
RXCJ0107.7+5408	$5.8478^{+0.3030}_{-0.3117}$	0.1066	$1.62 \pm 0.15$	4
RXCJ1314.4-2515	-	0.2439	$3.89 \pm 0.28$	1
RXCJ1514.9-1523	$8.8607^{+0.4054}_{-0.4578}$	0.2226	$1.64 \pm 0.50$	16
RXCJ2003.5-2323	$8.9919^{+0.4444}_{-0.4885}$	0.3171	$12.47 \pm 1.20$	1
MACSJ1149.5+2223	$10.4178^{+0.5207}_{-0.5451}$	0.545	$2.54 \pm 1.22$	17
MACSJ0417.5-1154	$12.2503^{+0.5253}_{-0.5502}$	0.443	$\sim 20$	18
MACSJ0717.5+3745	$11.4871^{+0.5347}_{-0.5482}$	0.546	$157.54 \pm 6.82$	19
MACSJ1752.0+4440	$6.7475^{+0.4377}_{-0.4543}$	0.366	$11.84 \pm 1.56$	17
MACSJ0553.4-3342	$8.7720^{+0.4399}_{-0.4629}$	0.431	$6.87 \pm 2.96$	17
MACSJ0416.1-2403	-	0.396	$1.14 \pm 1.43$	20
CIZAJ1938.3+5409	$7.5779^{+0.2876}_{-0.2809}$	0.26	$0.36 \pm 0.16$	15
CL0016+16	$9.7937^{+0.5293}_{-0.5314}$	0.5456	$7.43 \pm 1.63$	21
CL0217+70	-	0.0655	$0.62 \pm 0.01$	22
CL1446+26	-	0.37	$4.75 \pm 0.49$	1
CL1821+643	-	0.299	$2.85 \pm 1.20$	23
1E0657-56	$13.1003^{+0.2874}_{-0.2931}$	0.2965	$23.68 \pm 2.30$	1
El Gordo	$10.7536^{+0.4781}_{-0.4721}$	0.87	$10.20 \pm 0.99$	24

Table 3.3: Collection of clusters known to host a radio halo. Col. 1: Cluster name; Col. 2: SZ mass proxy  $M_{500}$  (Planck Collaboration et al., 2016b); Col. 3: Redshift; Col. 4: Radio power of the RH at 1.4 GHz; Col. 5: **References.** (1) [Giovannini et al. \(2009\)](#); (2) [Murgia et al. \(2010\)](#); (3) [Giovannini et al. \(2011\)](#); (4) [van Weeren et al. \(2011\)](#); (5) [Govoni et al. \(2011\)](#); (6) [Macario et al. \(2011\)](#); (7) [Govoni et al. \(2012\)](#); (9) [Vacca et al. \(2011\)](#); (10) [Farnsworth et al. \(2013\)](#); (11) [van Weeren et al. \(2013\)](#); (12) [van Weeren et al. \(2014\)](#); (13) [Giacintucci et al. \(2013\)](#); (14) [de Gasperin et al. \(2015\)](#); (15) [Bonafede et al. \(2015\)](#); (16) [Giacintucci et al. \(2011\)](#); (17) [Bonafede et al. \(2012\)](#); (18) [Dwarakanath et al. \(2011\)](#); (19) [Bonafede et al. \(2009\)](#); (20) [Pandey-Pommier et al. \(2015\)](#); (21) [Giovannini and Feretti \(2000\)](#); (22) [Brown et al. \(2011a\)](#); (23) [Bonafede et al. \(2014b\)](#); (24) [Lindner et al. \(2014\)](#).



# The Macs-Planck Radio Halo Project

---

## Contents

---

<b>4.1</b>	<b>Introduction</b> . . . . .	<b>39</b>
<b>4.2</b>	<b>Sample selection</b> . . . . .	<b>42</b>
<b>4.3</b>	<b>The ATCA sub-sample</b> . . . . .	<b>43</b>
4.3.1	Observations and data reduction . . . . .	43
4.3.2	Radio Images Processing . . . . .	45
4.3.2.1	Full resolution maps . . . . .	45
4.3.2.2	Tapering and diffuse source search . . . . .	45
4.3.2.3	Upper limit determination . . . . .	47
<b>4.4</b>	<b>The GMRT sub-sample</b> . . . . .	<b>48</b>
4.4.1	Observations and data reduction . . . . .	48
4.4.2	Tapering, diffuse source search and upper limit determination . . . . .	50

---

In this chapter I introduce the project in which I was involved during my thesis: The Macs-Planck Radio Halo Project. I will present the aims of the project, as well as the sample selection and the observations, data reduction and image reconstruction strategies. Finally, I will describe the radio images processing in search for diffuse sources and the approach followed to set upper detection limits.

## 4.1 Introduction

In recent years, the knowledge of the physical mechanisms responsible for the generation of RHs has moved towards a general consensus. The re-acceleration of relativistic electrons by the large scale turbulence generated in cluster mergers has now the status of the preferred scenario to explain the origin of RHs (see Sect. 3.4.1). However, we still need to fully test the correlation between mergers and RHs and to answer fundamental questions about the micro-physics of electron acceleration and transport mechanisms to fully understand the complex non-thermal processes in the ICM. An important attempt to solve this mystery are statistical studies of RHs and their connection with the dynamical state of their host systems.

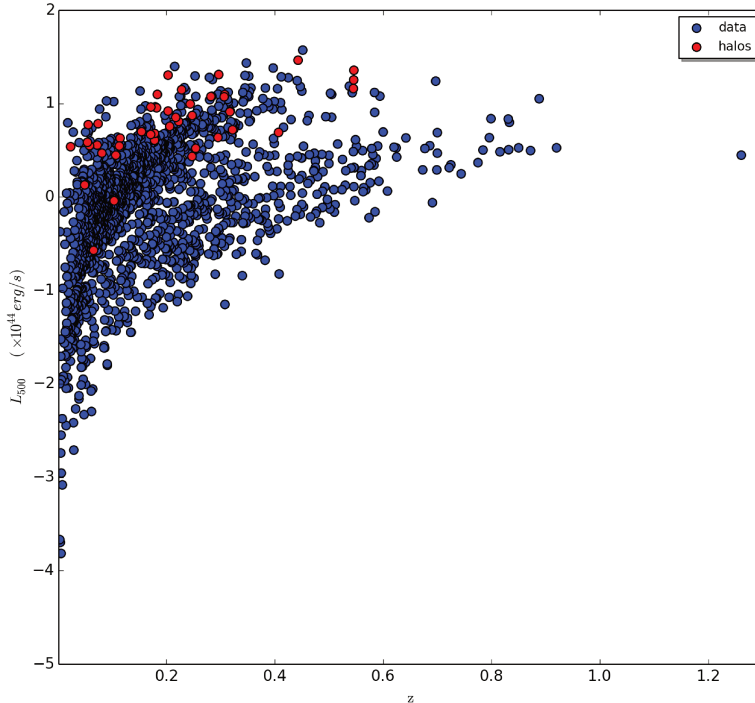


Figure 4.1: The 0.1-2.4 keV band luminosities  $L_{500}$  of the 1743 Meta-Catalogue of X-ray detected Cluster of Galaxies MCXC (Piffaretti et al., 2011) as a function of redshift in lin-log scale. Blue points correspond to detected clusters, while red points are those clusters with a detected RH. From this figure it is evident that RHs tend to appear in more X-ray luminous clusters.

We must mention that current knowledge of RHs is mostly based on high mass galaxy cluster samples (see Fig. 4.1). Mass-based selections are motivated by the assumption that the selection of high X-ray luminosity merging systems have more chances of detection of diffuse radio sources. An important attempt to start filling the mass selection gaps is the recent work done by Shakouri et al. (2016), where the authors investigated the presence of diffuse radio emission with a wide sample on X-ray morphology and in a wide range of masses. Several attempts to know the correlations of RHs with the host cluster properties in base of statistical considerations have been done (see e.g. Giovannini and Feretti, 2002b, and references therein). An important more recent study on RH occurrence is the Giant Metrewave Radio Telescope (GMRT) Radio Halo Survey (GRHS) (Venturi et al., 2007, 2008) and the extended sample (E-GRHS) (Kale et al., 2013, 2015), with the aim of exploring the origin and occurrence of RHs, as well as their connection with the dynamical state of the host systems. For their selection, the authors picked galaxy clusters with a redshift range  $z = 0.2-0.4$ , X-ray luminosities  $L_x$  (0.1-2.4 keV)  $> 5 \times 10^{44}$  erg s $^{-1}$  and declinations  $\delta > -31^\circ$  to ensure a good

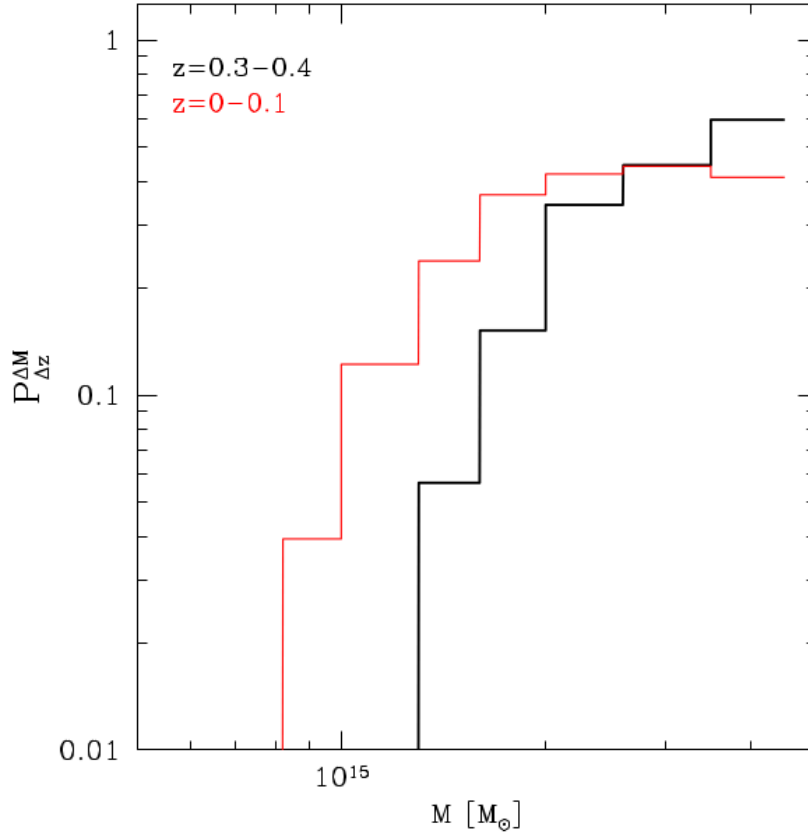


Figure 4.2: Predicted fraction of galaxy clusters hosting a RH observable at  $\sim$ GHz frequencies as a function of virial mass in two different redshift bins. The calculations are obtained from turbulent acceleration models. Notice that the fraction of RHs in the redshift window  $z = 0.3-0.4$  (shown in black) is larger than in the local bin  $z = 0-0.1$  (plotted in red) for larger virial masses.

uv-coverage with the GMRT. This sample is however effectively limited to  $z < 0.3$ . Although a number RHs have been discovered at  $z > 0.3$ , a complete statistical sample is missing in this redshift regime (see [Feretti et al., 2012](#)).

Moreover, apart from the lack of statistical studies, another motivation to explore higher redshifts, based on some current turbulence acceleration models (see [Cassano et al., 2004, 2006](#)) is the expectation that a larger fraction of RH occurrence may appear at the redshift range  $z = 0.3-0.4$  (Fig. 4.2). The reason for this is that most of the energy budget in the hierarchical grow of clusters is dissipated via massive mergers in this redshift range. In addition, at higher  $z$  stronger IC losses are expected to occur. It is then necessary to fill the observational gaps in order to complete the panorama on the nature of RHs. The aim of our work is to contribute in the filling of the redshift observational gap by extending the currently redshift limited statistics of RHs up to  $z=0.45$ .

## 4.2 Sample selection

The MACS-Planck Radio Halo Cluster Project (RHCP) was conceived as a continuation of the E-GRHS project (see Sect. 4.1). Our sample consists of a total 48 galaxy clusters, all of them taken from the MACS Brightest Cluster X-ray catalogue (Ebeling et al., 2010) and the list of newly discovered Planck SZ clusters confirmed with the XMM-Newton validation program available at the time of the proposal (see Planck Collaboration et al., 2011b). For the project, all the clusters from both samples that are located in the range  $z = 0.3-0.45$  were selected (see Fig. 4.3), resulting in 33 MACS clusters and 15 Planck SZ clusters.

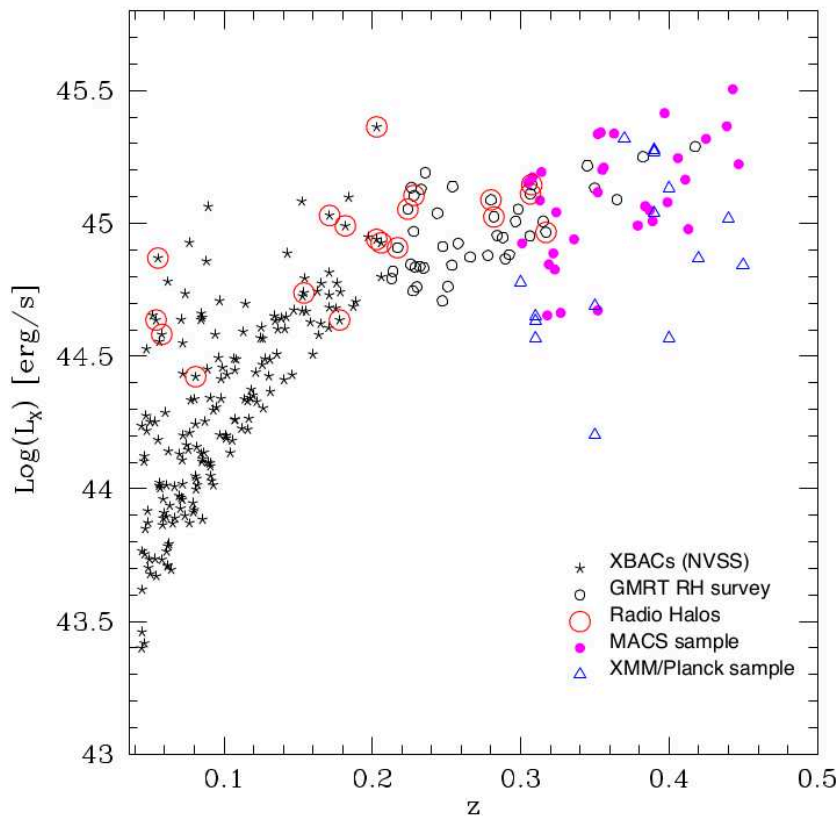


Figure 4.3: X-ray luminosity (0.1-2.4 keV) vs redshift for the MACS-Planck sample. Empty blue triangles correspond to XMM-Newton-Planck subsample and magenta filled circles are the MACS subsample. For comparison, different samples at lower redshifts are plotted in black. Open red circles indicate clusters hosting a RH.

From the total number of selected clusters, 32 were lacking public radio information until this project started. The declination range of the clusters in our sample required observations to be done with two different telescopes, depending on the declination of the targets. Based on the sources visibility and the uv-coverage constrains to achieve the desired sensitivities for detecting diffuse radio emission, the total sample was divided into two groups:

a) Those lying in the range of  $\delta > -40^\circ$  (25 clusters in total) were observed with the GMRT at  $\sim 325$  MHz.

b) The remaining seven galaxy cluster with  $\delta < -40^\circ$  were observed with the ATCA telescope. These observations are centred at 2.1 GHz with a bandwidth of 2000 MHz. The analysis of the ATCA sub-sample is the main object of this thesis.

## 4.3 The ATCA sub-sample

### 4.3.1 Observations and data reduction

The main information of the galaxy clusters from the ATCA sample appear in Table 4.1. In order to achieve the desired spatial scales sampled by the uv-coverage, radio observations of the ATCA sample were done with three separate array configurations for each observed cluster (Table 4.2) using the Compact Array Broadband Backend (CABB) correlator with a central frequency of 2.1 GHz and spanning 1.1-3.1 GHz (project ID C2679). Observations were carried out in continuum mode with the correlator set to produce  $2000 \times 1$  MHz channels. Details of the observations can be found in Table 4.2. The primary flux scale was set relative to the unresolved source PKS B1934-638 for which the detailed spectral behaviour is well understood. The amplitude gain variations were checked during the calibration of each observation for each sub-band image so as to be not higher than  $\sim 2\%$ .<sup>1</sup>

Radio frequency interference (RFI) and bad channels were excised manually from primary and secondary calibrators, as well as the target, by using a combination of clipping algorithms and visual inspection via the MIRIAD task PGFLAG (Sault et al., 1995). It was necessary to perform calibration on narrower frequency intervals due to the nature of CABB data. After a number of trials, we determined that 4 sub-bands of  $\sim 500$  MHz produce the optimal results for these data. Thus, the target, primary and secondary calibrator data were divided into the required sub-bands coined Block 1 (from 2.631 GHz to 3.100 GHz), Block 2 (from 2.131 GHz to 2.630 GHz), Block 3 (from 1.631 GHz to 2.130 GHz) and Block 4 (from 1.130 GHz to 1.630 GHz). Each sub-band was then self-calibrated in MIRIAD by using the task SELFCAL. Finally, the self-calibration solutions were saved by using the task UVAVER.

The data reduction followed the same procedure for all the galaxy cluster images of the sample except for PSZ2 G284.97-23.69 where it was promptly noticed the presence of diffuse radio emission in the cluster center. In this particular case, the self-calibration process was not applied as we noticed that the self-calibration process gives a bit higher rms noises. To excise phase errors we performed a detailed analysis of the uv-data. It was found that the data from the 6D array suffered from a bandpass ripple of unknown origin which persisted for 75 minutes on all baselines associated with antennas 5 and 6. This data was removed and

<sup>1</sup>see [http://www.atnf.csiro.au/observers/memos/d96783\\_1.pdf](http://www.atnf.csiro.au/observers/memos/d96783_1.pdf).

Table 4.1: Information of the clusters of the MACS-Planck ATCA sample. The names and alternative names of the clusters appear in Cols. 1 and 2. RA and DEC correspond to the coordinates for centring the ATCA observations (Cols. 3 and 4). The Planck Mass, X-ray luminosity and Redshift (Cols. 5, 6 and 7, respectively) are taken from [Planck Collaboration et al. \(2011b\)](#). \* See Sect. 5.4.2 for a deeper discussion on PLCK G334.8-38.0.

Cluster name	Alternative name(s)	RA (h m s)	DEC (° ' ")	$M_{500}$ (SZ) ( $\times 10^{14} M_{\odot}$ )	$L_{500}$ ( $\times 10^{44}$ erg/s)	Redshift
PSZ2 G285.63-17.23	PSZ1 G285.62-17.23 PLCK G285.6-17.2	08 43 44.40	-71 13 14.00	6.64±0.40	4.45±0.08	0.35
PSZ2 G262.73-40.92	PSZ1 G262.72-40.92 SPT-CLJ0438-5419 ACT-CL J0438-5419 PLCK G262.7-40.9	04 38 17.20	-54 19 25.10	7.46±0.36	9.94±0.47	0.421
PSZ2 G277.76-51.74	PSZ1 G277.75-51.71 SPT-CLJ0254-5857 PLCK G277.8-51.7	02 54 16.70	-58 56 44.00	9.69±0.38	9.46±0.07	0.438
PSZ2 G286.28-38.36	PSZ1 G286.27-38.39 PLCK G286.3-38.4	03 59 10.20	-72 04 46.10	5.94±0.40	4.07±0.02	0.307
PSZ2 G271.18-30.95	PSZ1 G271.18-30.95 SPT-CLJ0549-6205 PLCK G271.2-31.0	05 49 19.50	-62 05 16.00	7.37±0.32	18.95±0.16	0.37
PSZ2 G284.97-23.69	PLCKESZ G284.99-23.70 PLCK G285.0-23.7	07 23 18.40	-73 27 20.60	8.39±0.34	16.91±0.27	0.39
PLCK G334.8-38.0*	-	20 52 16.80	-61 12 29.40	-	-	0.35

a normal calibration was applied instead. Thereafter we continue the image processing in a similar way as in the rest of the sample.

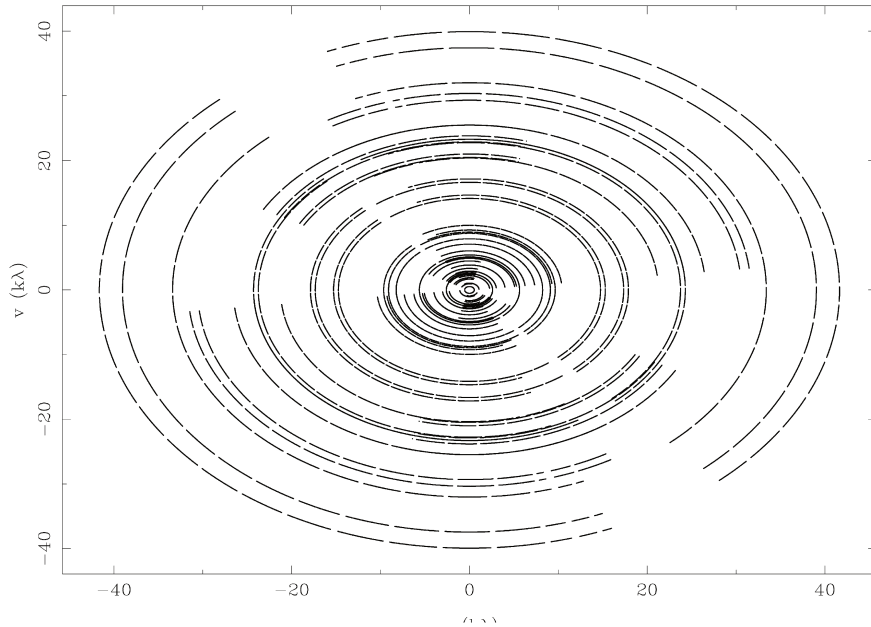


Figure 4.4: Example of uv-coverage of our ATCA observations in the 500 MHz band centred at 1.867 MHz. The wide-band of the full 2 GHz observations completes the coverage.

## 4.3.2 Radio Images Processing

### 4.3.2.1 Full resolution maps

For each observed cluster, four images were created, one for each of the 4 sub-bands, out to the second null in the point spread function by using the task INVERT and a Steer CLEAN (Steer et al., 1984) was applied to all sources within the primary beam. The sub-band images were then convolved to a common Gaussian, whose size corresponds to the lowest resolution image and then added together to create a final wide-band image (see Table 5.1). The noise levels in the sub-band images are very similar for the three highest bands and only differed slightly in the lowest frequency band; it was not necessary to weight the images relative to the sensitivities in the mosaicing process.

### 4.3.2.2 Tapering and diffuse source search

We proceeded to subtract the compact radio sources from the uv-data. Using the self-calibrated data, we imaged the visibilities for the longest baselines (uv-range from 3.6 to 40 k $\lambda$ , which translates to angular scales from  $\sim 5$  to  $\sim 57$  arcseconds) and subtracted the corresponding clean components from the self-calibrated uv-data by using the MIRAD task UVMODEL.

Table 4.2: Details of the observations towards the clusters selected for observations with ATCA. Cluster name (Col. 1); dates of observations (Col. 2) with different array configurations (Col. 3); Observation time (Col. 4); phase calibrator (Col. 5). The central frequency is at 2.1 GHz and the total observed bandwidth is 2 GHz.

Cluster name	Date	Config.	Observation time (min.)	Calibrator
PSZ2 G285.63-17.23	2015-Jun-12	1.5C	549	PKS B0606-795
	2012-Jun-29	750A	442	PKS B0606-795
	2012-Jun-07-08	6D	1132	PKS B0637-752
PSZ2 G262.73-40.92	2013-Mar-05	6A	353	PKS B0420-625
	2013-Feb-02	750C	354	PKS B0420-625
	2012-Nov-23	1.5C	354	PKS B0420-625
PSZ2 G277.76-51.74	2013-Sep-03-04	1.5A	1140	PKS B0302-623
	2013-Jul-31	750D	1061	PKS B0302-623
	2013-Aug-01	750D	152	PKS B0302-623
	2013-May-11-12	6C	1188	PKS B0302-623
PSZ2 G286.28-38.36	2013-Mar-05	6A	384	PKS B0252-712
	2012-Feb-02	750C	354	PKS B0252-712
	2012-Nov-23	1.5C	413	PKS B0252-712
PSZ2 G271.18-30.95	2013-Mar-05	6A	354	PKS B0420-625
	2013-Feb-02	750C	294	PKS B0420-625
	2012-Nov-23	1.5C	353	PKS B0420-625
PSZ2 G284.97-23.69	2012-Jun-08	6D	704	PKS B1036-697
	2012-Jun-09	6D	523	PKS B0606-795
	2012-Jun-29	750A	531	PKS B0606-795
	2013-Sep-06	1.5A	804	PKS B0606-795
PLCK G334.8-38.0	2013-Sep-03-04	1.5A	1131	PKS B0302-623
	2013-Jul-30	750D	1203	PKS B1934-638
	2013-May-12	6C	1297	PKS B1934-638

This creates a new uv-data set which was re-imaged. Again, none of the seven clusters showed the obvious presence of diffuse emission in the central area in the source subtracted high resolution images.

In order to investigate the possible presence of low-surface brightness radio emission in the clusters, the point source subtracted visibilities were re-imaged with a  $\text{robust}=0.5$  weighting and applying a  $\sim 9 \text{ k}\lambda$  Gaussian tapering. Traditionally, measurements of flux densities of RHs are reported at the central frequency of 1.4 GHz. It is worth noticing that from typical spectral behaviour of radio halos ( $\alpha \gtrsim 1$  synchrotron spectral index<sup>2</sup>) it is expected to have lower luminosities for higher frequencies. Even if the Block 4 sub-band would be ideal to do flux density measurements because of its lower central frequency, it is also strongly affected by RFI (50-60 % of the data was flagged). In our images we have comparable rms sensitivities for the frequency range running from Block 3 to Block 1. This set of conditions makes Block 3 centred at  $\sim 1.9$  GHz the most suitable sub-band to do flux density measurements. In Table 5.1 we report the main features for the set of the source subtracted Block 3 tapered images.

#### 4.3.2.3 Upper limit determination

Cluster radio images that showed no evidence of the presence of diffuse sources were used to set detection limits for possible diffuse radio emission. In order to set the detection upper limits, we took a similar approach to that used in, e.g., [Venturi et al. \(2008\)](#). Specifically, our procedure consists of the following steps:

1) We simulated a diffuse source with the MIRIAD task IMGGEN. The model consist of 5 low surface brightness concentric disks, the biggest with a diameter of 1 Mpc. To reproduce the typical profile of a RH, these disks area percentages are from largest to smallest: 100%, 60%, 33%, 25% and 12%. These disks contribute, respectively, the following percentage of the total flux of the simulated source: 72%, 20%, 5%, 2% and 1%.

2) The simulated source was added into the compact source subtracted uv-data of the corresponding observation on the sub-set coined Block3 ( $\sim 500$  MHz wide, see Sect. 4.3.1) for each galaxy cluster. This step was done by using the MIRIAD task UVMODEL, which generates a new uv-data set of the real data plus the simulated source. To perform the injection of the disk models we picked the 1 Mpc diameter circle centred on the cluster coordinates and five 1 Mpc areas inside the primary beam, without any trace of point sources and where there is no appearance of  $3\sigma$  contours due to artefacts on the original image plane. We made this choice under the considerations that there are more chances to have radio emission in the cluster area, and the injection of the model would enhance the real emission. The other 5 areas were chosen as "control" areas, to avoid as much as possible, to be affected by the presence of real sources or errors on the image reconstruction.

3) The model injected uv-data were re-imaged at low resolution applying a taper with the

<sup>2</sup>In this paper we use the convention  $S(\nu) \propto \nu^{-\alpha}$ , being  $S(\nu)$  the radio flux density.

following parameters on the MIRIAD task `invert`: `FWHM=20`, `robust=0.5`, `cell=4`, in order to achieve more sensitivity to the kind of emission of the simulated halos, as we have done in Sect. 4.3.2.2.

4) The injected fluxes of the different modelled disks were increased until we noticed that  $3\sigma$  contours appear uniformly on the injection areas.

It is worth noticing that we were able to recover from  $\sim 50\%$  to  $\sim 70\%$  of the original injected flux by measuring the total flux density in the areas of the image plane where the injections were done.

## 4.4 The GMRT sub-sample

### 4.4.1 Observations and data reduction

Observations of the GMRT sub-sample were carried out by recording the data each 16.1 seconds, covering bandwidths of 32 MHz with 256 channels. Details of the clusters belonging to the GMRT sub-sample appear in Table 4.3. The data reduction of the complete GMRT sub-sample was already performed by Huib Intema when this thesis project started (see [Macario et al., 2014](#)). The data was processed by using both the NRAO Astronomical Processing System (AIPS) package and the Source Peeling and Atmospheric Modelling (SPAM) software ([Intema et al., 2009](#)). The basic functionality needed was provided by AIPA for the largest part of the data reduction and SPAM was used to derive and apply the direction-dependent calibration during imaging. An effective bandwidth of 31.2 MHz, centred at 323 MHz, remains after the edition of the data. After applying the amplitude calibration to the target field, additional RFI flagging and frequency averaging to 24 channels (1.3 MHz each) was performed.

The target field was then self-calibrated with a simple point source model obtained from the NVSS ([Condon et al., 1998](#)) and WENSS ([Rengelink et al., 1997](#)). Several rounds of wide-field imaging, CLEAN deconvolution and self-calibration were needed, and only in the final round an amplitude calibration was applied in order to get corrections for antenna gain amplitude variations, by using a 1-minute time scale.

The gains per antenna were normalized before applying, by using only the target field scan closest in time to the flux calibrator scan. This enforces the correct flux scale across the whole observation run. Ionospheric calibration and imaging were applied to the data by using SPAM. We estimate that the average residual amplitude errors are  $\lesssim 8\%$ . When the calibration solutions converged, the final full resolution images were obtained, as well as the residual visibilities used to perform the diffuse source search and the fake halo injection.

Table 4.3: Information of the clusters of the MACS-Planck GMRT sample. RA and DEC correspond to the coordinates for centring the observations (Cols. 2 and 3). The X-ray (0.1 - 2 keV) Luminosity and Redshift (Cols. 4 and 6) are taken from the sample proposal, while the S-Z mass proxy  $M_{500}$  (Col. 5) was taken from [Planck Collaboration et al. \(2011b\)](#).

Cluster name	RA (h m s)	DEC	Lx ( $10^{44}$ erg/s)	$M_{500}$ ( $10^{14} M_{\odot}$ )	Redshift
MACSJ0011.7-1523	00h 11m 42.9s	-15 23 22	9.8	$5.06^{+0.58}_{-0.63}$	0.379
MACSJ0035.4-2015	00h 14m 18.9s	-20 15 48	13.1	n/a	0.352
MACSJ0152.5-2852	01h 52m 34.5s	-28 53 36	9.5	$5.93^{+0.52}_{-0.59}$	0.413
MACSJ0159.8-0849	01h 59m 49.4s	-08 49 59	18.0	$7.2^{+0.61}_{-0.68}$	0.406
MACSJ0242.5-2132	02h 42m 35.9s	-21 32 26	15.6	$7.64^{+0.48}_{-0.51}$	0.314
MACSJ0257.6-2209	02h 57m 41.1s	-22 09 18	7.7	$6.06^{+0.56}_{-0.59}$	0.322
MACSJ0404.6+1109	04h 04m 33.3s	+11 07 58	4.7	$7.71^{+0.66}_{-0.77}$	0.352
MACSJ0429.6-0253	04h 29m 36.0s	-02 53 08	12.0	n/a	0.399
MACSJ0520.7-1328	05h 20m 42.0s	-13 28 50	8.7	$6.24^{+0.52}_{-0.54}$	0.336
MACSJ0547.0-3904	05h 47m 01.5s	-39 04 26	7.0	$4.95^{+0.51}_{-0.54}$	0.319
MACSJ1206.2-0847	12h 06m 12.2s	-08 48 01	23.2	$11.18^{+0.48}_{-0.48}$	0.439
MACSJ1319.9+7003	13h 20m 08.4s	+70 04 37	4.6	$4.11^{+0.39}_{-0.43}$	0.327
MACSJ1427.6-2521	14h 27m 39.4s	-25 21 02	4.5	n/a	0.318
MACSJ1720.2+3536	17h 20m 16.8s	+35 36 26	11.2	$6.09^{+0.56}_{-0.59}$	0.387
MACSJ1731.6+2252	17h 31m 39.1s	+22 51 52	10.2	$8.27^{+0.54}_{-0.54}$	0.389
MACSJ1931.8-2634	19h 31m 49.6s	-26 34 34	21.7	$6.97^{+0.53}_{-0.56}$	0.352
MACSJ2049.9-3217	20h 49m 56.2s	-32 16 50	6.7	$5.37^{+0.59}_{-0.64}$	0.323
MACSJ2140.2-2339	21h 40m 15.2s	-23 39 40	12.2	n/a	0.313
MACSJ2229.7-2755	22h 29m 45.2s	-27 55 37	11.0	n/a	0.324
MACSJ2245.0+2637	22h 45m 04.6s	+26 38 05	8.4	n/a	0.301
PLCK G241.2-28.7	05h 42m 56.8s	-35 59 55	7.4	$7.36^{+0.50}_{-0.49}$	0.420
PLCK G272.9+48.8	11h 33m 10.5s	-09 28 52	13.6	$5.75^{+0.61}_{-0.66}$	0.400
PLCK G250.0+24.1	09h 32m 13.8s	-17 38 07	3.7	$6.65^{+0.52}_{-0.56}$	0.400
PLCK G100.2-30.4	23h 22m 14.9s	+28 31 14	3.69	n/a	0.310
PLCK G214.6+36.9	09h 08m 49.5s	+14 38 29	6.97(a)	n/a	0.450

#### 4.4.2 Tapering, diffuse source search and upper limit determination

The final residual uv-data FITS files provided by Huib Intema were converted to MIRIAD format by using the task *fits* and we performed the same tapering procedure described in Sect. 4.3.2.2. This means, the visibilities were re-imaged with a  $\text{robust}=0.5$  weighting and applying a  $\sim 9 \text{ k}\lambda$  Gaussian tapering. We then performed the same procedure as the one described in Sect. 4.3.2.3 for the injection of the fake halos on the residual visibilities in order to obtain the detection limits for the GMRT sub-sample.

In the next chapter we will see the results obtained from the complete analysis of the ATCA sub-sample, while in Chapter 6, I will present the preliminary results obtained from a first analysis of the already available GMRT data.

Cluster name	RA (h m s)	DEC	$L_x$ ( $10^{44}$ erg/s)	$M_{500}$ ( $10^{14} M_{\odot}$ )	$z$	Radio Info.
MACSJ0014.3-3022	00 14 18.9	-30 23 22	14.9	$9.84^{+0.39}_{-0.38}$	0.308	1 (RH)
MACSJ0308.9+2645	03 08 55.8	+26 45 37	16.2	$10.76^{+0.63}_{-0.65}$	0.356	2
MACSJ0358.8-2955	03 58 54.4	-29 55 32	20.8	$7.20^{+0.52}_{-0.50}$	0.425	2
MACSJ0417.5-1154	04 17 34.7	-11 54 33	32.0	$12.25^{+0.53}_{-0.55}$	0.443	3 (RH)
MACSJ0947.2+7623	09 47 13.0	+76 23 14	22.0	$5.62^{+0.45}_{-0.46}$	0.354	4
MACSJ0949.8+1708	09 49 51.7	+17 07 08	11.6	$8.24^{+0.46}_{-0.46}$	0.384	5
MACSJ1115.8+0129	11 15 52.0	+01 29 55	15.9	$6.86^{+0.53}_{-0.54}$	0.355	5
MACSJ1131.8-1955	11 31 54.4	-19 55 42	14.4	$8.97^{+0.46}_{-0.45}$	0.306	5 (RH)
MACSJ2228.5+2036	22 28 34.0	+20 37 18	14.6	$8.27^{+0.43}_{-0.45}$	0.411	5
MACSJ1532.8+3021	15 32 53.8	+30 20 58	21.8	n/a	0.363	5 (mH)
MACSJ2243.3-0935	22 43 21.1	-09 35 43	16.7	$9.99^{+0.44}_{-0.44}$	0.447	2
MACSJ2311.5+0338	23 11 33.1	+03 38 07	14.2	$7.48^{+0.41}_{-0.46}$	0.305	6
MACSJ2211.7-0349	22 11 46.0	-03 49 47	26.0	$10.50^{+0.50}_{-0.49}$	0.397	2
PLCK G287.0+32.9	11 50 49.2	-28 04 37	18.9	$14.69^{+0.39}_{-0.42}$	0.39	7 (dR)
PLCK G292.5+22.0	12 01 05.3	-39 52 26	6.00	$7.93^{+0.44}_{-0.46}$	0.30	8
PLCK G205.0-63.0	02 46 25.8	-20 33 17	4.28	$7.64^{+0.48}_{-0.51}$	0.31	8

Table 4.4: Clusters from the MACS-Planck Radio Halo Cluster Project with available deep radio public information. The  $L_x$  is in the [0.1 - 2 keV] band. References of radio information: (1) Govoni et al. (2001b), (2) GMRT archive, (3) Dwarakanath et al. (2011), (4) Gitti et al. (2006), (5) Venturi et al. (2008), (6) VLA archive, (7) Bagchi et al. (2011), (8) 21009.



# Analysis of the ATCA sub-sample

---

## Contents

---

<b>5.1</b>	<b>Radio image analysis</b> . . . . .	<b>53</b>
5.1.1	Full resolution maps . . . . .	53
5.1.2	Compact source subtracted tapered images . . . . .	54
<b>5.2</b>	<b>X-ray dynamical state of the ATCA clusters</b> . . . . .	<b>56</b>
<b>5.3</b>	<b>Results</b> . . . . .	<b>59</b>
5.3.1	A Radio Halo in PSZ2 G284.97-23.69 . . . . .	59
5.3.1.1	Detection of the source using PyBDSM . . . . .	62
5.3.1.2	Radio luminosity vs. cluster mass correlation . . . . .	64
5.3.2	Diffuse radio source in the cluster PSZ2 G262.73-40.92. . . . .	67
<b>5.4</b>	<b>Clusters without diffuse radio emission</b> . . . . .	<b>68</b>
5.4.1	The Cool-core cluster PSZ2 G271.18-30.95 . . . . .	68
5.4.1.1	Highly disturbed clusters without radio emission . . . . .	69
5.4.2	The triple system of low mass clusters PLCK G334.8-38.0 . . . . .	70
5.4.2.1	Detection limits . . . . .	71
<b>5.5</b>	<b>Conclusions</b> . . . . .	<b>72</b>

---

In this section I present the results obtained after the analysis of the radio observations from the ATCA sub-sample. The main results obtained during the work of my PhD thesis appear in this chapter. The results were published in: [Martinez Aviles et al. \(2016\)](#) and Martinez Aviles et al. (Submitted).

## 5.1 Radio image analysis

### 5.1.1 Full resolution maps

As described in the previous chapter, we have produced both the full resolution and tapered images for each galaxy cluster observed with the ATCA. The radio contours of the central

Table 5.1: Properties of the full resolution band-width radio maps in centred at 2.1 GHz. Col. 1: cluster name; Col. 2: rms noise; Col. 3: beam size and Col. 4: position angle

Cluster name	rms noise ( $\mu\text{Jy}/\text{beam}$ )	Beam Size ( $''\times''$ )	PA (deg)
PSZ2 G285.63-17.23	22.4	$6.85 \times 4.07$	-8.13
PSZ2 G262.73-40.92	19.7	$6.39 \times 4.15$	-2.45
PSZ2 G277.76-51.74	15.4	$5.55 \times 4.25$	1.99
PSZ2 G284.97-23.69	11.3	$5.20 \times 4.38$	-42.31
PSZ2 G286.28-38.36	19.4	$5.00 \times 4.46$	-11.00
PSZ2 G271.18-30.95	22.1	$5.80 \times 4.21$	-1.30
PLCK G334.8-38.0	16.1	$3.19 \times 2.20$	9.96

area from our full resolution images are overlaid on the XMM-Newton X-ray images in Fig. 5.1 (yellow contours). In Figs. A.1 and A.2 we show the high resolution ATCA radio maps for the wide field ( $\sim 34 \text{ arcmin}^2$ ) and the zoomed cluster regions ( $\sim 9 \text{ arcmin}^2$ ). The final deep ATCA images root mean squared (rms) noise is measured with AIPS TVSTAT at the field centre in regions inside the primary beam without any trace of point sources or diffuse emission. The information of the images (rms noises and resolutions) is shown in Table 5.1. A visual inspection of the central area (where the clusters lie) of each of the seven full resolution images does not reveal obvious presence of diffuse radio emission.

### 5.1.2 Compact source subtracted tapered images

In Table 5.2 we report the main features for the set of the source subtracted Block 3 tapered images. In search of residual diffuse emission in the cluster areas we set the classical  $3\sigma$  contours in the tapered images. In some cases, we did find contours that correspond to positions of point sources visible in the full resolution maps, due to an imperfect point source subtraction or to the presence of some extended emission candidates.

Apart from the full resolution radio contours, in Fig.5.1 we show the radio contours for the tapered images where we discovered the presence of possible diffuse sources overlaid on the XMM-Newton X-ray images. The analysis of these set of images led us to suspect the presence of diffuse sources in two out of our seven ATCA clusters: PSZ2 G284.97-23.69 (top-right panel in Fig. 5.1, see Sect. 5.3.1) and PSZ2 G262.73-40.92 (Sect. 5.3.2, top-left panel in Fig.5.1).

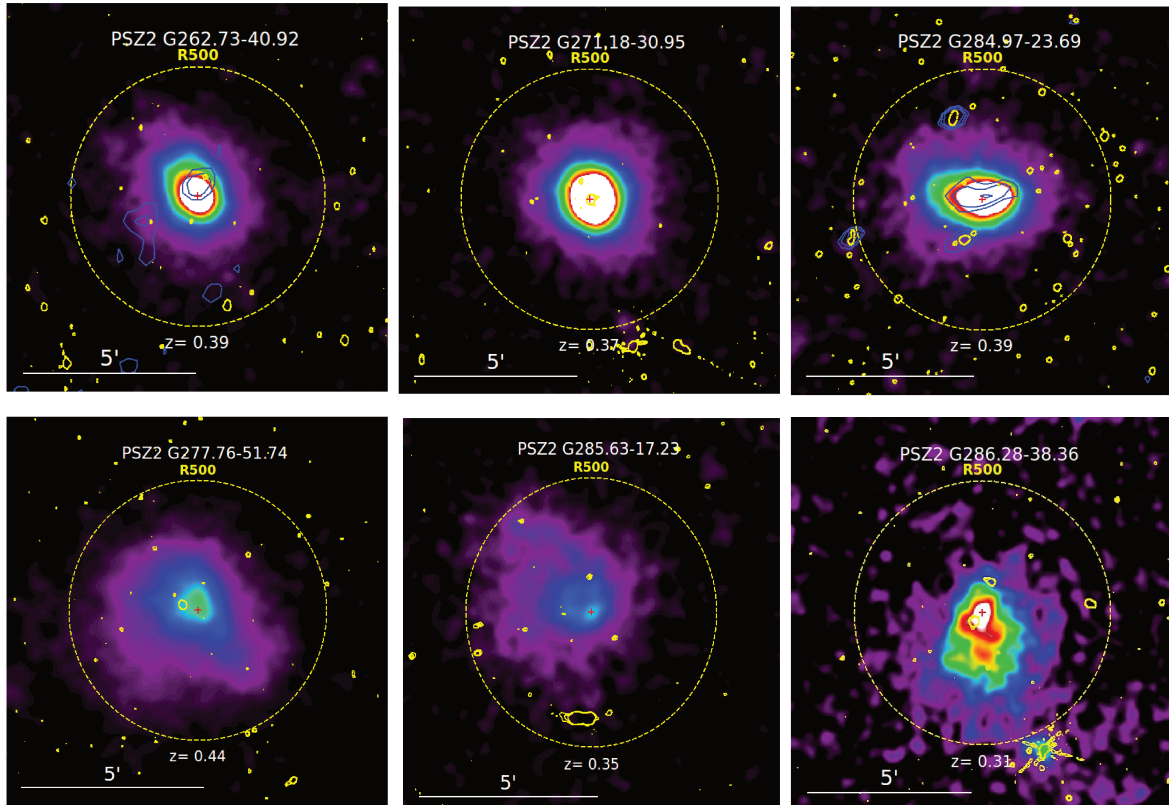


Figure 5.1: XMM-Newton smoothed images in the [0.3-2] keV band of the ATCA cluster sample overlaid with the  $3\sigma \times (1, \sqrt{2}, 2)$  contours of the full resolution wide band radio maps (see Table 5.1 and Figs. A.1 and A.2) in yellow and the same contour levels for the Block 3 low resolution compact source subtracted maps for the two clusters with diffuse radio emission (see Sects. 5.3.1 and 5.3.2) in blue. The images are scaled to a self-similar model. The colours are selected so that the images would be identical if clusters obeyed strict self similarity, which give us a visual hint of the dynamical state of the clusters.

Table 5.2: Information of source subtracted Block 3 tapered images. The rms noises of the corresponding maps are presented in Col. 2. and the beam sizes and position angles appear in Cols. 3 and 4 respectively.

Cluster name	RMS ( $\mu\text{Jy}/\text{Beam}$ )	Beam Size ( $''\times''$ )	PA (deg)
PSZ2 G285.63-17.23	92	$43 \times 17$	89.07
PSZ2 G262.73-40.92	83	$32 \times 25$	-7.67
PSZ2 G277.76-51.74	65	$35 \times 28$	58.04
PSZ2 G286.28-38.36	57	$28 \times 26$	-46.47
PSZ2 G271.18-30.95	74	$31 \times 25$	-28.70
PLCK G334.8-38.0	71	$34 \times 23$	2.96
PSZ2 G284.97-23.69	51	$31 \times 23$	-81.17

## 5.2 X-ray dynamical state of the ATCA clusters

The present X-ray analysis was performed by my collaborators Jessica Democles, Gabriel Pratt and Monique Arnaud, whom I warmly thank for the results appearing in this section. All the clusters of the ATCA sample benefit from X-ray observations from the XMM-Newton space telescope as part of the validation program of Planck cluster candidates. For the processing, the background of the X-ray images has been subtracted. The X ray images are corrected from surface brightness dimming with redshift, divided by emissivity in the energy band, taking in account absorption from the Galaxy and the response of the instrument. The full X-ray data processing is detailed in [Planck Collaboration et al. \(2011b\)](#). The cluster mass,  $M_{500}$ , and corresponding  $R_{500}$ , are derived iteratively using the low scatter  $M_{500}-Y_X$  scaling relation from [Planck Collaboration et al. \(2011b\)](#), where  $Y_X$  is the product of the gas mass within  $R_{500}$  and the X-ray temperature in the  $[0.15 - 0.75] R_{500}$  aperture. The density profiles were derived from the surface brightness profile centered on the X-ray emission peak, using the PSF-deconvolution and deprojection method of [Croston et al. \(2008\)](#). From this analysis, we compute two morphological parameters :

a) The surface brightness concentration parameter  $C$ :

$$C = \frac{S_X(< R_{\text{in}})}{S_X(< R_{\text{out}})} \quad (5.1)$$

the ratio of the surface brightnesses  $S_X$  within an inner aperture  $R_{\text{in}}$  and a global aperture  $R_{\text{out}}$ .  $S_X$  is the PSF-corrected surface brightness, derived from the emission measure profile. Introduced in [Santos et al. \(2008\)](#) using  $R_{\text{in}} = 40$  kpc and  $R_{\text{out}} = 400$  kpc, this parameter have been widely used to probe the core properties of clusters up to high redshift (e.g. [Santos et al., 2010](#); [Hudson et al., 2010](#); [Pascut and Ponman, 2015](#)). Here we choose to use scaled apertures since the clusters of our sample cover a wide redshift range, with  $R_{\text{in}} = 0.1 \times$

$R_{500}$ , corresponding to the typical size of the cool-core, and  $R_{\text{out}} = 0.5 \times R_{500}$ , which is a characteristic size for the total flux.

b) The X-ray centroid-shift  $w$ , as defined in, for example, [Böhringer et al. \(2010\)](#) within 10 circular apertures from 0.1 to 1  $R_{500}$  excising the first central aperture:

$$w = \left[ \frac{1}{N+1} \sum (\Delta_i - \langle \Delta \rangle)^2 \right]^{1/2} \times \frac{1}{R_{500}} \quad (5.2)$$

where  $\Delta_i$  is the distance between the emission weighted centroid within the  $i$ th aperture and the X-ray peak,  $N$  the number of apertures

The centroid-shift is computed on the background-subtracted, exposure-corrected co-added X-ray count images in the 0.3-2 keV energy band after removal and refilling of the point sources as in [Böhringer et al. \(2010\)](#).

The results are visualized in Fig. 5.2, where we overplot for comparison the positions of objects from the `REXCESS` (open grey circles; see [Böhringer et al., 2010](#), for the centroid-shift values). Fig. 5.2 includes also the systems in common between the samples of [Cassano et al. \(2013\)](#) and [Planck Collaboration et al. \(2011a\)](#) (blue points), for which we have computed the concentration parameter and the centroid-shift values as described above for the RHCP-ATCA sample.

The horizontal and vertical dashed lines of Fig. 5.2 indicate characteristic threshold values of each parameter that are typically used to separate out, respectively, cool-core and morphologically disturbed systems. Following [Pratt et al. \(2009\)](#), we use a value of  $w > 0.01$  as indicative of a morphologically disturbed system. Similarly, we define targets with  $C > 0.35$  (equivalent to the central density criterion used by [Pratt et al. \(2009\)](#)) as being centrally peaked and thus cool-core systems.

We stress here that the limits indicated with dashed lines in Fig.5.2 were obtained for the local `REXCESS` sample. Also the sample analysed by [\(Cassano et al., 2013\)](#) is mostly made up by lower redshift clusters compared to our targets. In addition, we recall that, instead of using scaled apertures, [Cassano et al. \(2013\)](#) adopted fixed physical sizes for computing the two parameters  $w$  (500 kpc) and  $C$  ( $S_x(<100 \text{ kpc})/S_x(500 \text{ kpc})$ ). Their choice was based on the theoretical consideration that, for a typical  $\sim 1$  Mpc-size RH, 500 kpc is expected to delimitate the region where the energy of the merger is dissipated in particle acceleration. These factors are however not expected to make our analysis significantly different from the approach of [Cassano et al. \(2013\)](#), since recent works have proven that the adopted morphological parameters neither depend significantly on the size of the central region selected to estimate them (e.g. good agreement between  $w$  measured within  $R_{500}$  and  $0.5 R_{500}$ ), nor are limited by resolution issues up to  $z \sim 1$  clusters (e.g. [Bartalucci et al., 2017](#), [Lovisari et al.](#), private communication). Our new estimates of the  $C$  and  $w$  parameters, however, indicate that one of the radio-loud clusters in [Cassano et al. \(2013\)](#) falls in the relaxed part of the plot.

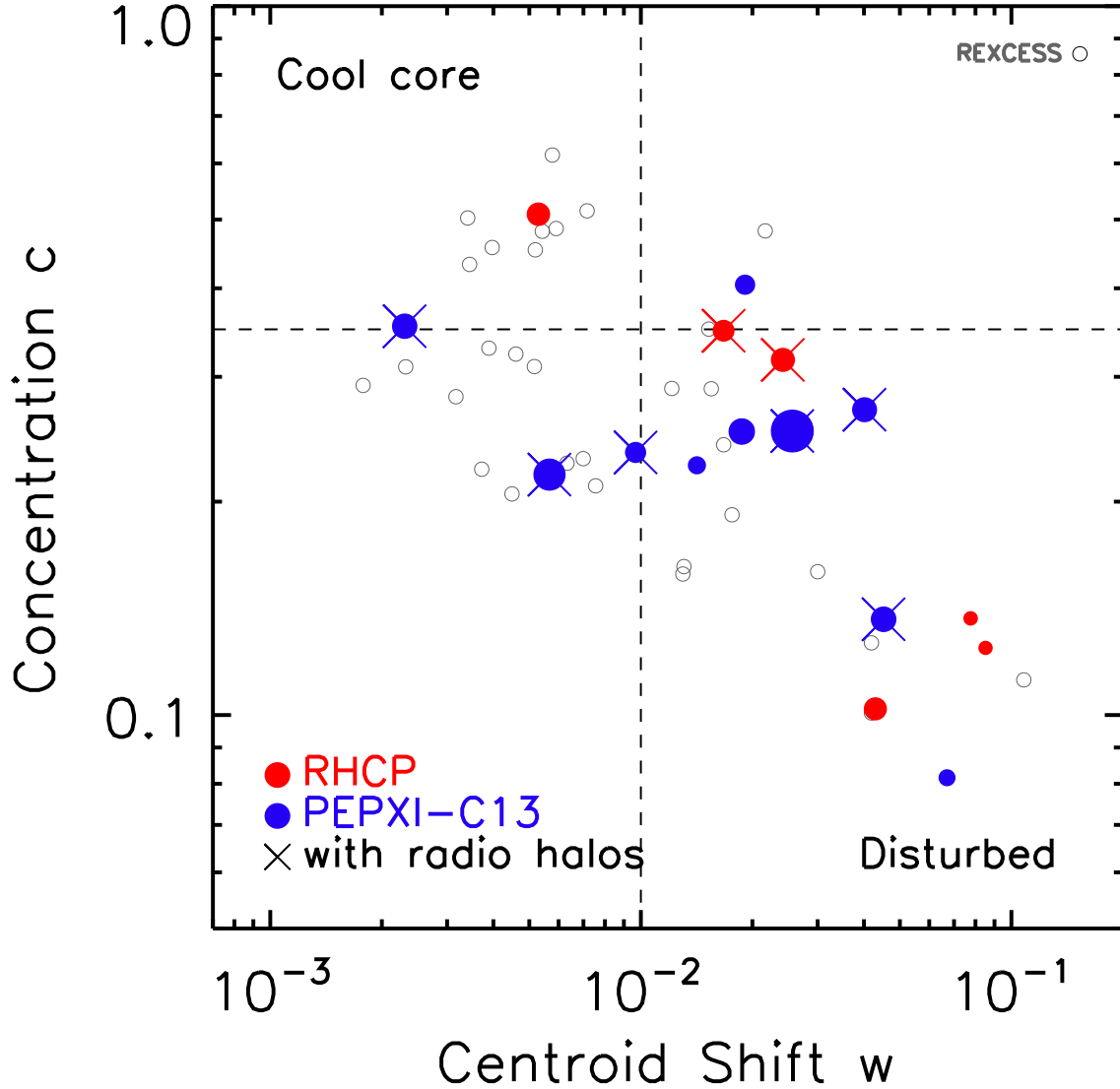


Figure 5.2: Concentration parameter  $C$  vs. centroid shift  $w$  for the galaxy clusters of the ATCA-RHCP sample analysed in this paper (red filled circles). For comparison, we also show the clusters in the sample of Cassano et al. (2013) that appear in the sub-sample of Planck clusters studied by Planck Collaboration et al. (2011a) (PEPXI-C13, blue filled circles) for which we applied our algorithm to compute the  $w$  values within  $R_{500}$ . The size of the circles is proportional to the  $\log(M_{500})$ , in the range  $[14.67-15.3]$ , and clusters with detected radio haloes are marked with a cross. The characteristic thresholds indicating cool-cores and morphologically disturbed systems (dashed lines) are from the REXCESS study (Böhringer et al., 2007). The REXCESS clusters are shown as open circles.

## 5.3 Results

### 5.3.1 A Radio Halo in PSZ2 G284.97-23.69

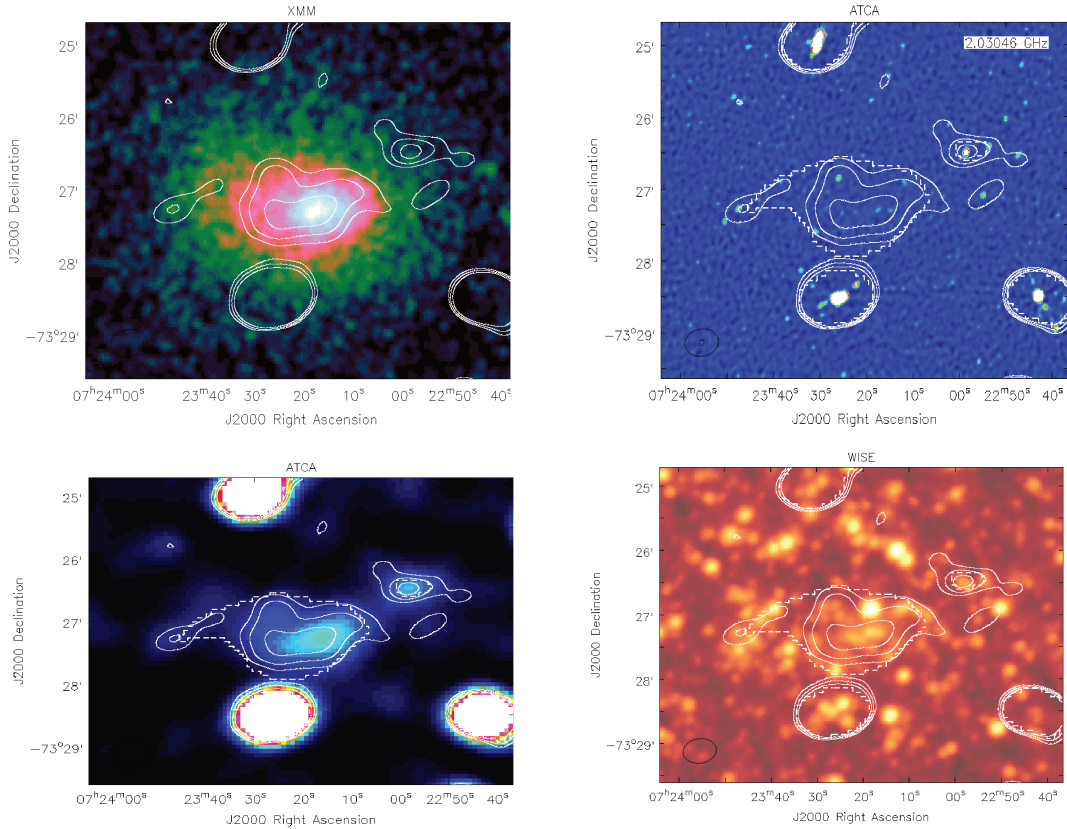


Figure 5.3: PSZ2 G284.97-23.69 radio contours of the ATCA tapered image centred at 1.867 GHz overlaid on: the smoothed raw XMM image in the [0.3-2.0] keV energy band (top, left panel); the full band high resolution ATCA radio image (top, right panel); the Block 3 tapered radio image without compact source subtraction (bottom, left panel) and the 4.6 micron WISE image (bottom, right panel). Dashed contours correspond to the islands of significant emission detected by PyBDSM on the Block 3 tapered map (cyan contours in Fig.5.5). The continuous curves trace instead “classical”  $3, 3 \times \sqrt{2}, 6 \sigma$  contours (i.e. with the  $51.1 \mu\text{Jy}/\text{beam}$  rms value of the map estimated by hand on the Block 3 tapered map at  $\sim 30$  arcsec resolution; see Table 5.2).

In Sect. 5.1.2 we have seen that the compact source subtracted Block 3 tapered image of PSZ2 G284.97-23.69 shows the presence of radio contours close to the central cluster coordinates. Contours of the low-resolution radio map of PSZ2 G284.97-23.69 are overlaid on the X-ray XMM image of the same sky region in Fig. 5.3, top, left panel. The morphology of the diffuse radio source matches very closely the thermal ICM X-ray emission in terms of

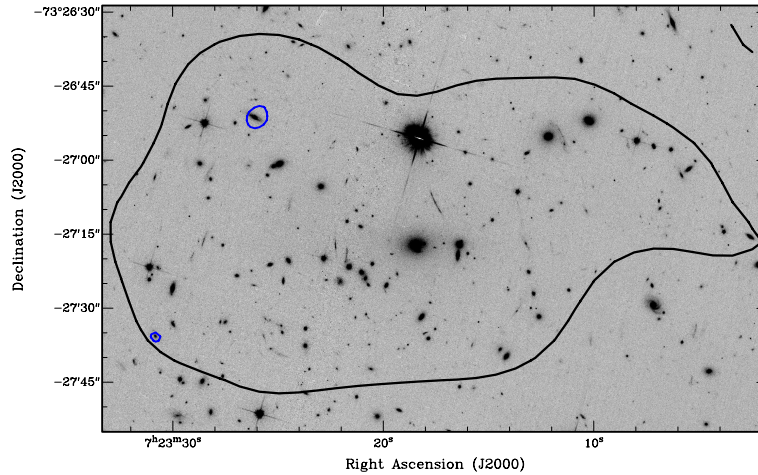


Figure 5.4: Zoom in the HST-ACS image of PSZ2 G284.97-23.69 central field (available in the HST archive). For reference, the  $3\sigma$  contour of the ATCA tapered image centred at 1.867 GHz is shown in black. The blue contours indicate sources of significant radio emission in the full-resolution deep ATCA image of the cluster (i.e.  $5 \times \text{rms}$  of the final wide-band ATCA map shown in Fig. A.2).

extension and of elongation (with a main axis along the east–west direction). PSZ2 G284.97-23.69 is the second more luminous and more massive cluster in the sample (see Table 4.1). Based on its disturbed morphology ( $w = 0.028 \pm 0.001$ ) and concentration parameter ( $C = 0.317 \pm 0.005$ ) it falls in a quadrant of dynamically disturbed systems (Fig. 5.2), with a relatively high  $C$  parameter, though. The same contours are overlaid on the 4.6 micron WISE image (bottom, right panel of Fig. 5.3), where we can see the presence of galaxies inside the contours. This galaxies, however do not show any obvious counterparts in the full resolution wide band ATCA radio image (top, right panel).

As explained in Sect. 4.3.2.2, we now examine the radio flux density of the diffuse source on the tapered image relative to Block 3, i.e. the image centred at 1.867 GHz and characterised by an average rms noise level of  $51.1 \mu\text{Jy}/\text{beam}$  (Table 5.2). The total flux density was first measured on the Block 3 tapered image without compact source subtraction, by integration over the source image within  $3\sigma$  contours using the AIPS task TVSTAT. By overlaying the  $5\sigma$  contours corresponding to the full-resolution wide-band radio map on the optical image of the cluster central region, we identify two point-like significant objects lying within the region occupied by the diffuse source on the low-resolution radio map. The two compact radio sources show quite clear optical counterparts (see Fig. 5.4). We measured their flux densities using the AIPS verb JMFIT and we subtracted them from the total flux density measured inside the  $3\sigma$  contours of the tapered image. To verify that large-scale diffuse emission is not caused by the blending of discrete sources and to get a complementary measurement, we calculated the flux density of the residual diffuse emission by integrating the surface brightness in the same region considered before, i.e. within the  $3\sigma$  level of the non-

Images ID	Angular size ( $' \times '$ )	Physical size (kpc $\times$ kpc)	Flux (mJy)
ID 1	$2.34 \times 1.34$	$742 \times 425$	$2.02 \pm 0.25$
ID 2	"	"	$2.11 \pm 0.26$
ID 2 ss	"	"	$1.95 \pm 0.25$
ID 1	$2.98 \times 1.60$	$945 \times 507$	$2.37 \pm 0.34$
ID 2	"	"	$2.53 \pm 0.35$
ID 2 ss	"	"	$2.17 \pm 0.44$

Table 5.3: Physical properties of the diffuse radio source at 1.867 GHz from tapered images. *Col. 1* gives the identification numbers of the tapered images on which we have performed the measurements: ID 1: Image with source subtraction in uv-data; ID 2: Image without source subtraction in uv-data; ID 2 ss: Image of ID2 after removing by hand the flux of point sources identified in the image plane. *Col. 2* and *Col. 3* correspond to the angular and physical size of the source, respectively (see text). *Col. 4* reports the flux of the diffuse radio sources as measured with TVSTAT within the  $3\sigma$  contours of the map with ID 2 (*top*), with TVSTAT within the  $3\sigma$  contours calculated by PyBDSM for the map with ID 2 (*bottom*).

point source subtracted tapered map (ID 1 in Table 5.3). The results of these flux density measurements are given in the top part of Table 5.3. The error in flux density is calculated following the formula:

$$\Delta F = \sqrt{(\sigma_{rms})^2 N_{beam} + 0.01 F^2} \quad (5.3)$$

where  $F$  is the measured flux density and  $N_{beam}$  is the number of beams contained in the measured area.

Table 5.3 shows the results of the different flux density measurements; all the values are consistent within the error bars. The flux measurement that we adopt in our following analysis is the one measured in the tapered map with point source subtracted from the uv-plane labelled in the following ID1 (see Table 5.3), for which we obtain a flux density of  $2.02 \pm 0.25$  mJy at 1.867 GHz.

In order to get an estimate of the size of the diffuse radio source, we measured the smallest ellipse that fully contains the  $3\sigma$  contours of the Block 3 tapered map without point source subtraction (ID2 in Table 5.3). We obtain an angular extent of  $2.34' \times 1.34'$ , which, for our cosmology, corresponds to a major and minor axis of  $\sim 742$  kpc and 425 kpc, respectively (see Table 5.3).

Finally, we measured with TVSTAT the total flux density on the ID1 and ID2 maps by following the contours of the significant islands of emission identified by the automatic source finder software PyBDSM around the diffuse source (dashed contours in Fig. 5.3; see 5.3.1.1 for details on the use of PyBDSM). The results obtained following this final method are given

in the bottom part of Table 5.3.

These flux measurements, the size and remarkable morphology resemblance between radio contours and X-ray morphology, plus the disturbed dynamical state suggested by its X-ray morphology and density profile, allows us to confidently classify the diffuse source in PSZ2 G284.97-23.69 as a classical RH.

### 5.3.1.1 Detection of the source using PyBDSM

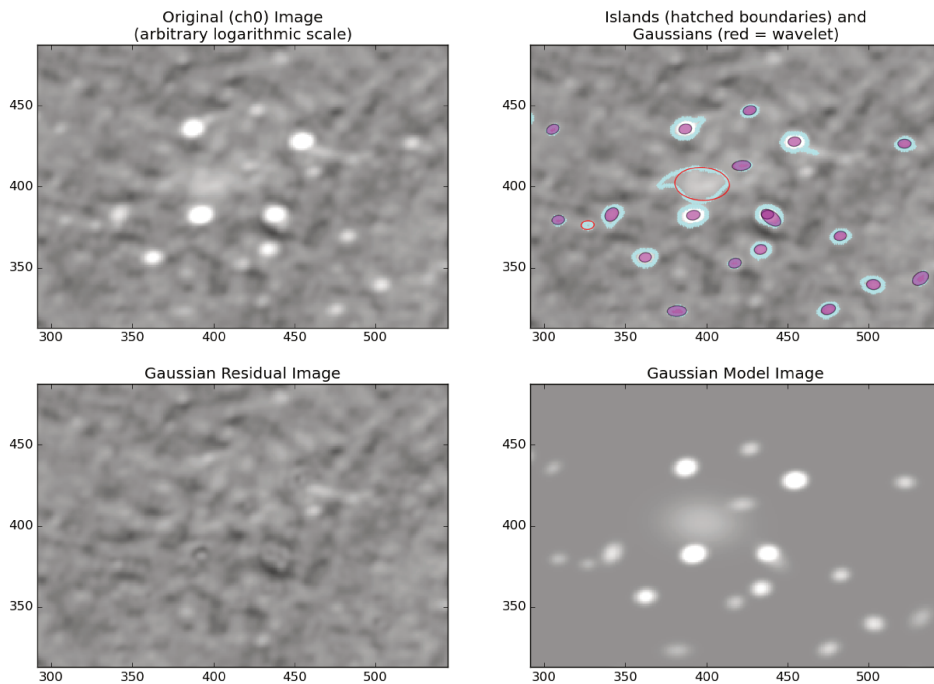


Figure 5.5: Output of the PyBDSM source finder tool. The axis units are in pixels. From *left to right* and from *top to bottom*: Original image on which PyBDSM is run (in this example, the ID2 map of Table 5.3); islands of significant emission (cyan contours) and fitted Gaussians that model identified sources overlaid on the ID2 map; residual after the subtraction of the fitted sources; model of the reconstructed sky. The big red ellipse corresponds to the diffuse emission in the centre of the cluster.

The use of packages for the automatic detection of radio sources is becoming more and more necessary and common, especially in the era of the new generation of deep and wide radio surveys. In this framework, and in order to get a complementary measure of the total flux density of the diffuse radio source, we ran the automatic source finder PyBDSM (Mohan and Rafferty, 2015) on the tapered images with and without point source subtraction from the uv-data. It is worth noting that PyBDSM finds significant emission in both maps, corre-

sponding to the diffuse radio source that we found by visual inspection and analysis on the maps (see e.g. Fig. 5.5).

We used the threshold technique of the PyBDSM `process_image` task<sup>1</sup>, which locates islands of emission above some multiple of the noise in the image (`thresh_isl` parameter, set to  $3\sigma$  here). This determines the region where fitting is done. In addition, we set to  $5\sigma$  the source detection threshold in number of sigma above the mean (`thresh_pix` parameter). Finally, we activated the wavelet module of `process_image` (i.e. `atrous_do=True`), which improves the detection of diffuse sources by doing wavelet transforms at increasing scales of the residual image after subtraction of the initial fitted Gaussians. The modelled Gaussians are shown in the bottom right panel of Fig. 5.5, while the top right panel shows the islands of significant emission (cyan) and the position of the fitted Gaussians. Violet ellipses indicate the sources identified on the input radio map (top left), while the red empty ellipse shows the extended source recovered through the wavelet analysis. As shown in the residual maps (bottom left), we nicely managed to fit most of the source components, in particular the central diffuse source.

The final output catalogs of PyBDSM give a list of all the Gaussian functions fitted to model the significant emission within the input radio maps and give a source list where different Gaussians are grouped together if they satisfy objective criteria to be considered as a single source. For each detected source, PyBDSM provides the values of the FWHM of the major and minor axis and the total integrated Stokes I flux density. To subtract by hand the contribution of point sources from the ID2 map (case reported as ID2ss in Table 5.3), we ran PyBDSM on the full-resolution Block 3 image of the cluster. The values of the flux densities of compact sources obtained in this way and contained within the cyan region of Fig. 5.5 were then subtracted from the value of the total flux density of the diffuse source obtained in the ID 2 case.

The size and flux density of the newly detected radio halo are given as an output of PyBDSM, being  $5.76 \text{ arcmin} \times 4.34 \text{ arcmin}$  ( $914 \text{ kpc} \times 689 \text{ kpc}$ ) and  $4.91 \pm 0.04 \text{ mJy}$  for the map with ID1. In the case of ID2 and ID2ss, we obtained a halo size of  $4.48 \text{ arcmin} \times 2.70 \text{ arcmin}$ , and flux densities of  $4.08 \pm 0.07 \text{ mJy}$  and  $3.72 \pm 0.16 \text{ mJy}$ , respectively.

We note here that, compared to classical measurements performed “by hand” (Sect. 5.3.1 and Table 5.3), PyBDSM gives systematically higher values of both source sizes and total flux densities. This is because with classical methods we integrate the surface brightness of the diffuse source within a region delimited by the  $3\sigma$  contours, while this same region is used by PyBDSM as a support to fit one (or multiple) Gaussian function(s) giving the total flux density of the source(s) whose size is reconstructed based on moment analysis. This last method tends to include flux density coming from regions outside the original islands of significant emission, in particular when the wavelet module, which decomposes the residual image that results from the normal fitting of Gaussians into wavelet images of various scales,

---

<sup>1</sup>See [http://www.astron.nl/citt/pybdsm/process\\_image.html#general-reduction-parameters](http://www.astron.nl/citt/pybdsm/process_image.html#general-reduction-parameters) for detailed instructions of `process_image`.

is activated<sup>2</sup>.

Both methods are based on different assumptions. In the case of classical “by-hand” measurements, for instance, it is assumed that the mean value of the surface brightness of all pixels within  $3\sigma$  contours multiplied by the number of synthesised beams within the considered region is a proper measurements of the integrated flux density for the whole RH. Instead, in the case of PyBDSM, it is assumed that sources are correctly modelled by one or more Gaussian functions of increasing size. We do not conclude that one method is better than the other since they are based on different approaches, but we definitely recommend not directly comparing results obtained through a mix of the two different methods when producing plots such as our Fig. 5.12.

### 5.3.1.2 Radio luminosity vs. cluster mass correlation

We calculated the power of the newly discovered diffuse radio source and compared it with radio powers of previously discovered halos. We selected objects firmly classified as giant radio halos (i.e. with diffuse emission extending beyond the cluster core), whose flux density has been measured through radio interferometric observations and with a point source identification and subtraction strategy very similar to ours, and with information about  $M_{500}$  in the PSZ2 cluster catalog [Planck Collaboration et al. \(2015\)](#). The list of sources is presented in Appendix C.1 Table 4.

In order to convert all values to the cosmology adopted in this paper and to take into account some inconsistencies found for published radio powers, such as use of different cosmologies or the lack of the application of the k-correction, we compiled the total flux densities of RHs reported in the literature (see Tables 3.2 and 3.3). We then calculated radio powers using the formula:

$$L_\nu = 4\pi D_L^2 S_\nu (1+z)^{\alpha-1} \quad (5.4)$$

where  $D_L$  is the luminosity distance of the cluster. Whenever a measured value of the spectral index is not available, we adopted  $\alpha=1.3$ .

Traditionally RH powers are reported at 1.4 GHz; however, owing to the lower quality of the Block 4 image centred at 1.381 GHz, we considered the most reliable sub-band map (centred at 1.867 GHz) and then extrapolated to obtain the 1.4 GHz radio power. As the spectral index of the radio source is too uncertain over the ATCA band due to the very low surface brightness of the object, we undertake this extrapolation assuming the value of  $\alpha=1.3$ . We obtain a value for the radio power at 1.4 GHz of  $1.72 \pm 0.22 \times 10^{24}$  W/Hz.

In Fig. 5.12 we plot the radio power vs. cluster mass for the RH in PSZ2 G284.97-23.69 (shown as a red star) as compared to all halos included in Appendix C.1, Table 4, which are indicated by triangles (colour-coded based on the redshift of their host clusters), except when they are classified as ultra steep spectrum (USS) radio halos and/or when their flux was

<sup>2</sup>atrous\_do parameter set to True. See [http://www.astron.nl/citt/pybdsm/process\\_image.html#a-trous-wavelet-decomposition-module](http://www.astron.nl/citt/pybdsm/process_image.html#a-trous-wavelet-decomposition-module)

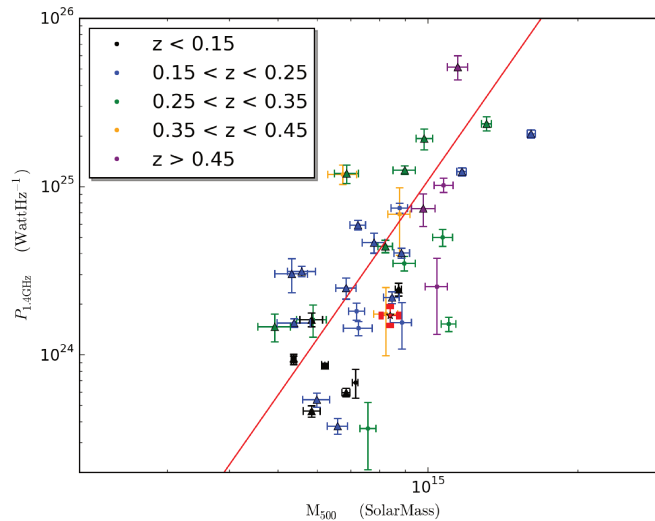


Figure 5.6: Synchrotron power of RHs at 1.4 GHz ( $P_{1.4GHz}$ ) vs. cluster mass  $M_{500}$  from [Planck Collaboration et al. \(2015\)](#). Symbols are colour-coded depending on the redshift of RH hosting clusters. The red line is the fit derived in the present paper, including only the RHs with radio fluxes measured at 1.4 GHz (indicated by triangles; see also Table ??). Analogously to [Cassano et al. \(2013\)](#), we exclude for the fitting ultra-steep spectrum RHs and halos detected in frequencies different from 1.4 GHz, both shown in dots (see Table 4 in Appendix C.1). The red star corresponds to PSZ2 G284.97-23.69 detected in this work. When the spectral index is unknown (including PSZ2 G284.97-23.69) we assume the value of  $\alpha=1.3$ .

not measured at  $\approx 1.4$  GHz (see Appendix C.1 Table 4), in which case they appear as dots (keeping the same colour code). Analogously to [Cassano et al. \(2013\)](#), we fit a power-law relation using linear regression in the log–log space and adopt a BCES–bisector regression algorithm [Akritas and Bershady \(1996\)](#). For the fitting, shown as a red line in Fig. 5.12 and characterised by a slope of  $4.24 \pm 0.14$ , we consider only the RHs represented as triangles in Fig. 5.12. The best fit derived by [Cassano et al. \(2013\)](#), traditionally reported in the literature, has a slope of  $3.77 \pm 0.57$ . For completeness we also derived the value for the slope using all radio powers of halos present in Table 4 of Appendix C.1 for the best fit, which is  $4.05 \pm 0.09$ . The three results are consistent within the error bars. The RH in PSZ2 G284.97-23.69 is slightly under-luminous with respect to the best-fit relation, but is within the scatter of the observed data points. We also point out that, based on the present radio data, we do not find a clear trend with redshift of the  $P_{1.4} - M_{500}$  correlation.

Following [Cassano et al. \(2007\)](#), we show in Fig. 5.7 the position of the newly detected radio halo on the plot of radio halo sizes as a function of the virial radius of their host clusters. There is evidence that powerful radio halos are also bigger and hosted by more massive systems [Giovannini and Feretti \(2000\)](#); [Kempner and Sarazin \(2001\)](#); [Cassano et al.](#)

(2007); Murgia et al. (2009). Although it is a massive cluster ( $M_{500} \sim 8.39 \times 10^{14} M_{\odot}$ ), PSZ2 G284.97-23.69 hosts a quite small radio halo of radius  $\sqrt{a * b} \sim 281$  kpc, where  $a$  and  $b$  are the semi-major and semi-minor axis derived in Sect. 5.3.1. However, if we consider the correlation between the size of the radio halos and the virial radius of their hosting clusters (Fig. 5.7), we see that PSZ2 G284.97-23.69 (red point) follows the trend of other radio loud clusters. This probably occurs because PSZ2 G284.97-23.69 is at a relatively high redshift ( $z \sim 0.39$ ), which means that its virial radius, and thus its radio halo, is smaller (owing to the cosmological growth and virialisation of galaxy clusters) than those of nearby clusters with the same mass.

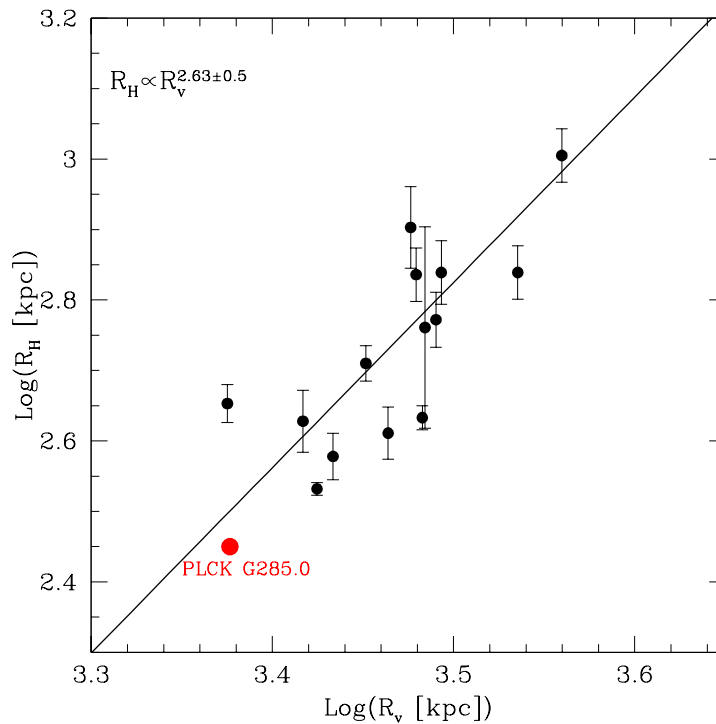


Figure 5.7: Correlation between radio halo sizes and the virial radius of their host clusters [see Cassano et al. (2007)]. The newly detected radio halo in PSZ2 G284.97-23.69 is indicated in red.

### 5.3.2 Diffuse radio source in the cluster PSZ2 G262.73-40.92.

The tapered compact source subtracted image on the field of the cluster PSZ2 G262.73-40.92 shows the presence of a candidate diffuse source close to the cluster central coordinates. The high resolution image reveals the presence of a very faint point source in the region of the diffuse emission, with a possible counterpart on the IR map (Fig. 5.8), for which we measured a flux density of 0.33 mJy. We measured the total flux density inside the  $3\sigma$  contours (shown in cyan color in Fig. 5.8) of the diffuse emission in the compact source subtracted tapered image in Block 3, characterized by a rms noise of  $83 \mu\text{Jy}/\text{beam}$  (see Table 5.1). We obtained a flux density of 1.18 mJy inside the  $3\sigma$  contours. The region shows an elliptical shape, with a major axis of 63 arcseconds and a minor axis of 50 arcseconds, which for our cosmology corresponds to a physical size of  $349 \text{ kpc} \times 277 \text{ kpc}$  at the cluster redshift. According to the X-ray morphological analysis, PSZ2 G262.73-40.92 is a merging, but probably moderately disturbed cluster, lying close to our cut line of cool-core clusters, with a concentration parameter  $C = 0.348 \pm 0.005$  and a centroid shift  $w = 0.016 \pm 0.001$  (see Fig. 5.2). It is important to note that the diffuse source present in the residual map follows the emission from the galaxies in the WISE images (Fig. 5.8), and is offset from the cluster X-ray emission (Fig. 5.1, top, left panel). Some similar results have been found by Govoni et al. (2012), where the authors find cases where the diffuse radio emission can be quite asymmetric with respect to the X-ray gas distribution, and tend to follow more closely the galaxy distribution rather than the intra-cluster gas distribution. Given the size and position of the source, plus the close-to-relaxed dynamical state of the host cluster, a classification of the source is challenging with our data.

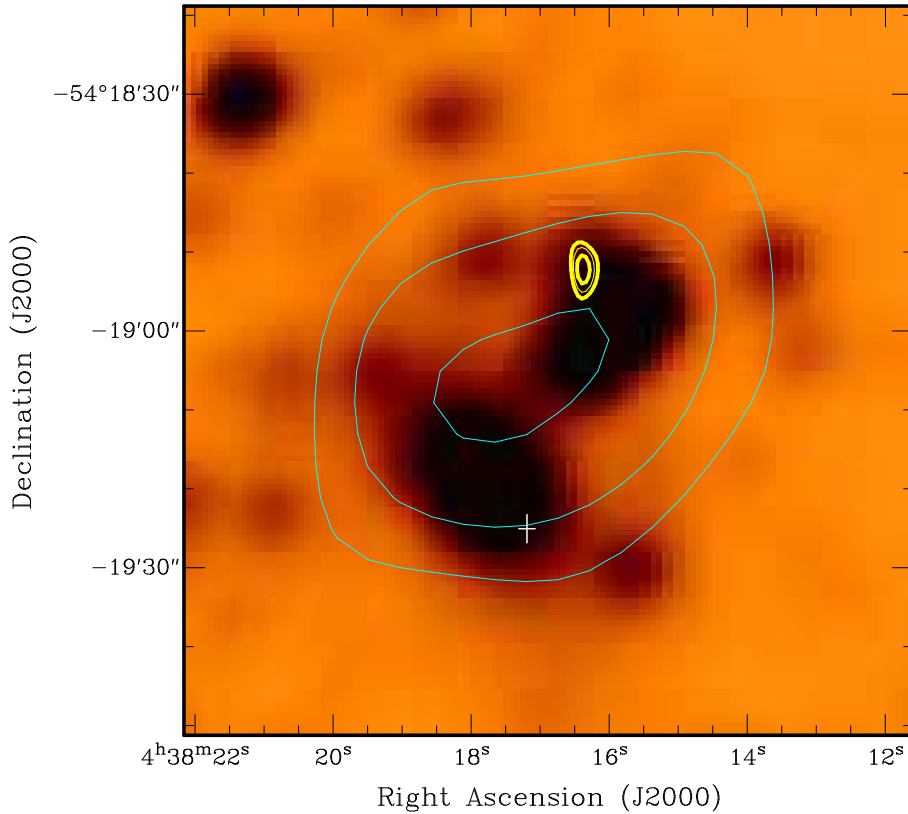


Figure 5.8: WISE 4.6 microns image of the central area of PSZ2 G262.73-40.92. The center of the X-ray emission is marked as a white cross.  $3\sigma \times (1, \sqrt{2}, 2)$  contours of the compact source subtracted tapered radio image appear in cyan, while yellow contours are the same contour levels from the high resolution Block 3 radio map.

## 5.4 Clusters without diffuse radio emission

### 5.4.1 The Cool-core cluster PSZ2 G271.18-30.95

PSZ2 G271.18-30.95 has the highest X-ray luminosity of the ATCA sample, although it is not the most massive cluster (see Table 4.1). Within the sample it has also the highest concentration parameter ( $C = 0.509 \pm 0.004$ ) and the lowest centroid shift ( $w = 0.005 \pm 0.001$ ). This positions it as a clear cool-core non disturbed cluster. Unsurprisingly, as in  $\sim 70\%$  of cool-core clusters (Gitti et al., 2015) our high resolution radio map shows the presence of a strong radio source coincident with the cluster center (see Fig. 5.1 top middle panel and Fig. A.2 bottom panels), with a flux density of  $\sim 10$  mJy at  $\sim 1.9$  GHz. From the Hubble space telescope optical image there is an evident connection between the radio source and the BCG. Moreover, by measuring the flux densities of the central source in the different sub-bands (Blocks 1 to 4, see Sect. 4.3.1) we estimate a spectral index for the central compact source of  $\alpha \approx 0.6$ .

It is known that radio mini-halos are usual in the center of cool-core clusters, surrounding the central active radio galaxy and extending to the radius of the cluster cooling region (see e.g. [Giacintucci et al., 2017b](#), and references therein). To further investigate the possible presence of a radio mini-halo, we did several tests by imaging at  $\sim 10$  arcsec resolution without compact source subtraction and using different weighting for the tapering. None of our maps show evidence of extended diffuse emission at the typical mini-halo scales. We point out, however, that the presence of the compact source at the cluster center and the presence of a strong source close to the cluster made the imaging and the compact source subtraction problematic in this particular case.

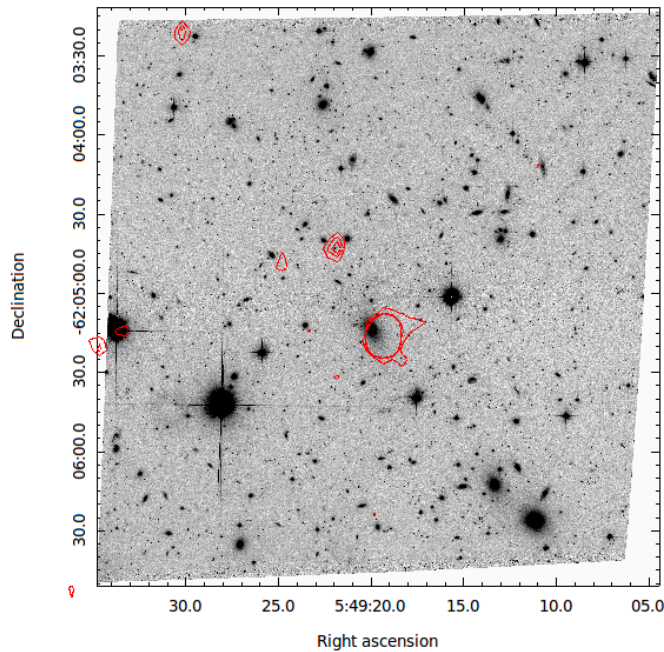


Figure 5.9: HST archive image of the central area of PSZ2 G271.18-30.95 with  $3\sigma \times (1, 2, 3)$  full band high resolution contours of the central radio source overlaid in red.

#### 5.4.1.1 Highly disturbed clusters without radio emission

Three of the seven galaxy clusters of the ATCA sample showed evidence of being both highly disturbed (see Fig. 5.1 lower panels and the three red circles in the bottom right of Fig. 5.2) and with low concentration parameters. PSZ2 G277.76-51.74, the most massive cluster of the sample, has also the lowest concentration parameter ( $C = 0.102 \pm 0.002$ ) and shows a centroid shift  $w = 0.042 \pm 0.001$ . On the other hand, PSZ2 G285.63-17.23 has the highest centroid shift ( $w = 0.081 \pm 0.003$ ,  $C = 0.124 \pm 0.006$ ). Finally PSZ2 G286.28-38.36 shows also signs of being highly disturbed ( $w = 0.078 \pm 0.005$ ,  $C = 0.137 \pm 0.008$ ). None of these

clusters show hints of diffuse radio emission on our maps.

We have mentioned in Sect. 3.4 that there are actually cases of disturbed clusters lacking radio halos. [Russell et al. \(2011\)](#) show that A2146 possesses no diffuse emission despite being clearly a merging cluster (see also [White et al., 2015b](#), for a detailed study of the dynamical status of the cluster). However, in this particular case the mass of the cluster is quite low ( $4.3 \times 10^{14} M_{\odot}$ ) which could be the reason for the lack of a radio halo. This explanation could not be necessarily the case for our three non-detections. Our three radio quiet clusters are more massive (see Table 4.1) than at least six detected radio loud clusters (A545, A746, A1995, A2034, A2254, A2255), all of them with masses  $M_{500} < \sim 5.9 \times 10^{14} M_{\odot}$ , but also at lower redshifts ( $z < 0.318$ ). Moreover, the X-ray analysis of our three ATCA non-detections show that they lie among the most disturbed and with lowest concentration parameters in our sample (see Fig. 5.12). The implications of this section will be discussed in Sect. 5.5.

## 5.4.2 The triple system of low mass clusters PLCK G334.8-38.0

Among the radio quiet clusters of our sample, one has not been analysed in the same way as the other six. PLCK G334.8-38.0 consist of three X-ray components visible in the XMM-Newton image separated by  $\sim 7'$ . The redshift of the system has been obtained from the Fe L complex detection in the spectral analysis one of the components, obtaining a value of  $z = 0.35$ , and assuming to be the same for the three components. By using limited statistics, temperatures in the (2-3)keV bands were obtained, suggesting masses of  $(1.55, 0.91 \text{ and } 0.92) \times 10^{14} M_{\odot}$ . It is important to notice, however, that the measurements of redshift and masses for this triple system are quite challenging, and the case deserves further investigation (see [Planck Collaboration et al., 2016a](#)). For these reasons we can not analyse the system by proceeding in the same way we have done for the other clusters of the sample. We notice, however, that the mass of the components, even taken all together ( $M \sim 3.4 \times 10^{14} M_{\odot}$ ), is significantly lower than the typical mass of radio loud systems.

Although our radio images do not show the presence of any significant diffuse radio emission in either of the triple system regions, we noticed the presence of a tailed radio galaxy coincident with X-ray region "C" in Figure 5.10. We show the source on Figure 5.11. There is evidence that tail radio galaxies can be used as tracers of galaxy clusters (e.g. [Fomalont and Bridle \(1978\)](#); [Burns and Owen \(1979\)](#); [Blanton et al. \(2001\)](#); [Smolčić et al. \(2007\)](#); [Giacintucci and Venturi \(2009\)](#)). The interaction of the radio lobes with the ICM causes in general some distortion on their geometry ([Smolčić et al., 2007](#)). In the case of the tail radio galaxy detected in the field of PLCK G334.8-38.0, the bending of the radio lobes is minor, being the orientation of the bending opposite to the direction connecting two of the members of the triple system (A and C in Fig. 5.10).

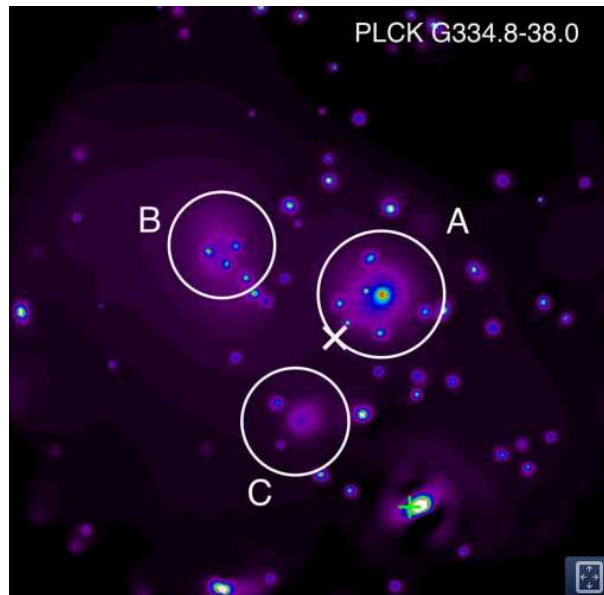


Figure 5.10: XMM-Newton wavelet filtered [0.3-2] keV image of the triple system PLCK G334.8-38.0. Extended components found in the XMM-Newton image are marked with letters. The circles denote the estimated  $R_{500}$  radius for each component. Credit: [Planck Collaboration et al. \(2011b\)](#)

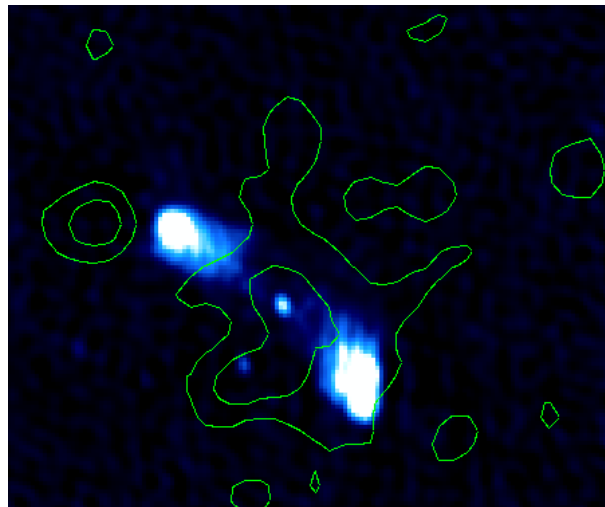


Figure 5.11: High resolution radio image at 2.1 GHz of a tailed radio galaxy corresponding to the X-ray source "C" of Figure 5.10. The green contours are from the XMM image of the corresponding region.

#### 5.4.2.1 Detection limits

In Fig. 5.12 we show the upper limits for the non-detections on the ATCA sample, obtained as illustrated in Sect. 4.3.2.3, as red arrows on the  $P_{1.4GHz}$  vs.  $M_{500}$  plot. We compare

our calculated values with those obtained by [Venturi et al. \(2008\)](#) and [Kale et al. \(2013\)](#) (blue arrows in Fig. 5.12), measured using GMRT images, with the modelled halo injections performed at 610 MHz. Our calculated ATCA upper limits appear higher in the plot as a consequence of the combination of two effects. The first one is that the redshift range of our sample is higher than previous studies (these being effectively limited to  $z < 0.3$ , see Sect. 4.1). In our calculation of the radio power, we have the luminosity distance factor that scales as  $D_{\text{Lum}}(z)^2$ . The second and most important effect is the frequencies of the ATCA observations. We recall that our upper limit injections were done at  $\sim 1.9$  GHz, and by assuming a typical spectral behaviour of RHs (with spectral index  $\alpha=1.3$ ), we obtain higher values for the radio power when we rescale the flux density from 1.9 GHz to 1.4 GHz. The values of our calculated upper limits appear in Table 5.4. It is worth mentioning that the power of the giant RH discovered in PSZ2 G284.97-23.69 and some other RHs reported in the literature lie close (or even below) the radio power regime of the upper limits obtained for our ATCA observations. This could imply that the measured flux density of our detected sources could be underestimated.

Table 5.4: Upper limits obtained for the ATCA cluster images without traces of diffuse radio emission. The calculated logarithm of the radio power at 1.4 GHz, by assuming a spectral index of 1.3, for the total flux density of the injected fake radio halo model in the Block 3 sub-band (1.9 GHz) appears in Column 2.

Cluster name	Log $P_{1.4\text{GHz}}$ ( $\text{WHz}^{-1}$ )
PSZ2 G285.63-17.23	24.46
PSZ2 G277.76-51.74	24.57
PSZ2 G286.28-38.36	24.19
PSZ2 G271.18-30.95	24.39

## 5.5 Conclusions

With our high-sensitivity wide-band (1.1 - 3.1 GHz) ATCA observations we present a complete analysis in search of diffuse radio emission on the ATCA sub-sample of the MACS-Planck RHCP. Moreover, we performed an X-ray analysis of the sample in order to relate the non-thermal emission with the dynamical state of the clusters. Among the seven targets, only two clusters show a confirmed or tentative diffuse radio emission. We reported the presence of a giant radio halo in PSZ2 G284.97-23.69 and found a new candidate diffuse source in PSZ2 G262.73-40.92. The X-ray morphological analysis based on XMM-Newton observations indicates that those objects are most likely disturbed systems, based in particular on the centroid shift indicator ( $w$ ), with a concentration parameter ( $C$ ) not far from the threshold adopted to separate merging and relaxed clusters.

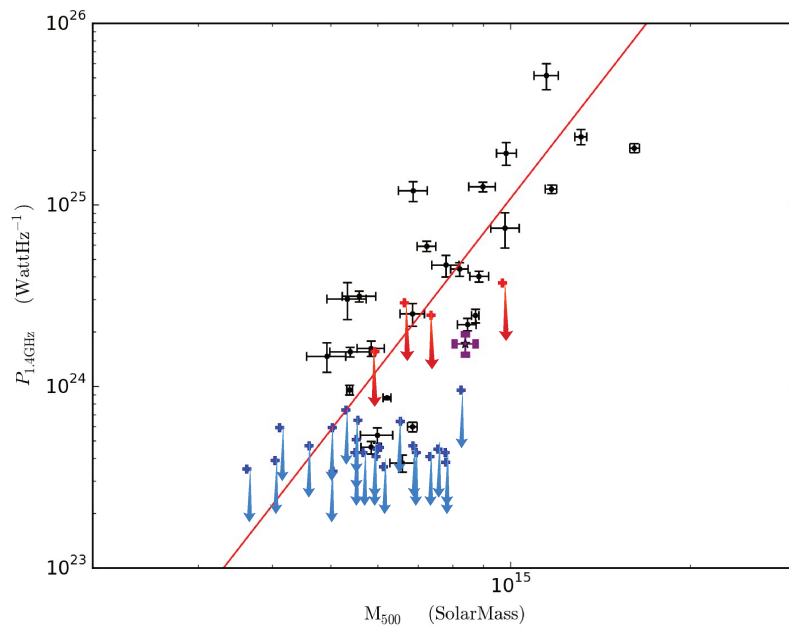


Figure 5.12: Synchrotron power of RHs at 1.4 GHz ( $P_{1.4GHz}$ ) versus cluster mass  $M_{500}$  (from (Planck Collaboration et al., 2016b)). Detected radio halos reported in the literature measured at 1.4 GHz are shown in black dots. The red line is the best fit for the black dots. The purple star corresponds to the radio halo on PSZ2 G284.97-23.69. The blue arrows correspond to detection limits appearing in Cassano et al. (2013) and references therein. The red arrows are the upper limits for the non-detections presented in this paper (see Table 5.4).

In the case of PSZ2 G284.97-23.69, both the diffuse nature of the source, which is not related to blending of compact radio objects, and the comparison of our high-sensitivity tapered radio map to the X-ray image of the cluster allow us to classify the detected emission as a classical RH. First, the morphology and size of the diffuse radio source indicate a very similar distribution of the non-thermal ICM and the thermal component, traced by its X-ray bremsstrahlung radiation. Similarly to most known RHs, our newly detected halo is thus hosted by a massive cluster ( $8.4 \times 10^{14} M_{\odot}$ ). The detected RH seems to be slightly under-luminous compared to objects hosted by clusters in a similar mass range, as shown in the  $P_{1.4GHz}$  vs  $M_{500}$  plot (purple star in Fig. 5.12); although it is not a clear outlier like the RH discovered by Bonafede et al. (2015). It is, however, one of the lowest luminosity radio halos detected at  $z > 0.35$ . It is expected that radio halos and their hosting clusters develop complex patterns with time in the radio–mass (or X-ray luminosity) diagram as a result of the evolution of cluster dynamics and particle acceleration and spectra (e.g. Donnert et al., 2013). For most of their lifetimes these systems are expected to be “off-state” (i.e. under-luminous) or in the region spanned by the correlation leading to an apparent bimodality (e.g. Brunetti et al., 2009; Cassano et al., 2013). In this respect under-luminous systems are expected to be generally associated with both young or old mergers (Donnert et al., 2013); naively PSZ2 G284.97-23.69 could be in one of these stages. On the other hand the spectrum of radio halos also plays a role, with ultra-steep-spectrum radio halos, which are expected in less powerful mergers and at higher redshift (as a result of stronger IC losses), being statistically under-luminous (Cassano et al., 2006; Brunetti et al., 2008; Cassano et al., 2010b).

The classification of the candidate diffuse radio source in PSZ2 G262.73-40.92 is more challenging, given its size, position with respect to the X-ray emission and the dynamical state of the host cluster, being just in our cut line for cool-core/non cool-core clusters. We noticed, however, that the radio emission seems to follow the emission of the cluster galaxies in the WISE image, as have been found by other RHs in previous studies (Govoni et al., 2012).

Our sample contains one clearly relaxed cool-core cluster. The wide band full resolution radio image of PSZ2 G271.18-30.95 shows the presence of a compact radio source, which coincides with the cluster BCG visible in the Hubble image of the cluster. We performed several trials in search of the presence of a radio mini-halo surrounding the central radio galaxy, by imaging at mini-halo scale resolutions and with different weighting in the tapering. We didn’t find evidence of a mini-halo in our images. However, we noticed that the compact source subtraction was challenging with our data, probably because the presence of some calibration errors.

The triple system of low mass clusters PLCK G334.8-38.0 lacked the presence of diffuse radio emission and the low statistics for the X-ray analysis prevented us to perform the diagnosis of its dynamical state. In concordance with previous studies (Fomalont and Bridle, 1978; Burns and Owen, 1979; Blanton et al., 2001; Smolčić et al., 2007; Giacintucci and Venturi, 2009), we discovered the presence of a tail radio galaxy coincident with one of the components of the triple system.

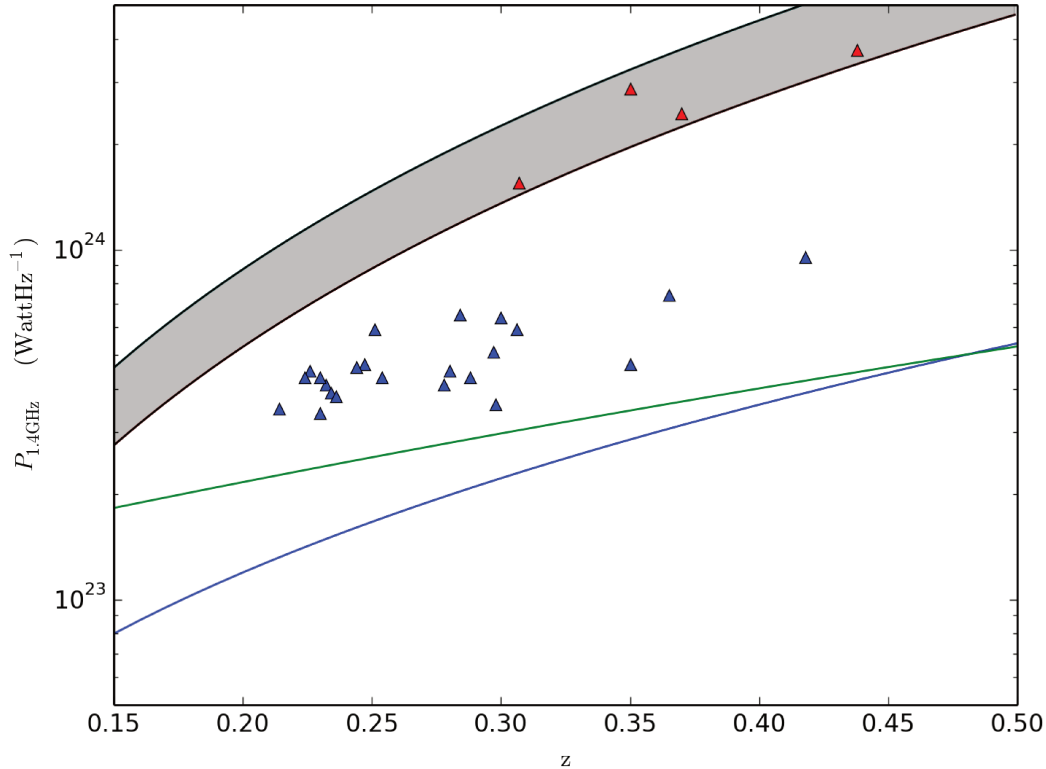


Figure 5.13: Upper limit radio powers rescaled at 1.4 GHz vs. redshift for our ATCA observations (red triangles) and GMRT observations [Venturi et al. \(2008\)](#) & [Kale et al. \(2013\)](#) (blue triangles). The lower (upper) border of the grey band corresponds to the lowest (highest) detection limit of injected fluxes, i.e. 3 mJy (5 mJy) for our ATCA images. The green and blue lines show the minimum power at 1.4 GHz of detectable radio halos in the EMU survey as derived in [Cassano et al. \(2012\)](#).

Finally, three of the clusters of our sample that have clear X-ray morphological indicators of being highly disturbed (PSZ2 G277.76-51.74, PSZ2 G285.63-17.23, PSZ2 G286.28-38.36) do not present any bright diffuse emission. With their calculated upper limits lying on the  $P_{1.4} - M_{500}$  correlation (see Fig. 5.12), we do not have elements enough to discriminate if they are still consistent with the correlation or under luminous with respect to it. Hypothetical RH could be either “classical” halos, i.e. almost consistent with the correlation, or under luminous RHs with ultra-steep radio spectra, detectable with low frequency radio observations (these are particularly expected in high- $z$  clusters, see [Cassano et al., 2006](#)). The challenging hypothesis to be tested would be if those clusters are “radio-quiet”. We have seen that there are cases of disturbed clusters lacking radio halos. [Russell et al. \(2011\)](#) show that the galaxy cluster A2146 poses no diffuse emission despite being clearly a merging cluster

(see also [White et al., 2015b](#), for a detailed study of the dynamical status of the cluster). However, in this particular case the mass of the cluster is quite low ( $4.3 \times 10^{14} M_{\odot}$ ) which could be the reason for the lack of a radio halo. We noticed that a number of clusters with lower masses than those of our three highly disturbed radio quiet cluster host radio halos, but all of them at lower redshifts.

The calculated upper limits indicated in Fig. 5.12 are significantly higher compared to other works ([Cassano et al., 2013](#)), even if the rms sensitivities reached in all these analyses are comparable. This is explained by the fact that previously published upper limits are based either on lower-frequency (mostly 610 MHz) observations ([Venturi et al., 2008](#); [Kale et al., 2013](#)) or on lower-redshift ATCA cluster samples ([Shakouri et al., 2016](#), , Shakouri et al. submitted). In the first case (and keeping in mind that we convert radio powers to the reference frequency of 1.4 GHz), the same rms sensitivity at 1.9 GHz and 610 MHz translates to a higher 1.4 GHz radio halo luminosity upper limit for the 1.9 GHz case, due to the spectral steepness of radio halos (we rescaled by assuming a spectral index  $\alpha=1.3$  to be consistent with [Cassano et al., 2013](#)). In the second case, the clusters are observed at the same frequency, but located at  $z \sim 0.15$ , which, due to the  $D_{\text{Lum}}(z)^2$  factor, translates into  $\sim 10$  higher upper limits in radio power compared to lower redshift ATCA observations.

To be able to distinguish between "radio-quiet" or "under-luminous" diffuse emission in the three disturbed galaxy clusters in our sample, it is clear that more sensitive and lower-frequency radio observations are needed. In Fig. 5.13 we compare the detection upper limits obtained for our ATCA observations (red triangles) with previous upper limits taken with the GMRT at 610 MHz (blue triangles) as a function of redshift. The green and blue lines show the minimum power at 1.4 GHz of detectable radio halos in the Evolutionary Map of the Universe (EMU) survey for different signal to noise levels as derived in [Cassano et al. \(2012\)](#) (see Sect. 5 and Eqs. 9 and 10 in their paper). The EMU survey will produce a deep radio continuum survey of the Southern Sky with rms noises of  $\sim 10 \mu\text{Jy}/\text{beam}$ , comparable to our best rms noise of  $\sim 11 \mu\text{Jy}/\text{beam}$ , but with lower resolution ( $\sim 10$  arcseconds, [Norris et al., 2011](#)), resulting in a better sensitivity at lower frequencies (1.3 GHz). From Fig. 5.13 we note that EMU will have the sensitivity to discover possible halos in clusters that presently are undetected in both GMRT and ATCA samples.

# A first analysis of the GMRT sub-sample

---

## Contents

---

<b>6.1 Full resolution and tapered residual radio maps . . . . .</b>	<b>77</b>
<b>6.2 X-ray-optical dynamical analysis of GMRT sub-sample . . . . .</b>	<b>77</b>
<b>6.3 Radio properties of GMRT sub-sample . . . . .</b>	<b>82</b>
6.3.1 Classification 1 clusters . . . . .	82
6.3.2 Classification 2 . . . . .	83
6.3.3 Classification 3 and 4 . . . . .	84
6.3.4 Clusters with missing dynamical state analysis . . . . .	84
<b>6.4 Detection limits . . . . .</b>	<b>85</b>

---

In this chapter I present a first analysis on the radio maps available for the GMRT sub-sample and the results for the upper limits obtained from the fake halo injections performed in the available residual visibilities. The main idea of this chapter is to show the state of art of the already available radio information and to pave the way on the work needed to publish all the data of the MACS-Planck RHCP.

## 6.1 Full resolution and tapered residual radio maps

In Sect. 4.4.1 we described the procedure of data reduction and image reconstruction for the GMRT sub-sample. In Table 6.1 we show the main features (rms noise and resolution) for the corresponding full resolution images. The images themselves are shown in Appendix. The main characteristics of the residual tapered images appear in Table 6.2. From these set of images we were able to perform a first analysis on the presence of diffuse emission on the GMRT sub-sample.

## 6.2 X-ray-optical dynamical analysis of GMRT sub-sample

19 out of our 25 clusters of the GMRT sub-sample benefit from a homogeneous analysis of their dynamical state. In their analysis, the authors followed a different approach that the one we took on Sect. 5.2.

Table 6.1: Characteristics of high resolution GMRT radio maps.

Cluster name	RMS noise ( $\mu\text{Jy}/\text{beam}$ )	Beam Size ("×")	PA (deg)
MACSJ1720.2+3536	58.25	$9.61 \times 7.85$	54.63
MACSJ1931.8-2634	113.34	$11.81 \times 7.60$	5.15
MACSJ2140.2-2339	60.11	$13.62 \times 7.97$	13.06
MACSJ2229.7-2755	130.31	$14.01 \times 9.03$	0.87
MACSJ2245.0+2637	101.65	$9.81 \times 8.72$	49.07
MACSJ0011.7-1523	73.88	$13.63 \times 7.37$	52.39
MACSJ0159.8-0849	100.44	$12.26 \times 7.96$	67.90
MACSJ0242.6-2132	106.78	$10.70 \times 8.62$	15.38
MACSJ0429.6-0253	223.75	$10.59 \times 10.05$	59.58
MACSJ0547.0-3904	112.07	$15.06 \times 7.45$	11.46
MACSJ1427.6-2521	73.60	$12.11 \times 7.82$	10.04
MACSJ0520.7-1328	125.96	$12.49 \times 7.95$	12.03
MACSJ1206.2-0847	102.12	$11.27 \times 7.62$	44.96
MACSJ1319.9+7003	63.97	$13.73 \times 8.19$	-23.01
MACSJ0257.6-2209	119.82	$13.41 \times 8.57$	19.13
MACSJ2049.9-3217	69.75	$15.04 \times 7.38$	4.58
MACSJ0035.4-2015	343.42	$10.98 \times 7.76$	50.16
MACSJ0404.6+1109	85.57	$9.85 \times 7.78$	66.79
MACSJ1731.6+2252	60.24	$10.44 \times 7.36$	65.13
MACSJ0152.5-2852	177.21	$12.09 \times 7.40$	22.32
PLCK G100.2-30.4	141.16	$11.22 \times 8.74$	15.30
PLCK G272.9+48.8	52.16	$9.70 \times 8.33$	19.56
PLCK G250.0+24.1	234.20	$11.25 \times 8.87$	27.95
PLCK G214.6+36.9	208.98	$10.25 \times 8.80$	55.76
PLCK G241.2-28.7	136.02	$16.61 \times 8.82$	-2.55

Table 6.2: Characteristics of residual tapered GMRT radio maps.

Cluster name	RMS noise ( $\mu\text{Jy}/\text{Beam}$ )	Beam Size ("×")	PA (deg)
MACSJ1720.2+3536	420.40	35.91 × 28.36	62.49
MACSJ1931.8-2634	526.42	36.77 × 30.31	37.33
MACSJ2140.2-2339	273.45	34.61 × 32.60	42.39
MACSJ2229.7-2755	431.98	41.52 × 33.48	49.76
MACSJ2245.0+2637	420.19	35.26 × 32.79	1.26
MACSJ0011.7-1523	299.22	39.83 × 31.97	28.30
MACSJ0159.8-0849	411.71	34.26 × 30.27	61.74
MACSJ0242.6-2132	416.89	38.20 × 30.20	49.08
MACSJ0429.6-0253	722.29	37.15 × 31.97	-86.85
MACSJ0547.0-3904	427.22	38.51 × 25.54	31.72
MACSJ1427.6-2521	420.31	43.48 × 36.42	25.41
MACSJ0520.7-1328	815.88	40.27 × 30.11	22.82
MACSJ1206.2-0847	868.71	42.33 × 34.46	15.03
MACSJ1319.9+7003	565.69	41.21 × 31.70	-9.68
MACSJ0257.6-2209	604.62	39.83 × 32.70	64.03
MACSJ2049.9-3217	344.50	39.97 × 29.16	36.63
MACSJ0035.4-2015	1263.40	43.79 × 28.95	61.98
MACSJ0404.6+1109	527.77	38.57 × 33.29	75.71
MACSJ1731.6+2252	261.00	35.01 × 28.94	64.70
MACSJ0152.5-2852	956.13	36.13 × 26.48	41.08
PLCK G100.2-30.4	942.45	39.22 × 33.45	36.37
PLCK G272.9+48.8	316.40	36.42 × 31.57	71.57
PLCK G250.0+24.1	763.20	37.28 × 33.74	57.07
PLCK G214.6+36.9	745.13	39.75 × 30.49	53.14
PLCK G241.2-28.7	574.16	43.06 × 31.47	27.37

In [Mann and Ebeling \(2012\)](#), the authors performed an X-ray-optical classification of cluster mergers from a sample of 108 of the most X-ray luminous clusters observed with *Chandra*, and with optical data obtained with the UH2.2m telescope, the Sloan Digital Sky Survey (SDSS), the Digitalized Sky Survey (DSS) and the Hubble Space Telescope (HST). The approach followed by the authors considers that, on cluster scales, the member galaxies can be considered to be fast-moving particles with a very small cross section for collision. On the other side, the intra-cluster gas is highly collisional and will be subject to intense ram pressure and shock heating during a merger. The result of this will be that the strongly self-interacting gas is slowed during the merger, while the galaxies will pass through, slowed only by gravity via the process of dynamical friction. This implies that a pronounced spatial segregation of gas and galaxies provides evidence of a recent or an ongoing merger (e.g. [Smith et al., 2005](#); [Shan et al., 2010](#)). On the other hand, an excellent alignment of the intra-cluster gas distribution and the BCG is considered typical of relaxed systems. In this analysis, [Mann and Ebeling \(2012\)](#) identified the BCG-X-ray offset by using the location of the X-ray peak and the overall centroid of the diffuse X-ray emission. A third qualitative diagnosis of the dynamical state of the clusters was the visual classification of the morphology of the X-ray contours and the degree of alignment of the BCG and the X-ray peak. The assigned codes and classification criteria from relaxed to extremely disturbed are ([Mann and Ebeling, 2012](#)):

- (1) Pronounced cool core, perfect alignment of X-ray peak and single BCG.
- (2) Good optical-X-ray alignment, concentric contours.
- (3) Non concentric contours, obvious small scale substructure.
- (4) Poor X-ray-optical alignment, multiple peaks, ambiguous BCG.

The classification of each of the 19 MACS-Planck RHCP GMRT sub-sample appear in Table 6.3. The quantities appearing in the table taken from [Mann and Ebeling \(2012\)](#) correspond to the X-ray peak-BCG separation (Col. 2); the X-ray-centroid-BCG separation (Col. 3) and the classification criteria in different numerical codes described above (Col. 4). In the following sections we will divide the GMRT sample based on the classification appearing in Column 4 and provide a short description of their radio properties.

Table 6.3: Morphological data for the MACS clusters from Mann and Ebeling (2012).

Cluster name	Peak Separation ( $\sigma$ ) (kpc)	Centre separation ( $\sigma$ ) (kpc)	Morphological code
MACSJ1720.2+3536	1.5 (4.2)	22.2 (2.14)	1
MACSJ1931.8-2634	15.3 (4.8)	3.9 (0.61)	1
MACSJ2140.2-2339	0.5 (2.1)	7.8 (1.10)	1
MACSJ2229.7-2755	3.9 (4.4)	7.3 (0.61)	1
MACSJ2245.0+2637	8.8 (3.9)	8.0 (2.40)	1
MACSJ0011.7-1523	3.8 (4.4)	7.1 (1.56)	1
MACSJ0159.8-0849	2.8 (3.6)	7.2 (2.93)	1
MACSJ0242.6-2132	7.1 (3.8)	4.1 (0.19)	1
MACSJ0429.6-0253	12.8 (4.6)	19.5 (2.31)	1
MACSJ0547.0-3904	0.6 (2.7)	9.9 (0.98)	1
MACSJ1427.6-2521	0.7 (2.7)	2.5 (0.08)	1
MACSJ0520.7-1328	8.4 (3.7)	10.2 (0.39)	2
MACSJ1206.2-0847	8.3 (5.2)	33.8 (0.59)	2
MACSJ1319.9+7003	7.6 (4.3)	37.7 (2.24)	2
MACSJ0257.6-2209	2.6 (3.7)	18.0 (0.46)	2
MACSJ2049.9-3217	18.0 (4.0)	25.5 (6.53)	3
MACSJ0035.4-2015	15.7 (3.9)	11.8 (0.28)	3
MACSJ0404.6+1109	58.6 (4.9)	69.7 (3.17)	4
MACSJ1731.6+2252	66.7 (4.9)	31.4 (3.18)	4

## 6.3 Radio properties of GMRT sub-sample

### 6.3.1 Classification 1 clusters

MACSJ1720.2+3536 is classified as morphological code 1, despite having a relatively large centre separation (22.2 kpc, see Table 6.3). The full resolution GMRT radio map shows the presence of a strong ( $\sim 11$  mJy) compact source coincident with the cluster BCG. It is however visible in the full resolution map the presence of some diffuse emission, probably related to the compact central source, in the west direction. The residual tapered map shows the presence of  $3\sigma$  contours surrounding the central radio source, and the presence of a large scale, north-south oriented elongated structure ( $\sim 876$  kpc) towards the east direction.

MACSJ1931.8-2634 has the highest peak separation (15.3 kpc) for the MACS clusters with morphological code (1). The full resolution radio map shows the presence of very strong activity from radio galaxies in the central coordinates. It is visible from the low resolution residual map that some  $3\sigma$  contours appear in the NW-SE direction across the clusters area. It is however difficult to assess the reliability of this residual emission because the quality of the image, as we noticed some phase errors present in very bright sources in the radio map.

MACSJ2140.2-2339 has the lowest peak separation (0.5 kpc) from all the clusters with morphological classification. The full resolution radio map shows the presence of compact sources in the central area with some diffuse emission related. The tapered residual map  $3\sigma$  contours in the cluster area are always associated to very faint radio emission, probably diffuse, but related to the activity of radio galaxies.

MACSJ2229.7-2755 shows the presence of some diffuse emission always related to the activity of radio galaxies in the full resolution map and no significant emission in the residual maps that could lead us to suspect of the presence of any RH, relic or mini-halo.

MACSJ2245.0+2637 has a bright central radio source in the full resolution map and shows some contours in the residual tapered radio map. The central low resolution  $3\sigma$  contours are obviously related to the presence of the central compact radio source, which could give us a hint of the presence of a radio mini-halo, while there are other two roundish  $3\sigma$  contours which are difficult to classify.

MACSJ0011.7-1523 presents two bright compact radio sources in the cluster center in the full resolution radio map. In the tapered map it is noticed the presence of radio contours close to one of this radio sources, and probably related to it. The second visible  $3\sigma$  contour in the cluster area appears in towards the north,  $\sim 0.5$  Mpc away from the center, roundish in shape ( $\sim 255$  kpc diameter). Again, it is difficult to classify the diffuse sources in one of our three main categories.

A central radio source is present in the full resolution image of MACSJ0159.8-0849 which is probably related to the  $3\sigma$  contour visible in the tapered residual radio map. This cluster shows no obvious evidence of diffuse radio sources that are independent from the activity of radio galaxies.

MACSJ0242.6-2132 full resolution map has a bright radio source in the central coordinates, whose subtraction was problematic due to the presence of errors in the uv-data. This makes the low resolution map not reliable for our search for diffuse sources.

The full resolution radio image of our last three galaxy clusters with morphological code (1) shows that these three clusters contain a compact central radio source. However, no contours appear in the correspondent residual tapered map: This is the case for MACSJ0429.6-0253, the second largest peak separation (12.8 kpc) for our morphological code 1 MACS clusters, also with a relatively high centre separation (19.5); MACSJ1427.6-2521, the one with the lowest centre separation, and finally the cluster MACSJ0547.0-3904, with relatively low values for both peak and centre separation.

It is important to notice that the full resolution radio images of all of our MACS clusters classified (1) by [Mann and Ebeling \(2012\)](#) show the presence of a central radio source and none of them shows obvious presence of a RH, as expected from the turbulence models. There are, however, some candidates to host a radio relic (check!) or radio mini-halos (check!), synchrotron radio phenomena that are thought to be related to the interaction of the ICM with radio galaxies present in the cluster center or peripheral regions.

### 6.3.2 Classification 2

MACSJ0520.7-1328 full resolution map shows the presence of a compact source in center. Although the cluster region doesn't show interesting features concerning diffuse radio sources, a peripheral diffuse source was discovered at  $\sim 8$  arcminutes south-east of the cluster center. A following *Chandra* archival X-ray analysis, together with optical/IR data, allowed to the discovery of a new galaxy cluster called 1 WGA 0521. Although difficult to classify as a RH or relic, the importance of this discovery is the fact that the analysis led to the discovery of a previously unknown cluster. A full analysis of this cluster appeared in [Macario et al. \(2014\)](#).

MACSJ1206.2-0847 has a compact radio source in center, where there is clear presence of some errors in the uv-data. The low resolution tapered map shows the presence of  $3\sigma$  roundish contour in the cluster peripheries, which are not reliable given the quality of the data.

MACSJ1319.9+7003 low resolution residual tapered map showed no presence of  $3\sigma$  contours in the cluster centred Mpc diameter circle.

MACSJ0257.6-2209 shows some hints of possible diffuse radio source in the cluster center in the full resolution map. Interestingly, the tapered residual map contains  $3\sigma$  contours on Mpc scale size, centred in the cluster central coordinates, making MACSJ0257.6-2209 a good candidate for hosting a Giant RH.

### 6.3.3 Classification 3 and 4

MACSJ2049.9-3217 shows the presence of large scale  $3\sigma$  contours in the residual tapered map, coincident with the cluster center. The full resolution map shows the presence of a faint compact radio source inside the contours, but probably not completely responsible for the emission visible in the tapered residual map. We then propose MACSJ2049.9-3217 as a candidate for hosting a RH.

MACSJ0035.4-2015 full resolution map shows no presence of compact sources in the cluster area. It is however notable from bright sources in the field that some errors in the uv-data are still present. Indeed, the tapered residual map has the highest rms noise in our GMRT sub-sample ( $1263 \mu\text{Jy}/\text{beam}$ ), showing the presence of two roundish  $3\sigma$  contours inside the cluster Mpc diameter circle. Given the quality of the data, it is difficult to assess the status of MACSJ0035.4-2015 as a candidate for hosting diffuse radio sources.

MACSJ0404.6+1109 full resolution map shows the presence of a compact source in center despite being classified as (4), meaning a "highly disturbed" cluster. However, the tapered residual map showed no evidence of any diffuse radio source in the cluster area.

MACSJ1731.6+2252 shows very interesting activity of radio galaxies in the cluster area in the full resolution map. Moreover, some arc-like features were also noted, probably being due to some gravitational lensing on the cluster. Unfortunately, the subtraction of the compact sources in the cluster area showed the presence of some errors, making the classification of MACSJ1731.6+2252 as a candidate host for diffuse radio emission challenging with our available data.

### 6.3.4 Clusters with missing dynamical state analysis

MACSJ0152.5-2852 full resolution map shows the presence of a group of faint compact radio sources inside the Mpc diameter circle centred on the cluster. It is visible from bright compact sources in the same map that there are still some errors in the uv-data, making the rms noise of the residual tapered map relatively high ( $\sim 956 \mu\text{Jy}/\text{beam}$ ). This map, however, shows no presence of  $3\sigma$  contours in the cluster area.

PLCK G100.2-30.4 shows the presence of small scale  $3\sigma$  contours in the residual tapered map, with no obvious relation with radio galaxies visible in the full resolution map. Despite having a relatively high rms noise in the tapered residual map ( $\sim 942 \mu\text{Jy}/\text{beam}$ ), we consider PLCK G100.2-30.4 as a candidate to host a diffuse source, although difficult to classify.

PLCK G272.9+48.8 tapered residual map has elongated contours inside the central Mpc diameter circle, with no obvious correspondence with radio galaxies. We classify PLCK G272.9+48.8 as a candidate for being a host for diffuse radio emission, although we can't classify the kind of source.

PLCK G250.0+24.1 tapered residual map shows the presence of roundish  $3\sigma$  contours inside the cluster area, with probable relation with a faint compact radio source present in the full resolution map, and the presence of  $3\sigma$  contours in peripheral regions of the cluster, with

some probable relation with faint compact sources. We can suspect of PLCK G250.0+24.1 being a candidate to host a double radio relic.

PLCK G214.6+36.9 shows no hint of diffuse emission either in the full resolution or in the tapered residual maps.

PLCK G241.2-28.7 presents elongated  $3\sigma$  contours offset towards the north of the cluster center, without obvious relation with radio galaxies in the full resolution radio map. We classify PLCK G241.2-28.7 as a candidate to host a radio relic.

## 6.4 Detection limits

Regardless of the status of the galaxy cluster as a candidate to host a radio source, we performed the injections of the fake RH in the whole GMRT sample, with the exception of MACSJ0520.7-1328, being the only image of our sample with an already confirmed radio source (see 6.3.2). The values for the upper limit radio powers rescaled at 1.4 GHz appear in Table 6.4.

In Fig. 6.1 we show the classical  $P_{1.4}$  vs  $M_{500}$  plot, the same as Fig. 5.12, but this time including our new calculated upper limits for the GMRT sub-sample. Most of our new upper limits (green dots in Fig. 6.1) lie in the same radio power range ( $\sim 3 \times 10^{23}$  -  $\sim 10^{24} W/Hz$ ) as those obtained by Venturi (2008) & Kale (2013) (blue dots) with the exception of four upper limits a bit super-luminous with respect to the rest of the GMRT sub-sample. In Fig. 6.2 however, we can notice that two of our calculated upper limits already reach some of the limits expected from the EMU survey (green triangles over blue bottom line), which means that with a good combination of redshift and data quality, the GMRT can provide with some examples of the results expected from new generation radio telescopes.

Table 6.4: GMRT upper limits

Cluster name	Upper limit $\text{Log}(P_{1.4})$
MACSJ1720.2+3536	23.84
MACSJ1931.8-2634	24.11
MACSJ2140.2-2339	23.56
MACSJ2229.7-2755	23.59
MACSJ2245.0+2637	23.85
MACSJ0011.7-1523	23.61
MACSJ0159.8-0849	23.83
MACSJ0242.6-2132	23.56
MACSJ0429.6-0253	23.97
MACSJ0547.0-3904	23.73
MACSJ1427.6-2521	23.33
MACSJ1206.2-0847	23.92
MACSJ1319.9+7003	23.76
MACSJ0257.6-2209	23.74
MACSJ2049.9-3217	23.59
MACSJ0035.4-2015	24.01
MACSJ0404.6+1109	23.84
MACSJ1731.6+2252	23.54
MACSJ0152.5-2852	24.24
PLCK G100.2-30.4	23.88
PLCK G272.9+48.8	23.57
PLCK G250.0+24.1	24.15
PLCK G214.6+36.9	24.10
PLCK G241.2-28.7	24.02

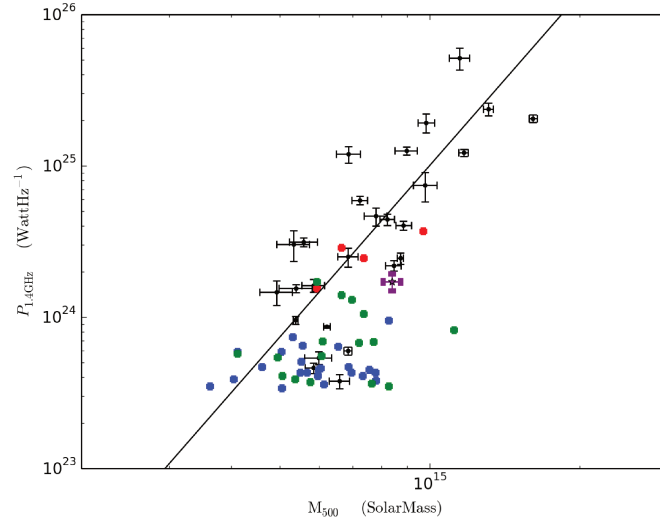


Figure 6.1: Same as Fig. 5.12. Green dots correspond to our newly calculated upper limits from GMRT sub-sample. Most of the values for the upper limit radio powers are comparable to results obtained by Venturi (2008) & Kale (2013) with the GMRT at 610 MHz.

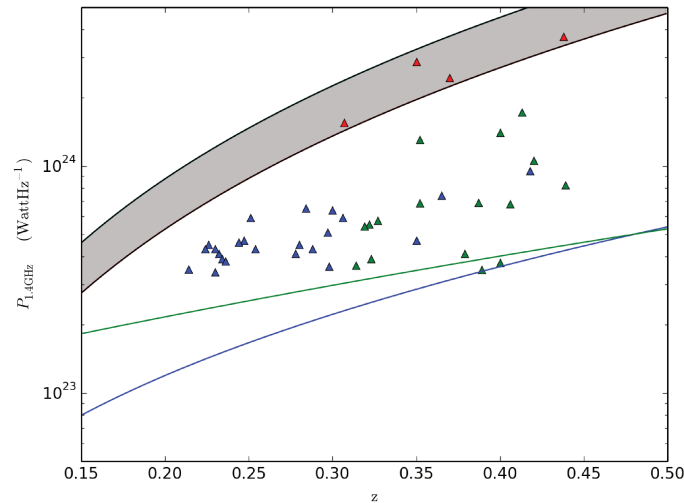


Figure 6.2: Same as Fig. 5.13 but this time including our newly calculated upper limits for the GMRT RHCP sample (green triangles). Notice that two of our calculated upper limits coincide with the upper limits expected from the EMU survey.



# Conclusion and Perspectives

---

In this thesis, I showed the results of my collaboration on the MACS-Planck Radio Halo Cluster Project. The aim of my work was to finish the analysis of the seven intermediate redshift ( $z=0.3-0.45$ ) galaxy clusters observed with the ATCA in search for diffuse radio sources and the relation of the non-thermal emission with the dynamical state of the clusters by performing an X-ray analysis.

Our radio analysis allowed us to discover a new giant Radio Halo and a candidate diffuse source, both in disturbed clusters according to the X-ray analysis and both with relatively high values of the concentration parameter. Our ATCA sub-sample contained one cool-core cluster, which radio analysis doesn't reveal the presence of a mini-halo. Three of our analysed clusters showed evidence of being highly disturbed, and none of them showed traces of hosting a diffuse radio source in our data. The X-ray analysis of a low-mass triple system was impossible given the low X-ray statistics available for the system for which we didn't find evidence of a diffuse radio source. We were able to calculate upper limits for possible RHs in the case of the non-detections. Our upper limits are  $\sim 10$  times higher than previously calculated upper limits, given the combination of the higher redshift of the sample compared to previous works and the higher frequencies of observation with the ATCA. Finally, we were able to perform a first analysis of the already available GMRT sub-sample of the MACS-Planck RHCP.

In our analysis we do not have a clear trend of any dependency of  $P_{1.4}$  vs  $M_{500}$  correlation as a function of redshift (Fig. 5.12). We also noted that the claimed bi-modality of "radio load" clusters hosting a RH and "radio quiet" clusters start to be questioned at the light of recent discoveries such as the outlier discovered by Bonafede et al. (2015) and a number of halos with ultra steep spectrum. It is, however, still difficult to obtain a strong conclusion because of the lack of statistics. New generation surveys, such as EMU, are expected to increase the number of diffuse radio sources, and therefore provide better statistics. I naively speculate that more sources would also make things more difficult to classify, revealing features of the ICM, or beyond, that are actually hidden from our observation capabilities (see e.g. Giovannini et al., 2015, and references therein). Better observations may also reveal cases of RHs that are related to the activity of cluster galaxies, as it can be the case of PSZ2 G262.73-40.92 in our ATCA sub-sample, has been found by other authors (e.g. Govoni et al., 2012; Bonafede et al., 2014a), and probably it is the case for a number of the cases in the GMRT sub-sample described in Sect. 6.3.

Based on the conclusions of my work it is evident that it would be necessary to go to lower frequencies and higher sensitivities. New exciting results in this direction are being achieved

by LOFAR. For instance, the LOFAR Two-metre Sky Survey (LoTSS) is a deep 120-168 MHz imaging survey that will eventually cover the entire northern sky. In the release of the preliminary images, an excess of 44 000 sources are detected in an area of over 350 square degrees. It is expected that LoTSS will reveal many new examples RHs and other kind of diffuse radio sources, and to unveil hidden features of the already known examples. In the preliminary data release more than 30 massive detected galaxy clusters lie within the mapped region, giving the possibility of performing studies of interesting objects and provides an unbiased sample needed to better understand the prevalence of RHs and other diffuse sources in galaxy clusters (Shimwell et al., 2017). One of the main scientific motivations for LoTSS is the detection of radio emission associated with the ICM of 100 galaxy clusters at  $z > 0.6$  (Enßlin and Röttgering, 2002; Cassano et al., 2010a).

Detection of new sources will demand the need to update the  $P_{1.4}$  vs  $M_{500}$  plot. A big number of other RHs have been discovered since the time for the publishing of Cassano et al. (2013), although measured in frequencies different then 1.4 GHz (This is particularly true in the case of ongoing LOFAR surveys). With all the new expected knowledge, a revision of the scaling relations for giant RHs will be urgent. During the experiments performed in the work done for this thesis, we found that plotting every RH find in Tables 3.2 and 3.3 we still recognize a trend, but with a considerable dispersion of the points. The difficulty of interpreting this plot is that these sources have been detected by different instruments and at different frequencies of observation. Therefore, it is extremely important to perform observations with the same instrument in order to be able to do fair comparisons of, for instance, flux density measurements of different objects.

We have mentioned the need of low frequency observations in the search for diffuse synchrotron sources. But it is as important to have higher frequency observations, for instance, to be able to perform spectral index studies. In this case, in this moment, a very adapted instrument is the Karl G. Jansky Very Large Array (JVLA) covering the frequency range from 1 to 6.5 GHz (e.g. van Weeren et al., 2017b) for follow up pointed observations, without forgetting the EMU survey that will cover the whole southern hemisphere, and part of the northern hemisphere (up to  $\delta = 30^\circ$ ).

Make measurements of flux densities in a more uniform way, either by using automatic tools or by following an approach that is not reduced to the measurements inside  $3\sigma$  contours. For instance it could be very important to follow systematically a method similar to the one adopted by Murgia et al. (2009) for mini-halos. In this case the radio surface brightness profile of the diffuse source is fitted with an exponential law and integrated within a certain physical distance from the cluster center. In the case for RH, it would be necessary then to find the best function to fit the surface brightness profile.

Connecting with the mentioned big surveys, the need of large numbers statistics, etc., and based on my experience on reducing the ATCA data for this work, an inevitable conclusion is that the need of automatic data reduction methods is urgent. Apart for the time saving, and the decrease of the computational cost, these techniques will have the virtue of being homogeneous, avoiding to introduce a human bias in the measurements related to the different

approaches adopted for the data reduction.

An important part of this work was the relation between the non-thermal emission and the dynamical state of the host cluster. In this thesis we have seen different approaches to obtain a diagnosis of the clusters dynamical state, mainly based on the X-ray/Optical information. There are still some controversies on what are, for instance, the borders between cool-core/non-cool-core or relaxed/disturbed clusters. In our ATCA sample we found that slightly different choices for measurements, or threshold values, can change the diagnosis of the dynamical state of the cluster. Actually, this issue was highly discussed internally with our collaborators, and one of the "hot topics" in the Physics of the Intra-Cluster Medium (PICM) 2017 conference. I hope that better understanding of diffuse radio sources will shed light on this issue in the near future.

I believe that we are currently living the end of an age in the studies of diffuse synchrotron sources related to the ICM, and the beginning of a new one. I am sure that new generation powerful radio telescopes will transform our understanding of these sources in unexpected ways by showing us all what is below the surface: we have just seen the tip of the iceberg. A promising instrument that will unveil a lot of the radio "secrets" of the Universe is the SKA. We do not have time here to discuss all the scientific goals included in this ambitious project, but I would like to mention the expectations in the matter of non-thermal emission from galaxy clusters. Based on realistic simulated observations of 2-years all-sky survey with the first phase SKA1, in combination with newly developed deconvolution algorithms based on sparse representations and optimised for the detection of faint diffuse astronomical sources, it is expected that a completely independent catalog of new candidates of diffuse cluster sources up to  $z \sim 0.7$  can be obtained (Ferrari et al., 2015). From predictions for SKA1 surveys at low (100-300 MHz) and mid (1-2 GHz) frequencies assuming the expected sensitivities and spatial resolutions of SKA1, it is expected to discovery of 1000 ultra-steep-spectrum halos and to detect for the very first time "off state" RHs. It is also expected that at least 2500 giant RHs will be discovered by SKA1-LOW surveys up to  $z \sim 0.6$ . Moreover, SKA1 surveys will be highly competitive with present and future SZ-surveys in the detection of high-redshift massive objects (Cassano et al., 2015). We are living, beyond any doubt, the renaissance of radio astronomy.



APPENDIX A

# High resolution images of the ATCA sub-sample

---

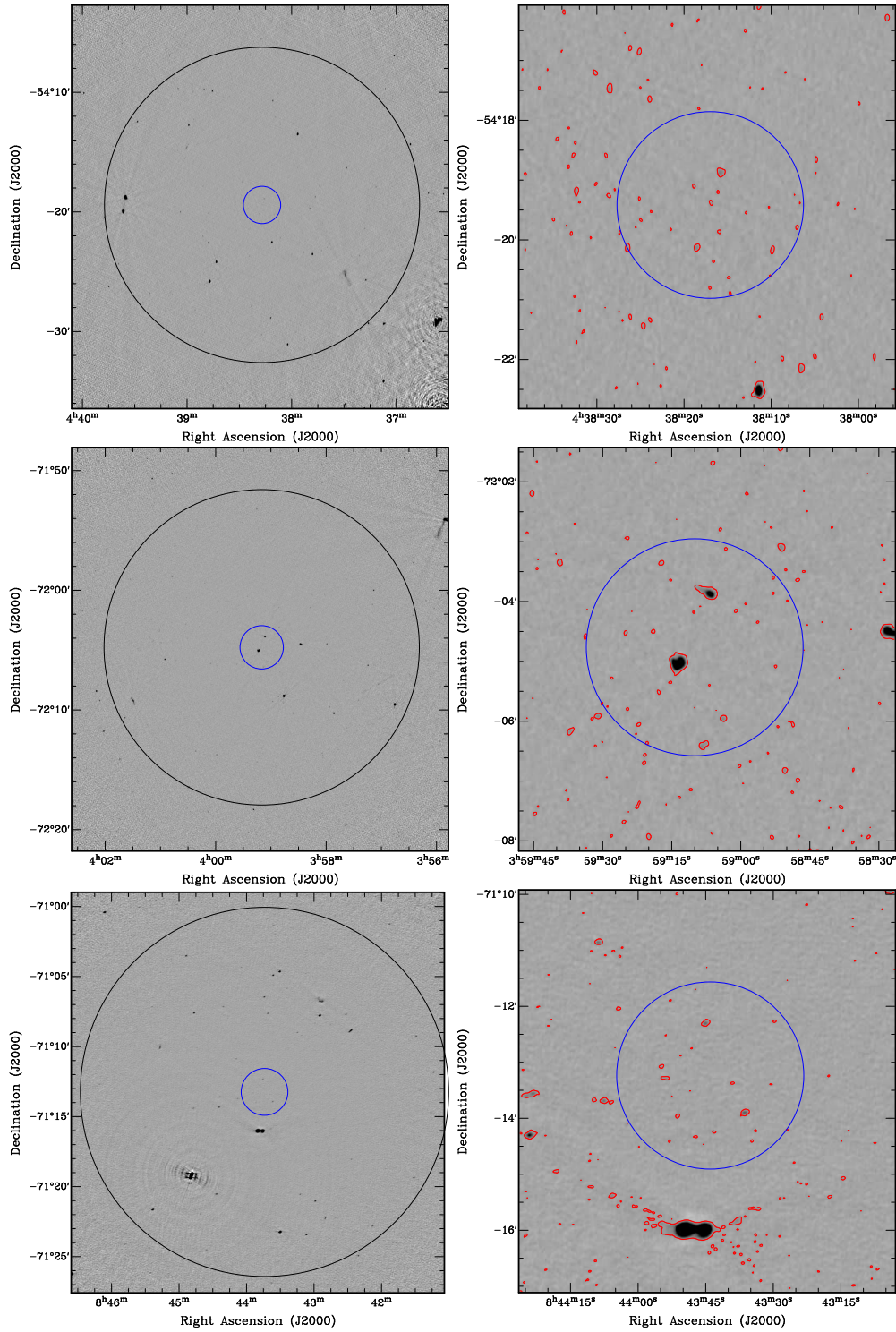


Figure A.1: Final full-resolution, wide-band ATCA images of the cluster sample. *Left panels:* Full field image centred on cluster coordinates. The outer circle denotes the boundary of the primary beam with a radius of  $\sim 0.22$  degrees. The central 1 Mpc-diameter region is indicated by the inner, blue smaller circle. *Right panels:* Zoom into the central area with  $3\sigma$  contours of the corresponding map overlaid in red. *Top:* PSZ2 G262.73-40.92; *Middle:* PSZ2 G286.28-38.36; *Bottom:* PSZ2 G285.63-17.23.

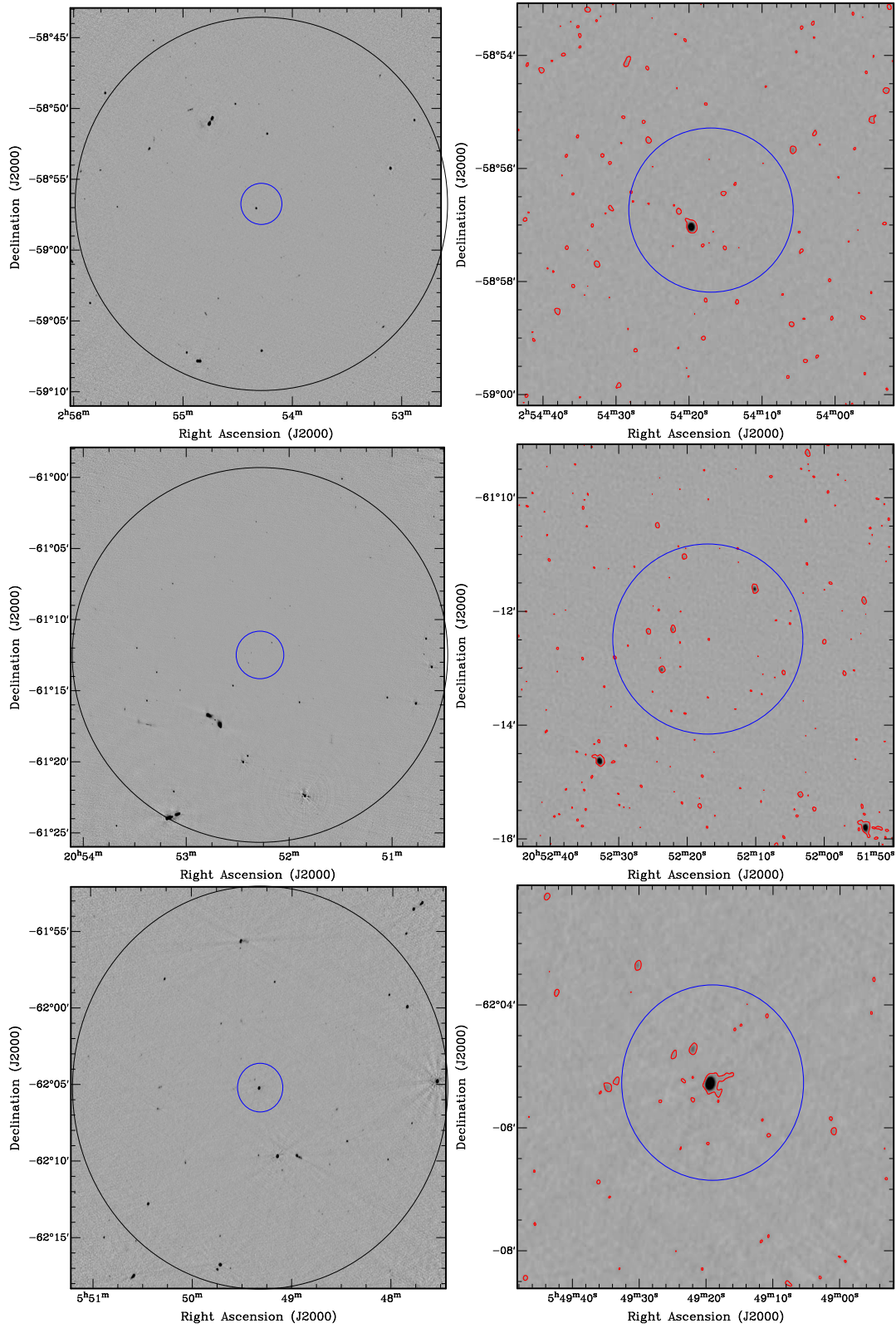


Figure A.2: Same as Fig. A.1. *Top*: PSZ2 G277.76-51.74; *Middle*: PLCK G334.8-38.0; *Bottom*: PSZ2 G271.18-30.95.



APPENDIX B

# High resolution radio images of the GMRT sub-sample

---

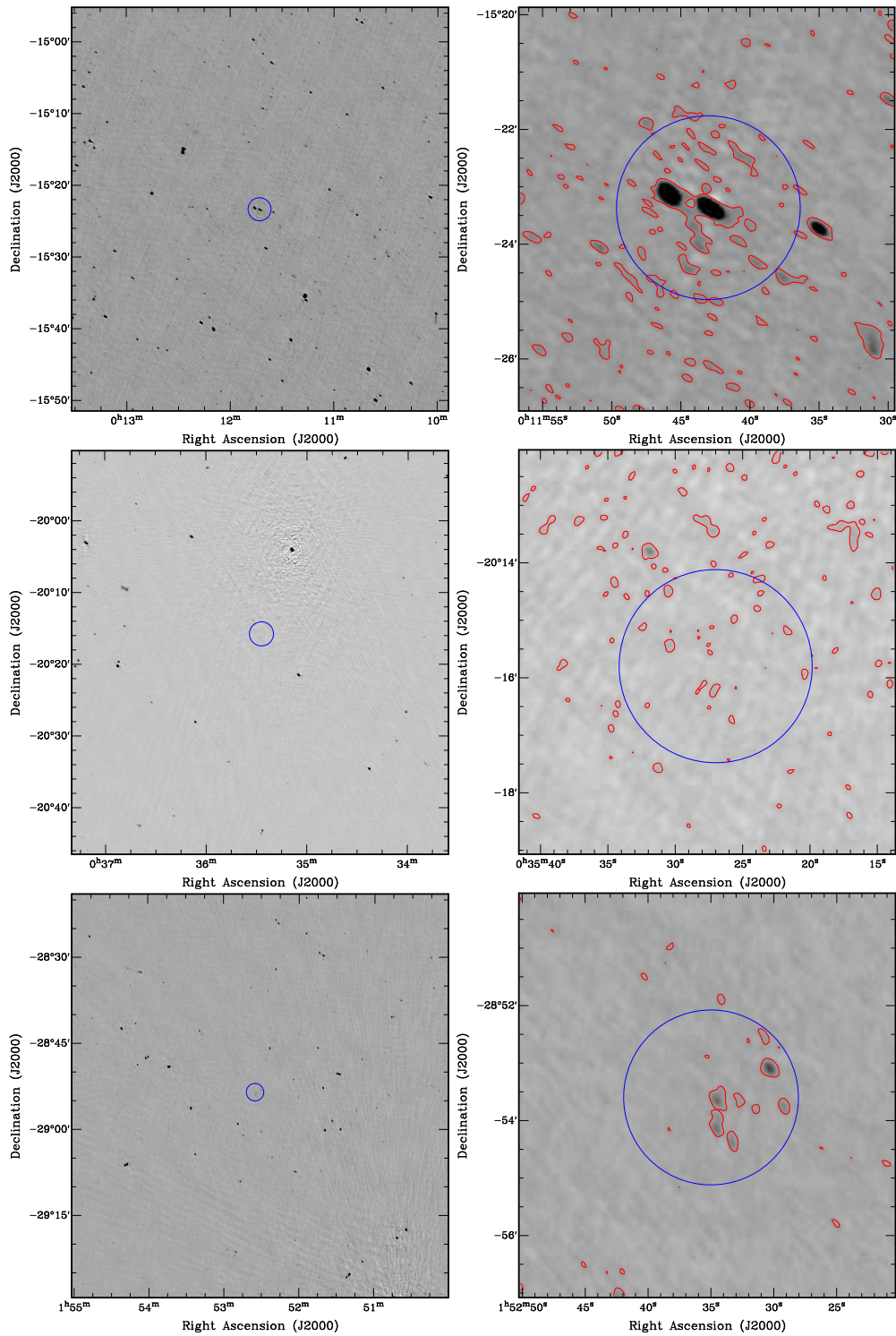


Figure B.1: Same as Fig. A.1. *Top*: MACSJ0011.7-1523 ; *Middle*: MACSJ0035.4-2015; *Bottom*: MACSJ0152.5-2852.

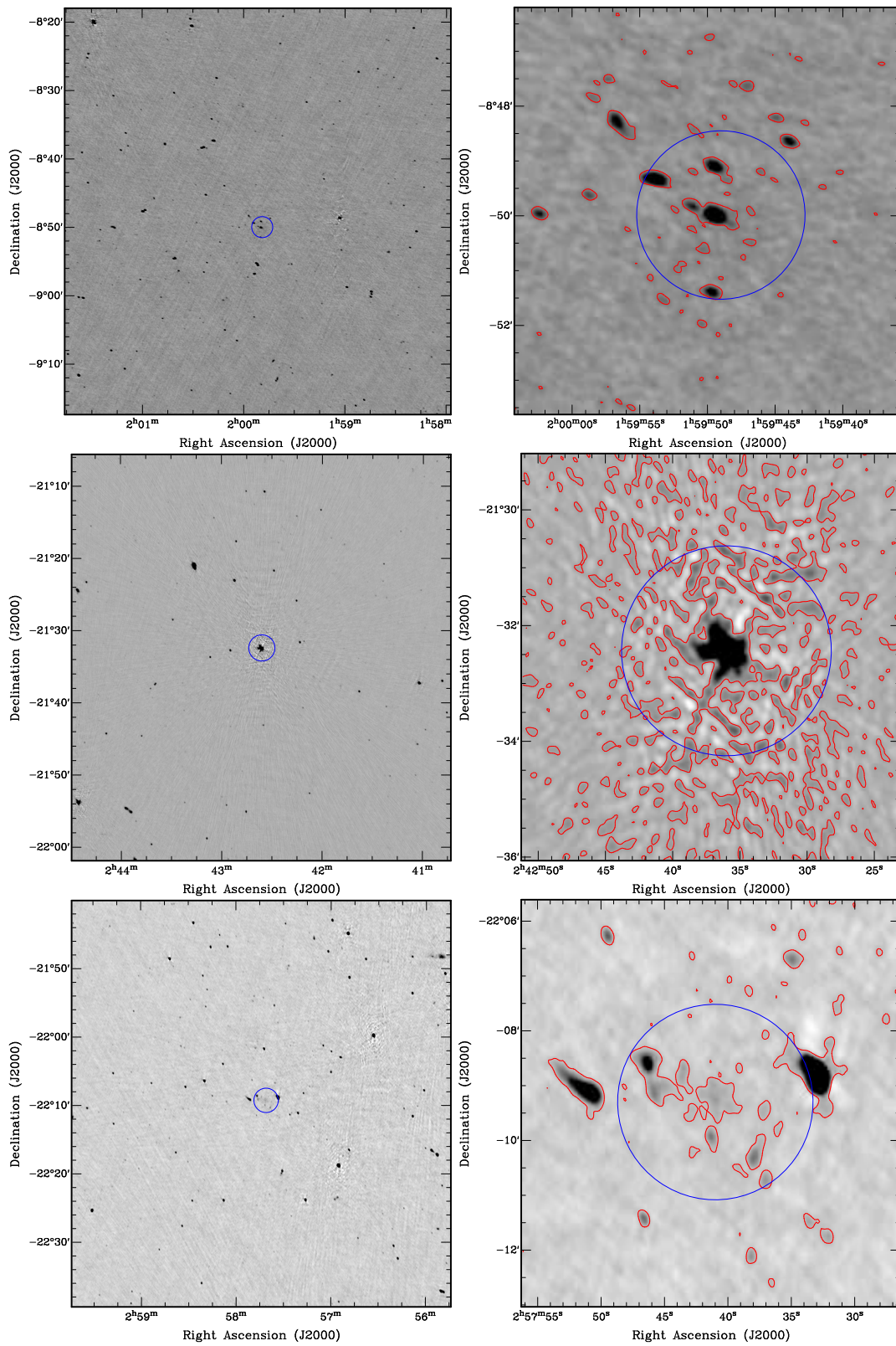


Figure B.2: Same as Fig. A.1. *Top*: MACSJ0159.8-0849 ; *Middle*: MACSJ0242.6-2132; *Bottom*: MACSJ0257.6-2209.

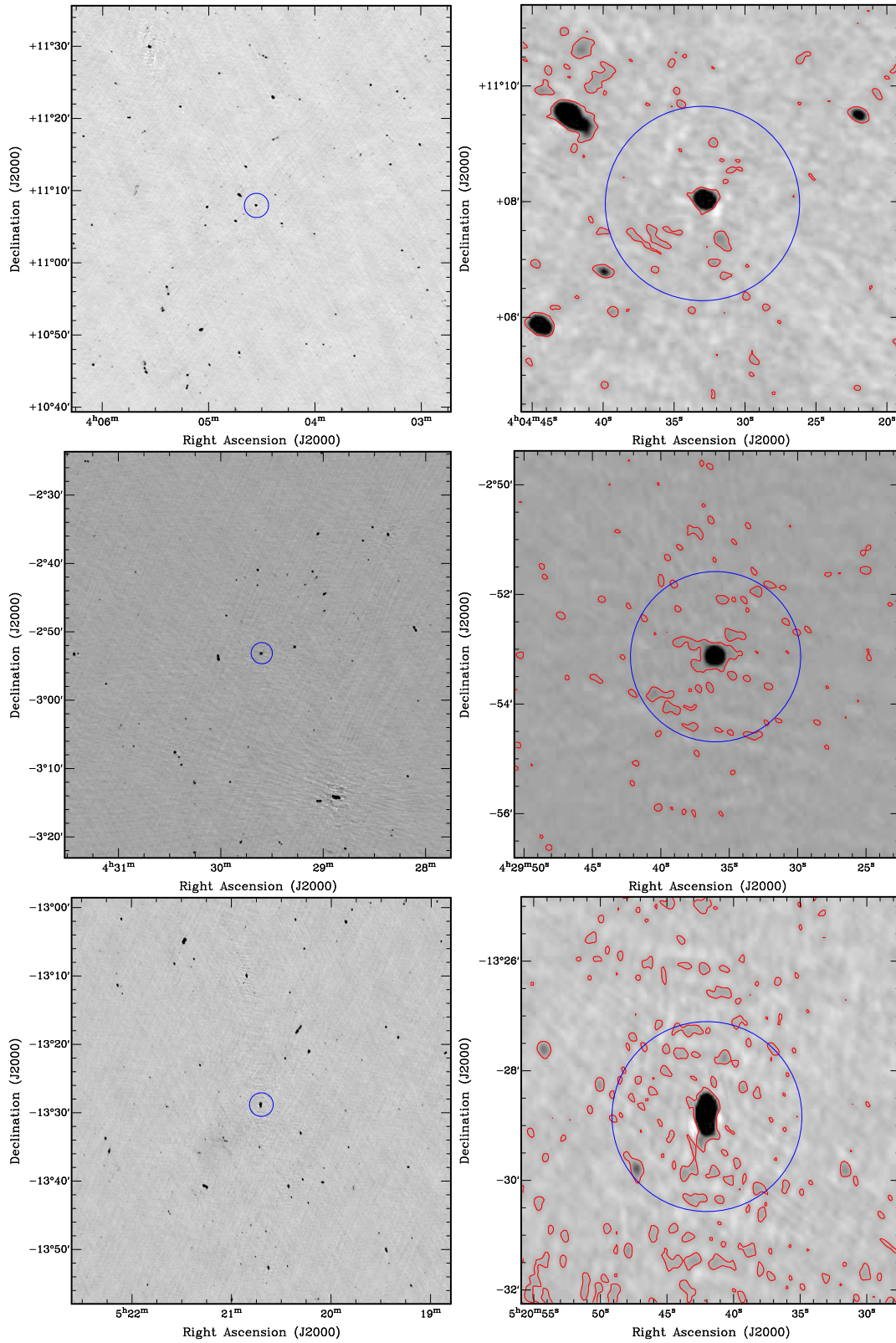


Figure B.3: Same as Fig. A.1. *Top:* MACSJ0404.6+1109; *Middle:* MACSJ0429.6-0253; *Bottom:* MACSJ0520.7-1328.

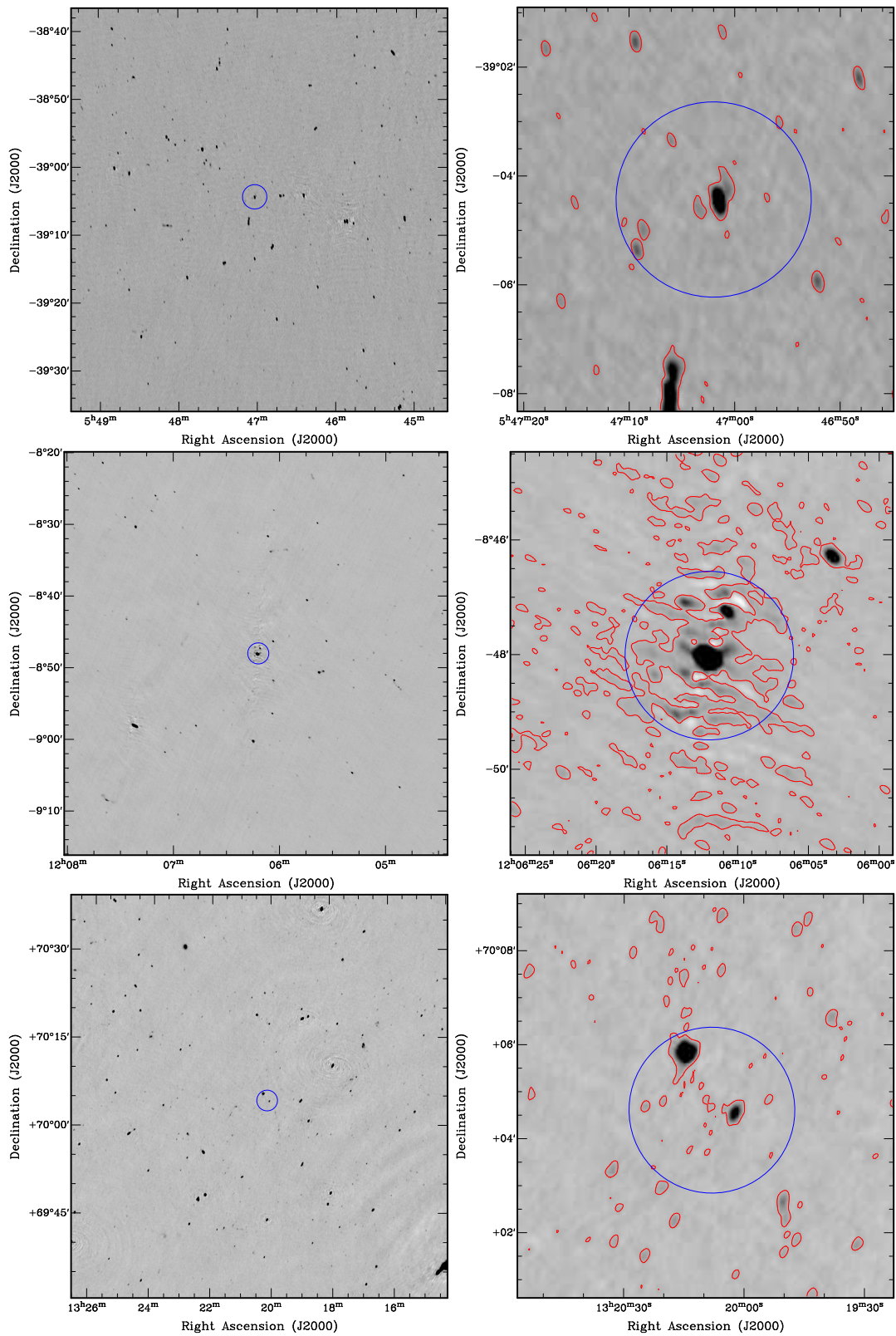


Figure B.4: Same as Fig. A.1. *Top*: MACSJ0547.0-3904; *Middle*: MACSJ1206.2-0847; *Bottom*: MACSJ1319.9+7003.

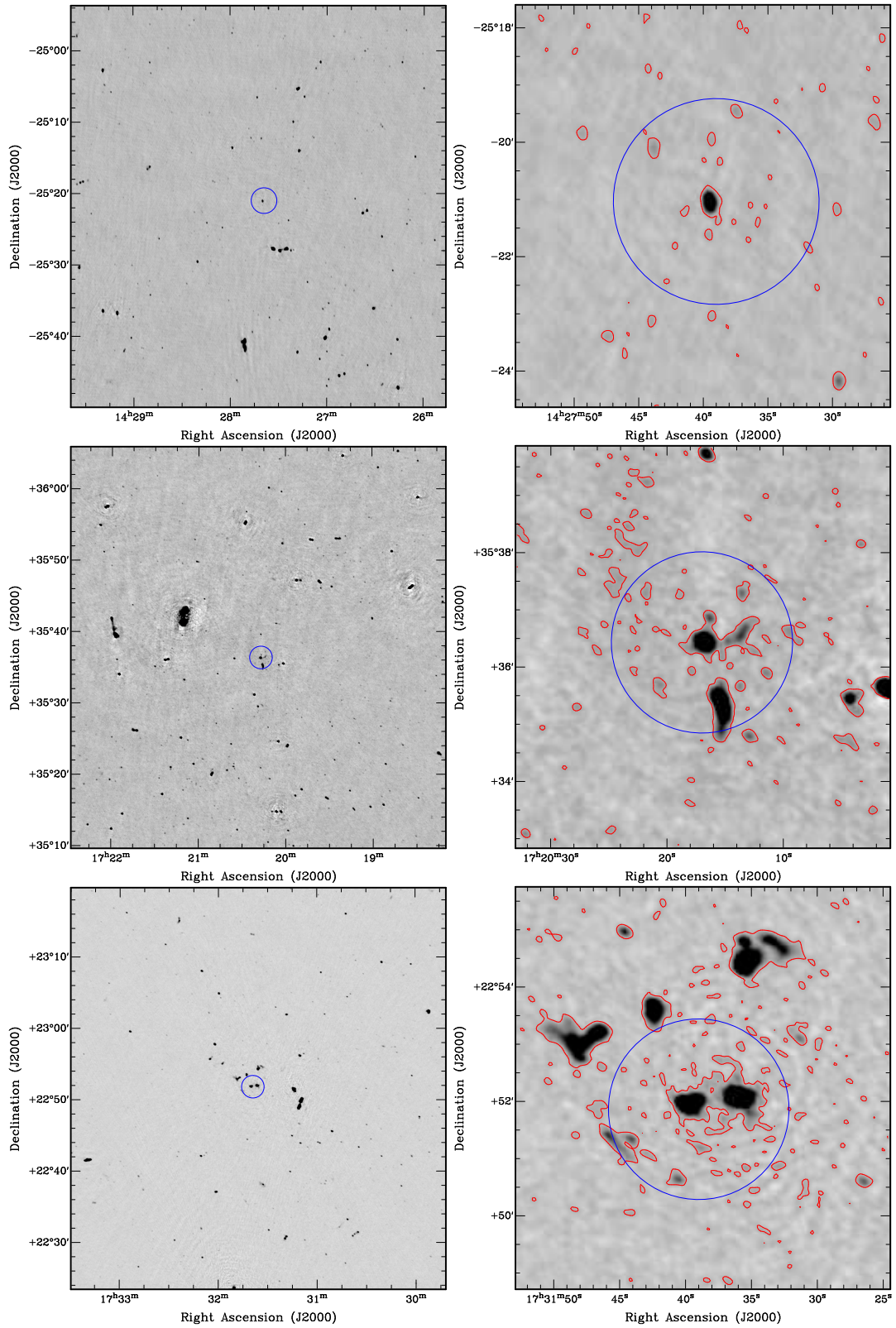


Figure B.5: Same as Fig. A.1. *Top*: MACSJ1427.6-2521; *Middle*: MACSJ1720.2+3536; *Bottom*: MACSJ1731.6+2252.

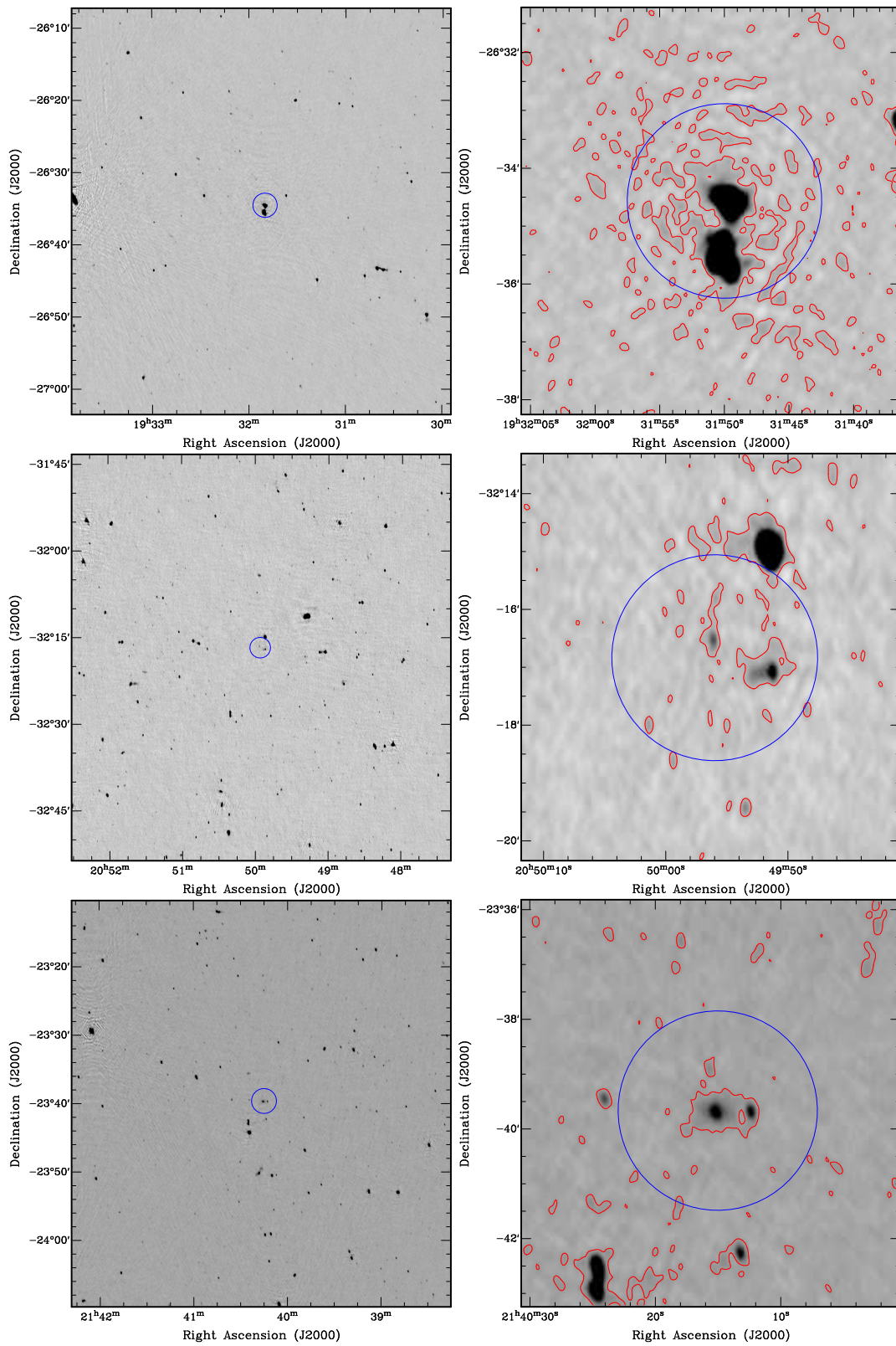


Figure B.6: Same as Fig. A.1. *Top:* MACSJ1931.8-2634; *Middle:* MACSJ2049.9-3217; *Bottom:* MACSJ2140.2-2339.

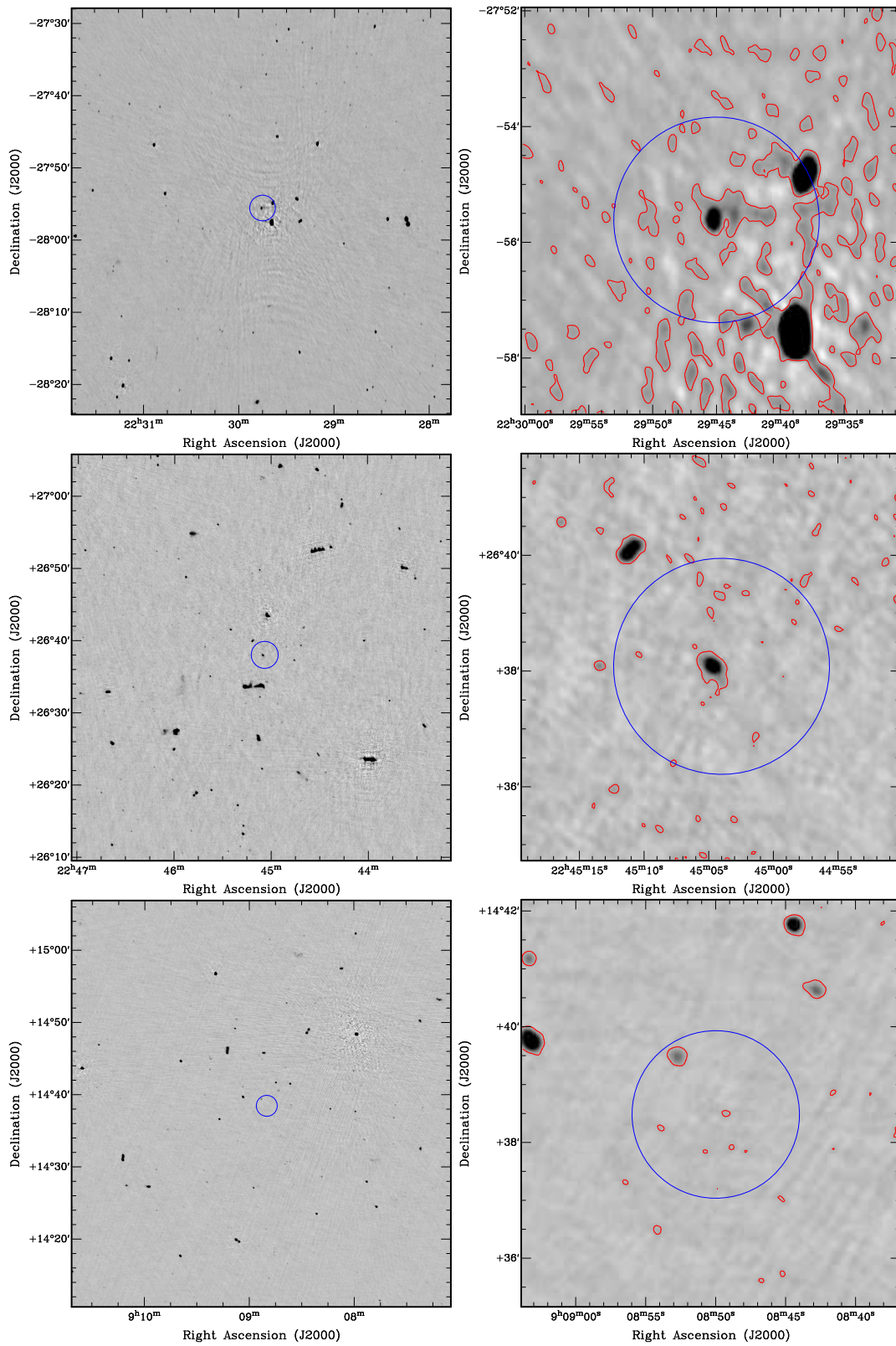


Figure B.7: Same as Fig. A.1. *Top*: MACSJ2229.7-2755; *Middle*: MACSJ2245.0+2637; *Bottom*: PLCK G214.6+36.9.

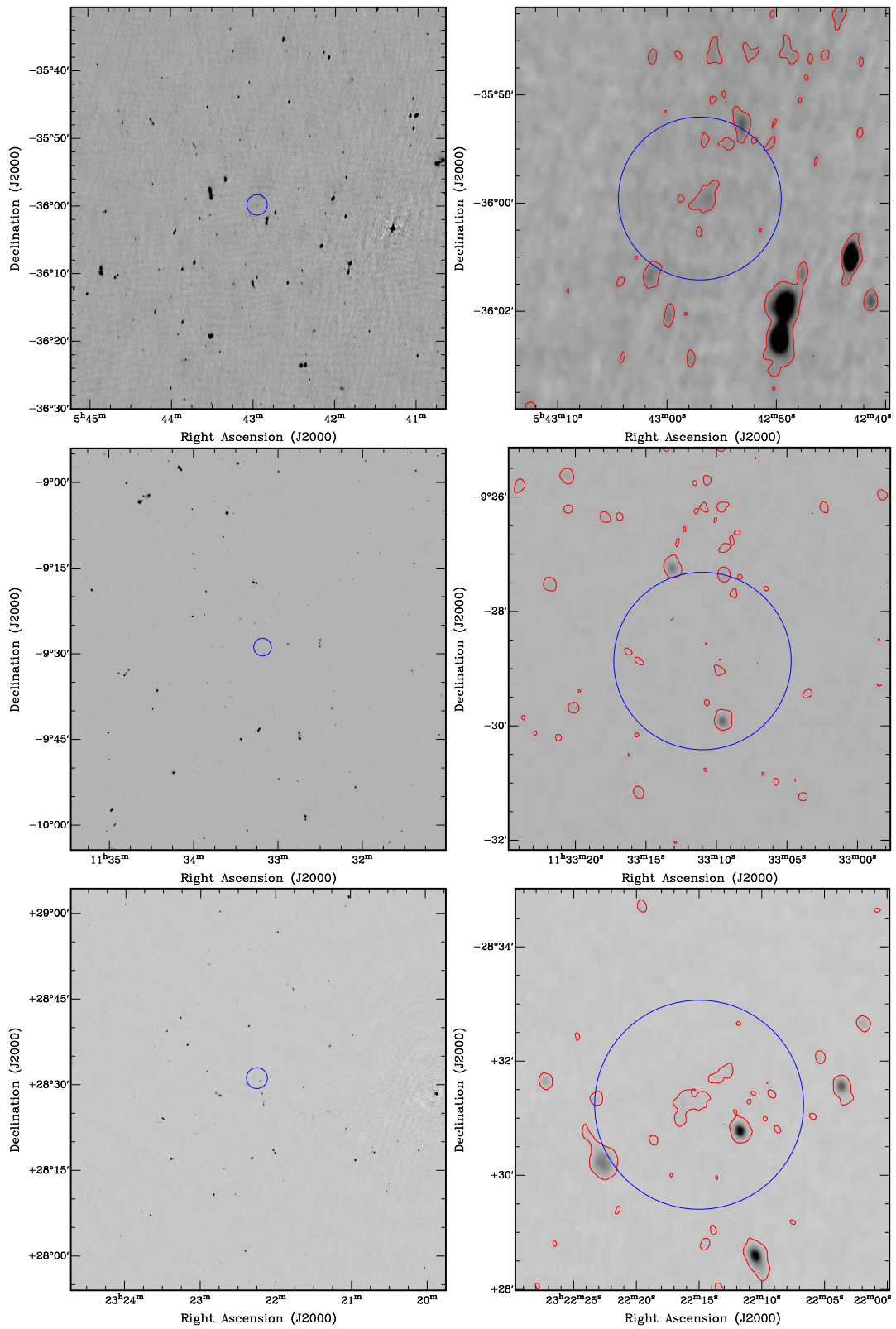


Figure B.8: Same as Fig. A.1. *Top:* PLCK G241.2-28.7; *Middle:* PLCK G272.9+48.8; *Bottom:* PLCK G100.2-30.4.

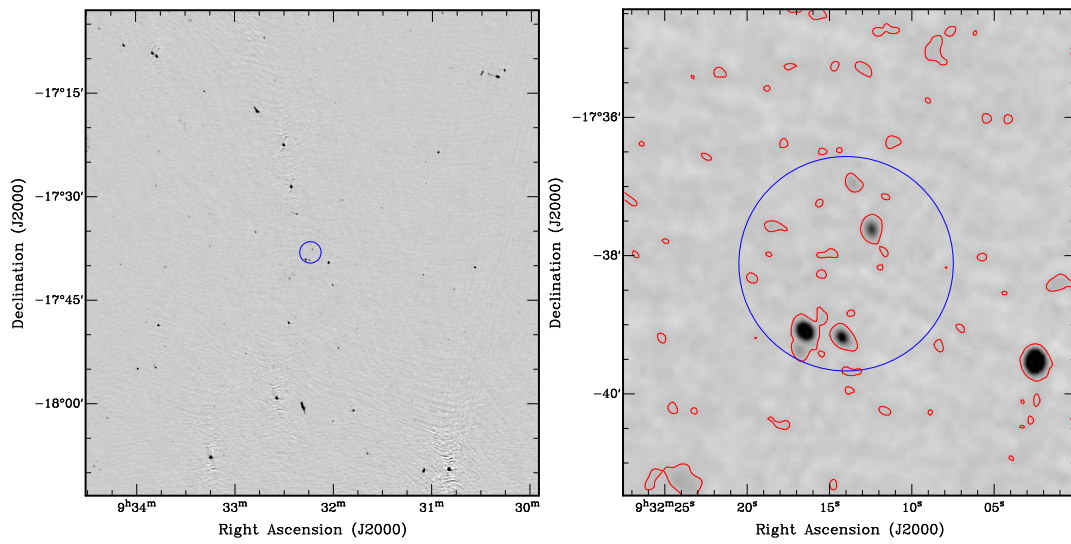


Figure B.9: Same as Fig. A.1. PLCK G250.0+24.1.

# Papers Published

---

## Contents

---

<b>C.1 ATCA observations of the MACS-Planck Radio Halo Cluster Project. I. New detection of a radio halo in PLCK G285.0-23.7 . . . . .</b>	<b>107</b>
<b>C.2 ATCA observations of the MACS-Planck Radio Halo Cluster Project II. Radio observations of intermediate redshift ATCA cluster sample . . . . .</b>	<b>119</b>

---

## **C.1 ATCA observations of the MACS-Planck Radio Halo Cluster Project. I. New detection of a radio halo in PLCK G285.0-23.7**

# ATCA observations of the MACS-Planck Radio Halo Cluster Project

## I. New detection of a radio halo in PLCK G285.0-23.7

G. Martinez Aviles<sup>1,\*</sup>, C. Ferrari<sup>1</sup>, M. Johnston-Hollitt<sup>2</sup>, L. Pratley<sup>2</sup>, G. Macario<sup>1</sup>, T. Venturi<sup>3</sup>, G. Brunetti<sup>3</sup>, R. Cassano<sup>3</sup>, D. Dallacasa<sup>4,3</sup>, H. T. Intema<sup>5</sup>, S. Giacintucci<sup>6</sup>, G. Hurier<sup>7</sup>, N. Aghanim<sup>7</sup>, M. Douspis<sup>7</sup> and M. Langer<sup>7</sup>

<sup>1</sup> Laboratoire Lagrange, Université Côte d’Azur, Observatoire de la Côte d’Azur, CNRS, Blvd de l’Observatoire, CS 34229, 06304 Nice cedex 4, France

<sup>2</sup> School of Chemical & Physical Sciences, Victoria University of Wellington, PO Box 600, Wellington 6140, New Zealand

<sup>3</sup> INAF- Osservatorio di Radioastronomia, via P. Gobetti 101, I-40129, Bologna, Italy

<sup>4</sup> Department of Physics and Astronomy, UniBO, via Ranzani 1, I-40127 Bologna, Italy

<sup>5</sup> Leiden Observatory, Leiden University, Niels Bohrweg 2, NL-2333CA, Leiden, The Netherlands

<sup>6</sup> Department of Astronomy, University of Maryland, College Park, MD 20742-2421, USA

<sup>7</sup> Institut d’Astrophysique Spatiale, CNRS, Univ. Paris-Sud, Université Paris-Saclay, Bât. 121, 91405 Orsay cedex, France

Received April 25, 2016; accepted June 24, 2016

### ABSTRACT

**Aims.** We investigate the possible presence of diffuse radio emission in the intermediate redshift, massive cluster PLCK G285.0-23.7 ( $z=0.39$ ,  $M_{500} = 8.39 \times 10^{14} M_{\odot}$ ).

**Methods.** Our 16cm-band ATCA observations of PLCK G285.0-23.7 allow us to reach a rms noise level of  $\sim 11 \mu\text{Jy}/\text{beam}$  on the wide-band (1.1–3.1 GHz), full-resolution ( $\sim 5$  arcsec) image of the cluster, making it one of the deepest ATCA images yet published. We also re-image visibilities at lower resolution in order to achieve a better sensitivity to low-surface-brightness extended radio sources.

**Results.** We detect one of the lowest luminosity radio halos known at  $z>0.35$ , characterised by a slight offset from the well-studied 1.4 GHz radio power vs. cluster mass correlation. Similarly to most known radio-loud clusters (i.e. those hosting diffuse non-thermal sources), PLCK G285.0-23.7 has a disturbed dynamical state. Our analysis reveals a similarly elongated X-ray and radio morphology. While the size of the radio halo in PLCK G285.0-23.7 is smaller than lower redshift radio-loud clusters in the same mass range, it shows a similar correlation with the cluster virial radius, as expected in the framework of hierarchical structure formation.

**Key words.** galaxies: clusters: general – galaxies: clusters: individual: PLCK G285.0-23.7 – galaxies: clusters: intracluster medium  
radiation mechanisms: non-thermal – radio: continuum: galaxies

## 1. Introduction

Radio halos (RHs) are Mpc-scale diffuse synchrotron sources observed in the central regions of galaxy clusters (see e.g. Feretti et al. 2012, for a recent observational review). Radio halos are found in about one-third of massive clusters (see Cuciti et al. 2015, for an updated study) and are located in merging systems (e.g. Cassano et al. 2013; see Bonafede et al. 2014 for a case of radio halo in an apparently relaxed system).

It is generally believed that turbulence induced by mergers in galaxy clusters can reaccelerate the relativistic electrons responsible for the origin of radio halos (see e.g. Brunetti et al. 2001; Petrosian 2001; Brunetti & Jones 2014, for reviews). This scenario naturally explains the connection between radio halos and mergers; however, it also poses fundamental questions on the micro-physics of the mechanisms that are responsible for the acceleration and transport of these relativistic electrons (see Miniati 2015; Brunetti & Lazarian 2016, for recent discussions).

The study of the connection between radio halos and the thermal properties of the hosting clusters sheds light on these mechanisms and in general on the interplay between thermal and non-thermal components in these systems.

Several correlations between thermal and non-thermal properties of galaxy clusters have been found ( $P_{1.4-LX}$ ,  $P_{1.4-Mass}$ ,  $P_{1.4-Y_{500}}$ ; where  $P_{1.4}$  and  $Y_{500}$  are, respectively, the radio power of halos at 1.4 GHz and the cluster integrated SZ signal within the radius at which the mean mass density is 500 times the critical density at the cluster redshift  $R_{500}$ ; see e.g. Basu 2012; Cassano et al. 2013). In this respect radio follow up of X-ray or mass-selected samples of galaxy clusters provide a unique way to probe the formation of radio halos and their connection with cluster mergers. Models predict that the bulk of radio halos should be generated at  $z=0.2-0.4$  (e.g. Cassano et al. 2006), yet current statistical studies are available only for a limited range of masses and redshifts (e.g. Cuciti et al. 2015).

In this framework, this work is part of the MACS-Planck Radio Halo Cluster Project (Macario et al. 2014) conceived to explore the origin and occurrence of RHs and their connection with the dynamical state of the host systems by extending previous studies to a higher redshift range. Feretti et al. (2012) show that the redshift distribution of clusters hosting RHs is homogeneous up to  $z=0.35$ , but statistically incomplete at higher redshifts. Our sample includes 32 intermediate redshift clusters ( $0.3 < z < 0.45$ ), which are being analysed through deep  $\sim 325$  MHz GMRT or  $\sim 2.1$  GHz ATCA observations, depending on the dec-

\* Gerardo.Martinez-Aviles@oca.eu

**Table 1.** Details of our ATCA observations towards PLCK G285.0-23.7 : dates of observations (Col. 1) with different array configurations (Col. 2); Observation time (Col. 3); phase calibrator (Col. 4). The observations were taken at a central frequency of 2.1 GHz and a bandwidth of 2 GHz

Date	Config.	Obs. time (min.)	Calibrator
2012-Jun-8	6D	704.0	PKS B1036-697
2012-Jun-9	6D	523.3	PKS B0606-795
2012-Jun-29	750A	531.3	PKS B0606-795
2013-Sep-6	1.5A	803.6	PKS B0606-795

lication of the targets. In this paper we present the discovery of a RH in PLCK G285.0-23.7, which is a massive cluster ( $M_{500} = 8.39 \times 10^{14} M_{\odot}$  Planck Collaboration et al. 2011) located at redshift  $z=0.39$ .

In the following, Sect. 2 describes the ATCA observations of PLCK G285.0-23.7 together with the data reduction and the image reconstruction strategy. The physical properties of the detected diffuse radio source and our analysis of its nature are presented in Sect. 3. Our study is discussed and concluded in Sect. 4. In the  $\Lambda$ CDM cosmology adopted throughout this paper (with  $H_0=70 \text{ km s}^{-1} \text{ Mpc}^{-1}$ ,  $\Omega_M=0.3$ ,  $\Omega_{\Lambda}=0.7$ ), 1 arcsec corresponds to 5.29 kpc at the redshift of PLCK G285.0-23.7.

## 2. Radio observations and data reduction

Radio observations of PLCK G285.0-23.7 were undertaken on the Australia Telescope Compact Array (ATCA) in three separate array configurations (6D, 750A, 1.5A) using the Compact Array Broadband Backend (CABB) correlator with a central frequency of 2.1 GHz and spanning 1.1-3.1 GHz. Observations were carried out in continuum mode with the correlator set to produce  $2000 \times 1$  MHz channels. Details of the observations can be found in Table 1. The primary flux scale was set relative to the unresolved source PKS B1934-638 for which the detailed spectral behaviour is well understood over the ATCA band. The phase calibration was initially performed relative to PKS B1036-697 for first of two observations in the 6D configuration which commenced on 8 June 2012. However, it was quickly noted that PKS B1036-697 was partially confused in this configuration and so this calibrator was replaced with PKS B0606-795 for the remaining observation run.

Radio frequency interference (RFI) and bad channels were manually excised from the target and primary and secondary calibrators using a combination of clipping algorithms and visual inspection via the PGFLAG task within MIRIAD (Sault et al. 1995). Owing to the nature of CABB data, it is necessary to perform calibration and cleaning on narrower frequency intervals. The precise intervals used depend on properties of the observations (phase stability) and the complexity of sources in the field, which affects the success of cleaning. We conducted a number of trials and determined that  $\sim 500$  MHz  $\times$  4 sub-bands produce the optimal results for these data. Thus, the target, primary, and secondary calibrator data were divided into the required sub-bands centred at 1.381 (from 1.130 GHz to 1.630 GHz), 1.867 (from 1.631 GHz to 2.130 GHz), 2.380 (from 2.131 GHz to 2.630 GHz), and 2.769 MHz (from 2.631 GHz to 3.100 GHz). Each sub-band was then calibrated in MIRIAD as per standard proce-

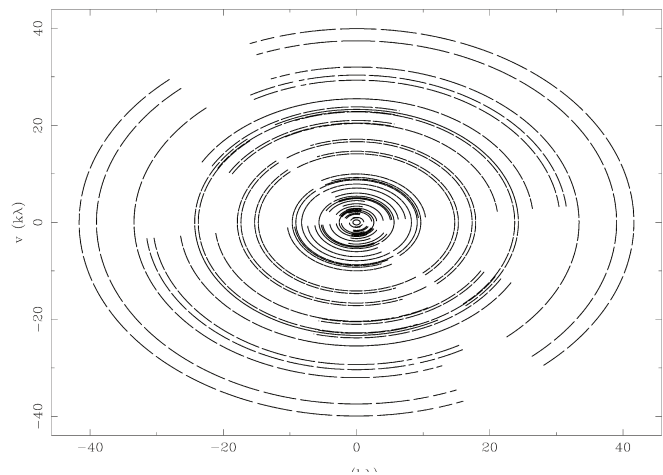


**Fig. 1.** uv-coverage of PLCK G285.0-23.7 observations in the 500 MHz band centred at 1.867 MHz. The wide-band of the full 2 GHz observations completes the coverage.

**Table 2.** Properties of the full-resolution (*first five rows*) and tapered (*last five rows*) radio maps in different frequency bands centred at  $\nu_0$ . The band-width is  $\sim 500$  MHz for IDs from “Block 1” to “Block 4”; it includes the total frequency range of observations (see Table 1) for the “Wide-band” ID.

Band ID	$\nu_0$ (GHz)	RMS noise ( $\mu\text{Jy}/\text{beam}$ )	Beam Size (“ $\times$ ”)	PA (deg)
Full-resolution images				
Block 1	2.769	20.1	$2.46 \times 2.09$	-41.24
Block 2	2.380	19.9	$2.88 \times 2.45$	-41.52
Block 3	1.867	18.1	$3.62 \times 3.10$	-35.24
Block 4	1.381	25.3	$5.19 \times 4.38$	-42.31
Wide-band	2.030	11.3	$5.20 \times 4.38$	-42.31
Tapered images				
Block 1	2.769	31.6	$30.54 \times 19.69$	83.92
Block 2	2.380	38.1	$30.46 \times 20.75$	-89.52
Block 3	1.867	51.1	$30.96 \times 22.68$	-81.17
Block 4	1.381	71.3	$31.03 \times 23.93$	-72.66
Wide-band	2.030	25.3	$31.48 \times 25.09$	-73.07

dures outlined in the 2014 MIRIAD manual to produce four continuum images. During this procedure it became apparent that data from the 6D array suffered from a bandpass ripple on all baselines associated with antennas 5 and 6 which persisted for 75 minutes. This effect is a transient error of unknown origin seen rarely in ATCA data and was not evident in data from the 750A or 1.5A configuration. Attempts to correct for this proved unsuccessful and baselines to antennas 5 and 6 were removed for this configuration over this time. An example of the resultant uv-coverage for the combination of all three configurations for the 1.867 GHz sub-band image is shown in Fig. 1.

Following calibration, sub-band images were created out to the second null in the point spread function using the task INVERT and a Steer CLEAN (Steer et al. 1984) was applied to all sources within the primary beam. Two bright sources (at coordinates RA=07:19:25.285, Dec=-73:32:21.16 and RA=07:23:30.799, Dec=-73:08:40.16) with fluxes of just

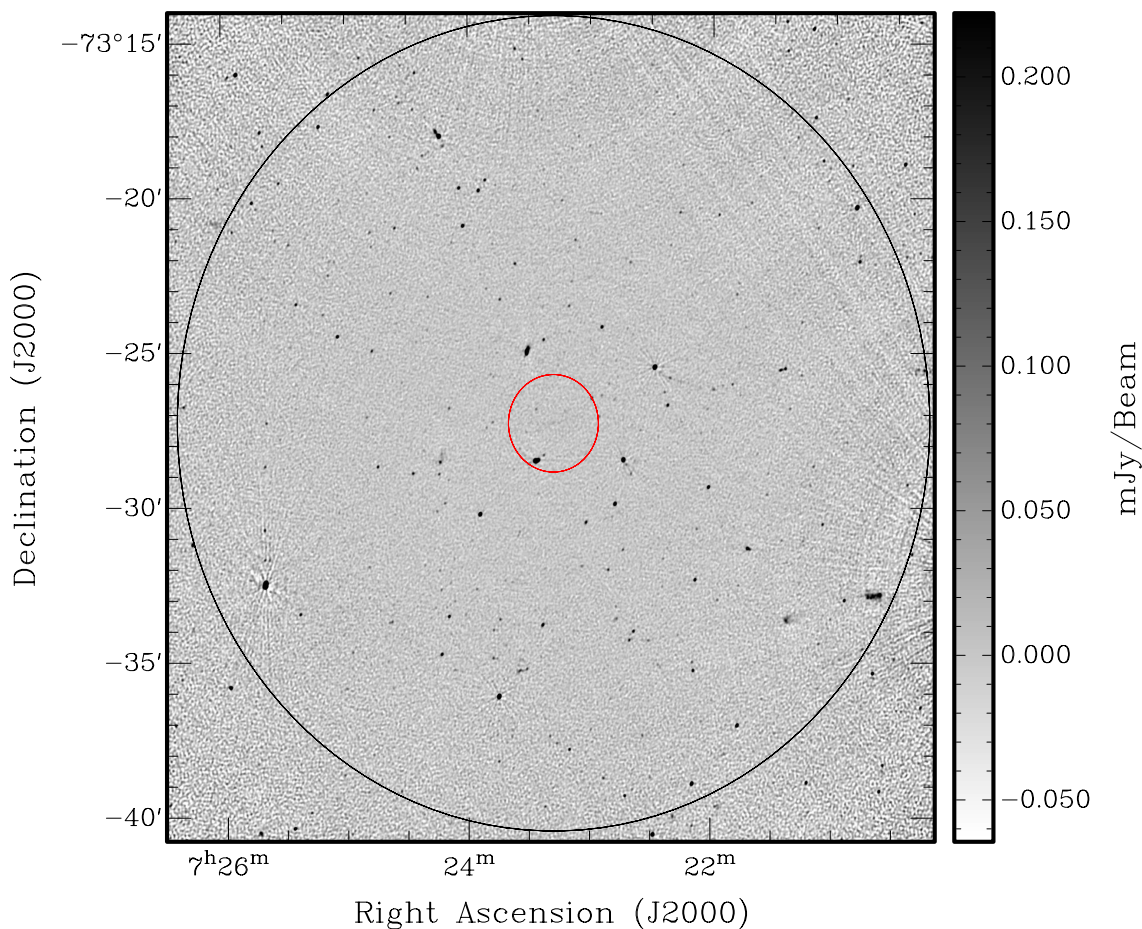


**Fig. 2.** Final full-resolution, wide-band image of PLCK G285.0-23.7. The outer, big circle denotes the boundary of the primary beam with a radius of  $\sim 0.22$  degrees. The central 1 Mpc diameter region is indicated by the inner, smaller red circle. The rms noise of this image is  $11.3 \mu\text{Jy}/\text{beam}$  and the resolution is  $5''$ .

over 100 mJy sitting just outside of the primary beam were difficult to clean. They were modelled and subtracted from all of the visibility data and the sub-bands were re-imaged. Details of the resultant sub-band images are presented in Table 2. The first 200 MHz of the band is strongly affected by RFI meaning the image at 1.3 GHz has the lowest sensitivity.

The sub-band images were convolved with a Gaussian to a common resolution, slightly lower than the lowest resolution sub-band image. The sub-band images were then added together to create a final wide-band image (see Table 2). As the noise levels in the sub-band images are mostly identical for the three highest bands and only differed marginally in the lowest frequency band, it was not necessary to weight the images relative to the sensitivities in the mosaicing process. The final deep ATCA image achieves a root mean squared (rms) noise of  $\sim 11 \mu\text{Jy}/\text{beam}$  measured with AIPS TVSTAT at the field centre in regions inside the primary beam without any trace of point sources or diffuse emission. We get a dynamic range of 10,000:1, making it one of the deepest, highest dynamic range ATCA images yet published, equal to the recent image of the Bullet Cluster at  $11 \mu\text{Jy}/\text{beam}$  (Shimwell et al. 2014, 2015). The image is shown in Fig. 2.

A visual inspection of our full-resolution ATCA image of PLCK G285.0-23.7 shows no obvious presence of diffuse radio emission in the central area where the cluster lies (see Fig. 2 and Fig. 3 for a zoomed version on the cluster). In order to investigate the possible presence of low-surface-brightness diffuse sources in the cluster, visibilities were re-imaged with a

robust=0.5 weighting and a  $\sim 9 \text{ k}\lambda$  Gaussian tapering was applied allowing a FWHM of  $\approx 30$  arcsec (see Table 2). Again, data were imaged in each of the four sub-bands with the taper applied and then mosaicked into a single deep map (see Table 2). A diffuse, low-surface-brightness source is detected coincident with the cluster core.

### 3. Results

#### 3.1. Detection and characterisation of a radio halo in PLCK G285.0-23.7

Contours of the low-resolution radio map of PLCK G285.0-23.7 are overlaid on the X-ray XMM image of the same sky region in Fig. 4. The morphology of the diffuse radio source matches very closely the thermal ICM X-ray emission in terms of extension and of elongation (with a main axis along the east-west direction). This, together with the disturbed dynamical state of the cluster suggested by its X-ray morphology and density profile (Planck Collaboration et al. 2011), allows us to confidently classify the diffuse source in PLCK G285.0-23.7 as a classical RH.

We now examine the radio flux density of the diffuse source on the tapered image relative to Block 3 (ID 2 in Table 3), i.e. the image centred at 1.867 GHz and characterised by an average rms noise level of  $51.1 \mu\text{Jy}/\text{beam}$  (Table 2), as it shows the best sensitivity to the diffuse radio emission. Owing to the typical spectral behaviour of radio halos (with synchrotron spectral

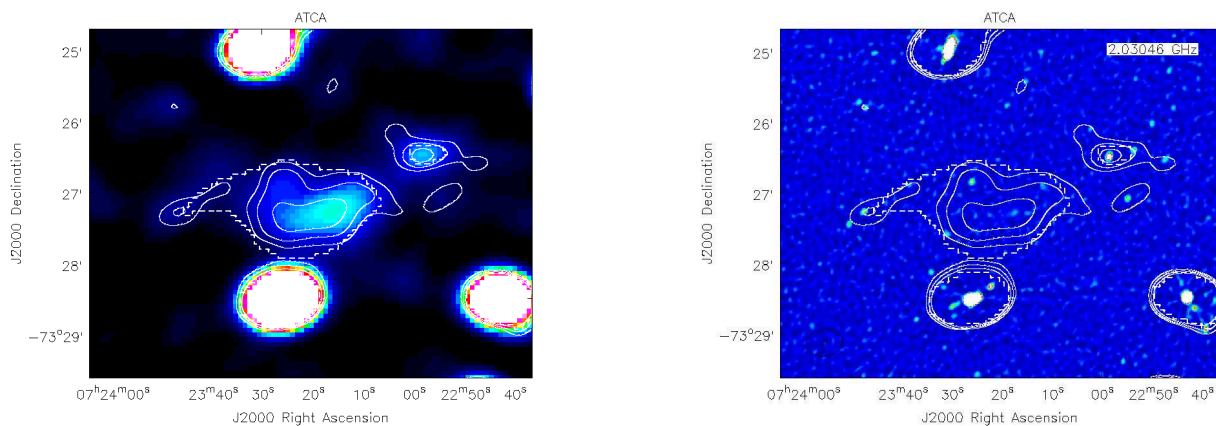


**Fig. 3.** Contours of the ATCA tapered image centred at 1.867 GHz are overlaid on the ATCA wide-band tapered (*left*) and full-resolution maps (*right*). Dashed contours correspond to the islands of significant emission detected by PyBDSM on the Block 3 tapered map (cyan contours in Fig.A.1). The continuous curves trace instead “classical”  $3, 3 \times \sqrt{2}, 6 \sigma$  contours (i.e. with the  $51.1 \mu\text{Jy}/\text{beam}$  rms value of the map estimated by hand on the Block 3 tapered map at  $\sim 30$  arcsec resolution; see Table 2).

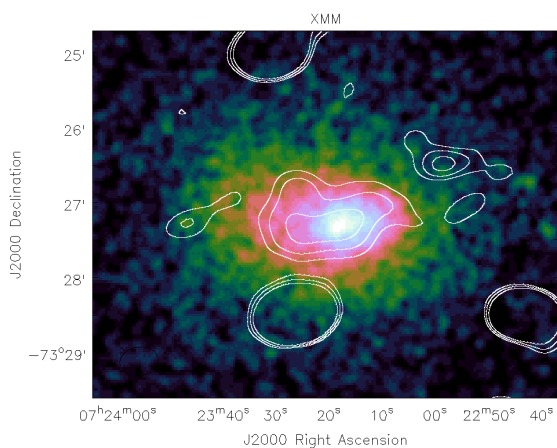


**Fig. 4.** Radio contours of the ATCA tapered image centred at 1.867 GHz overlaid on the smoothed raw XMM image in the [0.3-2.0] keV energy band of PLCK G285.0-23.7 (Planck Collaboration et al. 2011). Contour levels are the same as in Fig. 3.

index  $\alpha \gtrsim 1$ )<sup>1</sup>, the rms sensitivity of our maps is comparable from Block 1 to Block 3; however, a lower luminosity is expected for the diffuse radio source at the higher frequencies sampled by Blocks 1 and 2. In terms of sensitivity to steep synchrotron sources, Block 4 would have been the optimal frequency range in which to measure the radio halo flux density, if it had not been badly affected by RFI ( $\sim 60\%$  of the data were flagged).

The total flux density was first measured on the Block 3 tapered image by integration over the source image within  $3\sigma$  contours using the AIPS task TVSTAT. By overlaying the  $5\sigma$  contours corresponding to the full-resolution wide-band radio map on the optical image of the cluster central region, we identify two point-like significant objects lying within the region occupied by the diffuse source on the low-resolution radio map. The two compact radio sources show quite clear optical counterparts (see Fig. 5). We measured their flux densities using the AIPS

<sup>1</sup> In this paper we use the convention  $S(\nu) \propto \nu^{-\alpha}$ , with  $S(\nu)$  being the radio flux density.

Images ID	Angular size ( $' \times '$ )	Physical size (kpc $\times$ kpc)	Flux (mJy)
ID 1	$2.34 \times 1.34$	$742 \times 425$	$2.02 \pm 0.25$
ID 2	"	"	$2.11 \pm 0.26$
ID 2 ss	"	"	$1.95 \pm 0.25$
ID 1	$2.98 \times 1.60$	$945 \times 507$	$2.37 \pm 0.34$
ID 2	"	"	$2.53 \pm 0.35$
ID 2 ss	"	"	$2.17 \pm 0.44$

**Table 3.** Physical properties of the diffuse radio source at 1.867 GHz from tapered images. *Col. 1* gives the identification numbers of the tapered images on which we have performed the measurements: ID 1: Image with source subtraction in uv-data; ID 2: Image without source subtraction in uv-data; ID 2 ss: Image of ID2 after removing by hand the flux of point sources identified in the image plane. *Col. 2* and *Col. 3* correspond to the angular and physical size of the source, respectively (see text). *Col. 4* reports the flux of the diffuse radio sources as measured with TVSTAT within the  $3\sigma$  contours of the map with ID 2 (*top*), with TVSTAT within the  $3\sigma$  contours calculated by PyBDSM for the map with ID 2 (*bottom*).

verb JMFIT and we subtracted them from the total flux density measured inside the  $3\sigma$  contours of the tapered image.

To verify that large-scale diffuse emission is not caused by the blending of discrete sources and to get a complementary flux measurement, we then produced an image of the diffuse cluster emission by subtracting compact sources in the uv-plane. We first identified the clean components of the discrete sources by using only the longest baselines (uv-range 3.6-40.0 k $\lambda$ ). These components were then subtracted from the original data set in the uv-plane by using the MIRIAD task UVMODEL. At this point, we calculated the flux density of the residual diffuse emission by integrating the surface brightness down to the same region considered before, i.e. within the  $3\sigma$  level of the non-point source subtracted tapered map (ID 1 in Table 3). The results of these flux density measurements are given in the top part of Table 3. The error in flux density is calculated following the formula  $\Delta F = \sqrt{(\sigma_{rms})^2 N_{beam} + 0.01 F^2}$ , where  $F$  is the measured flux density and  $N_{beam}$  is the number of beams contained in the measured area.

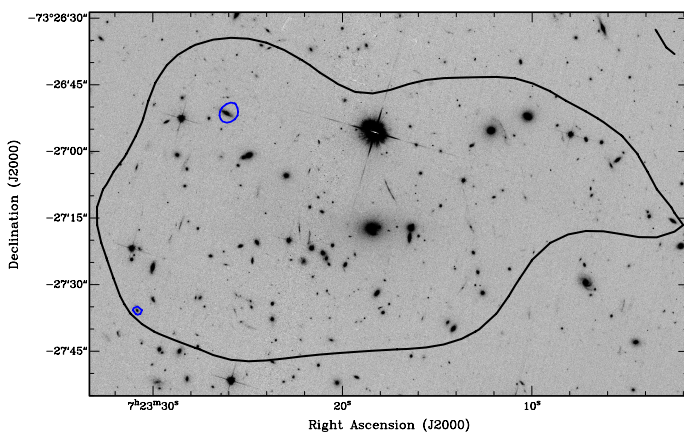


**Fig. 5.** Zoom in the HST-ACS image of PLCK G285.0-23.7 central field (available in the HST archive). For reference, the  $3\sigma$  contour of the ATCA tapered image centred at 1.867 GHz is shown in black. The blue contours indicate sources of significant radio emission in the full-resolution deep ATCA image of the cluster (i.e.  $5 \times \text{rms}$  of the final wide-band ATCA map shown in Fig. 2).

Table 3 shows the results of the different flux density measurements; all the values are consistent within the error bars. The flux measurement that we adopt in our following analysis is the one measured in the tapered map with point source subtracted from the uv-plane (ID1 in Table 3), for which we obtain a flux density of  $2.02 \pm 0.25$  mJy at 1.867 GHz.

In order to get an estimate of the size of the diffuse radio source, we measured the smallest ellipse that fully contains the  $3\sigma$  contours of the Block 3 tapered map without point source subtraction (ID2 in Table 3). We obtain an angular extent of  $2.34' \times 1.34'$ , which, for our cosmology, corresponds to a major and minor axis of  $\sim 742$  kpc and 425 kpc, respectively (see Table 3).

Finally, we measured with TVSTAT the total flux density on the ID1 and ID2 maps by following the contours of the significant islands of emission identified by the source finder software PyBDSM around the diffuse source (dashed contours in Fig. 3; see Appendix A for details on the use of PyBDSM). The results obtained following this final method are given in the bottom part of Table 3.

### 3.2. Radio luminosity vs. cluster mass correlation

We calculated the power of the newly discovered diffuse radio source and compared it with radio powers of previously discovered halos. We selected objects firmly classified as giant radio halos (i.e. with diffuse emission extending beyond the cluster core), whose flux density has been measured through radio interferometric observations and with a point source identification and subtraction strategy very similar to ours, and with information about  $M_{500}$  in the PSZ2 cluster catalog (Planck Collaboration et al. 2015). The list of sources is presented in Table 4.

In order to convert all values to the cosmology adopted in this paper and to take into account some inconsistencies found for published radio powers, we compiled the total flux densities of RHs reported in the literature (see Table 4). We then calculated radio powers using the formula  $L_\nu = 4\pi D_L^2 S_\nu (1+z)^{\alpha-1}$ , where  $D_L$  is the luminosity distance of the cluster. Whenever a measured value of the spectral index is not available, we adopted  $\alpha=1.3$ .

Traditionally RH powers are reported at 1.4 GHz; however, owing to the lower quality of the Block 4 image centred at 1.381 GHz, we considered the most reliable sub-band map (centred at 1.867 GHz) and then extrapolated to obtain the 1.4 GHz radio

power. As the spectral index of the radio source is too uncertain over the ATCA band owing to the very low surface brightness of the object, we undertake this extrapolation assuming the value of  $\alpha=1.3$ . We obtain a value for the radio power at 1.4 GHz of  $1.72 \pm 0.22 \times 10^{24}$  W/Hz.

In Fig. 6 we plot the radio power vs. cluster mass for the RH in PLCK G285.0-23.7 (shown as a red star) as compared to all halos included in Table 4, which are indicated by triangles (colour-coded based on the redshift of their host clusters), except when they are classified as ultra steep spectrum (USS) radio halos and/or when their flux was not measured at  $\approx 1.4$  GHz (see Table 4), in which case they appear as dots (keeping the same colour code). Analogously to Cassano et al. (2013), we fit a power-law relation using linear regression in the log-log space and adopt a BCES-bisector regression algorithm (Akritas & Bershady 1996). For the fitting, shown as a red line in Fig. 6 and characterised by a slope of  $4.24 \pm 0.14$ , we consider only the RHs represented as triangles in Fig. 6. The best fit derived by Cassano et al. (2013), traditionally reported in the literature, has a slope of  $3.77 \pm 0.57$ . For completeness we also derived the value for the slope using all radio powers of halos present in Table 4 for the best fit, which is  $4.05 \pm 0.09$ . The three results are consistent within the error bars. The RH in PLCK G285.0-23.7 is slightly under-luminous with respect to the best-fit relation, but is within the scatter of the observed data points. We also point out that, based on the present radio data, we do not find a clear trend with redshift of the  $P_{1.4} - M_{500}$  correlation.

Following Cassano et al. (2007), we show in Fig. 7 the position of the newly detected radio halo on the plot of radio halo sizes as a function of the virial radius of their host clusters. There is evidence that powerful radio halos are also bigger and hosted by more massive systems (e.g. Giovannini & Feretti 2000; Kempner & Sarazin 2001; Cassano et al. 2007; Murgia et al. 2009). Although it is a massive cluster ( $M_{500} \sim 8.39 \times 10^{14} M_\odot$ ), PLCK G285.0-23.7 hosts a quite small radio halo of radius  $\sqrt{a * b} \sim 281$  kpc, where  $a$  and  $b$  are the semi-major and semi-minor axis derived in Sect. 3.1. However, if we consider the correlation between the size of the radio halos and the virial radius of their hosting clusters (Fig. 7), we see that PLCK G285.0-23.7 (red point) follows the trend of other radio loud clusters. This occurs because PLCK G285.0-23.7 is at a relatively high redshift ( $z \sim 0.39$ ), which means that its virial radius, and thus its radio halo, is smaller (owing to the cosmological growth and virialisation of galaxy clusters) than those of nearby clusters with the same mass.

## 4. Discussion and conclusions

We present high-sensitivity and wide-band (1.1 – 3.1 GHz) ATCA observations of the galaxy cluster PLCK G285.0-23.7, which reveals the presence of a diffuse radio source with an extension (major axis) of  $\approx 700$  kpc and a total 1.4 GHz power of  $\approx 1.7 \times 10^{24}$  W/Hz, as extrapolated from measurements in the 500 MHz-wide sub-band centred at 1.867 GHz.

Both the diffuse nature of the source, which is not related to blending of compact radio objects, and the comparison of our high-sensitivity tapered radio map to the X-ray image of the cluster allow us to classify the detected emission as a classical RH. First, the morphology and size of the diffuse radio source indicate a very similar distribution of the non-thermal ICM and the thermal component, traced by its X-ray bremsstrahlung radiation. Similarly to most known RHs, our newly detected halo is thus hosted by a massive cluster ( $8.4 \times 10^{14} M_\odot$ ), and there are strong indications that it is a merging system.

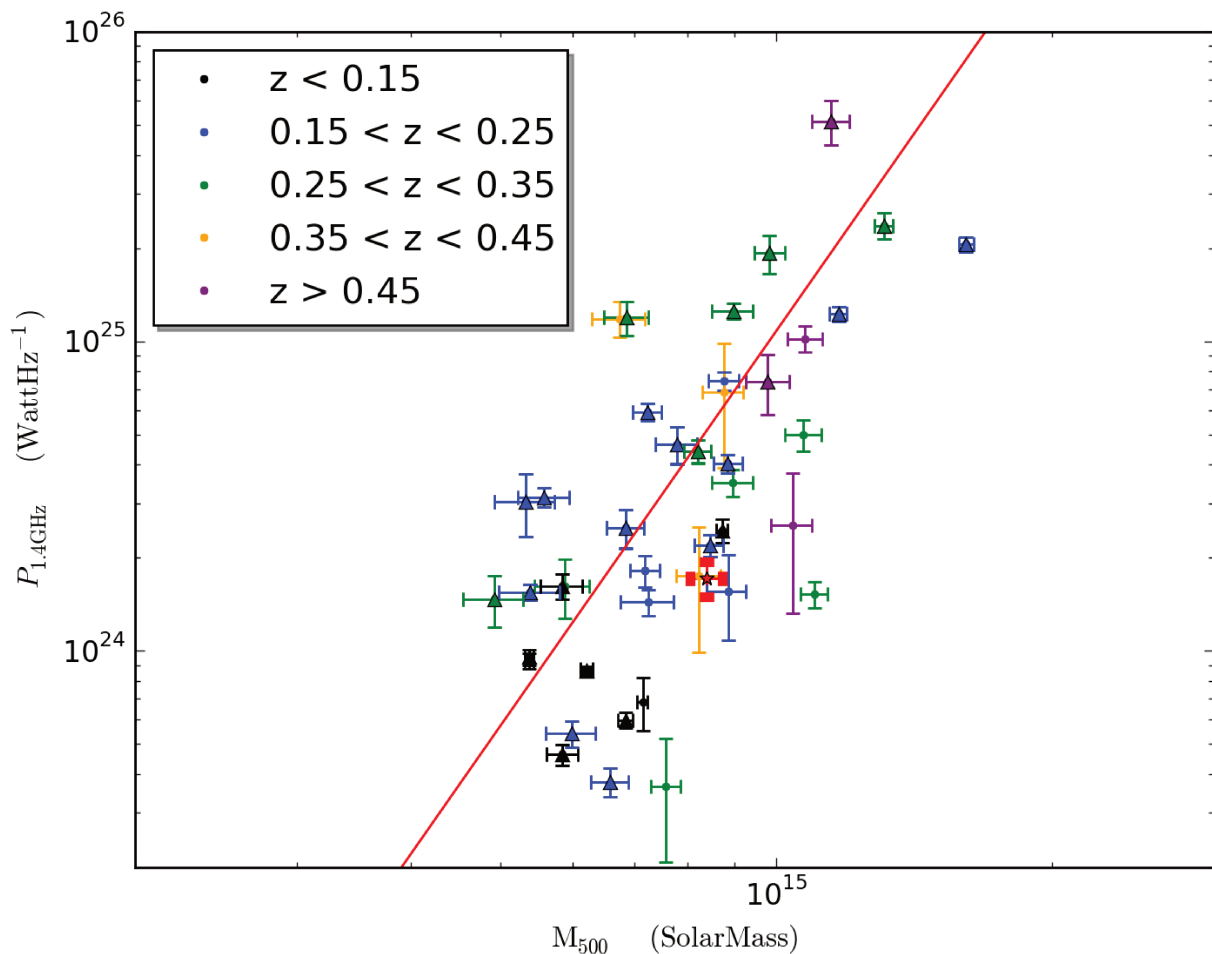


**Fig. 6.** Synchrotron power of RHs at 1.4 GHz ( $P_{1.4\text{GHz}}$ ) vs. cluster mass ( $M_{500}$  from Planck Collaboration et al. 2015). Symbols are colour-coded depending on the redshift of RH hosting clusters. The red line is the fit derived in the present paper, including only the RHs with radio fluxes measured at 1.4 GHz (indicated by triangles; see also Table 4). Analogously to Cassano et al. (2013), we exclude for the fitting ultra-steep spectrum RHs and halos detected in frequencies different from 1.4 GHz, both shown in dots (see Table 4). The red star corresponds to PLCK G285.0-23.7 detected in this work. When the spectral index is unknown (including PLCK G285.0-23.7) we assume the value of  $\alpha=1.3$ .

Our wide-band full-resolution radio map of PLCK G285.0-23.7 is one of the deepest ATCA images yet published, reaching an rms level of  $\sim 11 \mu\text{Jy}/\text{beam}$  with a synthesised beam size of few arcsec, i.e. the kind of sensitivity expected for the upcoming continuum ASKAP-EMU survey (Norris et al. 2011). Despite the depth and quality of our radio observations, the detection of the diffuse source required a tapered weighting (see Table 2), which has allowed the detection of one of the lowest luminosity RH in the sub-sample of known radio-loud clusters at  $z>0.35$  (Fig. 6). This analysis is thus a very good example of the impact that the 30,000 square degrees ( $\text{Dec}<30^\circ$ ) EMU survey will have on statistical studies of the non-thermal component of the ICM, if an appropriate data reduction strategy, which includes data tapering and compact source subtraction, is implemented.

The measurements of the halo radio power can be significantly biased by several factors. First of all, the quality of our map centred at  $\sim 1.4$  GHz does not allow a proper detection and flux density measurement of the RH, which can instead be reliably measured in the sub-band image centred at  $\sim 1.8$  GHz. Since an in-band spectral index cannot be derived from our data, a value  $\alpha=1.3$  is assumed here to get the  $k$ -corrected 1.4 GHz

luminosity plotted in Fig. 6. The other significant uncertainty in comparing our measurement to literature values is intrinsically related to the relative depth of the different published maps and to the method adopted for flux density measurements. Here we measure the flux density on images with point source subtraction both on the uv-data and on the image plane, showing that our different measurements are consistent within the error bars (see Table 3). It is worth mentioning that the telescope only measures power on the spatial scales of the sampled uv-coverage, which could limit the total power measured from the radio halo. This would be especially the case if the uv-coverage happened to lack at the physical scales of the radio halo.

With these elements in mind, the newly detected RH seems to be slightly under-luminous compared to objects hosted by clusters in a similar mass range, as shown in the  $P_{1.4\text{GHz}}$  vs.  $M_{500}$  plot of Fig. 6; however, it is not a clear outlier like the RH recently discovered by Bonafede et al. (2015).

It is expected that radio halos and their hosting clusters develop complex patterns with time in the radio–mass (or X-ray luminosity) diagram as a result of the evolution of cluster dynamics and particle acceleration and spectra (e.g. Donnert et al.

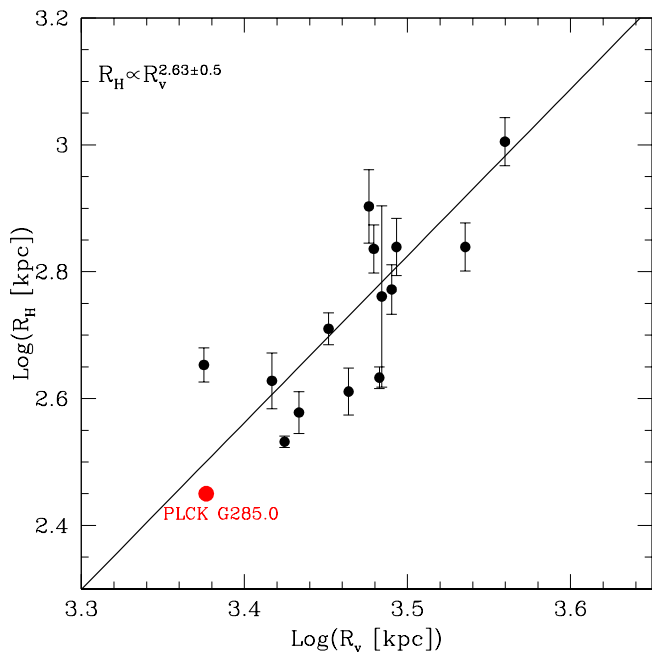


**Fig. 7.** Correlation between radio halo sizes and the virial radius of their host clusters (see Cassano et al. 2007). The newly detected radio halo in PLCK G285.0-23.7 is indicated in red.

2013). For most of their lifetimes these systems are expected to be “off-state” (i.e. under-luminous) or in the region spanned by the correlation leading to an apparent bimodality (e.g. Brunetti et al. 2009; Cassano et al. 2013). In this respect under-luminous systems are expected to be generally associated with both young or old mergers (Donnert et al. 2013); naively PLCK G285.0-23.7 could be in one of these stages. On the other hand the spectrum of radio halos also plays a role, with ultra-steep-spectrum radio halos, which are expected in less powerful mergers and at higher redshift (as a result of stronger IC losses), being statistically under-luminous (Cassano et al. 2006; Brunetti et al. 2008; Cassano et al. 2010) (see Fig. 6).

The new generation of more sensitive radio telescopes will allow us to discriminate between these two possible scenarios in the case of PLCK G285.0-23.7 and similarly weak radio loud clusters through deeper multi-frequency radio observations.

*Acknowledgements.* We thank the referee for providing constructive comments and help in improving the contents of this paper. We warmly thank Gianluca Castignani for very useful discussions and Gabriel Pratt, Monique Arnaud, and Iacopo Bartalucci for supplying the X-ray images. GMA is supported by the Erasmus Mundus Joint Doctorate Program by Grants Number 2013-1471 from the agency EACEA of the European Commission. GMA, CF, and MJ-H acknowledge financial support from *Programme National Cosmologie et Galaxies (PNCG)* and *Université de Nice-Sophia Antipolis – Programme Professeurs Invités 2015*. MJ-H acknowledges the Marsden Fund administered by the Royal Society of New Zealand on behalf of the Ministry of Business, Innovation and Employment. LP is funded via Marsden Funding to MJ-H. The Australia Telescope Compact Array is part of the Australia Telescope National Facility, which is funded by the Australian Government for operation as a National Facility managed by CSIRO. The results of this paper are partially based on data retrieved from the ESA Planck Legacy Archive, NASA SkyView, and the Hubble Legacy Archive, which is a collaboration between the Space Telescope Science Institute (STScI/NASA), the Space Telescope European Coordinating Facility (ST-ECF/ESA), and the Canadian Astronomy Data Centre (CAD/C/NRC/CSA).

## References

Akritas, M. G. & Bershadsky, M. A. 1996, *ApJ*, 470, 706

- Bacchi, M., Feretti, L., Giovannini, G., & Govoni, F. 2003, *A&A*, 400, 465  
 Basu, K. 2012, *MNRAS*, 421, L112  
 Bonafede, A., Brüggén, M., van Weeren, R., et al. 2012, *MNRAS*, 426, 40  
 Bonafede, A., Intema, H., Brüggén, M., et al. 2015, *MNRAS*, 454, 3391  
 Bonafede, A., Intema, H. T., Brüggén, M., et al. 2014, *MNRAS*, 444, L44  
 Brunetti, G., Cassano, R., Dolag, K., & Setti, G. 2009, *A&A*, 507, 661  
 Brunetti, G., Giacintucci, S., Cassano, R., et al. 2008, *Nature*, 455, 944  
 Brunetti, G. & Jones, T. W. 2014, *International Journal of Modern Physics D*, 23, 30007  
 Brunetti, G. & Lazarian, A. 2016, *MNRAS*, 458, 2584  
 Brunetti, G., Setti, G., Feretti, L., & Giovannini, G. 2001, *MNRAS*, 320, 365  
 Cassano, R., Brunetti, G., & Setti, G. 2006, *MNRAS*, 369, 1577  
 Cassano, R., Brunetti, G., Setti, G., Govoni, F., & Dolag, K. 2007, *MNRAS*, 378, 1565  
 Cassano, R., Etori, S., Brunetti, G., et al. 2013, *ApJ*, 777, 141  
 Cassano, R., Etori, S., Giacintucci, S., et al. 2010, *ApJ*, 721, L82  
 Clarke, T. E. & Ensslin, T. 2006, *Astronomische Nachrichten*, 327, 553  
 Cuciti, V., Cassano, R., Brunetti, G., et al. 2015, *A&A*, 580, A97  
 Dallacasa, D., Brunetti, G., Giacintucci, S., et al. 2009, *ApJ*, 699, 1288  
 Donnert, J., Dolag, K., Brunetti, G., & Cassano, R. 2013, *MNRAS*, 429, 3564  
 Farnsworth, D., Rudnick, L., Brown, S., & Brunetti, G. 2013, *ApJ*, 779, 189  
 Feretti, L., Fusco-Femiano, R., Giovannini, G., & Govoni, F. 2001, *A&A*, 373, 106  
 Feretti, L., Giovannini, G., Govoni, F., & Murgia, M. 2012, *A&A Rev.*, 20, 54  
 Giacintucci, S., Dallacasa, D., Venturi, T., et al. 2011, *A&A*, 534, A57  
 Giacintucci, S., Kale, R., Wik, D. R., Venturi, T., & Markevitch, M. 2013, *ApJ*, 766, 18  
 Giacintucci, S., Venturi, T., Cassano, R., Dallacasa, D., & Brunetti, G. 2009, *ApJ*, 704, L54  
 Giovannini, G., Bonafede, A., Feretti, L., et al. 2009, *A&A*, 507, 1257  
 Giovannini, G. & Feretti, L. 2000, *New A*, 5, 335  
 Govoni, F., Feretti, L., Giovannini, G., et al. 2001, *A&A*, 376, 803  
 Govoni, F., Murgia, M., Feretti, L., et al. 2005, *A&A*, 430, L5  
 Kempner, J. C. & Sarazin, C. L. 2001, *ApJ*, 548, 639  
 Kim, K.-T., Kronberg, P. P., Dewdney, P. E., & Landecker, T. L. 1990, *ApJ*, 355, 29  
 Liang, H., Hunstead, R. W., Birkinshaw, M., & Andreani, P. 2000, *ApJ*, 544, 686  
 Lindner, R. R., Baker, A. J., Hughes, J. P., et al. 2014, *ApJ*, 786, 49  
 Macario, G., Intema, H. T., Ferrari, C., et al. 2014, *A&A*, 565, A13  
 Macario, G., Markevitch, M., Giacintucci, S., et al. 2011, *ApJ*, 728, 82  
 Miniati, F. 2015, *ApJ*, 800, 60  
 Mohan, N. & Rafferty, D. 2015, *PyBDSM: Python Blob Detection and Source Measurement*, *Astrophysics Source Code Library*  
 Murgia, M., Govoni, F., Markevitch, M., et al. 2009, *A&A*, 499, 679  
 Norris, R. P., Afonso, J., Bacon, D., et al. 2013, *PASA*, 30, e020  
 Norris, R. P., Hopkins, A. M., Afonso, J., et al. 2011, *PASA*, 28, 215  
 Petrosian, V. 2001, *ApJ*, 557, 560  
 Planck Collaboration, Ade, P. A. R., Aghanim, N., et al. 2015, *ArXiv e-prints* [arXiv:1502.01598]  
 Planck Collaboration, Aghanim, N., Arnaud, M., et al. 2011, *A&A*, 536, A9  
 Sault, R. J., Teuben, P. J., & Wright, M. C. H. 1995, in *Astronomical Society of the Pacific Conference Series*, Vol. 77, *Astronomical Data Analysis Software and Systems IV*, ed. R. A. Shaw, H. E. Payne, & J. J. E. Hayes, 433  
 Shakouri, S., Johnston-Hollitt, M., & Pratt, G. W. 2016, *MNRAS*  
 Shimwell, T. W., Brown, S., Feain, I. J., et al. 2014, *MNRAS*, 440, 2901  
 Shimwell, T. W., Markevitch, M., Brown, S., et al. 2015, *MNRAS*, 449, 1486  
 Steer, D. G., Dewdney, P. E., & Ito, M. R. 1984, *A&A*, 137, 159  
 Vacca, V., Govoni, F., Murgia, M., et al. 2011, *A&A*, 535, A82  
 van Weeren, R. J., Brüggén, M., Röttgering, H. J. A., et al. 2011, *A&A*, 533, A35  
 van Weeren, R. J., Fogarty, K., Jones, C., et al. 2013, *ApJ*, 769, 101  
 van Weeren, R. J., Röttgering, H. J. A., Brüggén, M., & Cohen, A. 2009, *A&A*, 505, 991  
 Venturi, T., Giacintucci, S., Dallacasa, D., et al. 2013, *A&A*, 551, A24

**Table 4.** Collection of clusters known to host a giant radio halo (see Sect. 3.2). Clusters marked with <sup>U</sup> host USS radio halos. Col. 1: Cluster name; Col. 2: SZ mass proxy ( $M_{500}$ ) from the last PSZ2 Planck cluster catalog (Planck Collaboration et al. 2015); Col. 3: Redshift from PSZ2 Planck cluster catalog (Planck Collaboration et al. 2015); Col. 4: Radio flux density at frequency given in Col. 5; Col. 6: Radio Power at 1.4 GHz; Col. 7: References to the radio flux density.

Name	$M_{SZ}$ ( $\times 10^{14} M_{\odot}$ )	$z$	Flux density (mJy)	Freq. (GHz)	Power at 1.4 GHz ( $\times 10^{24} WHz^{-1}$ )	References
A209	$8.4642^{+0.2837}_{-0.3160}$	0.206	$16.9 \pm 1$	1.4	$2.19 \pm 0.17$	1
A520	$7.8003^{+0.4033}_{-0.4131}$	0.203	$34.4 \pm 1.5$	1.4	$4.65 \pm 0.63$	2
A521 <sup>U</sup>	$7.2556^{+0.4743}_{-0.4887}$	0.2475	$6.4 \pm 0.6$	1.4	$1.44 \pm 0.14$	3
A545	$5.3940^{+0.4059}_{-0.4098}$	0.154	$23 \pm 1$	1.4	$1.55 \pm 0.09$	4
A665	$8.8590^{+0.3230}_{-0.3202}$	0.1818	$43.1 \pm 2.2$	1.4	$4.03 \pm 0.28$	5
A697 <sup>U</sup>	$10.9984^{+0.3716}_{-0.3671}$	0.282	$5.2 \pm 0.5$	1.4	$1.53 \pm 0.15$	6
A746	$5.3352^{+0.3917}_{-0.4028}$	0.2323	$18 \pm 4$	1.382	$3.03 \pm 0.69$	6
A754 <sup>U</sup>	$6.8539^{+0.1249}_{-0.1277}$	0.0542	$83 \pm 5$	1.4	$0.60 \pm 0.04$	7
A773	$6.8474^{+0.3362}_{-0.3110}$	0.2172	$12.7 \pm 1.3$	1.4	$2.50 \pm 0.36$	2
A1300 <sup>U</sup>	$8.9713^{+0.4587}_{-0.4537}$	0.3075	$130 \pm 10$	0.325	$3.55 \pm 0.35$	8
A1351	$6.8676^{+0.3799}_{-0.3812}$	0.322	$32.4 \pm 3.2$	1.4	$11.97 \pm 1.51$	9
A1656	$7.1652^{+0.0674}_{-0.1073}$	0.0231	$720 \pm 130$	1.0	$0.69 \pm 0.13$	10
A1689	$8.7689^{+0.3368}_{-0.3368}$	0.1832	$91.6 \pm 2.7$	1.2	$7.46 \pm 0.52$	11
A1758	$8.2173^{+0.2727}_{-0.2824}$	0.2799	$16.7 \pm 0.8$	1.4	$4.42 \pm 0.37$	1
A1914	$7.2358^{+0.2582}_{-0.2612}$	0.1712	$64 \pm 3$	1.4	$5.91 \pm 0.38$	4
A1995	$4.9242^{+0.3773}_{-0.3691}$	0.3179	$4.1 \pm 0.7$	1.4	$1.47 \pm 0.28$	1
A2034	$5.8503^{+0.2294}_{-0.2337}$	0.113	$13.6 \pm 1.0$	1.4	$0.46 \pm 0.04$	1
A2163	$16.1164^{+0.2968}_{-0.2922}$	0.203	$155 \pm 2$	1.4	$20.58 \pm 1.17$	12
A2219	$11.6918^{+0.2500}_{-0.2743}$	0.228	$81 \pm 4$	1.4	$12.24 \pm 0.65$	4
A2254	$5.5870^{+0.3597}_{-0.3548}$	0.178	$33.7 \pm 1.8$	1.4	$3.14 \pm 0.22$	2
A2255	$5.3828^{+0.0586}_{-0.0612}$	0.0809	$56 \pm 3$	1.4	$0.93 \pm 0.06$	13
A2256	$6.2107^{+0.1012}_{-0.0915}$	0.0581	$103.4 \pm 1.1$	1.4	$0.87 \pm 0.02$	14
A2294	$5.9829^{+0.3671}_{-0.3741}$	0.178	$5.8 \pm 0.5$	1.4	$0.54 \pm 0.05$	1
A2319	$8.7351^{+0.1132}_{-0.1240}$	0.0557	$328 \pm 28$	1.4	$2.45 \pm 0.21$	15
A2744	$9.8356^{+0.3947}_{-0.3754}$	0.3066	$57.1 \pm 2.9$	1.4	$19.28 \pm 2.76$	2
A3411	$6.5925^{+0.3094}_{-0.3106}$	0.1687	$4.8 \pm 0.5$	1.4	$0.38 \pm 0.04$	16
A3888	$7.1948^{+0.2639}_{-0.2590}$	0.151	$27.57 \pm 3.13$	1.867	$1.89 \pm 0.22$	17
PLCKG285.0-23.7	$8.3925^{+0.3332}_{-0.3404}$	0.39	$2.02 \pm 0.25$	1.867	$1.72 \pm 0.22$	18
PLCKG171.9-40.7 <sup>U</sup>	$10.7102^{+0.4931}_{-0.4963}$	0.27	$18 \pm 2$	1.4	$4.98 \pm 0.58$	19
RXCJ0949.8+1708	$8.2387^{+0.4644}_{-0.4561}$	0.38	$21.0 \pm 2.2$	0.323	$1.75 \pm 0.76$	20
RXCJ0107.7+5408	$5.8478^{+0.3030}_{-0.3117}$	0.1066	$55 \pm 5$	1.382	$1.62 \pm 0.15$	6
RXCJ1514.9-1523	$8.8607^{+0.4054}_{-0.4578}$	0.2226	$102 \pm 9$	0.327	$1.56 \pm 0.48$	21
RXCJ2003.5-2323	$8.9919^{+0.4444}_{-0.4885}$	0.3171	$35 \pm 2$	1.4	$12.54 \pm 0.75$	9
MACSJ1149.5+2223 <sup>U</sup>	$10.4178^{+0.5207}_{-0.5451}$	0.545	$29 \pm 4$	0.323	$2.54 \pm 1.22$	22
MACSJ0717.5+3745	$11.4871^{+0.5347}_{-0.5482}$	0.546	$41.5 \pm 4.1$	1.4	$51.45 \pm 8.43$	23

Table 4. continued.

Name	$M_{SZ}$ ( $\times 10^{14} M_{\odot}$ )	$z$	Flux density (mJy)	Freq. (GHz)	Power at 1.4 GHz ( $\times 10^{24} WHz^{-1}$ )	References
MACSJ1752.0+4440	$6.7475^{+0.4377}_{-0.4543}$	0.366	$164 \pm 13$	0.323	$11.84 \pm 1.56$	22
MACSJ0553.4-3342	$8.7720^{+0.4399}_{-0.4629}$	0.431	$62 \pm 5$	0.323	$6.87 \pm 2.96$	22
CIZAJ1938.3+5409	$7.5779^{+0.2876}_{-0.2809}$	0.26	$11.0 \pm 1.2$	0.323	$0.36 \pm 0.16$	20
CL0016+16	$9.7937^{+0.5293}_{-0.5314}$	0.5456	$5.5 \pm 0.5$	1.4	$7.43 \pm 1.63$	5
1E0657-56	$13.1003^{+0.2874}_{-0.2931}$	0.2965	$78 \pm 5$	1.4	$23.68 \pm 2.30$	24
El Gordo	$10.7536^{+0.4781}_{-0.4721}$	0.87	$2.43 \pm 0.18$	2.1	$10.20 \pm 0.99$	25

**References.** (1) Giovannini et al. (2009); (2) Govoni et al. (2001); (3) Dallacasa et al. (2009); (4) Bacchi et al. (2003); (5) Giovannini & Feretti (2000); (6) van Weeren et al. (2011); (7) Macario et al. (2011); (8) Venturi et al. (2013); (9) Giacintucci et al. (2009); (10) Kim et al. (1990); (11) Vacca et al. (2011); (12) Feretti et al. (2001); (13) Govoni et al. (2005); (14) Clarke & Ensslin (2006); (15) Farnsworth et al. (2013); (16) van Weeren et al. (2013); (17) Shakouri et al. (2016); (18) This paper; (19) Giacintucci et al. (2013); (20) Bonafede et al. (2015); (21) Giacintucci et al. (2011); (22) Bonafede et al. (2012); (23) van Weeren et al. (2009); (24) Liang et al. (2000); (25) Lindner et al. (2014).

## Appendix A: Detection of the source using PyBDSM

The use of packages for the automatic detection of radio sources is becoming more and more necessary and common, especially in the era of the new generation of deep and wide radio surveys that will ultimately bring to the SKA a revolutionary view of the long-wavelength sky (see e.g. Norris et al. 2013). In this framework, and in order to get a complementary measure of the total flux density of the diffuse radio source, we ran the automatic source finder PyBDSM (Mohan & Rafferty 2015) on the tapered images with and without point source subtraction from the uv-data. It is worth noting that PyBDSM finds significant emission in both maps, corresponding to the diffuse radio source that we found by visual inspection and analysis on the maps (see e.g. Fig. A.1).

We used the threshold technique of the PyBDSM `process_image` task<sup>2</sup>, which locates islands of emission above some multiple of the noise in the image (`thresh_isl` parameter, set to  $3\sigma$  here). This determines the region where fitting is done. In addition, we set to  $5\sigma$  the source detection threshold in number of sigma above the mean (`thresh_pix` parameter). Finally, we activated the wavelet module of `process_image` (i.e. `atrous_do=True`), which improves the detection of diffuse sources by doing wavelet transforms at increasing scales of the residual image after subtraction of the initial fitted Gaussians. The modelled Gaussians are shown in the bottom right panel of Fig. A.1, while the top right panel shows the islands of significant emission (cyan) and the position of the fitted Gaussians. Violet ellipses indicate the sources identified on the input radio map (top left), while the red empty ellipse shows the extended source recovered through the wavelet analysis. As shown in the residual maps (bottom left), we nicely managed to fit most of the source components, in particular the central diffuse source.

The final output catalogs of PyBDSM give a list of all the Gaussian functions fitted to model the significant emission within the input radio maps and give a source list where different Gaussians are grouped together if they satisfy objective criteria to be considered as a single source. For each detected source, PyBDSM provides the values of the FWHM of the major and minor axis and the total integrated Stokes I flux density. To subtract the contribution of point sources in the ID2ss case reported in Table 3, we ran PyBDSM on the full-resolution Block 3 image of the cluster. The flux densities of compact sources obtained in this way and contained within the cyan region of Fig. A.1 were then subtracted from the total flux density of the diffuse source obtained in the ID 2 case.

The size and flux density of the newly detected radio halo are given as an output of PyBDSM, being  $5.76 \text{ arcmin} \times 4.34 \text{ arcmin}$  ( $914 \text{ kpc} \times 689 \text{ kpc}$ ) and  $4.91 \pm 0.04 \text{ mJy}$  for the map with ID1. In the case of ID2 and ID2ss, we obtained a halo size of  $4.48 \text{ arcmin} \times 2.70 \text{ arcmin}$ , and flux densities of  $4.08 \pm 0.07 \text{ mJy}$  and  $3.72 \pm 0.16 \text{ mJy}$ , respectively.

We note here that, compared to classical measurements performed “by hand” (Sect. 3.1 and Table 3), PyBDSM gives systematically higher values of both source sizes and total flux densities. This is because with classical methods we integrate the surface brightness of the diffuse source within a region delimited by the  $3\sigma$  contours, while this same region is used by PyBDSM as a support to fit one (or multiple) Gaussian function(s) giving the total flux density of the source(s) whose size is reconstructed based on moment analysis. This last method tends to include flux

density coming from regions outside the original islands of significant emission, in particular when the wavelet module, which decomposes the residual image that results from the normal fitting of Gaussians into wavelet images of various scales, is activated<sup>3</sup>.

Both methods are based on different assumptions. In the case of classical “by-hand” measurements, for instance, it is assumed that the mean value of the surface brightness of all pixels within  $3\sigma$  contours multiplied by the number of synthesised beams within the considered region is a proper measurements of the integrated flux density for the whole RH. Instead, in the case of PyBDSM, it is assumed that sources are correctly modelled by one or more Gaussian functions of increasing size. We do not conclude that one method is better than the other since they are based on different approaches, but we definitely recommend not directly comparing results obtained through a mix of the two different methods when producing plots such as our Fig. 6.

<sup>2</sup> See [http://www.astron.nl/citt/pybdsm/process\\_image.html#general-reduction-parameters](http://www.astron.nl/citt/pybdsm/process_image.html#general-reduction-parameters) for detailed instructions of `process_image`.

<sup>3</sup> `atrous_do` parameter set to `True`. See [http://www.astron.nl/citt/pybdsm/process\\_image.html#a-trous-wavelet-decomposition-module](http://www.astron.nl/citt/pybdsm/process_image.html#a-trous-wavelet-decomposition-module)

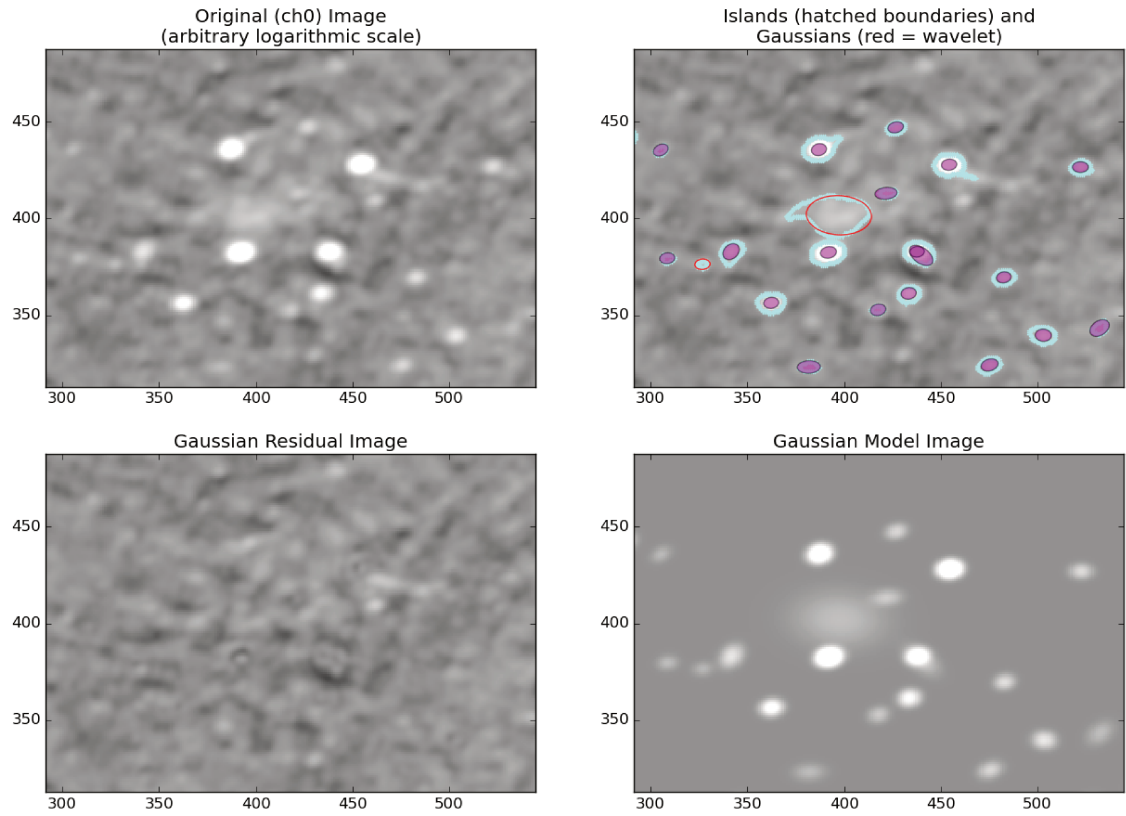


**Fig. A.1.** Output of the PyBDSM source finder tool. The axis units are in pixels. From *left to right* and from *top to bottom*: Original image on which PyBDSM is run (in this example, the ID2 map of Table 3); islands of significant emission (cyan contours) and fitted Gaussians that model identified sources overlaid on the ID2 map; residual after the subtraction of the fitted sources; model of the reconstructed sky. The big red ellipse corresponds to the diffuse emission in the centre of the cluster.

**C.2 ATCA observations of the MACS-Planck Radio Halo Cluster Project II. Radio observations of intermediate redshift ATCA cluster sample**

# ATCA observations of the MACS-Planck Radio Halo Cluster Project

## II. Radio observations of an intermediate redshift cluster sample

G. Martinez Aviles,<sup>1,\*</sup> M. Johnston-Hollitt<sup>2,3</sup>, C. Ferrari<sup>1</sup>, T. Venturi<sup>4</sup>, J. Democles<sup>5</sup>, D. Dallacasa<sup>6,4</sup>, R. Cassano<sup>4</sup>, G. Brunetti<sup>4</sup>, S. Giacintucci<sup>7</sup>, G. W. Pratt<sup>5</sup>, M. Arnaud<sup>5</sup>, N. Aghanim<sup>8</sup>, S. Brown<sup>9</sup>, M. Douspis<sup>8</sup>, J. Hurier<sup>8</sup>, H. T. Intema<sup>10</sup>, M. Langer<sup>8</sup>, G. Macario<sup>1</sup>, and E. Pointecouteau<sup>11,12</sup>

<sup>1</sup> Université Côte d'Azur, Observatoire de la Côte d'Azur, CNRS, Laboratoire Lagrange, Bd de l'Observatoire, CS 34229, 06304 Nice cedex 4, France

<sup>2</sup> School of Chemical & Physical Sciences, Victoria University of Wellington, PO Box 600, Wellington 6140, New Zealand

<sup>3</sup> Peripety Scientific Ltd., PO Box 11355 Manners Street, Wellington 6142, New Zealand

<sup>4</sup> INAF- Istituto di Radioastronomia, via P. Gobetti 101, I-40129, Bologna, Italy

<sup>5</sup> Laboratoire AIM, IRFU/Département d'Astrophysique – CEA/DRF – CNRS – Université Paris Diderot, Bât. 709, CEA-Saclay, 91191 Gif-sur-Yvette Cedex, France

<sup>6</sup> Department of Physics and Astronomy, UniBO, Via Gobetti 93/2, I-40129 Bologna, Italy

<sup>7</sup> Naval Research Laboratory, 4555 Overlook Avenue SW, Code 7213, Washington, DC 20375, USA

<sup>8</sup> Institut d'Astrophysique Spatiale, CNRS, Univ. Paris-Sud, Université Paris-Saclay, Bât. 121, 91405 Orsay cedex, France

<sup>9</sup> Department of Physics & Astronomy, University of Iowa

<sup>10</sup> Leiden Observatory, Leiden University, Niels Bohrweg 2, NL-2333CA, Leiden, The Netherlands

<sup>11</sup> CNRS; IRAP; 9 Av. colonel Roche, BP 44346, F-31028 Toulouse cedex 4, France

<sup>12</sup> Université de Toulouse; UPS-OMP; IRAP; Toulouse, France

To be submitted

### ABSTRACT

**Aims.** A fraction of galaxy clusters host diffuse radio sources whose origin is investigated through multi-wavelength studies of cluster samples. We investigate the presence of diffuse radio emission in a sample of 7 galaxy clusters in the largely unexplored intermediate redshift range ( $0.3 < z < 0.44$ ).

**Methods.** In search for diffuse emission, deep radio imaging of the clusters are presented from wide band (1.1-3.1 GHz), full resolution ( $\sim 5$  arcsec) observations with the Australia Telescope Compact Array (ATCA). The visibilities are also imaged at lower resolution after point source modelling and subtraction and after a taper is applied in order to achieve better sensitivity to low surface brightness diffuse radio emission. In case of non-detection of diffuse sources, we set upper limits for the radio power of injected diffuse radio sources in the field of our observations. Furthermore, we discuss the dynamical state of the observed clusters based on a X-ray morphological analysis with XMM-Newton.

**Results.** We detect a giant Radio Halo in PSZ2 G284.97-23.69 ( $z=0.39$ ) and a possible diffuse source in the nearly relaxed cluster PSZ2 G262.73-40.92 ( $z=0.421$ ). Our sample contains three highly disturbed massive clusters without clear traces of diffuse emission at the observed frequencies. We were able to inject modelled radio halos with low values of total flux density to set upper detection limits, however, with our high-frequency observations we cannot exclude the presence of RH in these systems because of the sensitivity of our observations in combination with the high  $z$  of the observed clusters.

**Key words.** galaxies: clusters: general – galaxies: clusters: individual: PSZ2 G284.97-23.69, PSZ2 G285.63-17.23, PSZ2 G262.73-40.92, PSZ2 G277.76-51.74, PSZ2 G286.28-38.36, PSZ2 G271.18-30.95, PLCK G334.8-38.0 – galaxies: clusters: intracluster medium radiation mechanisms: non-thermal – radio: continuum: galaxies

## 1. Introduction

Observations of diffuse synchrotron radio emission in clusters of galaxies provide evidence of the interactions between ultra-relativistic particles and magnetic fields in the Intra Cluster Medium (ICM). At present, there are three main classes of large-scale diffuse radio emission in clusters; relics, haloes and mini-haloes.

Radio relics are large ( $\sim 1$  Mpc) polarized diffuse sources generally elongated in shape, present in the peripheral regions surrounding galaxy clusters. The mechanism responsible for their creation is associated with shocks generated in the ICM

caused by a merger (Brunetti & Jones 2014), although recently some relic-radio galaxy association has been discovered (see e.g. van Weeren et al. 2017). Radio mini-haloes are much smaller ( $\sim 100 - 500$  kpc) roundish sources present in cool-core clusters (Giacintucci et al. 2017), surrounding a radio-loud active galactic nucleus (AGN) present in the brightest cluster galaxy (BCG) (Govoni et al. 2009). The origin of mini-haloes is explained by a population of relativistic particles re-accelerated in the turbulence generated in the ICM by the mechanically-powerful AGN or by gas sloshing in the cluster cool core (Mazzotta & Giacintucci 2008), although these explanations are still debated.

Finally, radio halos (RHs) are Mpc-scale, low-surface brightness radio sources observed to be centered in galaxy clusters,

\* Gerardo.Martinez-Aviles@oca.eu

**Table 1.** Information of the clusters of the MACS-Planck RHCP ATCA sample. The names and alternative names of the clusters appear in Cols. 1 and 2. RA and DEC correspond to the coordinates for centring the ATCA observations (Cols. 3 and 4). The Planck Mass, X-ray luminosity and Redshift (Cols. 5, 6 and 7, respectively) are taken from Planck Collaboration et al. (2016). ★ See Sect. 2 for a deeper discussion on PLCK G334.8-38.0.

Cluster name	Alternative name(s)	RA (h m s)	DEC (° ' ")	$M_{500}$ (SZ) ( $\times 10^{14} M_{\odot}$ )	$L_{500}$ ( $\times 10^{44}$ erg/s)	Redshift
PSZ2 G285.63-17.23	PSZ1 G285.62-17.23 PLCK G285.6-17.2	08 43 44.40	-71 13 14.00	6.64±0.40	4.45±0.08	0.35
PSZ2 G262.73-40.92	PSZ1 G262.72-40.92 SPT-CLJ0438-5419 ACT-CL J0438-5419 PLCK G262.7-40.9	04 38 17.20	-54 19 25.10	7.46±0.36	9.94±0.47	0.421
PSZ2 G277.76-51.74	PSZ1 G277.75-51.71 SPT-CLJ0254-5857 PLCK G277.8-51.7	02 54 16.70	-58 56 44.00	9.69±0.38	9.46±0.07	0.438
PSZ2 G286.28-38.36	PSZ1 G286.27-38.39 PLCK G286.3-38.4	03 59 10.20	-72 04 46.10	5.94±0.40	4.07±0.02	0.307
PSZ2 G271.18-30.95	PSZ1 G271.18-30.95 SPT-CLJ0549-6205 PLCK G271.2-31.0	05 49 19.50	-62 05 16.00	7.37±0.32	18.95±0.16	0.37
PSZ2 G284.97-23.69	PLCKESZ G284.99-23.70 PLCK G285.0-23.7	07 23 18.40	-73 27 20.60	8.39±0.34	16.91±0.27	0.39
PLCK G334.8-38.0★	-	20 52 16.80	-61 12 29.40	-	-	0.35

with similar morphologies to the X-ray emission. Giant RH are the focus of this paper. In recent years, the knowledge of the origin of RHs has moved towards a general consensus. The generally accepted scenario for the mechanism responsible of this kind of diffuse emission is the re-acceleration of relativistic electrons by the large scale turbulence generated in cluster mergers (see e.g. Brunetti et al. 2001; Petrosian 2001; Brunetti & Jones 2014). In agreement with this model, it is known that RHs tend to occur more frequently in massive galaxy clusters (see Cuciti et al. 2015, for a recent discussion), and most of them show evidence of being merging systems. Moreover, a series of scaling relations between the thermal and non-thermal properties of galaxy clusters ( $P_{1.4}$ - $L_x$ ,  $P_{1.4}$ -Mass,  $P_{1.4}$ - $Y_{500}$ ; where  $P_{1.4}$  and  $Y_{500}$  are, respectively, the radio power of haloes at 1.4 GHz and the cluster integrated Sunyaev-Zel'dovich (SZ) signal within  $R_{500}^1$ ) have also been found (see e.g. Basu 2012; Cassano et al. 2013). The connection between mergers and the presence of a RH depends on a complex combination of mechanisms and energy budgets. There are a few cases reported in the literature of the presence of RHs in cool-core clusters, or clusters being minor mergers (see e.g. Kale & Parekh 2016; Bonafede et al. 2014, 2015; Sommer et al. 2017), and there is also evidence of merging clusters without detected RHs (Cassano et al. 2010; Russell et al. 2011).

Fundamental questions about the micro-physics of electron acceleration and transport mechanisms need still to be answered to characterise the non-thermal physics of clusters. Statistical studies of RHs and their host systems can shed light on the mechanisms needed to complete the picture of the physics of RHs

<sup>1</sup>  $R_{500}$  is the radius at which the mean mass density is 500 times the critical density at the cluster redshift.

and their connection with cluster mergers. Current knowledge of RHs is mostly based on high mass galaxy cluster samples. An important study on RH occurrence is the Giant Metrewave Radio Telescope (GMRT) Radio Halo Survey (GRHS) (Venturi et al. 2007, 2008) and the extended sample (E-GRHS) (Kale et al. 2013, 2015), with the aim of exploring the origin and occurrence of RHs, as well as their connection with the dynamical state of the host systems. The authors picked galaxy clusters with a redshift range  $z = 0.2-0.4$ , X-ray luminosities  $L_x$  (0.1-2.4 keV)  $> 5 \times 10^{44}$  erg s<sup>-1</sup> and declinations  $\delta > -31^\circ$  to ensure a good uv-coverage with the GMRT. This sample is however effectively limited to  $z < 0.33$ . Mass-based selections are motivated by the assumption that the selection of high X-ray luminosity merging systems have more chances of detection of diffuse radio sources. To start filling this observational gaps, previous works investigated the presence of diffuse radio emission with an unbiased sample on X-ray morphology and in a wide range of masses (Shakouri et al. 2016, Shakouri et al. submitted).

Although a number RHs have been discovered at  $z > 0.3$ , a complete statistical sample is missing in this redshift regime (see Feretti et al. 2012). On the other hand, it is expected from models (see Cassano et al. 2004, 2006) that a larger fraction of RH occurrence may appear at  $z=0.3-0.4$ . This is simply because most of the energy budget in the hierarchical grow of clusters is dissipated via massive mergers in this redshift range. In this paper, we present the results of a series of radio observations of seven galaxy clusters in this redshift regime performed with the ATCA telescope, together with an X-ray analysis of the dynamical status of the target clusters.

This work is organized in the following way: Sect. 2 describes the criteria for the sample selection. In Sect. 3 we present

the observations together with the data reduction and the image reconstruction strategy. The analysis of the high resolution, tapered and compact source subtracted radio images appears in Sect. 4. In Sect. 5 we present the X-ray morphological analysis of the cluster sample. The results of the paper appear in Sect. 6. Finally, the discussion and conclusions are presented in Sect. 7. Throughout this paper, we adopt the  $\Lambda$ CDM cosmology with the values  $H_0=70 \text{ km s}^{-1} \text{ Mpc}^{-1}$ ,  $\Omega_M=0.3$ ,  $\Omega_\Lambda=0.7$ .

## 2. Sample selection

This paper presents the results of a sub-sample of the MACS-Planck Radio Halo Cluster Project (RHCP). The project was conceived as a continuation of the E-GRHS project (see Sect. 1) by extending the statistics of RHs up to  $z=0.45$ . The Macs-Planck RHCP consists of a total 48 galaxy clusters, all of them taken from the MACS Brightest Cluster X-ray catalogue (Ebeling et al. 2010) and the list of newly discovered Planck SZ clusters confirmed with the XMM-*Newton* validation program (available at the time of the proposal, see Planck Collaboration et al. 2011b). For the project, all the clusters from both samples that are located in the range  $z = 0.3-0.45$  were selected. In our sample we have a total of 33 MACS clusters and 15 Planck SZ clusters. The scope of this paper is to publish the analysis of the ATCA sub-sample. Information about the complete sample will appear in a forthcoming paper (Venturi et al., in prep.).

From the total number of selected clusters, 32 were lacking published radio information. The declination range of the sample required observations to be done with two different telescopes, depending on the declination of the targets. Based on the targets visibility and the uv-coverage constraints to achieve the desired sensitivities to detect diffuse radio emission, a threshold of  $\delta = -40^\circ$  was defined. This threshold divided the total sample into two groups:

a) Those lying in the range of  $\delta > -40^\circ$  (25 clusters in total) were observed with the GMRT at  $\sim 325 \text{ MHz}$ , and the results of these observations will appear in a forthcoming paper (Venturi et al., in prep.).

b) The remaining seven galaxy clusters ATCA observations are centred at 2.1 GHz with a bandwidth of 2000 MHz. Information about the clusters from the ATCA sample appears in Table 1. It is worth mentioning that it was a matter of pure chance that all the clusters observed with the ATCA were Planck clusters.

It is important to mention that the measurements of redshift and mass for PLCK G334.8-38.0 are quite challenging being a low-mass triple system. Having very poor X-ray statistics we can not analyse the system by proceeding in the same way we have done for the other clusters of the sample. We notice, however, that the mass of the components, even taken all together ( $M \sim 3.4 \times 10^{14} M_\odot$ ), is significantly lower than the typical mass of known radio loud systems.

## 3. Radio observations and data reduction

Radio observations of the ATCA sample were done with three separate array configurations for each observed cluster (Table 2) using the Compact Array Broadband Backend (CABB) correlator with a central frequency of 2.1 GHz and spanning 1.1-3.1 GHz (project ID C2679). Observations were carried out in continuum mode with the correlator set to produce  $2000 \times 1 \text{ MHz}$  channels. Details of the observations can be found in Table 2. The primary flux scale was set relative to the unresolved source

PKS B1934-638 for which the detailed spectral behaviour is well understood. The amplitude gain variations were checked during the calibration of each observation for each sub-band image so as to be not higher than  $\sim 2\%$ .<sup>2</sup>

Radio frequency interference (RFI) and bad channels were excised manually from primary and secondary calibrators, as well as the target, by using a combination of clipping algorithms and visual inspection via the MIRIAD task PGFLAG (Sault et al. 1995). It was necessary to perform calibration on narrower frequency intervals due to the nature of CABB data. After a number of trials, we determined that 4 sub-bands of  $\sim 500 \text{ MHz}$  produce the optimal results for these data. Thus, the target, primary and secondary calibrator data are divided into the required sub-bands coined Block 1 (from 2.631 GHz to 3.100 GHz), Block 2 (from 2.131 GHz to 2.630 GHz), Block 3 (from 1.631 GHz to 2.130 GHz) and Block 4 (from 1.130 GHz to 1.630 GHz). Each sub-band is then self-calibrated in MIRIAD by using the task SELF-CAL. Finally, the self-calibration solutions were saved by using the task UVAVER.

## 4. Radio analysis

### 4.1. High resolution images

Four images were created, one for each of the 4 sub-bands, out to the primary beam by using the task INVERT and a Steer CLEAN (Steer et al. 1984) was applied to all sources within the primary beam. The sub-band images were then convolved to a common size by application of a Gaussian corresponding to the lowest resolution image and then added together to create a final wide-band image (see Table 3). The noise levels in the sub-band images are very similar for the three highest bands and only differed slightly in the lowest frequency band; it was not necessary to weight the images relative to the sensitivities in the mosaicing process.

The radio contours of the central Mpc diameter area from our high resolution images are overlaid on the XMM-*Newton* X-ray images in Fig. 1 (yellow contours). In Figs. A.1 and A.2 we show the high resolution ATCA radio maps for the wide field and the zoomed cluster regions<sup>3</sup>. The final deep ATCA images root mean squared (rms) noise is measured with AIPS TVSTAT at the field centre in regions inside the primary beam without any trace of point sources or diffuse emission. The information of the images (rms noises and resolutions) is shown in Table 3. A visual inspection of the seven high resolution images does not reveal obvious presence of diffuse radio emission in the central area where the clusters of the sample lie.

### 4.2. Tapering and diffuse source search

We proceeded to subtract the compact radio sources from the uv-data. Using the self-calibrated data, we imaged the visibilities for the longest baselines (uv-range from 3.6 to 40  $k\lambda$ , which translates to angular scales from  $\sim 5$  to  $\sim 57$  arcseconds) and subtracted the corresponding clean components from the self-calibrated uv-data by using the MIRAD task UVMODEL. This creates a new uv-data set which was re-imaged. Again, none of the seven clusters showed the obvious presence of diffuse emission in the central area in the compact source subtracted high resolution images.

<sup>2</sup> see <http://www.atnf.csiro.au/observers/memos/d96783> 1.pdf.

<sup>3</sup> The high resolution images from PSZ2 G284.97-23.69 have been published in Martinez Aviles et al. (2016).

**Table 2.** Details of the observations towards the clusters selected for observations with ATCA. Cluster name (Col. 1); dates of observations (Col. 2) with different array configurations (Col. 3); Observation time (Col. 4); phase calibrator (Col. 5). The central frequency is at 2.1 GHz and the total observed bandwidth is 2 GHz.

Cluster name	Date	Config.	Observation time (min.)	Calibrator
PSZ2 G285.63-17.23	2015-Jun-12	1.5C	549	PKS B0606-795
	2012-Jun-29	750A	442	PKS B0606-795
	2012-Jun-07-08	6D	1132	PKS B0637-752
PSZ2 G262.73-40.92	2013-Mar-05	6A	353	PKS B0420-625
	2013-Feb-02	750C	354	PKS B0420-625
	2012-Nov-23	1.5C	354	PKS B0420-625
PSZ2 G277.76-51.74	2013-Sep-03-04	1.5A	1140	PKS B0302-623
	2013-Jul-31	750D	1061	PKS B0302-623
	2013-Aug-01	750D	152	PKS B0302-623
	2013-May-11-12	6C	1188	PKS B0302-623
PSZ2 G286.28-38.36	2013-Mar-05	6A	384	PKS B0252-712
	2012-Feb-02	750C	354	PKS B0252-712
	2012-Nov-23	1.5C	413	PKS B0252-712
PSZ2 G271.18-30.95	2013-Mar-05	6A	354	PKS B0420-625
	2013-Feb-02	750C	294	PKS B0420-625
	2012-Nov-23	1.5C	353	PKS B0420-625
PSZ2 G284.97-23.69	2012-Jun-08	6D	704	PKS B1036-697
	2012-Jun-09	6D	523	PKS B0606-795
	2012-Jun-29	750A	531	PKS B0606-795
	2013-Sep-06	1.5A	804	PKS B0606-795
PLCK G334.8-38.0	2013-Sep-03-04	1.5A	1131	PKS B0302-623
	2013-Jul-30	750D	1203	PKS B1934-638
	2013-May-12	6C	1297	PKS B1934-638

**Table 3.** Properties of the full resolution and the Block 3 compact source subtracted tapered 2000 MHz band-width radio maps centred at 2.1 GHz. The rms noise of the images appears in Col. 2, while the resolutions and position angles are shown in Cols. 3 and 4, respectively.

Cluster Name	rms noise ( $\mu$ Jy/beam)		Beam size ( $'' \times ''$ )		PA (deg)	
	Full resolution	Taper	Full resolution	Taper	Full resolution	Taper
PSZ2 G285.63-17.23	22.4	92	$6.85 \times 4.07$	$43 \times 17$	-8.13	89.07
PSZ2 G262.73-40.92	19.7	83	$6.39 \times 4.15$	$32 \times 25$	-2.45	-7.67
PSZ2 G277.76-51.74	15.4	65	$5.55 \times 4.25$	$35 \times 28$	1.99	58.04
PSZ2 G286.28-38.36	19.4	57	$5.00 \times 4.46$	$28 \times 26$	-11.00	-46.47
PSZ2 G271.18-30.95	22.1	74	$5.80 \times 4.21$	$31 \times 25$	-1.30	-28.70
PSZ2 G284.97-23.69	11.3	51	$5.20 \times 4.38$	$31 \times 23$	-42.31	-81.17
PLCK G334.8-38.0	16.1	71	$3.19 \times 2.20$	$34 \times 23$	9.96	2.96

In order to investigate the possible presence of low-surface brightness radio emission in the clusters, the point source subtracted visibilities were re-imaged with a robust=0.5 weighting and applying a  $\sim 9$  k $\lambda$  Gaussian taper. Traditionally, measurements of flux densities of RHs are reported at the central frequency of 1.4 GHz. It is worth mentioning that from the typical spectral behaviour of radio halos ( $\alpha \gtrsim 1$  synchrotron spectral index<sup>4</sup>) it is expected lower luminosities for higher frequencies. Because of its lower central frequency, the Block 4 sub-band would be ideal to do flux density measurements, but it is also strongly affected by RFI (50-60 % of the data was flagged).

<sup>4</sup> In this paper we use the convention  $S(\nu) \propto \nu^{-\alpha}$ , being  $S(\nu)$  the radio flux density.

In our images we have comparable rms sensitivities for the frequency range running from Block 3 to Block 1. This set of conditions makes Block 3 centred at  $\sim 1.9$  GHz the most suitable sub-band to do flux density measurements. In Table 3 we report the main features for the set of the source subtracted Block 3 tapered images.

In search of residual diffuse emission in the cluster areas we set the classical  $3\sigma$  contours in the compact source subtracted Block 3 tapered images. In some cases, we did find contours that correspond to positions of point sources visible in the high resolution maps, due to an imperfect point source subtraction or to the presence of some extended emission candidates (see Sect. 6). Radio images that showed no evidence of the presence

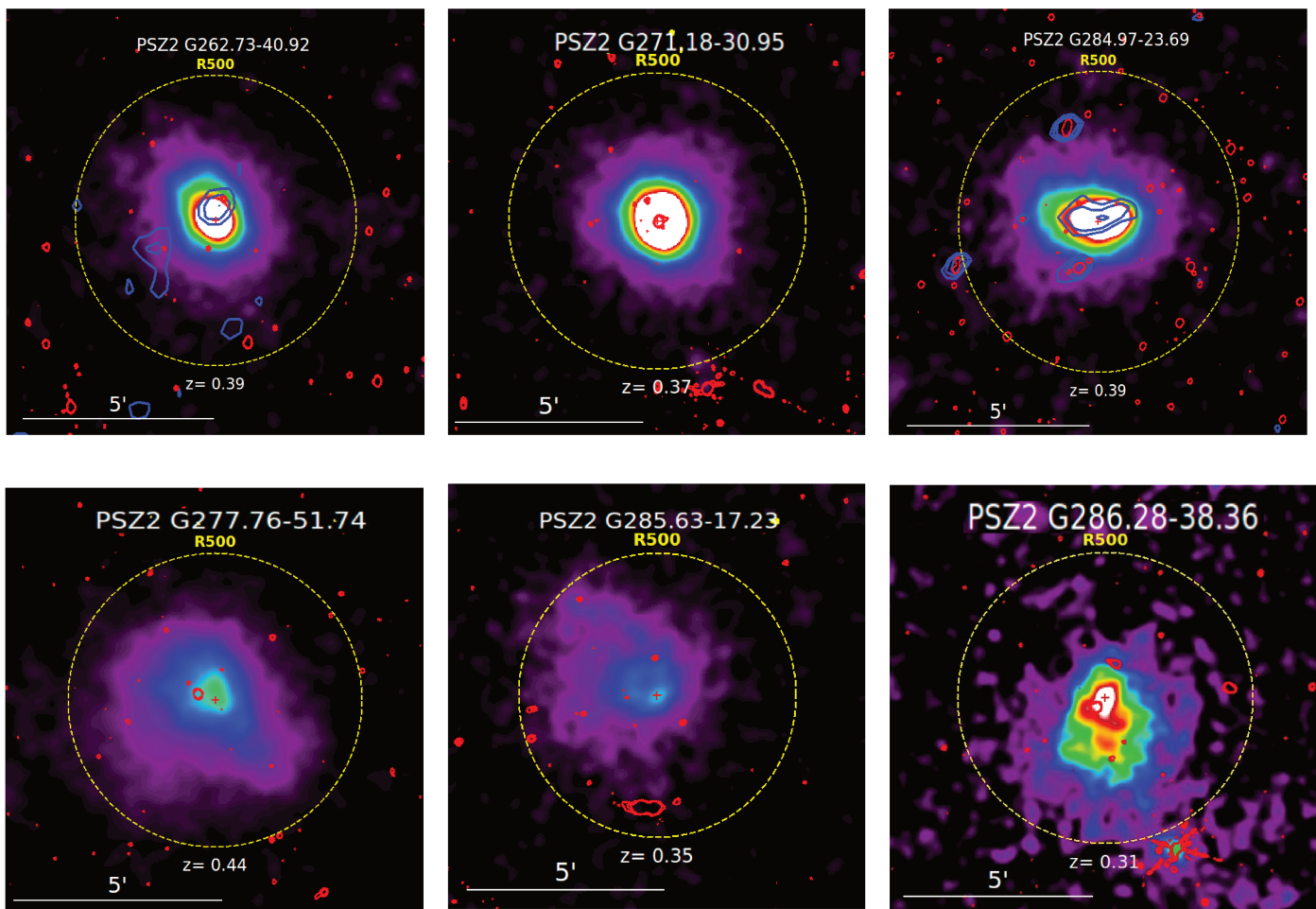


**Fig. 1.** XMM-Newton smoothed images in the [0.3-2] keV band of the ATCA cluster sample overlaid with the  $3\sigma \times (1, \sqrt{2}, 2)$  contours of the high resolution wide band radio maps (see Table 3 and Figs. A.1 and A.2) in red and the same contour levels for the Block 3 low resolution compact source subtracted maps for the two clusters with diffuse radio emission (see Sect. 6) in blue. The background of the X-ray images has been subtracted. The X ray images are corrected from surface brightness dimming with redshift, divided by emissivity in the energy band, taking in account absorption from the Galaxy and the response of the instrument. Finally the images are scaled to a self-similar model. The colours are selected so that the images would look identical when scaled by their mass if they were at the same distance, which give us a visual hint of the dynamical state of the clusters.

of diffuse sources were used to set detection limits for possible diffuse radio emission, as described below.

#### 4.3. Upper limit determination

To set the detection upper limits for possible diffuse radio emission in our ATCA observations, we took a similar approach to that used in, e.g. Venturi et al. (2008). Specifically, our procedure consists of the following steps:

- 1) We simulated a diffuse source with the MIRIAD task IMGEN. The model consist of 5 low surface brightness concentric disks, the biggest with a diameter of 1 Mpc in the corresponding redshift of the respective galaxy cluster image. To reproduce the typical profile of a RH, these disks area percentages are from largest to smallest: 100%, 60%, 33%, 25% and 12%. These disks contribute, respectively, the following percentage of the total flux of the simulated source: 72%, 20%, 5%, 2% and 1%.

- 2) The simulated source was added into the compact source subtracted uv-data of the corresponding observation on the subset coined Block3 ( $\sim 500$  MHz wide, see Sect. 3) for each galaxy cluster. This step was done by using the MIRIAD task

UVMODEL, which generates a new uv-data set of the real data plus the simulated source. To perform the injection of the spheric models we picked the 1 Mpc diameter circle centred on the cluster coordinates and five 1 Mpc areas inside the primary beam, without any trace of point sources and where there is no appearance of  $3\sigma$  contours due to artefacts on the original image plane.

- 3) The model injected uv-data were imaged at low resolution applying a taper with the following parameters on the MIRIAD task invert: FWHM=20, robust=0.5, cell=4, in order to achieve more sensitivity to the kind of emission of the simulated halos, as we have done in Sect. 4.2.

- 4) The injected fluxes of the different modelled disks were increased until we noticed that  $3\sigma$  contours appear uniformly on the injection areas, with a size large enough ( $\sim 500$  kpc diameter) to allow us to recognize it as a candidate RH.

It is worth noticing that we were able to recover from  $\sim 50\%$  to  $\sim 70\%$  of the original injected flux by measuring the total flux density in the areas of the image plane where the injections were done.

In the range of rms noises and resolutions of our images (see Table 3), we determined that RH models with a total flux density of 3-5 mJy are the lowest values that can be injected in our images to be considered as upper limits of detection. The radio powers for the detection limits calculated at 1.4 GHz by using the whole injected flux densities, assuming a spectral index of 1.3, are shown in Table 4.

## 5. X-ray dynamical state of the ATCA clusters

All the clusters of the ATCA sample benefit from X-ray observations from the XMM-Newton space telescope as part of the validation program of Planck cluster candidates. The X-ray data processing is detailed in Planck Collaboration et al. (2011b). The cluster mass,  $M_{500}$ , and corresponding  $R_{500}$ , are derived iteratively using the low scatter  $M_{500}-Y_X$  scaling relation from Planck Collaboration et al. (2011b), where  $Y_X$  is the product of the gas mass within  $R_{500}$  and the X-ray temperature in the  $[0.15 - 0.75] R_{500}$  aperture. The density profiles were derived from the surface brightness profile centered on the X-ray emission peak, using the PSF-deconvolution and deprojection method of Croston et al. (2008). From this analysis, we compute two morphological parameters :

a) The surface brightness concentration parameter  $C$ :

$$C = \frac{S_X(< R_{in})}{S_X(< R_{out})} \quad (1)$$

the ratio of the surface brightnesses  $S_X$  within an inner aperture  $R_{in}$  and a global aperture  $R_{out}$ .  $S_X$  is the PSF-corrected surface brightness, derived from the emission measure profile. Introduced in Santos et al. (2008) using  $R_{in} = 40$  kpc and  $R_{out} = 400$  kpc, this parameter has been widely used to probe the core properties of clusters up to high redshift (e.g. Santos et al. 2010; Hudson et al. 2010; Pascut & Ponman 2015). Here we choose to use scaled apertures since the clusters of our sample cover a wide redshift range, with  $R_{in} = 0.1 \times R_{500}$ , corresponding to the typical size of the cool-core, and  $R_{out} = 0.5 \times R_{500}$ , which is a characteristic size for the total flux.

b) The X-ray centroid-shift  $w$ , as defined in, for example, Böhringer et al. (2010) within 10 circular apertures from 0.1 to  $1 R_{500}$  excising the first central aperture:

$$w = \left[ \frac{1}{N+1} \sum (\Delta_i - \langle \Delta \rangle)^2 \right]^{1/2} \times \frac{1}{R_{500}} \quad (2)$$

where  $\Delta_i$  is the distance between the emission weighted centroid within the  $i$ th aperture and the X-ray peak,  $N$  the number of apertures

The centroid-shift is computed on the background-subtracted, exposure-corrected co-added X-ray count images in the 0.3-2 keV energy band after removal and refilling of the point sources as in Böhringer et al. (2010).

The results are shown in Fig. 2, where we overplot for comparison the positions of objects from the REXCESS (open grey circles; see Böhringer et al. 2010, for the centroid-shift values). Fig. 2 includes also the systems in common between the samples of Cassano et al. (2013) and Planck Collaboration et al. (2011a) (blue points), for which we have computed the concentration parameter and the centroid-shift values as described above for the ATCA sample.

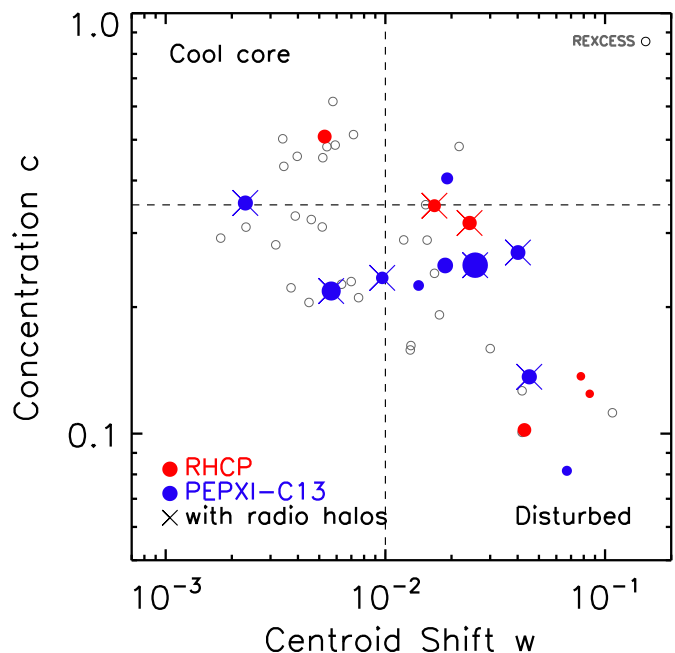


**Fig. 2.** Concentration parameter  $C$  vs. centroid shift  $w$  for the galaxy clusters of the RHCP sample analysed in this paper (red filled circles). For comparison, we also show the clusters in the sample of Cassano et al. (2013) that appear in the sub-sample of Planck clusters studied by Planck Collaboration et al. (2011a) (PEPXI-C13, blue filled circles) for which we applied our algorithm to compute the  $w$  values within  $R_{500}$ . The size of the circles is proportional to the  $\log(M_{500})$ , in the range  $[14.67-15.3]$ , and clusters with detected radio haloes are marked with a cross. The characteristic thresholds indicating cool-cores and morphologically disturbed systems (dashed lines) are from the REXCESS study (Böhringer et al. 2007). The REXCESS clusters are shown as open circles.

The horizontal and vertical dashed lines of Fig. 2 indicate characteristic threshold values of each parameter that are typically used to separate out, respectively, cool-core and morphologically disturbed systems. Following Pratt et al. (2009), we use a value of  $w > 0.01$  as indicative of a morphologically disturbed system. Similarly, we define targets with  $C > 0.35$  (equivalent to the central density criterion used by Pratt et al. (2009)) as being centrally peaked and thus cool-core systems.

We stress here that the limits indicated with dashed lines in Fig.2 were obtained for the local REXCESS sample. Also the sample analysed by (Cassano et al. 2013) is mostly made up by lower redshift clusters compared to our targets. In addition, we recall that, instead of using scaled apertures, Cassano et al. (2013) adopted fixed physical sizes for computing the two parameters  $w$  (500 kpc) and  $C$  ( $S_x(<100 \text{ kpc})/S_x(500 \text{ kpc})$ ). Their choice was based on the theoretical consideration that, for a typical  $\sim 1$  Mpc-size RH, 500 kpc is expected to delimitate the region where the energy of the merger is dissipated in particle acceleration. These factors are however not expected to make our analysis significantly different from the approach of Cassano et al. (2013), since recent works have proven that the adopted morphological parameters neither depend significantly on the size of the central region selected to estimate them (e.g. good agreement between  $w$  measured within  $R_{500}$  and  $0.5 R_{500}$ ), nor are limited by resolution issues up to  $z \sim 1$  clusters (e.g. Bartalucci et al. 2017, Lovisari et al., private communication). Our new estimates of the  $C$  and  $w$  parameters, however, indicate that one of the radio-loud

clusters in Cassano et al. (2013) falls in the relaxed part of the plot.

## 6. Results

### 6.1. Giant radio halo in PSZ2 G284.97-23.69

In Martinez Aviles et al. (2016) we reported the discovery of a Giant Radio Halo in PSZ2 G284.97-23.69 (named in our previous publication PLCK G285.0-23.7). Being the only confirmed Giant RH discovered in this set of observations, it is important to discuss it in the complete context of the whole ATCA sample. PSZ2 G284.97-23.69 is the second most luminous and massive cluster in the sample (see Table 1). Based on its disturbed morphology ( $w = 0.028 \pm 0.001$ ) and concentration parameter ( $C = 0.317 \pm 0.005$ ) it falls in a quadrant of dynamically disturbed systems, with a relatively high  $C$  parameter, though. The size and orientation of the  $3\sigma$  contours on the Block 3 tapered radio map have a remarkable coincidence with the X-ray morphology (see Fig. 4 in Martinez Aviles et al. 2016). The detected RH seems to be slightly under-luminous compared to objects hosted by clusters in a similar mass range, as shown in the  $P_{1.4\text{GHz}}$  vs  $M_{500}$  plot (purple star in Fig. 4); although it is not a clear outlier like the RH discovered by Bonafede et al. (2015). It is, however, one of the lowest luminosity radio halos detected at  $z > 0.35$ .

### 6.2. Diffuse radio source in the cluster PSZ2 G262.73-40.92.

According to the X-ray morphological analysis, PSZ2 G262.73-40.92 is a merging, but probably moderately disturbed cluster, lying close to our cut line of cool-core clusters, with a concentration parameter  $C = 0.348 \pm 0.005$  and a centroid shift  $w = 0.016 \pm 0.001$  (see Fig. 2). The tapered compact source subtracted image in the field of the cluster PSZ2 G262.73-40.92 shows the presence of a candidate diffuse source close to the cluster central position. The high resolution image reveals the presence of a very faint point source in the region of the diffuse emission, with a possible counterpart on the IR map (Fig. 3), for which we measured a flux density of  $0.33 \pm 0.04$  mJy. We measured the total flux density inside the  $3\sigma$  contours (shown in cyan color in Fig. 3) of the diffuse emission in the compact source subtracted tapered image in Block 3, characterized by a rms noise of  $83 \mu\text{Jy}/\text{beam}$  (see Table 3). We obtained a flux density of  $1.18 \pm 0.12$  mJy inside the  $3\sigma$  contours. The region shows an elliptical shape, with a major axis of 63 arcseconds and a minor axis of 50 arcseconds, which for our cosmology corresponds to a physical size of  $349 \text{ kpc} \times 277 \text{ kpc}$  at the cluster redshift. It is important to note that the diffuse source present in the residual map follows the emission from the galaxies in the WISE images (Fig. 3), and is offset from the cluster X-ray emission (Fig. 1, top, left panel), which makes the confirmation and possible classification of the source challenging with our data.

### 6.3. Clusters without diffuse radio emission

#### 6.3.1. The Cool-core cluster PSZ2 G271.18-30.95

PSZ2 G271.18-30.95 has the highest X-ray luminosity of the ATCA sample, although it is not the most massive (see Table 1). Within the sample it has also the highest concentration parameter ( $C = 0.509 \pm 0.004$ ) and the lowest centroid shift ( $w = 0.005 \pm 0.001$ ). This positions it as a clear cool-core non disturbed cluster. Unsurprisingly, as in  $\sim 70\%$  of cool-core clusters (Gitti et al. 2015) our high resolution radio map shows the pres-

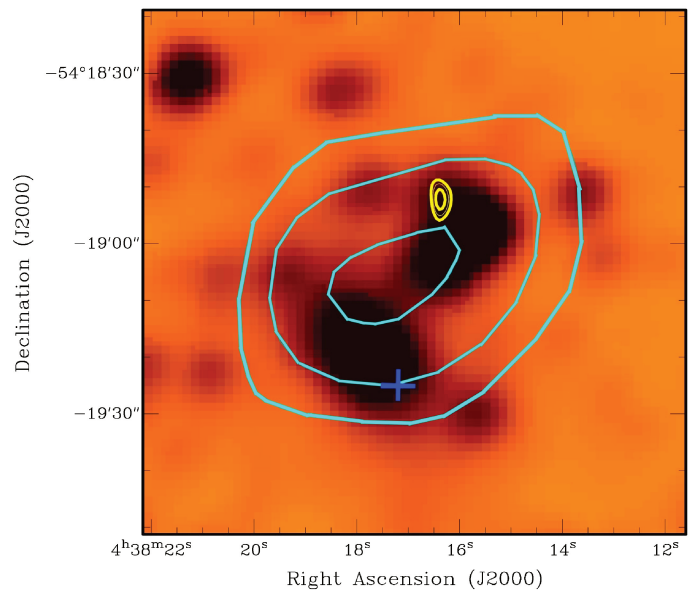


**Fig. 3.** WISE 4.6 microns image of the central area of PSZ2 G262.73-40.92. The center of the X-ray emission is marked as a blue cross.  $3\sigma \times (1, \sqrt{2}, 2)$  contours of the compact source subtracted tapered radio image appear in cyan, while yellow contours are the same contour levels from the high resolution Block 3 radio map.

ence of a strong radio source coincident with the cluster center (see Fig. 1 top middle panel and Fig. A.2 bottom panels), with a flux density of  $\sim 10$  mJy at  $\sim 1.9$  GHz. From the Hubble space telescope optical image there is an evident connection between the radio source and the BCG. Moreover, by measuring the flux densities of the central source in the different sub-bands (Blocks 1 to 4, see Sect. 3) we estimate a spectral index for the central compact source of  $\alpha \approx 0.6$ .

It is known that radio mini-halos are usually located in the center of cool-core clusters, surrounding the central active radio galaxy and extending to the radius of the cluster cooling region (see e.g. Giacintucci et al. 2017, and references therein). To further investigate the possible presence of a radio mini-halo, we did several tests by imaging at  $\sim 10$  arcsec resolution without compact source subtraction and using different values for the taper. None of our maps show evidence of extended diffuse emission at the typical mini-halo scales. We point out, however, that the presence of the compact source at the cluster center and the presence of a strong source close to the cluster made the imaging and the compact source subtraction problematic in this particular case.

#### 6.3.2. Highly disturbed clusters without radio emission

Three of the seven galaxy clusters of the ATCA sample showed evidence of being both highly disturbed (see Fig. 1 lower panels and the three red circles in the bottom right of Fig. 2) and with low concentration parameters. PSZ2 G277.76-51.74, the most massive cluster of the sample, has also the lowest concentration parameter ( $C = 0.102 \pm 0.002$ ) and shows a centroid shift  $w = 0.042 \pm 0.001$ . On the other hand, PSZ2 G285.63-17.23 has the highest centroid shift ( $w = 0.081 \pm 0.003$ ,  $C = 0.124 \pm 0.006$ ). Finally PSZ2 G286.28-38.36 shows also signs of being highly

disturbed ( $w = 0.078 \pm 0.005$ ,  $C = 0.137 \pm 0.008$ ). None of these clusters show hints of diffuse radio emission on our maps.

### 6.3.3. Detection limits

In Fig. 4 we show the upper limits for the non-detections on the ATCA sample as red arrows on the  $P_{1.4\text{GHz}}$  vs.  $M_{500}$  plot. We compare our calculated values with those obtained by Venturi et al. (2008) and Kale et al. (2013) (blue arrows in Fig. 4), measured using GMRT images, with the modelled halo injections performed at 610 MHz. Our calculated ATCA upper limits appear higher in the plot as a consequence of the combination of two effects. The first one is that the redshift range of our sample is higher than previous studies (effectively limited to  $z < 0.3$ , see Sect. 1). In our calculation of the radio power, we have the luminosity distance factor that scales as  $D_{\text{Lum}}(z)^2$ . The second and most important effect is the frequencies of the ATCA observations. We recall that our upper limit injections were done at  $\sim 1.9$  GHz, and assuming a typical spectral behaviour of RHs (with spectral index  $\alpha=1.3$ ) we obtain higher values of the radio power when we rescale to 1.4 GHz. The values of our calculated upper limits appear in Table 4. It is worth mentioning that the power of the giant RH discovered in PSZ2 G284.97-23.69 and some other RHs reported in the literature lie close (or even below) the radio power regime of the upper limits obtained for our ATCA observations. This could imply that the measured flux density of our detected sources could be underestimated.

**Table 4.** Upper limits obtained for the ATCA cluster images without traces of diffuse radio emission. The calculated logarithm of the radio power at 1.4 GHz, by assuming a spectral index of 1.3, for the total flux density of the injected fake radio halo model in the Block 3 sub-band (1.9 GHz) appears in Column 2.

Cluster name	Log $P_{1.4\text{GHz}}$ ( $\text{WHz}^{-1}$ )
PSZ2 G285.63-17.23	24.46
PSZ2 G277.76-51.74	24.57
PSZ2 G286.28-38.36	24.19
PSZ2 G271.18-30.95	24.39

## 7. Discussion and conclusions

A full analysis in search of diffuse radio emission on the ATCA sub-sample of the MACS-Planck RHCP is presented in this paper.

Among the seven targets, only two clusters show a confirmed or tentative diffuse radio emission. We reported the presence of a giant radio halo in PSZ2 G284.97-23.69 and found a new candidate diffuse source in PSZ2 G262.73-40.92. The X-ray morphological analysis based on XMM-Newton observations indicates that those objects are most likely disturbed systems, based in particular on the centroid shift indicator ( $w$ ), with a concentration parameter ( $C$ ) not far from the threshold adopted to separate merging and relaxed clusters.

This is not totally unexpected. Our choice for the limits for cool-core/non cool-core and relaxed/disturbed systems is based on the limits for  $C$  and  $w$  adopted and obtained empirically from the local ( $z = 0.055 - 0.183$ ) REXCESS cluster sample (Böhringer et al. 2007), in which two disturbed cool-core clusters are detected (Pratt et al. 2009; Böhringer et al. 2010). Fur-

thermore, the results of McDonald et al. (2017) on the SPT sample suggest that the evolution of the core and outer regions are decoupled, which would indicate that there is no reason why a cluster cannot be a cool-core and disturbed as well.

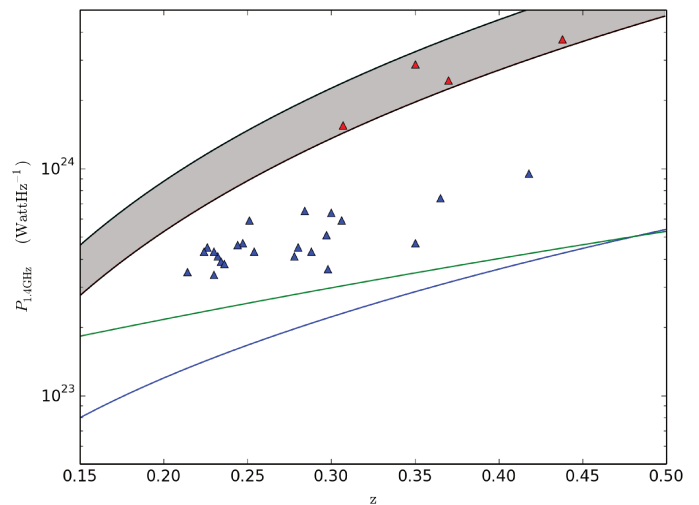


**Fig. 5.** Upper limit radio powers rescaled at 1.4 GHz vs. redshift for our ATCA observations (red triangles) and GMRT observations Venturi (2008) & Kale (2013) (blue triangles). The lower (upper) border of the grey band corresponds to the lowest (highest) detection limit of injected fluxes, i.e. 3 mJy (5 mJy) for our ATCA images. The green and blue lines show the minimum power at 1.4 GHz of detectable radio halos in the EMU survey as derived in Cassano et al. (2012).

Those clusters of our sample that have clear X-ray morphological indicators of being highly disturbed do not present any bright diffuse emission. Currently, these clusters (upper limits) are still consistent with being on the  $P_{1.4} - M_{500}$  correlation. Future deeper observations will have to determine if these halos could be under-luminous and fall below the correlation. Hypothetical RH could be either “classical” halos, i.e. almost consistent with the correlation, or under luminous RHs with ultra-steep radio spectra, detectable with low frequency radio observations (these are particularly expected in high- $z$  clusters, see Cassano et al. 2006). The challenging hypothesis to be tested would be if those clusters are “radio-quiet”. There are actually cases of disturbed clusters lacking radio halos. Russell et al. (2011) show that the galaxy cluster A2146 possesses no diffuse emission despite being clearly a merging cluster (see also White et al. 2015, for a detailed study of the dynamical status of the cluster). However, in this particular case the mass of the cluster is quite low ( $4.3 \times 10^{14} M_{\odot}$ ) which could be the reason for the lack of a detectable radio halo.

Indeed, upper limits indicated in Fig. 4 are significantly higher compared to other works (Cassano et al. 2013), even if the rms sensitivities reached in all these analyses are comparable. This is explained by the fact that previously published upper limits are based either on lower-frequency (mostly 610 MHz) observations (Venturi et al. 2008; Kale et al. 2013) or on lower-redshift ATCA cluster samples (Shakouri et al. 2016, Shakouri et al. submitted). In the first case (and keeping in mind that we convert radio powers to the reference frequency of 1.4 GHz), the same rms sensitivity at 1.9 GHz and 610 MHz translates to a higher 1.4 GHz radio halo luminosity upper limit for the 1.9 GHz

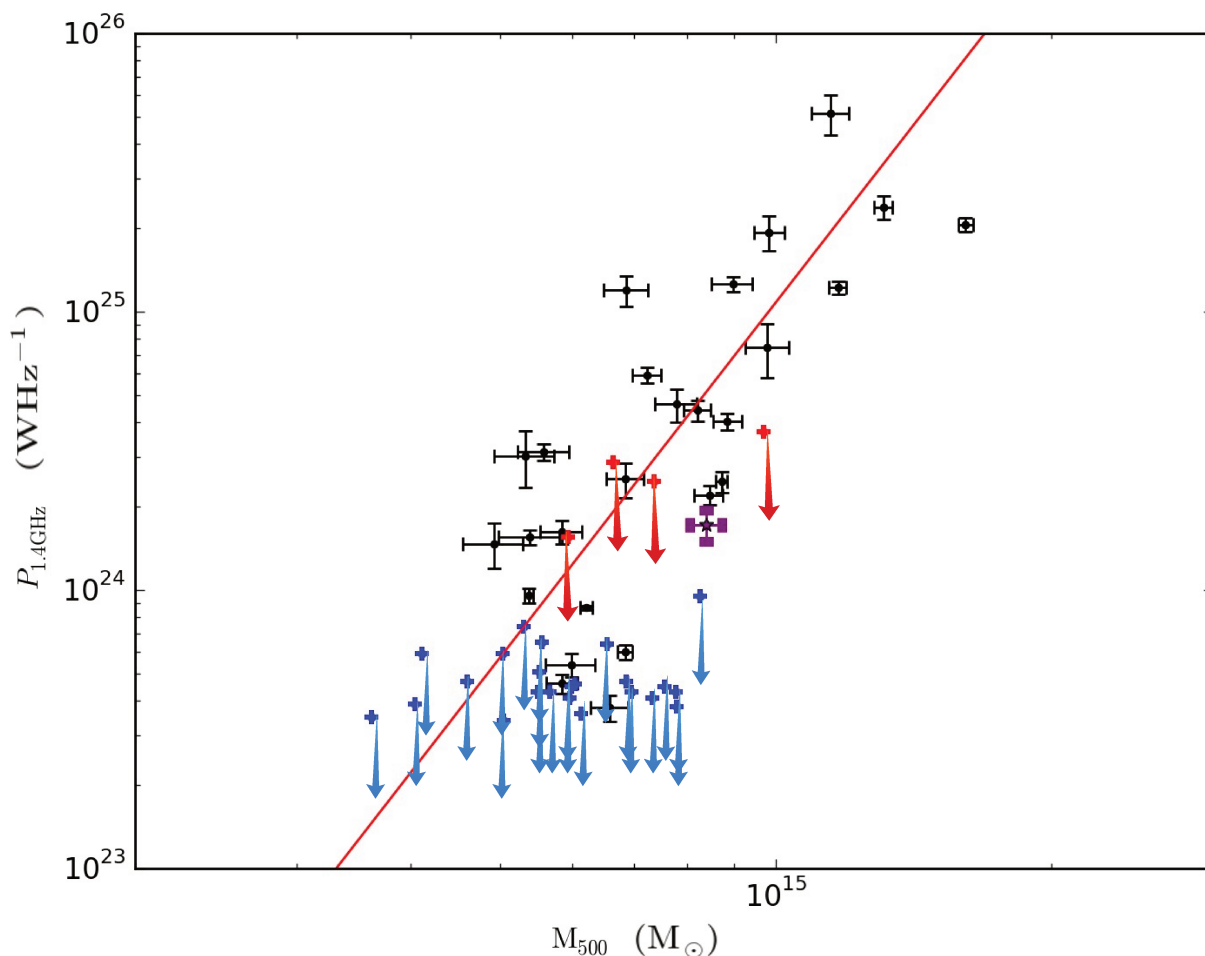


**Fig. 4.** Synchrotron power of RHs at 1.4 GHz ( $P_{1.4\text{GHz}}$ ) versus cluster mass  $M_{500}$  (from Planck Collaboration et al. 2016). Detected radio halos reported in the literature measured at 1.4 GHz (see Martinez Aviles et al. 2016) are shown in black dots. The red line is the best fit for the black dots. The purple star corresponds to the radio halo on PSZ2 G284.97-23.69. The blue arrows correspond to detection limits appearing in Cassano et al. (2013) and references therein. The red arrows are the upper limits for the non-detections presented in this paper (see Table 4).

case, due to the spectral steepness of radio halos (we rescaled by assuming a spectral index  $\alpha=1.3$  to be consistent with Cassano et al. 2013). In the second case, the clusters are observed at the same frequency, but located at  $z\sim 0.15$ , which, due to the  $D_{\text{Lum}}(z)^2$  factor, translates into  $\sim 10$  higher upper limits in radio power compared to lower redshift ATCA observations.

To be able to distinguish between "radio-quiet" or "under-luminous" diffuse emission in the three disturbed galaxy clusters in our sample, it is clear that more sensitive and lower-frequency radio observations are needed. Instruments such as the JVLA, the upgraded GMRT or the LOFAR Two-metre Sky Survey (see e.g. Shimwell et al. 2017) are already improving the observational capabilities needed for this kind of studies by reaching better sensitivities. As an example of the expected power of future instruments, in Fig. 5 we compare the detection upper limits obtained for our ATCA observations (red triangles) with previous upper limits taken with the GMRT at 610 MHz (blue triangles) as a function of redshift. The green and blue lines show the minimum power at 1.4 GHz of detectable radio halos in the Evolutionary Map of the Universe (EMU) survey for different signal to noise levels as derived in Cassano et al. (2012) (see Sect. 5

and Eqs. 9 and 10 in their paper). The EMU survey will produce a deep radio continuum survey of the Southern Sky with rms noises of  $\sim 10\mu\text{Jy}/\text{beam}$ , comparable to our best rms noise of  $\sim 11\mu\text{Jy}/\text{beam}$ , but with lower resolution ( $\sim 10$  arcseconds, Norris et al. 2011), resulting in a better sensitivity at lower frequencies (1.3 GHz). From Fig. 5 we note that EMU will have the sensitivity to discover possible halos in clusters that presently are undetected in both GMRT and ATCA samples.

*Acknowledgements.* The authors would like to warmly thank Roberto Ricci for useful discussions on the preparation of this paper. GMA is supported by the Erasmus Mundus Joint Doctorate Program by Grants Number 2013-1471 from the agency EACEA of the European Commission. GMA, CF and MJ-H acknowledge financial support from *Programme National Cosmologie et Galaxies (PNCG)* and *Université de Nice-Sophia Antipolis – Programme Professeurs Invités 2015*. MJ-H acknowledges the Marsden Fund administered by the Royal Society of New Zealand on behalf of the Ministry of Business, Innovation and Employment. TV, RC and GB acknowledge partial support from PRIN-INAF 2014 grant. The research leading to these results has received funding from the European Research Council under the European Union's Seventh Framework Programme (FP7/2007-2013) / ERC grant agreement no. 340519. Basic research in radio astronomy at the Naval Research Laboratory is supported by 6.1 Base funding. The Australia Telescope Compact Array is part of the Australia Telescope National Facility which is funded by the Australian Government for operation as a National Facility managed by CSIRO. The results of these paper are

partially based on data retrieved from the ESA Planck Legacy Archive, NASA SkyView and the Hubble Legacy Archive, which is a collaboration between the Space Telescope Science Institute (STScI/NASA), the Space Telescope European Coordinating Facility (ST-ECF/ESA) and the Canadian Astronomy Data Centre (CADC/NRC/CSA).

## References

- Bartalucci, I., Arnaud, M., Pratt, G. W., et al. 2017, *A&A*, 598, A61
- Basu, K. 2012, *MNRAS*, 421, L112
- Böhringer, H., Pratt, G. W., Arnaud, M., et al. 2010, *A&A*, 514, A32
- Böhringer, H., Schuecker, P., Pratt, G. W., et al. 2007, *A&A*, 469, 363
- Bonafede, A., Intema, H., Brügger, M., et al. 2015, *MNRAS*, 454, 3391
- Bonafede, A., Intema, H. T., Brügger, M., et al. 2014, *MNRAS*, 444, L44
- Brunetti, G. & Jones, T. W. 2014, *International Journal of Modern Physics D*, 23, 30007
- Brunetti, G., Setti, G., Feretti, L., & Giovannini, G. 2001, *MNRAS*, 320, 365
- Cassano, R., Brunetti, G., Norris, R. P., et al. 2012, *A&A*, 548, A100
- Cassano, R., Brunetti, G., & Setti, G. 2004, *Journal of Korean Astronomical Society*, 37, 589
- Cassano, R., Brunetti, G., & Setti, G. 2006, *MNRAS*, 369, 1577
- Cassano, R., Etori, S., Brunetti, G., et al. 2013, *ApJ*, 777, 141
- Cassano, R., Etori, S., Giacintucci, S., et al. 2010, *ApJ*, 721, L82
- Croston, J. H., Pratt, G. W., Böhringer, H., et al. 2008, *A&A*, 487, 431
- Cuciti, V., Cassano, R., Brunetti, G., et al. 2015, *A&A*, 580, A97
- Ebeling, H., Edge, A. C., Mantz, A., et al. 2010, *MNRAS*, 407, 83
- Feretti, L., Giovannini, G., Govoni, F., & Murgia, M. 2012, *A&A Rev.*, 20, 54
- Giacintucci, S., Markevitch, M., Cassano, R., et al. 2017, *ApJ*, 841, 71
- Gitti, M., Tozzi, P., Brunetti, G., et al. 2015, *Advancing Astrophysics with the Square Kilometre Array (AASKA14)*, 76
- Govoni, F., Murgia, M., Markevitch, M., et al. 2009, *A&A*, 499, 371
- Hudson, D. S., Mittal, R., Reiprich, T. H., et al. 2010, *A&A*, 513, A37
- Kale, R. & Parekh, V. 2016, *MNRAS*, 459, 2940
- Kale, R., Venturi, T., Giacintucci, S., et al. 2015, *A&A*, 579, A92
- Kale, R., Venturi, T., Giacintucci, S., et al. 2013, *A&A*, 557, A99
- Martinez Aviles, G., Ferrari, C., Johnston-Hollitt, M., et al. 2016, *A&A*, 595, A116
- Mazzotta, P. & Giacintucci, S. 2008, *ApJ*, 675, L9
- McDonald, M., Allen, S. W., Bayliss, M., et al. 2017, *ArXiv e-prints* [arXiv:1702.05094]
- Norris, R. P., Hopkins, A. M., Afonso, J., et al. 2011, *PASA*, 28, 215
- Pascut, A. & Ponman, T. J. 2015, *MNRAS*, 447, 3723
- Petrosian, V. 2001, *ApJ*, 557, 560
- Planck Collaboration, Ade, P. A. R., Aghanim, N., et al. 2011a, *A&A*, 536, A11
- Planck Collaboration, Ade, P. A. R., Aghanim, N., et al. 2016, *A&A*, 594, A27
- Planck Collaboration, Aghanim, N., Arnaud, M., et al. 2011b, *A&A*, 536, A9
- Pratt, G. W., Croston, J. H., Arnaud, M., & Böhringer, H. 2009, *A&A*, 498, 361
- Russell, H. R., van Weeren, R. J., Edge, A. C., et al. 2011, *MNRAS*, 417, L1
- Santos, J. S., Rosati, P., Tozzi, P., et al. 2008, *A&A*, 483, 35
- Santos, J. S., Tozzi, P., Rosati, P., & Böhringer, H. 2010, *A&A*, 521, A64
- Sault, R. J., Teuben, P. J., & Wright, M. C. H. 1995, in *Astronomical Society of the Pacific Conference Series*, Vol. 77, *Astronomical Data Analysis Software and Systems IV*, ed. R. A. Shaw, H. E. Payne, & J. J. E. Hayes, 433
- Shakouri, S., Johnston-Hollitt, M., & Pratt, G. W. 2016, *MNRAS*, 459, 2525
- Shimwell, T. W., Röttgering, H. J. A., Best, P. N., et al. 2017, *A&A*, 598, A104
- Sommer, M. W., Basu, K., Intema, H., et al. 2017, *MNRAS*, 466, 996
- Steer, D. G., Dewdney, P. E., & Ito, M. R. 1984, *A&A*, 137, 159
- van Weeren, R. J., Andrade-Santos, F., Dawson, W. A., et al. 2017, *Nature Astronomy*, 1, 0005
- Venturi, T., Giacintucci, S., Brunetti, G., et al. 2007, *A&A*, 463, 937
- Venturi, T., Giacintucci, S., Dallacasa, D., et al. 2008, *A&A*, 484, 327
- White, J. A., Canning, R. E. A., King, L. J., et al. 2015, *MNRAS*, 453, 2718

## Appendix A: High resolution radio images of ATCA sample

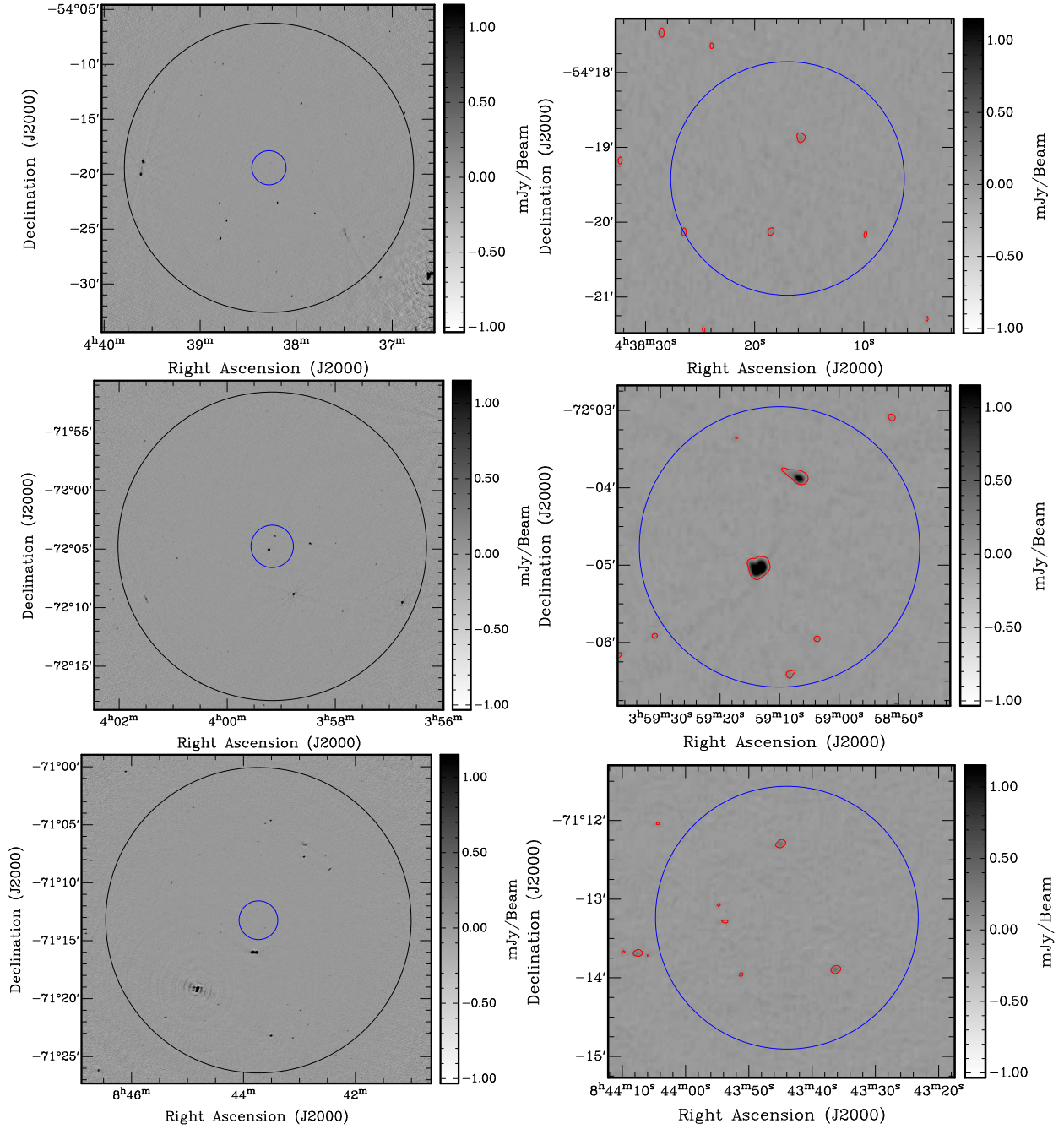


**Fig. A.1.** Final full-resolution, wide-band ATCA images of the cluster sample. *Left panels:* Full field image centred on cluster coordinates. The outer circle denotes the boundary of the primary beam with a radius of  $\sim 0.22$  degrees. The central 1 Mpc-diameter region is indicated by the inner, blue smaller circle. *Right panels:* Zoom into the central area with  $3\sigma$  contours of the corresponding map overlaid in red. *Top:* PSZ2 G262.73-40.92; *Middle:* PSZ2 G286.28-38.36; *Bottom:* PSZ2 G285.63-17.23.

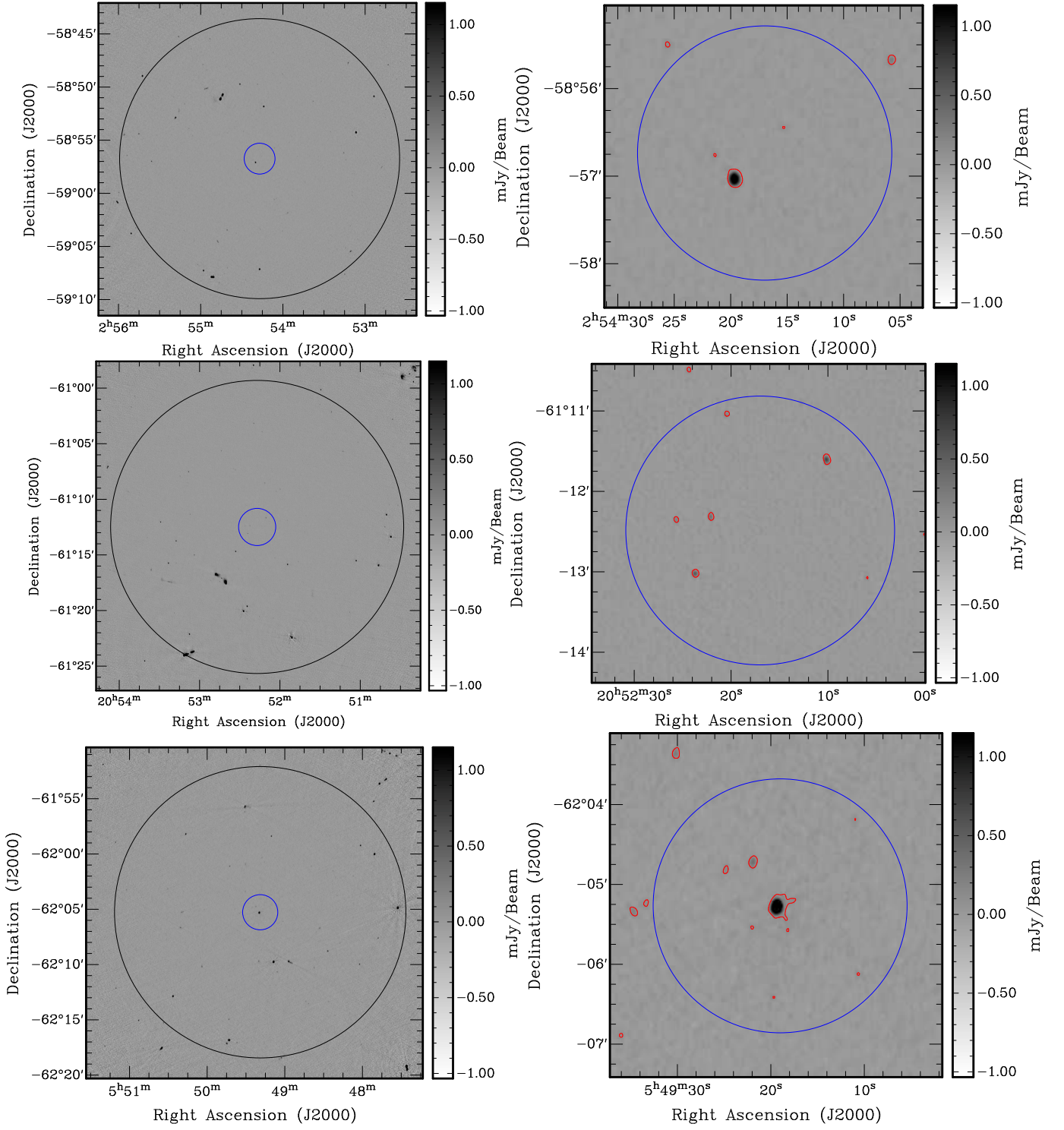


**Fig. A.2.** Same as Figure A.1. *Top:* PSZ2 G277.76-51.74; *Middle:* PLCK G334.8-38.0; *Bottom:* PSZ2 G271.18-30.95.



# List of Figures

1.1	Most of the electromagnetic spectrum coming from space is blocked by the Earth's atmosphere except for visible, radio, millimetre and sub-millimetre bands. Credit: Wikipedia. . . . .	2
1.2	Karl Jansky and the antenna used to make his historical radio observations. Photo: Bell Telephone Laboratories. . . . .	3
1.3	Image of the radio galaxy Cygnus A (3C 405), one of the brightest radio sources in the sky. Image courtesy of NRAO/AUI . . . . .	4
1.4	The radio sky at 408 MHz. Credit: C. Haslam et al., MPIfR, SkyView . . . . .	5
2.1	Optical image of the galaxy cluster MACSJ0520.7- 1328, one of our clusters from the MACS-Planck Radio Halo Cluster Project. Credit: Hubble Space Telescope archive. . . . .	17
2.2	Example of the multi-wavelength images of the Coma cluster. In the top left panel the Planck Sunyaev-Zeldovic image is shown, it looks like a spot of different temperature in the CMB. The top right panel shows the thermal X-ray emission of the cluster, from the ROSAT PSPC survey. In the bottom panel we show the ROSAT PSPC X-ray image overlaid with the optical DSS image of the cluster. Credit: European Space Agency. . . . .	19
2.3	The undistorted spectrum of the CMB (dashed line) and the distorted spectrum by the SZ effect (solid line). The CMB intensity increases at frequencies higher than $\sim 218$ GHz (Wien Regime) and decreases for lower frequencies (Rayleigh-Jeans regime). Credit: ned.ipac.caltech.edu. . . . .	22
3.1	Examples of different kinds of diffuse radio sources in galaxy clusters, shown as black contours overlaid on the X-ray images of the clusters. From left to right and from top to bottom: A radio halo in A2219; a halo plus a radio relic in A2744; a radio relic in A115; a complex halo + relic in A754; relics in A1664 and A548. Finally, a halo in A520; a radio mini-halo in A2029 and a radio halo + a double relic in RXCJ1314.4-2515. Image taken from <a href="#">Feretti et al. (2012)</a> . . . . .	24
3.2	LOFAR HBA 120-181 MHz images of a radio relic in the Toothbrush cluster, one of the brightest radio relic sources known. Credit: <a href="#">van Weeren et al. (2016)</a> . . . . .	26
3.3	$3\sigma \times 2n$ contours of the 617 MHz GMRT radio map of the cluster RX J1720.1+2638, overlaid on the optical r-band SDSS image of the same sky region. The contours show a typical radio mini-halo around the dominant galaxy of the cluster. Credit: <a href="#">Giacintucci et al. (2014a)</a> . . . . .	27

- 3.4 Contours of diffuse Westerbork Synthesis Radio Telescope (WSRT) 352 MHz radio emission over ROSAT PSPC diffuse X-ray emission of Coma cluster (see Fig. 2.2), a typical radio halo. Credit: [Brown and Rudnick \(2011\)](#). . . . 28
- 3.5 Distribution of galaxy clusters in the  $P_{1.4}$ - $L_{500}$  diagram. The blue filled dots corresponds to halos belonging to the EGRHS (see sect. 4.1), while radio powers taken from the literature are shown as open black dots. Halos with USS are shown in green. Blue arrows are radio upper limits and magenta arrows are upper limits for cool-core clusters. The black line is the best fit relation for RHs. The green line also fits USSRHs. The shadowed region is the 95% confidence region for the black line fit. Credit: [Cassano et al. \(2013\)](#). 33
- 3.6 Distribution of galaxy clusters in the  $P_{1.4}$ - $M_{500}$  plane. The symbols are the same as in Fig. 3.5. Credit: [Cassano et al. \(2013\)](#). . . . . 34
- 3.7 a) Concentration parameter  $c$  versus centroid shift  $w$  plane; b)  $w$  vs. power ratio  $P_3/P_0$ ; c)  $c$  vs  $P_3/P_0$ . Clusters hosting a RH are represented as red dots. Black, open dots are RH quiet clusters. gray filled dots are clusters of  $z > 0.32$  and blue open dots are mini halos. The dashed line values are the median values of each parameter (see text), splitting the diagrams into regions of "relaxed" and "disturbed" clusters. Most clusters hosting RHs fall into the disturbed quadrants. Credit: [Cassano et al. \(2010a\)](#). . . . . 35
- 4.1 The 0.1-2.4 keV band luminosities  $L_{500}$  of the 1743 Meta-Catalogue of X-ray detected Cluster of Galaxies MCXC ([Piffaretti et al., 2011](#)) as a function of redshift in lin-log scale. Blue points correspond to detected clusters, while red points are those clusters with a detected RH. From this figure it is evident that RHs tend to appear in more X-ray luminous clusters. . . . . 40
- 4.2 Predicted fraction of galaxy clusters hosting a RH observable at  $\sim$ GHz frequencies as a function of virial mass in two different redshift bins. The calculations are obtained from turbulent acceleration models. Notice that the fraction of RHs in the redshift window  $z = 0.3$ - $0.4$  (shown in black) is larger than in the local bin  $z = 0$ - $0.1$  (plotted in red) for larger virial masses. . . . . 41
- 4.3 X-ray luminosity (0.1-2.4 keV) vs redshift for the MACS-Planck sample. Empty blue triangles correspond to XMM-Newton-Planck subsample and magenta filled circles are the MACS subsample. For comparison, different samples at lower redshifts are plotted in black. Open red circles indicate clusters hosting a RH. . . . . 42
- 4.4 Example of uv-coverage of our ATCA observations in the 500 MHz band centred at 1.867 MHz. The wide-band of the full 2 GHz observations completes the coverage. . . . . 45

- 5.1 XMM-Newton smoothed images in the [0.3-2] keV band of the ATCA cluster sample overlaid with the  $3\sigma \times (1, \sqrt{2}, 2)$  contours of the full resolution wide band radio maps (see Table 5.1 and Figs. A.1 and A.2) in yellow and the same contour levels for the Block 3 low resolution compact source subtracted maps for the two clusters with diffuse radio emission (see Sects. 5.3.1 and 5.3.2) in blue. The images are scaled to a self-similar model. The colours are selected so that the images would be identical if clusters obeyed strict self similarity, which give us a visual hint of the dynamical state of the clusters. . . . . 55
- 5.2 Concentration parameter  $C$  vs. centroid shift  $w$  for the galaxy clusters of the ATCA-RHCP sample analysed in this paper (red filled circles). For comparison, we also show the clusters in the sample of Cassano et al. (2013) that appear in the sub-sample of Planck clusters studied by Planck Collaboration et al. (2011a) (PEPXI-C13, blue filled circles) for which we applied our algorithm to compute the  $w$  values within  $R_{500}$ . The size of the circles is proportional to the  $\log(M_{500})$ , in the range [14.67–15.3], and clusters with detected radio haloes are marked with a cross. The characteristic thresholds indicating cool-cores and morphologically disturbed systems (dashed lines) are from the REXCESS study (Böhringer et al., 2007). The REXCESS clusters are shown as open circles. . . . . 58
- 5.3 PSZ2 G284.97-23.69 radio contours of the ATCA tapered image centred at 1.867 GHz overlaid on: the smoothed raw XMM image in the [0.3-2.0] keV energy band (top, left panel); the full band high resolution ATCA radio image (top, right panel); the Block 3 tapered radio image without compact source subtraction (bottom, left panel) and the 4.6 micron WISE image (bottom, right panel). Dashed contours correspond to the islands of significant emission detected by PyBDSM on the Block 3 tapered map (cyan contours in Fig.5.5). The continuous curves trace instead “classical”  $3, 3 \times \sqrt{2}, 6 \sigma$  contours (i.e. with the  $51.1 \mu\text{Jy}/\text{beam}$  rms value of the map estimated by hand on the Block 3 tapered map at  $\sim 30$  arcsec resolution; see Table 5.2). . . . . 59
- 5.4 Zoom in the HST-ACS image of PSZ2 G284.97-23.69 central field (available in the HST archive). For reference, the  $3 \sigma$  contour of the ATCA tapered image centred at 1.867 GHz is shown in black. The blue contours indicate sources of significant radio emission in the full-resolution deep ATCA image of the cluster (i.e.  $5 \times$  rms of the final wide-band ATCA map shown in Fig. A.2). 60
- 5.5 Output of the PyBDSM source finder tool. The axis units are in pixels. From left to right and from top to bottom: Original image on which PyBDSM is run (in this example, the ID2 map of Table 5.3); islands of significant emission (cyan contours) and fitted Gaussians that model identified sources overlaid on the ID2 map; residual after the subtraction of the fitted sources; model of the reconstructed sky. The big red ellipse corresponds to the diffuse emission in the centre of the cluster. . . . . 62

- 5.6 Synchrotron power of RHs at 1.4 GHz ( $P_{1.4GHz}$ ) vs. cluster mass  $M_{500}$  from [Planck Collaboration et al. \(2015\)](#). Symbols are colour-coded depending on the redshift of RH hosting clusters. The red line is the fit derived in the present paper, including only the RHs with radio fluxes measured at 1.4 GHz (indicated by triangles; see also Table ??). Analogously to [Cassano et al. \(2013\)](#), we exclude for the fitting ultra-steep spectrum RHs and halos detected in frequencies different from 1.4 GHz, both shown in dots (see Table 4 in Appendix C.1). The red star corresponds to PSZ2 G284.97-23.69 detected in this work. When the spectral index is unknown (including PSZ2 G284.97-23.69) we assume the value of  $\alpha=1.3$ . . . . . 65
- 5.7 Correlation between radio halo sizes and the virial radius of their host clusters [see [Cassano et al. \(2007\)](#)]. The newly detected radio halo in PSZ2 G284.97-23.69 is indicated in red. . . . . 66
- 5.8 WISE 4.6 microns image of the central area of PSZ2 G262.73-40.92. The center of the X-ray emission is marked as a white cross.  $3\sigma \times (1, \sqrt{2}, 2)$  contours of the compact source subtracted tapered radio image appear in cyan, while yellow contours are the same contour levels from the high resolution Block 3 radio map. . . . . 68
- 5.9 HST archive image of the central area of PSZ2 G271.18-30.95 with  $3\sigma \times (1, 2, 3)$  full band high resolution contours of the central radio source overlaid in red. . . . . 69
- 5.10 XMM-Newton wavelet filtered [0.3-2] keV image of the triple system PLCK G334.8-38.0. Extended components found in the XMM-Newton image are marked with letters. The circles denote the estimated  $R_{500}$  radius for each component. Credit: [Planck Collaboration et al. \(2011b\)](#). . . . . 71
- 5.11 High resolution radio image at 2.1 GHz of a tailed radio galaxy corresponding to the X-ray source "C" of Figure 5.10. The green contours are from the XMM image of the corresponding region. . . . . 71
- 5.12 Synchrotron power of RHs at 1.4 GHz ( $P_{1.4GHz}$ ) versus cluster mass  $M_{500}$  (from [Planck Collaboration et al., 2016b](#)). Detected radio halos reported in the literature measured at 1.4 GHz are shown in black dots. The red line is the best fit for the black dots. The purple star corresponds to the radio halo on PSZ2 G284.97-23.69. The blue arrows correspond to detection limits appearing in [Cassano et al. \(2013\)](#) and references therein. The red arrows are the upper limits for the non-detections presented in this paper (see Table 5.4). . . . . 73

5.13	Upper limit radio powers rescaled at 1.4 GHz vs. redshift for our ATCA observations (red triangles) and GMRT observations <a href="#">Venturi et al. (2008)</a> & <a href="#">Kale et al. (2013)</a> (blue triangles). The lower (upper) border of the grey band corresponds to the lowest (highest) detection limit of injected fluxes, i.e. 3 mJy (5 mJy) for our ATCA images. The green and blue lines show the minimum power at 1.4 GHz of detectable radio halos in the EMU survey as derived in <a href="#">Cassano et al. (2012)</a> . . . . .	75
6.1	Same as Fig. 5.12. Green dots correspond to our newly calculated upper limits from GMRT sub-sample. Most of the values for the upper limit radio powers are comparable to results obtained by <a href="#">Venturi (2008)</a> & <a href="#">Kale (2013)</a> with the GMRT at 610 MHz. . . . .	87
6.2	Same as Fig. 5.13 but this time including our newly calculated upper limits for the GMRT RHCP sample (green triangles). Notice that two of our calculated upper limits coincide with the upper limits expected from the EMU survey. . . . .	87
A.1	Final full-resolution, wide-band ATCA images of the cluster sample. <i>Left panels:</i> Full field image centred on cluster coordinates. The outer circle denotes the boundary of the primary beam with a radius of $\sim 0.22$ degrees. The central 1 Mpc-diameter region is indicated by the inner, blue smaller circle. <i>Right panels:</i> Zoom into the central area with $3\sigma$ contours of the corresponding map overlaid in red. <i>Top:</i> PSZ2 G262.73-40.92; <i>Middle:</i> PSZ2 G286.28-38.36; <i>Bottom:</i> PSZ2 G285.63-17.23. . . . .	94
A.2	Same as Fig. A.1. <i>Top:</i> PSZ2 G277.76-51.74; <i>Middle:</i> PLCK G334.8-38.0; <i>Bottom:</i> PSZ2 G271.18-30.95. . . . .	95
B.1	Same as Fig. A.1. <i>Top:</i> MACSJ0011.7-1523; <i>Middle:</i> MACSJ0035.4-2015; <i>Bottom:</i> MACSJ0152.5-2852. . . . .	98
B.2	Same as Fig. A.1. <i>Top:</i> MACSJ0159.8-0849; <i>Middle:</i> MACSJ0242.6-2132; <i>Bottom:</i> MACSJ0257.6-2209. . . . .	99
B.3	Same as Fig. A.1. <i>Top:</i> MACSJ0404.6+1109; <i>Middle:</i> MACSJ0429.6-0253; <i>Bottom:</i> MACSJ0520.7-1328. . . . .	100
B.4	Same as Fig. A.1. <i>Top:</i> MACSJ0547.0-3904; <i>Middle:</i> MACSJ1206.2-0847; <i>Bottom:</i> MACSJ1319.9+7003. . . . .	101
B.5	Same as Fig. A.1. <i>Top:</i> MACSJ1427.6-2521; <i>Middle:</i> MACSJ1720.2+3536; <i>Bottom:</i> MACSJ1731.6+2252. . . . .	102
B.6	Same as Fig. A.1. <i>Top:</i> MACSJ1931.8-2634; <i>Middle:</i> MACSJ2049.9-3217; <i>Bottom:</i> MACSJ2140.2-2339. . . . .	103
B.7	Same as Fig. A.1. <i>Top:</i> MACSJ2229.7-2755; <i>Middle:</i> MACSJ2245.0+2637; <i>Bottom:</i> PLCK G214.6+36.9. . . . .	104

- B.8 Same as Fig. A.1. *Top*: PLCK G241.2-28.7; *Middle*: PLCK G272.9+48.8;  
*Bottom*: PLCK G100.2-30.4. . . . . 105
- B.9 Same as Fig. A.1. PLCK G250.0+24.1. . . . . 106

# List of Tables

2.1	Typical quantities of Galaxy Clusters . . . . .	18
2.2	Mass composition of Galaxy Clusters . . . . .	18
3.1	Characteristics of Radio Halos . . . . .	29
3.2	Collection of clusters known to host a radio halo. See continuation in Table	
3.3	. . . . .	36
3.3	Collection of clusters known to host a radio halo. Col. 1: Cluster name; Col. 2: SZ mass proxy $M_{500}$ (Planck Collaboration et al., 2016b); Col. 3: Redshift; Col. 4. Radio power of the RH at 1.4 GHz; Col. 5: <b>References.</b> (1) Giovannini et al. (2009); (2) Murgia et al. (2010);(3) Giovannini et al. (2011); (4) van Weeren et al. (2011); (5) Govoni et al. (2011); (6) Macario et al. (2011); (7) Govoni et al. (2012); (9) Vacca et al. (2011); (10) Farnsworth et al. (2013); (11) van Weeren et al. (2013); (12) van Weeren et al. (2014); (13) Giacintucci et al. (2013); (14) de Gasperin et al. (2015); (15) Bonafede et al. (2015); (16) Giacintucci et al. (2011); (17) Bonafede et al. (2012); (18) Dwarakanath et al. (2011); (19) Bonafede et al. (2009); (20) Pandey- Pommier et al. (2015); (21) Giovannini and Feretti (2000); (22) Brown et al. (2011a); (23) Bonafede et al. (2014b); (24) Lindner et al. (2014). . . . .	37
5.3	Physical properties of the diffuse radio source at 1.867 GHz from tapered images. <i>Col. 1</i> gives the identification numbers of the tapered images on which we have performed the measurements: ID 1: Image with source sub- traction in uv-data; ID 2: Image without source subtraction in uv-data; ID 2 ss: Image of ID2 after removing by hand the flux of point sources identified in the image plane. <i>Col. 2</i> and <i>Col. 3</i> correspond to the angular and phys- ical size of the source, respectively (see text). <i>Col. 4</i> reports the flux of the diffuse radio sources as measured with TVSTAT within the $3\sigma$ contours of the map with ID 2 ( <i>top</i> ), with TVSTAT within the $3\sigma$ contours calculated by PyBDSM for the map with ID 2 ( <i>bottom</i> ). . . . .	61



# Bibliography

- Abell, G. O. (1958). The Distribution of Rich Clusters of Galaxies. *ApJS*, 3:211. (Cited in page 20.)
- Abell, G. O., Corwin, Jr., H. G., and Olowin, R. P. (1989). A catalog of rich clusters of galaxies. *ApJS*, 70:1–138. (Cited in page 20.)
- Adam, R. (2015). *Observation des amas de galaxies par effet Sunyaev-Zel'dovich et de la polarisation du fond diffus cosmologique*. PhD thesis, Universite de Grenoble. (Cited in page 21.)
- Akritas, M. G. and Bershad, M. A. (1996). Linear Regression for Astronomical Data with Measurement Errors and Intrinsic Scatter. *ApJ*, 470:706. (Cited in page 65.)
- Bagchi, J., Sirothia, S. K., Werner, N., Pandge, M. B., Kantharia, N. G., Ishwara-Chandra, C. H., Gopal-Krishna, Paul, S., and Joshi, S. (2011). Discovery of the First Giant Double Radio Relic in a Galaxy Cluster Found in the Planck Sunyaev-Zel'dovich Cluster Survey: PLCK G287.0+32.9. *ApJ*, 736:L8. (Cited in page 51.)
- Bahcall, N. A., Ostriker, J. P., Perlmutter, S., and Steinhardt, P. J. (1999). The Cosmic Triangle: Revealing the State of the Universe. *Science*, 284:1481. (Cited in page 16.)
- Ballarati, B., Feretti, L., Ficarra, A., Giovannini, G., Nanni, M., Olori, M. C., and Gavazzi, G. (1981). 408 MHz observations of clusters of galaxies. I - Halo sources in the Coma-A 1367 supercluster. *A&A*, 100:323–325. (Cited in page 25.)
- Bartalucci, I., Arnaud, M., Pratt, G. W., Démoclès, J., van der Burg, R. F. J., and Mazzotta, P. (2017). Resolving galaxy cluster gas properties at  $z \sim 1$  with XMM-Newton and Chandra. *A&A*, 598:A61. (Cited in page 57.)
- Biviano, A. (2000). From Messier to Abell: 200 Years of Science with Galaxy Clusters. In *Constructing the Universe with Clusters of Galaxies*, page 1. (Cited in pages 15 and 20.)
- Blanton, E. L., Gregg, M. D., Helfand, D. J., Becker, R. H., and Leighly, K. M. (2001). The Environments of a Complete Moderate-Redshift Sample of FIRST Bent-Double Radio Sources. *AJ*, 121:2915–2927. (Cited in pages 70 and 74.)
- Boehringer, H. and Werner, N. (2009). X-ray Spectroscopy of Galaxy Clusters. *ArXiv e-prints*. (Cited in page 15.)
- Böhringer, H., Pratt, G. W., Arnaud, M., Borgani, S., Croston, J. H., Ponman, T. J., Ameglio, S., Temple, R. F., and Dolag, K. (2010). Substructure of the galaxy clusters in the REXCESS sample: observed statistics and comparison to numerical simulations. *A&A*, 514:A32. (Cited in pages 33 and 57.)

- Böhringer, H., Schuecker, P., Pratt, G. W., Arnaud, M., Ponman, T. J., Croston, J. H., Borgani, S., Bower, R. G., Briel, U. G., Collins, C. A., Donahue, M., Forman, W. R., Finoguenov, A., Geller, M. J., Guzzo, L., Henry, J. P., Kneissl, R., Mohr, J. J., Matsushita, K., Mullis, C. R., Ohashi, T., Pedersen, K., Pierini, D., Quintana, H., Raychaudhury, S., Reiprich, T. H., Romer, A. K., Rosati, P., Sabirli, K., Temple, R. F., Viana, P. T. P., Vikhlinin, A., Voit, G. M., and Zhang, Y.-Y. (2007). The representative XMM-Newton cluster structure survey (REXCESS) of an X-ray luminosity selected galaxy cluster sample. *A&A*, 469:363–377. (Cited in pages 21, 58 and 135.)
- Bonafede, A., Brüggén, M., van Weeren, R., Vazza, F., Giovannini, G., Ebeling, H., Edge, A. C., Hoeft, M., and Klein, U. (2012). Discovery of radio haloes and double relics in distant MACS galaxy clusters: clues to the efficiency of particle acceleration. *MNRAS*, 426:40–56. (Cited in pages 37 and 139.)
- Bonafede, A., Feretti, L., Giovannini, G., Govoni, F., Murgia, M., Taylor, G. B., Ebeling, H., Allen, S., Gentile, G., and Pihlström, Y. (2009). Revealing the magnetic field in a distant galaxy cluster: discovery of the complex radio emission from MACS J0717.5 +3745. *A&A*, 503:707–720. (Cited in pages 37 and 139.)
- Bonafede, A., Intema, H., Brüggén, M., Vazza, F., Basu, K., Sommer, M., Ebeling, H., de Gasperin, F., Röttgering, H. J. A., van Weeren, R. J., and Cassano, R. (2015). Radio haloes in Sunyaev-Zel'dovich-selected clusters of galaxies: the making of a halo? *MNRAS*, 454:3391–3402. (Cited in pages 37, 74, 89 and 139.)
- Bonafede, A., Intema, H. T., Brüggén, M., Girardi, M., Nonino, M., Kantharia, N., van Weeren, R. J., and Röttgering, H. J. A. (2014a). Evidence for Particle Re-acceleration in the Radio Relic in the Galaxy Cluster PLCKG287.0+32.9. *ApJ*, 785:1. (Cited in pages 26 and 89.)
- Bonafede, A., Intema, H. T., Brüggén, M., Russell, H. R., Ogrean, G., Basu, K., Sommer, M., van Weeren, R. J., Cassano, R., Fabian, A. C., and Röttgering, H. J. A. (2014b). A giant radio halo in the cool core cluster CL1821+643. *MNRAS*, 444:L44–L48. (Cited in pages 29, 37 and 139.)
- Borgani, S. and Guzzo, L. (2001). X-ray clusters of galaxies as tracers of structure in the Universe. *Nature*, 409:39–45. (Cited in page 15.)
- Bravi, L., Gitti, M., and Brunetti, G. (2016). Do radio mini-halos and gas heating in cool-core clusters have a common origin? *MNRAS*, 455:L41–L45. (Cited in page 27.)
- Brown, G. and Bethe, H. A. (1985). How a supernova explodes. *Scientific American*, 252:60–68. (Cited in page 7.)
- Brown, S., Duesterhoeft, J., and Rudnick, L. (2011a). Multiple Shock Structures in a Radio-selected Cluster of Galaxies. *ApJ*, 727:L25. (Cited in pages 37 and 139.)

- Brown, S., Emerick, A., Rudnick, L., and Brunetti, G. (2011b). Probing the Off-state of Cluster Giant Radio Halos. *ApJ*, 740:L28. (Cited in page 31.)
- Brown, S. and Rudnick, L. (2011). Diffuse radio emission in/around the Coma cluster: beyond simple accretion. *MNRAS*, 412:2–12. (Cited in pages 28 and 134.)
- Brüggen, M., Bykov, A., Ryu, D., and Röttgering, H. (2012). Magnetic Fields, Relativistic Particles, and Shock Waves in Cluster Outskirts. *Space Sci. Rev.*, 166:187–213. (Cited in page 25.)
- Brunetti, G. (2009). Constraining relativistic protons and magnetic fields in galaxy clusters through radio and  $\gamma$ -ray observations: the case of A2256. *A&A*, 508:599–602. (Cited in page 31.)
- Brunetti, G. (2011). Cosmic rays and diffuse non-thermal emission in galaxy clusters: an introduction. *Mem. Soc. Astron. Italiana*, 82:515. (Cited in page 25.)
- Brunetti, G. and Blasi, P. (2005). Alfvénic reacceleration of relativistic particles in galaxy clusters in the presence of secondary electrons and positrons. *MNRAS*, 363:1173–1187. (Cited in page 31.)
- Brunetti, G., Blasi, P., Reimer, O., Rudnick, L., Bonafede, A., and Brown, S. (2012). Probing the origin of giant radio haloes through radio and  $\gamma$ -ray data: the case of the Coma cluster. *MNRAS*, 426:956–968. (Cited in page 31.)
- Brunetti, G., Cassano, R., Dolag, K., and Setti, G. (2009). On the evolution of giant radio halos and their connection with cluster mergers. *A&A*, 507:661–669. (Cited in page 74.)
- Brunetti, G., Giacintucci, S., Cassano, R., Lane, W., Dallacasa, D., Venturi, T., Kassim, N. E., Setti, G., Cotton, W. D., and Markevitch, M. (2008). A low-frequency radio halo associated with a cluster of galaxies. *Nature*, 455:944–947. (Cited in pages 30 and 74.)
- Brunetti, G. and Jones, T. W. (2014). Cosmic Rays in Galaxy Clusters and Their Nonthermal Emission. *International Journal of Modern Physics D*, 23:30007. (Cited in pages 18, 25, 26, 28, 30 and 31.)
- Brunetti, G. and Lazarian, A. (2011). Acceleration of primary and secondary particles in galaxy clusters by compressible MHD turbulence: from radio haloes to gamma-rays. *MNRAS*, 410:127–142. (Cited in page 31.)
- Buote, D. A. (2001). On the Origin of Radio Halos in Galaxy Clusters. *ApJ*, 553:L15–L18. (Cited in page 32.)
- Burke, B. F. and Graham-Smith, F. (2014). *An Introduction to Radio Astronomy*. (Cited in page 11.)

- Burns, J. O. (1986). Very large structures in the universe. *Scientific American*, 255:38–47. (Cited in page 16.)
- Burns, J. O. and Owen, F. N. (1979). Radio sources in Zwicky clusters of galaxies. II - Detailed interferometer observations and analysis. *AJ*, 84:1478–1499. (Cited in pages 70 and 74.)
- Callingham, J. R., Gaensler, B. M., Zanardo, G., Staveley-Smith, L., Hancock, P. J., Hurley-Walker, N., Bell, M. E., Dwarakanath, K. S., Franzen, T. M. O., Hindson, L., Johnston-Hollitt, M., Kapińska, A., For, B.-Q., Lenc, E., McKinley, B., Morgan, J., Offringa, A. R., Procopio, P., Wayth, R. B., Wu, C., and Zheng, Q. (2016). Low radio frequency observations and spectral modelling of the remnant of Supernova 1987A. *MNRAS*, 462:290–297. (Cited in page 7.)
- Carlstrom, J. E., Holder, G. P., and Reese, E. D. (2002). Cosmology with the Sunyaev-Zel'dovich Effect. *ARA&A*, 40:643–680. (Cited in page 21.)
- Cassano, R., Bernardi, G., Brunetti, G., Brüggén, M., Clarke, T., Dallacasa, D., Dolag, K., Ettori, S., Giacintucci, S., Giocoli, C., Gitti, M., Johnston-Hollitt, M., Kale, R., Markevich, M., Norris, R., Pommier, M. P., Pratt, G., Rottgering, H. J. A., and Venturi, T. (2015). Cluster Radio Halos at the crossroads between astrophysics and cosmology in the SKA era. *Advancing Astrophysics with the Square Kilometre Array (AASKA14)*, page 73. (Cited in page 91.)
- Cassano, R. and Brunetti, G. (2005). Cluster mergers and non-thermal phenomena: a statistical magneto-turbulent model. *MNRAS*, 357:1313–1329. (Cited in page 30.)
- Cassano, R., Brunetti, G., Norris, R. P., Röttgering, H. J. A., Johnston-Hollitt, M., and Trasatti, M. (2012). Radio halos in future surveys in the radio continuum. *A&A*, 548:A100. (Cited in pages 75, 76 and 137.)
- Cassano, R., Brunetti, G., and Setti, G. (2004). Occurrence and Luminosity Functions of Giant Radio Halos from Magneto-Turbulent Model. *Journal of Korean Astronomical Society*, 37:589–592. (Cited in page 41.)
- Cassano, R., Brunetti, G., and Setti, G. (2006). Statistics of giant radio haloes from electron reacceleration models. *MNRAS*, 369:1577–1595. (Cited in pages 32, 41, 74 and 75.)
- Cassano, R., Brunetti, G., Setti, G., Govoni, F., and Dolag, K. (2007). New scaling relations in cluster radio haloes and the re-acceleration model. *MNRAS*, 378:1565–1574. (Cited in pages 65, 66 and 136.)
- Cassano, R., Ettori, S., Brunetti, G., Giacintucci, S., Pratt, G. W., Venturi, T., Kale, R., Dolag, K., and Markevitch, M. (2013). Revisiting Scaling Relations for Giant Radio Halos

- in Galaxy Clusters. *ApJ*, 777:141. (Cited in pages 32, 33, 34, 57, 58, 65, 73, 74, 76, 90, 134, 135 and 136.)
- Cassano, R., Ettori, S., Giacintucci, S., Brunetti, G., Markevitch, M., Venturi, T., and Gitti, M. (2010a). On the Connection Between Giant Radio Halos and Cluster Mergers. *ApJ*, 721:L82–L85. (Cited in pages 29, 32, 33, 34, 35, 90 and 134.)
- Cassano, R., Ettori, S., Giacintucci, S., Brunetti, G., Markevitch, M., Venturi, T., and Gitti, M. (2010b). On the Connection Between Giant Radio Halos and Cluster Mergers. *ApJ*, 721:L82–L85. (Cited in page 74.)
- Chandra (2016). Chandra. [http://chandra.si.edu/press/16\\_releases/press\\_083016.html](http://chandra.si.edu/press/16_releases/press_083016.html). [Online; accessed 23-May-2017]. (Cited in page 21.)
- Chon, G., Böhringer, H., and Zaroubi, S. (2015). On the definition of superclusters. *A&A*, 575:L14. (Cited in pages 16 and 17.)
- Clarke, R. W. (1966). Locating Radio Sources with the Moon. *Scientific American*, 214:30–41. (Cited in page 7.)
- Clarke, T. E. and Ensslin, T. (2006). Mergers, relics and magnetic fields: The complex case of A2256. *Astronomische Nachrichten*, 327:553. (Cited in page 26.)
- Condon, J. J., Cotton, W. D., Greisen, E. W., Yin, Q. F., Perley, R. A., Taylor, G. B., and Broderick, J. J. (1998). The NRAO VLA Sky Survey. *AJ*, 115:1693–1716. (Cited in page 48.)
- Courtois, H. (2016). *Voyage sur les flots de galaxies*. (Cited in page 16.)
- Croston, J. H., Pratt, G. W., Böhringer, H., Arnaud, M., Pointecouteau, E., Ponman, T. J., Sanderson, A. J. R., Temple, R. F., Bower, R. G., and Donahue, M. (2008). Galaxy-cluster gas-density distributions of the representative XMM-Newton cluster structure survey (REXCESS). *A&A*, 487:431–443. (Cited in page 56.)
- Cuciti, V., Cassano, R., Brunetti, G., Dallacasa, D., Kale, R., Ettori, S., and Venturi, T. (2015). Occurrence of radio halos in galaxy clusters. Insight from a mass-selected sample. *A&A*, 580:A97. (Cited in page 29.)
- de Blok, W. J. G., Fraternali, F., Heald, G. H., Adams, E. A. K., Bosma, A., Koribalski, B. S., and the HI Science Working Group (2015). The SKA view of the Neutral Interstellar Medium in Galaxies. *ArXiv e-prints*. (Cited in page 9.)
- de Gasperin, F., Intema, H. T., van Weeren, R. J., Dawson, W. A., Golovich, N., Wittman, D., Bonafede, A., and Brüggén, M. (2015). A powerful double radio relic system discovered in PSZ1 G108.18-11.53: evidence for a shock with non-uniform Mach number? *MNRAS*, 453:3483–3498. (Cited in pages 37 and 139.)

- DeBoer, D. R., Parsons, A. R., Aguirre, J. E., Alexander, P., Ali, Z. S., Beardsley, A. P., Bernardi, G., Bowman, J. D., Bradley, R. F., Carilli, C. L., Cheng, C., de Lera Acedo, E., Dillon, J. S., Ewall-Wice, A., Fadana, G., Fagnoni, N., Fritz, R., Furlanetto, S. R., Glendenning, B., Greig, B., Grobbelaar, J., Hazelton, B. J., Hewitt, J. N., Hickish, J., Jacobs, D. C., Julius, A., Kariseb, M., Kohn, S. A., Lekalake, T., Liu, A., Loots, A., MacMahon, D., Malan, L., Malgas, C., Maree, M., Martinot, Z., Mathison, N., Matsetela, E., Mesinger, A., Morales, M. F., Neben, A. R., Patra, N., Pieterse, S., Pober, J. C., Razavi-Ghods, N., Ringuette, J., Robnett, J., Rosie, K., Sell, R., Smith, C., Syce, A., Tegmark, M., Thyagarajan, N., Williams, P. K. G., and Zheng, H. (2017). Hydrogen Epoch of Reionization Array (HERA). *PASP*, 129(4):045001. (Cited in page 13.)
- Deiss, B. M., Reich, W., Lesch, H., and Wielebinski, R. (1997). The large-scale structure of the diffuse radio halo of the Coma cluster at 1.4GHz. *A&A*, 321:55–63. (Cited in page 29.)
- Dennison, B. (1980). Formation of radio halos in clusters of galaxies from cosmic-ray protons. *ApJ*, 239:L93–L96. (Cited in page 31.)
- Donnert, J., Dolag, K., Brunetti, G., and Cassano, R. (2013). Rise and fall of radio haloes in simulated merging galaxy clusters. *MNRAS*, 429:3564–3569. (Cited in page 74.)
- Dubner, G. and Giacani, E. (2015). Radio emission from supernova remnants. *A&A Rev.*, 23:3. (Cited in page 7.)
- Dulk, G. A. (1985). Radio emission from the sun and stars. *ARA&A*, 23:169–224. (Cited in page 6.)
- Dwarakanath, K. S., Malu, S., and Kale, R. (2011). Discovery of a Giant Radio Halo in a Massive Merging Cluster at  $z = 0.443$ . *Journal of Astrophysics and Astronomy*, 32:529–532. (Cited in pages 37, 51 and 139.)
- Ebeling, H., Edge, A. C., Mantz, A., Barrett, E., Henry, J. P., Ma, C. J., and van Speybroeck, L. (2010). The X-ray brightest clusters of galaxies from the Massive Cluster Survey. *MNRAS*, 407:83–93. (Cited in page 42.)
- Elitzur, M. (1995). Masers in the Sky. *Scientific American*, 272:68. (Cited in page 10.)
- Enßlin, T. A. and Röttgering, H. (2002). The radio luminosity function of cluster radio halos. *A&A*, 396:83–89. (Cited in page 90.)
- Ewen, H. I. (1953). Radio Waves from Interstellar Hydrogen. *Scientific American*, 189:42–46. (Cited in page 8.)
- Fanaroff, B. L. and Riley, J. M. (1974). The morphology of extragalactic radio sources of high and low luminosity. *MNRAS*, 167:31P–36P. (Cited in page 11.)

- Farnsworth, D., Rudnick, L., Brown, S., and Brunetti, G. (2013). Discovery of Megaparsec-scale, Low Surface Brightness Nonthermal Emission in Merging Galaxy Clusters Using the Green Bank Telescope. *ApJ*, 779:189. (Cited in pages 37 and 139.)
- Feretti, L. (1999). Observational Results on Cluster Diffuse Emission. In Boehringer, H., Feretti, L., and Schuecker, P., editors, *Diffuse Thermal and Relativistic Plasma in Galaxy Clusters*, page 3. (Cited in page 29.)
- Feretti, L. (2002). Observational Properties of Diffuse Halos in Clusters. In Pramesh Rao, A., Swarup, G., and Gopal-Krishna, editors, *The Universe at Low Radio Frequencies*, volume 199 of *IAU Symposium*, page 133. (Cited in page 32.)
- Feretti, L., Fusco-Femiano, R., Giovannini, G., and Govoni, F. (2001). The giant radio halo in Abell 2163. *A&A*, 373:106–112. (Cited in page 29.)
- Feretti, L. and Giovannini, G. (1996). Diffuse Cluster Radio Sources (Review). In Ekers, R. D., Fanti, C., and Padrielli, L., editors, *Extragalactic Radio Sources*, volume 175 of *IAU Symposium*, page 333. (Cited in page 25.)
- Feretti, L., Giovannini, G., Govoni, F., and Murgia, M. (2012). Clusters of galaxies: observational properties of the diffuse radio emission. *A&A Rev.*, 20:54. (Cited in pages 23, 24, 25, 29, 30, 41 and 133.)
- Fermi, E. (1949). On the Origin of the Cosmic Radiation. *Physical Review*, 75:1169–1174. (Cited in page 30.)
- Ferrari, C., Dabbech, A., Smirnov, O., Makhathini, S., Kenyon, J. S., Murgia, M., Govoni, F., Mary, D., Slezak, E., Vazza, F., Bonafede, A., Brugger, M., Johnston-Hollitt, M., Dehghan, S., Feretti, L., Giovannini, G., Vacca, V., Wise, M. W., Gitti, M., Arnaud, M., Pratt, G., Zarb Adami, K., and Colafrancesco, S. (2015). Non-thermal emission from galaxy clusters: feasibility study with SKA. *Advancing Astrophysics with the Square Kilometre Array (AASKA14)*, page 75. (Cited in page 91.)
- Ferrari, C., Govoni, F., Schindler, S., Bykov, A. M., and Rephaeli, Y. (2008). Observations of Extended Radio Emission in Clusters. *Space Sci. Rev.*, 134:93–118. (Cited in page 25.)
- Fomalont, E. B. and Bridle, A. H. (1978). The Radio Source 0915+320: A 'Wide-Angle-Tail' Source in a Group of Galaxies. *ApJ*, 223:L9–L12. (Cited in pages 70 and 74.)
- Giacintucci, S., Dallacasa, D., Venturi, T., Brunetti, G., Cassano, R., Markevitch, M., and Athreya, R. M. (2011). An unlikely radio halo in the low X-ray luminosity galaxy cluster RXC J1514.9-1523. *A&A*, 534:A57. (Cited in pages 37 and 139.)
- Giacintucci, S., Kale, R., Wik, D. R., Venturi, T., and Markevitch, M. (2013). Discovery of a Giant Radio Halo in a New Planck Galaxy Cluster PLCKG171.9-40.7. *ApJ*, 766:18. (Cited in pages 37 and 139.)

- Giacintucci, S., Markevitch, M., Brunetti, G., ZuHone, J. A., Venturi, T., Mazzotta, P., and Bourdin, H. (2014a). Mapping the Particle Acceleration in the Cool Core of the Galaxy Cluster RX J1720.1+2638. *ApJ*, 795:73. (Cited in pages 27 and 133.)
- Giacintucci, S., Markevitch, M., Cassano, R., Venturi, T., Clarke, T. E., and Brunetti, G. (2017a). Occurrence of radio minihalos in a mass-limited sample of galaxy clusters. *ArXiv e-prints*. (Cited in pages 27 and 28.)
- Giacintucci, S., Markevitch, M., Cassano, R., Venturi, T., Clarke, T. E., and Brunetti, G. (2017b). Occurrence of Radio Minihalos in a Mass-limited Sample of Galaxy Clusters. *ApJ*, 841:71. (Cited in page 69.)
- Giacintucci, S., Markevitch, M., Venturi, T., Clarke, T. E., Cassano, R., and Mazzotta, P. (2014b). New Detections of Radio Minihalos in Cool Cores of Galaxy Clusters. *ApJ*, 781:9. (Cited in page 27.)
- Giacintucci, S. and Venturi, T. (2009). Tailed radio galaxies as tracers of galaxy clusters. Serendipitous discoveries with the GMRT. *A&A*, 505:55–61. (Cited in pages 70 and 74.)
- Giacintucci, S., Venturi, T., Macario, G., Dallacasa, D., Brunetti, G., Markevitch, M., Cassano, R., Bardelli, S., and Athreya, R. (2008). Shock acceleration as origin of the radio relic in A 521? *A&A*, 486:347–358. (Cited in page 26.)
- Giovannini, G., Bonafede, A., Brown, S., Feretti, L., Ferrari, C., Gitti, M., Govoni, F., Murgia, M., and Vacca, V. (2015). Mega-parsec scale magnetic fields in low density regions in the SKA era: filaments connecting galaxy clusters and groups. *Advancing Astrophysics with the Square Kilometre Array (AASKA14)*, page 104. (Cited in page 89.)
- Giovannini, G., Bonafede, A., Feretti, L., Govoni, F., Murgia, M., Ferrari, F., and Monti, G. (2009). Radio halos in nearby ( $z < 0.4$ ) clusters of galaxies. *A&A*, 507:1257–1270. (Cited in pages 37 and 139.)
- Giovannini, G. and Feretti, L. (2000). Halo and relic sources in clusters of galaxies. *New A*, 5:335–347. (Cited in pages 37, 65 and 139.)
- Giovannini, G. and Feretti, L. (2002a). Diffuse Radio Sources and Cluster Mergers: Radio Halos and Relics. In Feretti, L., Gioia, I. M., and Giovannini, G., editors, *Merging Processes in Galaxy Clusters*, volume 272 of *Astrophysics and Space Science Library*, pages 197–227. (Cited in page 29.)
- Giovannini, G. and Feretti, L. (2002b). Diffuse Radio Sources and Cluster Mergers: Radio Halos and Relics. In Feretti, L., Gioia, I. M., and Giovannini, G., editors, *Merging Processes in Galaxy Clusters*, volume 272 of *Astrophysics and Space Science Library*, pages 197–227. (Cited in page 40.)

- Giovannini, G., Feretti, L., Girardi, M., Govoni, F., Murgia, M., Vacca, V., and Bagchi, J. (2011). A giant radio halo in the low luminosity X-ray cluster Abell 523. *A&A*, 530:L5. (Cited in pages 37 and 139.)
- Giovannini, G., Feretti, L., and Stanghellini, C. (1991). The Coma cluster radio source 1253 + 275, revisited. *A&A*, 252:528–537. (Cited in page 25.)
- Giovannini, G., Tordi, M., and Feretti, L. (1999). Radio halo and relic candidates from the NRAO VLA Sky Survey. *New A*, 4:141–155. (Cited in pages 25 and 29.)
- Gitti, M., Brunetti, G., and Setti, G. (2002). Modeling the interaction between ICM and relativistic plasma in cooling flows: The case of the Perseus cluster. *A&A*, 386:456–463. (Cited in page 27.)
- Gitti, M., Feretti, L., and Schindler, S. (2006). Multifrequency VLA radio observations of the X-ray cavity cluster of galaxies RBS797: evidence of differently oriented jets. *A&A*, 448:853–860. (Cited in page 51.)
- Gitti, M., Tozzi, P., Brunetti, G., Cassano, R., Dallacasa, D., Edge, A., Ettori, S., Feretti, L., Ferrari, C., Giacintucci, S., Giovannini, G., Hogan, M., and Venturi, T. (2015). The SKA view of cool-core clusters: evolution of radio mini-halos and AGN feedback. *Advancing Astrophysics with the Square Kilometre Array (AASKA14)*, page 76. (Cited in page 68.)
- Gott, J. R. (2016). *The Cosmic Web: Mysterious Architecture of the Universe*. (Cited in page 16.)
- Govoni, F. (2006). Observations of magnetic fields in regular and irregular clusters. *Astronomische Nachrichten*, 327:539. (Cited in page 28.)
- Govoni, F., Enßlin, T. A., Feretti, L., and Giovannini, G. (2001a). A comparison of radio and X-ray morphologies of four clusters of galaxies containing radio halos. *A&A*, 369:441–449. (Cited in pages 29 and 32.)
- Govoni, F., Feretti, L., Giovannini, G., Böhringer, H., Reiprich, T. H., and Murgia, M. (2001b). Radio and X-ray diffuse emission in six clusters of galaxies. *A&A*, 376:803–819. (Cited in page 51.)
- Govoni, F., Ferrari, C., Feretti, L., Vacca, V., Murgia, M., Giovannini, G., Perley, R., and Benoist, C. (2012). Detection of diffuse radio emission in the galaxy clusters A800, A910, A1550, and CL 1446+26. *A&A*, 545:A74. (Cited in pages 37, 67, 74, 89 and 139.)
- Govoni, F., Markevitch, M., Vikhlinin, A., van Speybroeck, L., Feretti, L., and Giovannini, G. (2004). Chandra Temperature Maps for Galaxy Clusters with Radio Halos. *ApJ*, 605:695–708. (Cited in page 32.)

- Govoni, F., Murgia, M., Giovannini, G., Vacca, V., and Bonafede, A. (2011). The large-scale diffuse radio emission in A781. *A&A*, 529:A69. (Cited in pages 37 and 139.)
- Green, J., Van Langevelde, H. J., Brunthaler, A., Ellingsen, S., Imai, H., Vlemmings, W. H. T., Reid, M. J., and Richards, A. M. S. (2015). Maser Astrometry with VLBI and the SKA. *Advancing Astrophysics with the Square Kilometre Array (AASKA14)*, page 119. (Cited in page 10.)
- Gurzadyan, G. A. (1997). *The Physics and Dynamics of Planetary Nebulae*. (Cited in page 8.)
- Harrison, E. R. (1990). The Dark Night Sky Riddle - Olber's Paradox. In Bowyer, S. and Leinert, C., editors, *The Galactic and Extragalactic Background Radiation*, volume 139 of *IAU Symposium*, page 3. (Cited in page 4.)
- Harrison, E. R. (2000). *Cosmology. The science of the universe*. (Cited in page 12.)
- Henry, J. P., Briel, U. G., and Böhringer, H. (1998). The Evolution of Galaxy Clusters. *Scientific American*, 279:52–57. (Cited in pages 15, 16, 17 and 18.)
- Hood, A. W. and Hughes, D. W. (2011). Solar magnetic fields. *Physics of the Earth and Planetary Interiors*, 187:78–91. (Cited in page 6.)
- Hudson, D. S., Mittal, R., Reiprich, T. H., Nulsen, P. E. J., Andernach, H., and Sarazin, C. L. (2010). What is a cool-core cluster? a detailed analysis of the cores of the X-ray flux-limited HIFLUGCS cluster sample. *A&A*, 513:A37. (Cited in page 56.)
- Intema, H. T., van der Tol, S., Cotton, W. D., Cohen, A. S., van Bemmell, I. M., and Röttgering, H. J. A. (2009). Ionospheric calibration of low frequency radio interferometric observations using the peeling scheme. I. Method description and first results. *A&A*, 501:1185–1205. (Cited in page 48.)
- Jacoby (2016). A planetary nebula sampler — national optical astronomy observatory. [https://www.noao.edu/jacoby/pn\\_gallery.html](https://www.noao.edu/jacoby/pn_gallery.html). [Online; accessed 29-November-2016]. (Cited in page 8.)
- Jarvis, M., Bacon, D., Blake, C., Brown, M., Lindsay, S., Raccanelli, A., Santos, M., and Schwarz, D. J. (2015). Cosmology with SKA Radio Continuum Surveys. *Advancing Astrophysics with the Square Kilometre Array (AASKA14)*, page 18. (Cited in page 13.)
- Jeltema, T. E. and Profumo, S. (2011). Implications of Fermi Observations For Hadronic Models of Radio Halos in Clusters of Galaxies. *ApJ*, 728:53. (Cited in page 31.)
- Kale, R. and Parekh, V. (2016). How unusual is the cool-core radio halo cluster CL1821+643? *MNRAS*, 459:2940–2947. (Cited in page 29.)

- Kale, R., Venturi, T., Giacintucci, S., Dallacasa, D., Cassano, R., Brunetti, G., Cuciti, V., Macario, G., and Athreya, R. (2015). The Extended GMRT Radio Halo Survey. II. Further results and analysis of the full sample. *A&A*, 579:A92. (Cited in page 40.)
- Kale, R., Venturi, T., Giacintucci, S., Dallacasa, D., Cassano, R., Brunetti, G., Macario, G., and Athreya, R. (2013). The Extended GMRT Radio Halo Survey. I. New upper limits on radio halos and mini-halos. *A&A*, 557:A99. (Cited in pages 40, 72, 75, 76 and 137.)
- Kang, H., Ryu, D., and Jones, T. W. (2012). Diffusive Shock Acceleration Simulations of Radio Relics. *ApJ*, 756:97. (Cited in page 25.)
- Kempner, J. C. and Sarazin, C. L. (2001). Radio Halo and Relic Candidates from the Westerbork Northern Sky Survey. *ApJ*, 548:639–651. (Cited in page 65.)
- Keshet, U. and Loeb, A. (2010). Using Radio Halos and Minihalos to Measure the Distributions of Magnetic Fields and Cosmic Rays in Galaxy Clusters. *ApJ*, 722:737–749. (Cited in page 18.)
- Koeln Physikalisches Institut (2016). Molecules in space — universitat zu koln. <https://www.astro.uni-koeln.de/cdms/molecules>. [Online; accessed 30-November-2016]. (Cited in page 9.)
- Koester, B. P., McKay, T. A., Annis, J., Wechsler, R. H., Evrard, A., Bleem, L., Becker, M., Johnston, D., Sheldon, E., Nichol, R., Miller, C., Scranton, R., Bahcall, N., Barentine, J., Brewington, H., Brinkmann, J., Harvanek, M., Kleinman, S., Krzesinski, J., Long, D., Nitta, A., Schneider, D. P., Sneddin, S., Voges, W., and York, D. (2007). A MaxBCG Catalog of 13,823 Galaxy Clusters from the Sloan Digital Sky Survey. *ApJ*, 660:239–255. (Cited in page 20.)
- Koopmans, L., Pritchard, J., Mellema, G., Aguirre, J., Ahn, K., Barkana, R., van Bemmell, I., Bernardi, G., Bonaldi, A., Briggs, F., de Bruyn, A. G., Chang, T. C., Chapman, E., Chen, X., Ciardi, B., Dayal, P., Ferrara, A., Fialkov, A., Fiore, F., Ichiki, K., Illiev, I. T., Inoue, S., Jelic, V., Jones, M., Lazio, J., Maio, U., Majumdar, S., Mack, K. J., Mesinger, A., Morales, M. F., Parsons, A., Pen, U. L., Santos, M., Schneider, R., Semelin, B., de Souza, R. S., Subrahmanyam, R., Takeuchi, T., Vedantham, H., Wagg, J., Webster, R., Wyithe, S., Datta, K. K., and Trott, C. (2015). The Cosmic Dawn and Epoch of Reionisation with SKA. *Advancing Astrophysics with the Square Kilometre Array (AASKA14)*, page 1. (Cited in page 13.)
- Kragh, H. (1999). *Cosmology and Controversy: The Historical Development of Two Theories of the Universe*. (Cited in page 12.)
- Kupriyanova, E. G., Kashapova, L. K., Reid, H. A. S., and Myagkova, I. N. (2016). Relationship of Type III Radio Bursts with Quasi-periodic Pulsations in a Solar Flare. *Sol. Phys.* (Cited in page 6.)

- Large, M. I., Mathewson, D. S., and Haslam, C. G. T. (1959). A High-Resolution Survey of the Coma Cluster of Galaxies at 408 Mc/s. *Nature*, 183:1663–1664. (Cited in page 25.)
- Lilley (1957). The absorption of radio waves in space. *Scientific American*. [Online; accessed 30-November-2016]. (Cited in page 9.)
- Lindner, R. R., Baker, A. J., Hughes, J. P., Battaglia, N., Gupta, N., Knowles, K., Marriage, T. A., Menanteau, F., Moodley, K., Reese, E. D., and Srianand, R. (2014). The Radio Relics and Halo of El Gordo, a Massive  $z = 0.870$  Cluster Merger. *ApJ*, 786:49. (Cited in pages 37 and 139.)
- Longair, M. S. (2013). *The Cosmic Century*. (Cited in pages 1, 2 and 3.)
- Lynden-Bell, D. (1969). Galactic Nuclei as Collapsed Old Quasars. *Nature*, 223:690–694. (Cited in page 11.)
- Macario, G., Intema, H. T., Ferrari, C., Bourdin, H., Giacintucci, S., Venturi, T., Mazzotta, P., Bartalucci, I., Johnston-Hollitt, M., Cassano, R., Dallacasa, D., Pratt, G. W., Kale, R., and Brown, S. (2014). Discovery of large-scale diffuse radio emission and of a new galaxy cluster in the surroundings of MACS J0520.7-1328. *A&A*, 565:A13. (Cited in pages 48 and 83.)
- Macario, G., Markevitch, M., Giacintucci, S., Brunetti, G., Venturi, T., and Murray, S. S. (2011). A Shock Front in the Merging Galaxy Cluster A754: X-ray and Radio Observations. *ApJ*, 728:82. (Cited in pages 37 and 139.)
- Macario, G., Venturi, T., Brunetti, G., Dallacasa, D., Giacintucci, S., Cassano, R., Bardelli, S., and Athreya, R. (2010). The very steep spectrum radio halo in Abell 697. *A&A*, 517:A43. (Cited in page 30.)
- Malik (2012). Cosmology with the cosmic microwave background. <http://article.sapub.org/10.5923.j.astronomy.20130202.01.html#Sec1>. [Online; accessed 17-July-2017]. (Cited in page 13.)
- Manchester, R. N. (2010). Detection of Gravitational Waves using Pulsar Timing. *ArXiv e-prints*. (Cited in page 10.)
- Mann, A. W. and Ebeling, H. (2012). X-ray-optical classification of cluster mergers and the evolution of the cluster merger fraction. *MNRAS*, 420:2120–2138. (Cited in pages 80, 81 and 83.)
- Markevitch, M. (2010). Intergalactic shock fronts. *ArXiv e-prints*. (Cited in page 26.)
- Markevitch, M. and Vikhlinin, A. (2007). Shocks and cold fronts in galaxy clusters. *Phys. Rep.*, 443:1–53. (Cited in page 26.)

- Martinez Aviles, G., Ferrari, C., Johnston-Hollitt, M., Pratley, L., Macario, G., Venturi, T., Brunetti, G., Cassano, R., Dallacasa, D., Intema, H. T., Giacintucci, S., Hurier, G., Aghanim, N., Douspis, M., and Langer, M. (2016). ATCA observations of the MACS-Planck Radio Halo Cluster Project. I. New detection of a radio halo in PLCK G285.0-23.7. *A&A*, 595:A116. (Cited in page 53.)
- Maughan, B. J., Jones, C., Forman, W., and Van Speybroeck, L. (2008). Images, Structural Properties, and Metal Abundances of Galaxy Clusters Observed with Chandra ACIS-I at  $0.1 < z < 1.3$ . *ApJS*, 174:117–135. (Cited in page 33.)
- Max-Planck-Gesellschaft (2014). Interstellar molecule with branched backbone. <https://www.mpg.de/8428517/interstellar-molecules>. [Online; accessed 16-July-2017]. (Cited in page 9.)
- Mazzotta, P. and Giacintucci, S. (2008). Do Radio Core-Halos and Cold Fronts in Non-Major-Merging Clusters Originate from the Same Gas Sloshing? *ApJ*, 675:L9. (Cited in page 27.)
- McNamara, G. (2008). *Clocks in the Sky: The Story of Pulsars*. (Cited in page 10.)
- Mitton, S. (2011). *Fred Hoyle*. (Cited in pages 2, 3 and 12.)
- Mohan, N. and Rafferty, D. (2015). PyBDSM: Python Blob Detection and Source Measurement. Astrophysics Source Code Library. (Cited in page 62.)
- Mohr, J. J., Fabricant, D. G., and Geller, M. J. (1993). Using X ray images to detect substructure in a sample of 40 Abell clusters. In Shull, J. M. and Thronson, H. A., editors, *Evolution of Galaxies and their Environment*. (Cited in page 33.)
- Munns, D. (2013). *A single Sky*. (Cited in page 3.)
- Murgia, M., Govoni, F., Feretti, L., and Giovannini, G. (2010). A double radio halo in the close pair of galaxy clusters Abell 399 and Abell 401. *A&A*, 509:A86. (Cited in pages 37 and 139.)
- Murgia, M., Govoni, F., Markevitch, M., Feretti, L., Giovannini, G., Taylor, G. B., and Carretti, E. (2009). Comparative analysis of the diffuse radio emission in the galaxy clusters A1835, A2029, and Ophiuchus. *A&A*, 499:679–695. (Cited in pages 66 and 90.)
- Narlikar, J. V. and Burbidge, G. (2008). *Facts and Speculations in Cosmology*. Cambridge University Press. (Cited in page 12.)
- Norris, R. P., Hopkins, A. M., Afonso, J., Brown, S., Condon, J. J., Dunne, L., Feain, I., Hollow, R., Jarvis, M., Johnston-Hollitt, M., Lenc, E., Middelberg, E., Padovani, P., Prandoni, I., Rudnick, L., Seymour, N., Umana, G., Andernach, H., Alexander, D. M., Appleton,

- P. N., Bacon, D., Banfield, J., Becker, W., Brown, M. J. I., Ciliegi, P., Jackson, C., Eales, S., Edge, A. C., Gaensler, B. M., Giovannini, G., Hales, C. A., Hancock, P., Huynh, M. T., Ibar, E., Ivison, R. J., Kennicutt, R., Kimball, A. E., Koekemoer, A. M., Koribalski, B. S., López-Sánchez, Á. R., Mao, M. Y., Murphy, T., Messias, H., Pimbblet, K. A., Raccanelli, A., Randall, K. E., Reiprich, T. H., Roseboom, I. G., Röttgering, H., Saikia, D. J., Sharp, R. G., Slee, O. B., Smail, I., Thompson, M. A., Urquhart, J. S., Wall, J. V., and Zhao, G.-B. (2011). EMU: Evolutionary Map of the Universe. *PASA*, 28:215–248. (Cited in page 76.)
- NRAO (2016). Thermal radio emission from hii regions — national radio astronomy observatory. <http://www.cv.nrao.edu/course/astr534/HIIRegions.html>. [Online; accessed 29-November-2016]. (Cited in page 8.)
- Nussbaumer, H. and Bieri, L. (2010). *Discovering the Expanding Universe*. (Cited in page 16.)
- Ostriker, J. P. (1971). The Nature of Pulsars. *Scientific American*, 224:48–60. (Cited in page 10.)
- Padovani, P. (2016). The Faint Radio Sky: Radio Astronomy Becomes Mainstream. In *Active Galactic Nuclei 12: A Multi-Messenger Perspective (AGN12)*, page 14. (Cited in pages 11 and 12.)
- Pandey-Pommier, M., van Weeren, R. J., Ogorean, G. A., Combes, F., Johnston-Hollitt, M., Richard, J., Bagchi, J., Guiderdoni, B., Jacob, J., Dwarakanath, K. S., Narasimha, D., Edge, A., Ebeling, H., Clarke, T. E., and Mroczkowski, T. (2015). A Steep spectrum radio halo in merging galaxy cluster- MACSJ0416.1-2403. In Martins, F., Boissier, S., Buat, V., Cambrésy, L., and Petit, P., editors, *SF2A-2015: Proceedings of the Annual meeting of the French Society of Astronomy and Astrophysics*. Eds.: F. Martins, S. Boissier, V. Buat, L. Cambrésy, P. Petit, pp.247-252, pages 247–252. (Cited in pages 37 and 139.)
- Pascut, A. and Ponman, T. J. (2015). The Chandra Deep Group Survey - cool core evolution in groups and clusters of galaxies. *MNRAS*, 447:3723–3744. (Cited in page 56.)
- Peebles, P. J. E., Page, Jr., L. A., and Partridge, R. B. (2009). *Finding the Big Bang*. (Cited in page 12.)
- Petrosian, V. and East, W. E. (2008). Heating and Acceleration of Intracluster Medium Electrons by Turbulence. *ApJ*, 682:175–185. (Cited in page 30.)
- Pfrommer, C. and Enßlin, T. A. (2004). Estimating galaxy cluster magnetic fields by the classical and hadronic minimum energy criterion. *MNRAS*, 352:76–90. (Cited in page 27.)
- Pfrommer, C., Springel, V., Enßlin, T. A., and Jubelgas, M. (2006). Detecting shock waves in cosmological smoothed particle hydrodynamics simulations. *MNRAS*, 367:113–131. (Cited in page 26.)

- Piffaretti, R., Arnaud, M., Pratt, G. W., Pointecouteau, E., and Melin, J.-B. (2011). The MCXC: a meta-catalogue of x-ray detected clusters of galaxies. *A&A*, 534:A109. (Cited in pages 40 and 134.)
- Piran, T. (1995). Binary Neutron Stars. *Scientific American*, 272:52–61. (Cited in page 10.)
- Planck Collaboration, Adam, R., Ade, P. A. R., Aghanim, N., Arnaud, M., Ashdown, M., Aumont, J., Baccigalupi, C., Banday, A. J., Barreiro, R. B., and et al. (2016a). Planck 2015 results. IX. Diffuse component separation: CMB maps. *A&A*, 594:A9. (Cited in page 70.)
- Planck Collaboration, Ade, P. A. R., Aghanim, N., Arnaud, M., Ashdown, M., Aumont, J., Baccigalupi, C., Balbi, A., Banday, A. J., Barreiro, R. B., and et al. (2011a). Planck early results. XI. Calibration of the local galaxy cluster Sunyaev-Zeldovich scaling relations. *A&A*, 536:A11. (Cited in pages 57, 58 and 135.)
- Planck Collaboration, Ade, P. A. R., Aghanim, N., Arnaud, M., Ashdown, M., Aumont, J., Baccigalupi, C., Banday, A. J., Barreiro, R. B., Barrena, R., and et al. (2015). Planck 2015 results. XXVII. The Second Planck Catalogue of Sunyaev-Zeldovich Sources. *ArXiv e-prints*. (Cited in pages 64, 65 and 136.)
- Planck Collaboration, Ade, P. A. R., Aghanim, N., Arnaud, M., Ashdown, M., Aumont, J., Baccigalupi, C., Banday, A. J., Barreiro, R. B., Barrena, R., and et al. (2016b). Planck 2015 results. XXVII. The second Planck catalogue of Sunyaev-Zeldovich sources. *A&A*, 594:A27. (Cited in pages 37, 73, 136 and 139.)
- Planck Collaboration, Aghanim, N., Arnaud, M., Ashdown, M., Aumont, J., Baccigalupi, C., Balbi, A., Banday, A. J., Barreiro, R. B., Bartelmann, M., and et al. (2011b). Planck early results. IX. XMM-Newton follow-up for validation of Planck cluster candidates. *A&A*, 536:A9. (Cited in pages 21, 42, 44, 49, 56, 71 and 136.)
- Poole, G. B., Fardal, M. A., Babul, A., McCarthy, I. G., Quinn, T., and Wadsley, J. (2006). The impact of mergers on relaxed X-ray clusters - I. Dynamical evolution and emergent transient structures. *MNRAS*, 373:881–905. (Cited in pages 33 and 34.)
- Postman, M., Lubin, L. M., Gunn, J. E., Oke, J. B., Hoessel, J. G., Schneider, D. P., and Christensen, J. A. (1996). The Palomar Distant Clusters Survey. I. The Cluster Catalog. *AJ*, 111:615. (Cited in page 20.)
- Pratt, G. W., Croston, J. H., Arnaud, M., and Böhringer, H. (2009). Galaxy cluster X-ray luminosity scaling relations from a representative local sample (REXCESS). *A&A*, 498:361–378. (Cited in page 57.)
- Rengelink, R. B., Tang, Y., de Bruyn, A. G., Miley, G. K., Bremer, M. N., Roettgering, H. J. A., and Bremer, M. A. R. (1997). The Westerbork Northern Sky Survey (WENSS),

- I. A 570 square degree Mini-Survey around the North Ecliptic Pole. *A&AS*, 124. (Cited in page 48.)
- Roettiger, K., Stone, J. M., and Burns, J. O. (1999). Magnetic Field Evolution in Merging Clusters of Galaxies. *ApJ*, 518:594–602. (Cited in page 30.)
- Rottgering, H. J. A., Wieringa, M. H., Hunstead, R. W., and Ekers, R. D. (1997). The extended radio emission in the luminous X-ray cluster A3667. *MNRAS*, 290:577–584. (Cited in page 26.)
- Russell, H. R., van Weeren, R. J., Edge, A. C., McNamara, B. R., Sanders, J. S., Fabian, A. C., Baum, S. A., Canning, R. E. A., Donahue, M., and O’Dea, C. P. (2011). A merger mystery: no extended radio emission in the merging cluster Abell 2146. *MNRAS*, 417:L1–L5. (Cited in pages 26, 29, 70 and 75.)
- Santos, J. S., Rosati, P., Tozzi, P., Böhringer, H., Ettori, S., and Bignamini, A. (2008). Searching for cool core clusters at high redshift. *A&A*, 483:35–47. (Cited in pages 34 and 56.)
- Santos, J. S., Tozzi, P., Rosati, P., and Böhringer, H. (2010). The evolution of cool-core clusters. *A&A*, 521:A64. (Cited in page 56.)
- Sarazin, C. L. (1988). *X-ray emission from clusters of galaxies*. (Cited in page 21.)
- Sarazin, C. L. (2002). The Physics of Cluster Mergers. In Feretti, L., Gioia, I. M., and Giovannini, G., editors, *Merging Processes in Galaxy Clusters*, volume 272 of *Astrophysics and Space Science Library*, pages 1–38. (Cited in page 18.)
- Sault, R. J., Teuben, P. J., and Wright, M. C. H. (1995). A Retrospective View of MIRIAD. In Shaw, R. A., Payne, H. E., and Hayes, J. J. E., editors, *Astronomical Data Analysis Software and Systems IV*, volume 77 of *Astronomical Society of the Pacific Conference Series*, page 433. (Cited in page 43.)
- Scharf, C. (2012). *Gravity’s Engines*. (Cited in page 21.)
- Schuecker, P., Böhringer, H., Reiprich, T. H., and Feretti, L. (2001). A systematic study of X-ray substructure of galaxy clusters detected in the ROSAT All-Sky Survey. *A&A*, 378:408–427. (Cited in page 32.)
- Shakouri, S., Johnston-Hollitt, M., and Pratt, G. W. (2016). The ATCA REXCESS Diffuse Emission Survey (ARDES) - I. Detection of a giant radio halo and a likely radio relic. *MNRAS*, 459:2525–2538. (Cited in pages 40 and 76.)
- Shan, H., Qin, B., Fort, B., Tao, C., Wu, X.-P., and Zhao, H. (2010). Offset between dark matter and ordinary matter: evidence from a sample of 38 lensing clusters of galaxies. *MNRAS*, 406:1134–1139. (Cited in page 80.)

- Shimwell, T. W., Luckin, J., Brügger, M., Brunetti, G., Intema, H. T., Owers, M. S., Röttgering, H. J. A., Stroe, A., van Weeren, R. J., Williams, W. L., Cassano, R., de Gasperin, F., Heald, G. H., Hoang, D. N., Hardcastle, M. J., Sridhar, S. S., Sabater, J., Best, P. N., Bonafede, A., Chyży, K. T., Enßlin, T. A., Ferrari, C., Haverkorn, M., Hoeft, M., Horellou, C., McKean, J. P., Morabito, L. K., Orrù, E., Pizzo, R., Retana-Montenegro, E., and White, G. J. (2016). A plethora of diffuse steep spectrum radio sources in Abell 2034 revealed by LOFAR. *MNRAS*, 459:277–290. (Cited in page 26.)
- Shimwell, T. W., Röttgering, H. J. A., Best, P. N., Williams, W. L., Dijkema, T. J., de Gasperin, F., Hardcastle, M. J., Heald, G. H., Hoang, D. N., Horneffer, A., Intema, H., Mahony, E. K., Mandal, S., Mechev, A. P., Morabito, L., Oonk, J. B. R., Rafferty, D., Retana-Montenegro, E., Sabater, J., Tasse, C., van Weeren, R. J., Brügger, M., Brunetti, G., Chyży, K. T., Conway, J. E., Haverkorn, M., Jackson, N., Jarvis, M. J., McKean, J. P., Miley, G. K., Morganti, R., White, G. J., Wise, M. W., van Bemmel, I. M., Beck, R., Brienza, M., Bonafede, A., Calistro Rivera, G., Cassano, R., Clarke, A. O., Cseh, D., Deller, A., Drabent, A., van Driel, W., Engels, D., Falcke, H., Ferrari, C., Fröhlich, S., Garrett, M. A., Harwood, J. J., Heesen, V., Hoeft, M., Horellou, C., Israel, F. P., Kapińska, A. D., Kunert-Bajraszewska, M., McKay, D. J., Mohan, N. R., Orrù, E., Pizzo, R. F., Prandoni, I., Schwarz, D. J., Shulevski, A., Sipior, M., Smith, D. J. B., Sridhar, S. S., Steinmetz, M., Stroe, A., Varenus, E., van der Werf, P. P., Zensus, J. A., and Zwart, J. T. L. (2017). The LOFAR Two-metre Sky Survey. I. Survey description and preliminary data release. *A&A*, 598:A104. (Cited in page 90.)
- SKA (2017). Square kilometre array. <http://skatelescope.org/project/>. [Online; accessed 19-May-2017]. (Cited in page 13.)
- Smith, G. P., Kneib, J.-P., Smail, I., Mazzotta, P., Ebeling, H., and Czoske, O. (2005). A Hubble Space Telescope lensing survey of X-ray luminous galaxy clusters - IV. Mass, structure and thermodynamics of cluster cores at  $z=0.2$ . *MNRAS*, 359:417–446. (Cited in page 80.)
- Smolčić, V., Schinnerer, E., Finoguenov, A., Sakelliou, I., Carilli, C. L., Botzler, C. S., Brusa, M., Scoville, N., Ajiki, M., Capak, P., Guzzo, L., Hasinger, G., Impey, C., Jahnke, K., Kartaltepe, J. S., McCracken, H. J., Mobasher, B., Murayama, T., Sasaki, S. S., Shioya, Y., Taniguchi, Y., and Trump, J. R. (2007). A Wide-Angle Tail Radio Galaxy in the COSMOS Field: Evidence for Cluster Formation. *ApJS*, 172:295–313. (Cited in pages 70 and 74.)
- Smoot, G. F., Bennett, C. L., Kogut, A., Wright, E. L., Aymon, J., Boggess, N. W., Cheng, E. S., de Amici, G., Gulkis, S., Hauser, M. G., Hinshaw, G., Jackson, P. D., Janssen, M., Kaita, E., Kelsall, T., Keegstra, P., Lineweaver, C., Loewenstein, K., Lubin, P., Mather, J., Meyer, S. S., Moseley, S. H., Murdock, T., Rokke, L., Silverberg, R. F., Tenorio, L., Weiss, R., and Wilkinson, D. T. (1992). Structure in the COBE differential microwave radiometer first-year maps. *ApJ*, 396:L1–L5. (Cited in page 13.)

- Steer, D. G., Dewdney, P. E., and Ito, M. R. (1984). Enhancements to the deconvolution algorithm 'CLEAN'. *A&A*, 137:159–165. (Cited in page 45.)
- Stott, J. P., Pimblet, K. A., Edge, A. C., Smith, G. P., and Wardlow, J. L. (2009). The evolution of the red sequence slope in massive galaxy clusters. *MNRAS*, 394:2098–2108. (Cited in page 20.)
- Sunyaev, R. A. and Zeldovich, Y. B. (1970). The interaction of matter and radiation in the hot model of the Universe, II. *Ap&SS*, 7:20–30. (Cited in page 21.)
- Sunyaev, R. A. and Zeldovich, Y. B. (1972). The Observations of Relic Radiation as a Test of the Nature of X-Ray Radiation from the Clusters of Galaxies. *Comments on Astrophysics and Space Physics*, 4:173. (Cited in page 21.)
- Tasse, C. (2008). *Host galaxies and environment of active galactic nuclei - a study of the XMM Large Scale Structure survey*. PhD thesis, Leiden Observatory, Leiden University, P.O. Box 9513, 2300 RA Leiden, The Netherlands. (Cited in page 11.)
- Turner, B. K. (1973). Interstellar Molecules. *Scientific American*, 228:50–69. (Cited in page 9.)
- Urry, C. M. and Padovani, P. (1995). Unified Schemes for Radio-Loud Active Galactic Nuclei. *PASP*, 107:803. (Cited in page 11.)
- Vacca, V., Govoni, F., Murgia, M., Giovannini, G., Feretti, L., Tugnoli, M., Verheijen, M. A., and Taylor, G. B. (2011). Discovery of diffuse radio emission in the galaxy cluster A1689. *A&A*, 535:A82. (Cited in pages 37 and 139.)
- van Weeren, R. J., Andrade-Santos, F., Dawson, W. A., Golovich, N., Lal, D. V., Kang, H., Ryu, D., Brüggén, M., Ogrear, G. A., Forman, W. R., Jones, C., Placco, V. M., Santucci, R. M., Wittman, D., Jee, M. J., Kraft, R. P., Sobral, D., Stroe, A., and Fogarty, K. (2017a). The case for electron re-acceleration at galaxy cluster shocks. *Nature Astronomy*, 1:0005. (Cited in page 26.)
- van Weeren, R. J., Brüggén, M., Röttgering, H. J. A., Hoeft, M., Nuza, S. E., and Intema, H. T. (2011). Radio continuum observations of new radio halos and relics from the NVSS and WENSS surveys. Relic orientations, cluster X-ray luminosity, and redshift distributions. *A&A*, 533:A35. (Cited in pages 37 and 139.)
- van Weeren, R. J., Brunetti, G., Brüggén, M., Andrade-Santos, F., Ogrear, G. A., Williams, W. L., Röttgering, H. J. A., Dawson, W. A., Forman, W. R., de Gasperin, F., Hardcastle, M. J., Jones, C., Miley, G. K., Rafferty, D. A., Rudnick, L., Sabater, J., Sarazin, C. L., Shimwell, T. W., Bonafede, A., Best, P. N., Bîrzan, L., Cassano, R., Chyży, K. T., Croston, J. H., Dijkema, T. J., Enßlin, T., Ferrari, C., Heald, G., Hoeft, M., Horellou, C., Jarvis, M. J., Kraft, R. P., Mevius, M., Intema, H. T., Murray, S. S., Orrú, E., Pizzo, R., Sridhar,

- S. S., Simionescu, A., Stroe, A., van der Tol, S., and White, G. J. (2016). LOFAR, VLA, and Chandra Observations of the Toothbrush Galaxy Cluster. *ApJ*, 818:204. (Cited in pages 26 and 133.)
- van Weeren, R. J., Fogarty, K., Jones, C., Forman, W. R., Clarke, T. E., Brüggen, M., Kraft, R. P., Lal, D. V., Murray, S. S., and Röttgering, H. J. A. (2013). Complex Diffuse Radio Emission in the Merging Planck ESZ Cluster A3411. *ApJ*, 769:101. (Cited in pages 37 and 139.)
- van Weeren, R. J., Intema, H. T., Lal, D. V., Bonafede, A., Jones, C., Forman, W. R., Röttgering, H. J. A., Brüggen, M., Stroe, A., Hoeft, M., Nuza, S. E., and de Gasperin, F. (2014). The Discovery of a Radio Halo in PLCK G147.3-16.6 at  $z = 0.65$ . *ApJ*, 781:L32. (Cited in pages 37 and 139.)
- van Weeren, R. J., Ogorean, G. A., Jones, C., Forman, W. R., Andrade-Santos, F., Pearce, C. J. J., Bonafede, A., Brüggen, M., Bulbul, E., Clarke, T. E., Churazov, E., David, L., Dawson, W. A., Donahue, M., Goulding, A., Kraft, R. P., Mason, B., Merten, J., Mroczkowski, T., Nulsen, P. E. J., Rosati, P., Roediger, E., Randall, S. W., Sayers, J., Umetsu, K., Vikhlinin, A., and Zitrin, A. (2017b). Chandra and JVLA Observations of HST Frontier Fields Cluster MACS J0717.5+3745. *ApJ*, 835:197. (Cited in page 90.)
- van Weeren, R. J., Röttgering, H. J. A., Brüggen, M., and Hoeft, M. (2010). Particle Acceleration on Megaparsec Scales in a Merging Galaxy Cluster. *Science*, 330:347. (Cited in page 26.)
- Vedantham, H. K., Koopmans, L. V. E., de Bruyn, A. G., Wijnholds, S. J., Brentjens, M., Abdalla, F. B., Asad, K. M. B., Bernardi, G., Bus, S., Chapman, E., Ciardi, B., Daiboo, S., Fernandez, E. R., Ghosh, A., Harker, G., Jelic, V., Jensen, H., Kazemi, S., Lambropoulos, P., Martinez-Rubi, O., Mellema, G., Mevius, M., Offringa, A. R., Pandey, V. N., Patil, A. H., Thomas, R. M., Veligatla, V., Yatawatta, S., Zaroubi, S., Anderson, J., Asgekar, A., Bell, M. E., Bentum, M. J., Best, P., Bonafede, A., Breitling, F., Broderick, J., Brüggen, M., Butcher, H. R., Corstanje, A., de Gasperin, F., de Geus, E., Deller, A., Duscha, S., Eislöffel, J., Engels, D., Falcke, H., Fallows, R. A., Fender, R., Ferrari, C., Frieswijk, W., Garrett, M. A., Griebmeier, J., Gunst, A. W., Hassall, T. E., Heald, G., Hoeft, M., Hörandel, J., Iacobelli, M., Juette, E., Kondratiev, V. I., Kuniyoshi, M., Kuper, G., Mann, G., Markoff, S., McFadden, R., McKay-Bukowski, D., McKean, J. P., Mulcahy, D. D., Munk, H., Nelles, A., Norden, M. J., Orru, E., Pandey-Pommier, M., Pizzo, R., Polatidis, A. G., Reich, W., Renting, A., Röttgering, H., Schwarz, D., Shulevski, A., Smirnov, O., Stappers, B. W., Steinmetz, M., Swinbank, J., Tagger, M., Tang, Y., Tasse, C., ter Veen, S., Thoudam, S., Toribio, C., Vocks, C., Wise, M. W., Wucknitz, O., and Zarka, P. (2015). Lunar occultation of the diffuse radio sky: LOFAR measurements between 35 and 80 MHz. *MNRAS*, 450:2291–2305. (Cited in page 7.)

- Venturi, T., Giacintucci, S., Brunetti, G., Cassano, R., Bardelli, S., Dallacasa, D., and Setti, G. (2007). GMRT radio halo survey in galaxy clusters at  $z = 0.2-0.4$ . I. The REFLEX sub-sample. *A&A*, 463:937–947. (Cited in pages 29 and 40.)
- Venturi, T., Giacintucci, S., Dallacasa, D., Cassano, R., Brunetti, G., Bardelli, S., and Setti, G. (2008). GMRT radio halo survey in galaxy clusters at  $z = 0.2-0.4$ . II. The eBCS clusters and analysis of the complete sample. *A&A*, 484:327–340. (Cited in pages 29, 40, 47, 51, 72, 75, 76 and 137.)
- Verschuur, G. (2007). *The Invisible Universe*. (Cited in pages 5, 7 and 9.)
- Vikhlinin, A., Voevodkin, A., Mullis, C. R., van Speybroeck, L., Quintana, H., McNamara, B. R., Gioia, I., Hornstrup, A., Henry, J. P., Forman, W. R., and Jones, C. (2003). Cosmological Constraints from the Evolution of the Cluster Baryon Mass Function at  $z \sim 0.5$ . *ApJ*, 590:15–25. (Cited in page 15.)
- Voges, W., Aschenbach, B., Boller, T., Bräuninger, H., Briel, U., Burkert, W., Dennerl, K., Englhauser, J., Gruber, R., Haberl, F., Hartner, G., Hasinger, G., Kürster, M., Pfeffermann, E., Pietsch, W., Predehl, P., Rosso, C., Schmitt, J. H. M. M., Trümper, J., and Zimmermann, H. U. (1999). The ROSAT all-sky survey bright source catalogue. *A&A*, 349:389–405. (Cited in page 21.)
- White, J. A., Canning, R. E. A., King, L. J., Lee, B. E., Russell, H. R., Baum, S. A., Clowe, D. I., Coleman, J. E., Donahue, M., Edge, A. C., Fabian, A. C., Johnstone, R. M., McNamara, B. R., O’Dea, C. P., and Sanders, J. S. (2015a). Dynamical analysis of galaxy cluster merger Abell 2146. *MNRAS*, 453:2718–2730. (Cited in page 29.)
- White, J. A., Canning, R. E. A., King, L. J., Lee, B. E., Russell, H. R., Baum, S. A., Clowe, D. I., Coleman, J. E., Donahue, M., Edge, A. C., Fabian, A. C., Johnstone, R. M., McNamara, B. R., O’Dea, C. P., and Sanders, J. S. (2015b). Dynamical analysis of galaxy cluster merger Abell 2146. *MNRAS*, 453:2718–2730. (Cited in pages 70 and 76.)
- Willson, M. A. G. (1970). Radio observations of the cluster of galaxies in Coma Berenices - the 5C4 survey. *MNRAS*, 151:1–44. (Cited in page 25.)
- Young, A. and Young, L. (1975). Venus. *Scientific American*, 233:70–78. (Cited in page 7.)
- Zarka, P. (2011). Recent advances in the search for radio emissions from exoplanets. In *EPSC-DPS Joint Meeting 2011*, page 1068. (Cited in page 7.)
- Zaroubi, S. (2013). The Epoch of Reionization. In Wiklind, T., Mobasher, B., and Bromm, V., editors, *The First Galaxies*, volume 396 of *Astrophysics and Space Science Library*, page 45. (Cited in page 13.)
- Zwicky, F. (1933). Die Rotverschiebung von extragalaktischen Nebeln. *Helvetica Physica Acta*, 6:110–127. (Cited in page 17.)